

Top-Quark Search in the Dilepton Channel in  
1.8-TeV Proton-Antiproton Collisions

Takeshi Chikamatsu

①

# **Top-Quark Search in the Dilepton Channel in 1.8-TeV Proton-Antiproton Collisions**

Takeshi Chikamatsu

A dissertation submitted to the Doctoral Program in Physics,  
The University of Tsukuba in partial fulfillment of requirements  
for the degree of Doctor of Philosophy (in Physics)

February 1994



## Abstract

A search for the top quark ( $t$ ) in  $p\bar{p}$  collisions at  $\sqrt{s} = 1.8$  TeV is described. We consider the  $t\bar{t}$  pairs, followed by semileptonic decays via real W bosons:  $t\bar{t} \rightarrow W^+b W^- \bar{b} \rightarrow l_1 l_2 X$ , where  $l_1$  and  $l_2$  are electrons or muons. Analysis is based on data with an integrated luminosity of  $21.4 \text{ pb}^{-1}$  collected with the CDF detector at Fermilab in the 1992-93 collider run. We observe two  $e\mu$  events with the total dilepton backgrounds of  $0.56 \pm 0.14$  events. We also determine the lower bound on the top quark mass to be  $120 \text{ GeV}/c^2$  at the 95% CL.

## Acknowledgements

My great thanks go to my advisor, Professor Kunitaka Kondo, for giving me the opportunity to participate in this experiment, for his continuous encouragement during my five-year graduate student career.

I would like to express my great appreciation to Drs. G.P. Yeh and Milciades Contreras, who are the co-leaders of the group for this analysis. I learned a lot of physics, techniques, and philosophies which were accumulated in the history of CDF. Their excellent guidance and useful suggestions have been indispensable in the analysis.

I wish to thank Drs. Luc Demortier and Lingfeng Song who devoted much time with me to discuss and checking out this analysis.

I also thank Dr. Alvin Tollestrup, who gave me a lot of useful comments on the analysis and encouraged me personally.

This physics results presented here were obtained in the collaboration of the Collider Detector at Fermilab. I thank all of the physicists, engineers, and technicians of the collaboration who made this work possible. Many people helped with the analysis in one way or another. I want to thank C. Campagnari, A. Gordon, H. Keutelian, S. Kim, J. Konigsberg, S. Kopp, T. Liss, M. Mangano, A. Mukherjee, C. Newman-Holms, J. Romano, Y. Seiya, L. Stanco, J. Wang, Q. Wang, and C. Wendt.

I also want to express my thanks to Carol Picciolo, Kyoko Kunori, and Mutsumi Uenishi for their secretary work.

Finally my best appreciation goes to my family for their hospitality and support throughout my hard days of experiments, analysis, and the work on this thesis. Especially, I would like to dedicate this thesis to my mother, who is facing difficult times in her life.

This work was supported by the U.S. Department of Energy and National Science Foundation; the Italian Istituto Nazionale di Fisica Nucleare; the Ministry of Science, Culture, and Education of Japan; the Natural Sciences and Engineering Research Coun-



cil of Canada; the A. P. Sloan Foundation; and the Alexander von Humboldt-Stiftung.

## Contents

### Chapter 1. Introduction

#### 1.1. The book

#### 1.2. The author

#### 1.3. Acknowledgments

#### 1.4. The history of the book

#### 1.5. The structure of the book

#### 1.6. The notation

#### 1.7. The bibliography

#### 1.8. The index

#### 1.9. The appendix

#### 1.10. The glossary

#### 1.11. The preface

#### 1.12. The introduction

#### 1.13. The conclusion

#### 1.14. The epilogue

#### 1.15. The afterword

#### 1.16. The notes

#### 1.17. The references

#### 1.18. The index

# Contents

Acknowledgements	i
List of Tables	vii
The CDF Collaboration	xi
<b>1 Introduction</b>	<b>1</b>
1.1 Theoretical indication for the top quark . . . . .	2
1.2 Indirect evidences for the existence of top quark . . . . .	3
1.3 Indirect constraints on the top mass . . . . .	5
1.4 Previous Searches . . . . .	6
1.4.1 Searches at $e^+e^-$ colliders . . . . .	6
1.4.2 Searches at $p\bar{p}$ colliders . . . . .	7
1.5 Heavy quark production and decay . . . . .	10
1.5.1 Production . . . . .	10
1.5.2 Fragmentation of heavy quark . . . . .	13
1.5.3 Decay of heavy quark . . . . .	13
1.5.4 Signature . . . . .	15
1.6 Collider Run . . . . .	16
<b>2 Apparatus</b>	<b>26</b>
2.1 Tevatron . . . . .	26



2.2	The CDF Detector . . . . .	27
2.2.1	Beam-beam counter . . . . .	28
2.2.2	Tracking . . . . .	29
2.2.3	Calorimetry . . . . .	30
2.2.4	Muon chamber . . . . .	31
2.3	Trigger . . . . .	32
2.3.1	Electron trigger . . . . .	33
2.3.2	Muon trigger . . . . .	34
2.3.3	Offline reconstruction . . . . .	35
3	Monte Carlo Simulation . . . . .	45
3.1	Monte Carlo Data Sets . . . . .	46
4	Event Selection . . . . .	49
4.1	Electron Identification in CDF . . . . .	49
4.1.1	Offline clustering . . . . .	49
4.1.2	Electron response corrections . . . . .	50
4.1.3	Central Electron Identification Variables . . . . .	50
4.1.4	Plug Electron Identification Variables . . . . .	55
4.2	Muon Identification in CDF . . . . .	57
4.2.1	Identification variables . . . . .	58
4.3	Lepton Isolation . . . . .	60
4.4	Jets . . . . .	62
4.5	Missing transverse energy . . . . .	63
5	Dilepton Event Selection . . . . .	82
5.1	Dilepton event class . . . . .	82
5.2	Lepton $P_T$ cut . . . . .	83
5.3	Lepton track isolation . . . . .	84
5.4	Oppositely charged leptons . . . . .	84

5.5	$Z^0$ removal	85
5.6	Missing transverse energy	85
5.7	Two jet cut for higher mass top search	87
5.8	Data Analysis	89
5.8.1	$e\mu$	89
5.8.2	$ee$ and $\mu\mu$	89
<b>6</b>	<b>Efficiency measurement</b>	<b>115</b>
6.1	Geometric and kinematic acceptance	116
6.2	Lepton Identification	118
6.2.1	Lepton identification efficiency from $Z$ events	119
6.2.2	Efficiency calculation from top Monte Carlo	123
6.3	Isolation	126
6.4	Event topology cuts	126
6.5	Two-jet cut	127
6.6	Trigger	128
6.7	Total detection efficiency	129
6.8	Systematic uncertainties	131
<b>7</b>	<b>Background studies</b>	<b>146</b>
7.1	Dielectron and Dimuon Backgrounds from Drell-Yan	146
7.2	$Z^0 \rightarrow \tau\tau$	149
7.3	Background from $WW$ and $WZ$	151
7.4	Background from heavy flavor production ( $b\bar{b}$ )	153
7.5	$Z^0 \rightarrow b\bar{b}$	154
7.6	$Wb\bar{b}, Wc\bar{c}$	155
7.7	Fake dilepton background	156
7.8	Background Summary and Checks	159
<b>8</b>	<b>Discussion</b>	<b>167</b>



8.1	Top quark search in the higher mass region . . . . .	167
8.2	Low mass top search and limits on $t\bar{t}$ production . . . . .	168
9	Conclusions . . . . .	173
A	Calculation of Upper Limits on Poisson Processes . . . . .	174
A.1	Upper limits without systematic uncertainties . . . . .	174
A.2	Upper Limits with systematic uncertainties . . . . .	175
	Bibliography . . . . .	179

## List of Tables

1.1	Decay modes for a $t\bar{t}$ pair and their branching ratios (to lowest order) assuming charged-current decays. The symbol $q$ stands for a light quark: $u, d, c, s$ . . . . .	15
2.1	Summary of calorimeter properties. CEM(CHA), PEM(PHA) and FEM(FHA) denote the central, plug and forward EM(HAD) calorimeters. The symbol $\oplus$ signifies that the constant term is added in quadrature in the resolution. . . . .	31
4.1	Central electron selection requirement . . . . .	54
4.2	Plug electron selection requirement . . . . .	56
4.3	Central muon selection requirement . . . . .	59
4.4	Comparison of tracking and calorimeter isolation variables. The efficiencies in first two columns are from Monte Carlo. The second two, are from data. See text for details. . . . .	61
5.1	The fractions of $t\bar{t} \rightarrow ll + X$ having 1) both leptons coming directly from the top quark decay, 2) at least one lepton coming from the decay of a bottom or charm quark, and 3) one or both leptons coming from a $\tau$ decays. In category 2), fractions of both opposite and same sign events are shown. Lepton identification cuts are imposed. All numbers are percentages. . . . .	85
5.2	The efficiency of the two-jet cut of different jet $E_T$ thresholds for top and WW Monte Carlo events. . . . .	88



5.3	Summary of dilepton selection criteria . . . . .	88
5.4	Numbers of data events surviving various consecutive cuts. . . . .	90
5.5	Characteristics of the top-quark candidate events. Observed calorimeter $E_T$ is used for jet clusters. . . . .	91
6.1	Fractions of $t\bar{t} \rightarrow ll + X$ having 1) both leptons coming directly from the top quark decay, 2) at least one lepton coming from the decay of a bottom or charm quark, and 3) leptons coming from other decays except 1) and 2). This was calculated at the parton level using ISAJET Monte Carlo program. . . . .	117
6.2	Geometric and kinematic acceptances for the top mass from 100- 160 GeV/c <sup>2</sup> . . . . .	117
6.3	Central electron selection efficiency from $Z \rightarrow ee$ in data. Both tight and loose selection efficiencies are listed. Efficiencies calculated from Z Monte Carlo are also shown in the last column . . . . .	122
6.4	Plug electron selection efficiency . . . . .	123
6.5	Central muon selection efficiency from $Z \rightarrow \mu\mu$ . Efficiencies from Z Monte Carlo are also shown. . . . .	124
6.6	Single lepton identification efficiency extracted from top Monte Carlo. Errors are statistical only. . . . .	124
6.7	The lepton selection efficiency for the top mass from 100-160 GeV/c <sup>2</sup> . Errors are statistical only. . . . .	126
6.8	Isolation cut efficiency for the top masses:100-160 GeV/c <sup>2</sup> . Errors are statistical only. . . . .	127
6.9	The combined efficiency of the dilepton charge, invariant mass, and miss- ing $E_T$ cuts for top masses from 100-160 GeV/c <sup>2</sup> . Errors are statistical only. . . . .	128
6.10	Single lepton trigger efficiency at each trigger level . . . . .	128
6.11	Trigger efficiency . . . . .	129

6.12	Total efficiency . . . . .	130
6.13	Dilepton efficiency for a top mass of $140 \text{ GeV}/c^2$ . . . . .	130
6.14	Summary of uncertainties in the acceptance calculation. . . . .	133
6.15	Systematic uncertainty in the two-jet cut . . . . .	134
7.1	Cut rejections. Each line is an independent cut. . . . .	147
7.2	Efficiencies of having two or more jets with different parton $P_T$ threshold with Drell-Yan masses. . . . .	148
7.3	Number of events expected from Drell-Yan background. . . . .	149
7.4	Event topology cut efficiencies for the $Z^0 \rightarrow \tau\tau$ background with a (20,20) $P_T$ cut. . . . .	150
7.5	Number of events expected from the $Z \rightarrow \tau\tau$ background in $21.4 \text{ pb}^{-1}$ with different lepton $P_T$ , and with and without the two-jet requirement. Errors are statistical only. . . . .	150
7.6	Detection efficiency for WW and WZ with a two-jet requirement . . . . .	152
7.7	Number of WW events expected in $21.4 \text{ pb}^{-1}$ . . . . .	152
7.8	Number of events expected from $b\bar{b}$ background for a run of $21.4 \text{ pb}^{-1}$ . . . . .	154
7.9	Fake rates for each lepton category ,before and after b subtraction. . . . .	157
7.10	Expected background due to hadron misidentification for 15 GeV and 20 GeV lepton $P_T$ cuts. All cuts except for the 2-jet cut are applied. Also shown are the number of same-sign events found in the data for these cuts. . . . .	158
7.11	Expected background due to hadron misidentification for 15 GeV and 20 GeV lepton $P_T$ cuts after the 2-jet cut is applied. Also shown are the number of same-sign events found in the data for these cuts. . . . .	158
7.12	Number of background events expected $21.4 \text{ pb}^{-1}$ and the number of events observed in the data. . . . .	160
7.13	Number of $e\mu$ background events expected in $21.4 \text{ pb}^{-1}$ and the number of opposite-charge dilepton events observed in the data after isolation cuts and a $P_T$ threshold of $15 \text{ GeV}/c$ . . . . .	161



8.1	Theoretical prediction of $t\bar{t}$ cross section from Ref [26]. Efficiency $\times$ branching ratio and expected number of events in $21.4\text{ pb}^{-1}$ , as a function of top mass. . . . .	168
8.2	Theoretical prediction of $t\bar{t}$ cross section from Ref [26]. Efficiency $\times$ branching ratio and expected number of events in $21.4\text{ pb}^{-1}$ , as a function of top mass. . . . .	171

## The CDF Collaboration

F. Abe,<sup>13</sup> M. Albrow,<sup>7</sup> D. Amidei,<sup>16</sup> C. Anway-Wiese,<sup>4</sup> G. Apollinari,<sup>26</sup> H. Areti,<sup>7</sup> P. Auchincloss,<sup>25</sup> F. Azfar,<sup>21</sup> P. Azzi,<sup>20</sup> N. Bacchetta,<sup>18</sup> W. Badgett,<sup>16</sup> M. W. Bailey,<sup>24</sup> J. Bao,<sup>33</sup> P. de Barbaro,<sup>25</sup> A. Barbaro-Galtieri,<sup>14</sup> V. E. Barnes,<sup>24</sup> B. A. Barnett,<sup>12</sup> P. Bartalini,<sup>23</sup> G. Bauer,<sup>15</sup> T. Baumann,<sup>9</sup> F. Bedeschi,<sup>23</sup> S. Behrends,<sup>2</sup> S. Belforte,<sup>23</sup> G. Bellettini,<sup>23</sup> J. Bellinger,<sup>32</sup> D. Benjamin,<sup>31</sup> J. Benloch,<sup>15</sup> D. Benton,<sup>21</sup> A. Beretvas,<sup>7</sup> J. P. Berge,<sup>7</sup> A. Bhatti,<sup>26</sup> K. Biery,<sup>11</sup> M. Binkley,<sup>7</sup> F. Bird,<sup>28</sup> D. Bisello,<sup>20</sup> R. E. Blair,<sup>1</sup> C. Blocker,<sup>28</sup> A. Bodek,<sup>25</sup> V. Bolognesi,<sup>23</sup> D. Bortoletto,<sup>24</sup> C. Boswell,<sup>12</sup> T. Boulos,<sup>14</sup> G. Brandenburg,<sup>9</sup> E. Buckley-Geer,<sup>7</sup> H. S. Budd,<sup>25</sup> K. Burkett,<sup>16</sup> G. Busetto,<sup>20</sup> A. Byon-Wagner,<sup>7</sup> K. L. Byrum,<sup>1</sup> C. Campagnari,<sup>7</sup> M. Campbell,<sup>16</sup> A. Caner,<sup>7</sup> W. Carithers,<sup>14</sup> D. Carlsmith,<sup>32</sup> A. Castro,<sup>20</sup> Y. Cen,<sup>21</sup> F. Cervelli,<sup>23</sup> J. Chapman,<sup>16</sup> G. Chiarelli,<sup>8</sup> T. Chikamatsu,<sup>30</sup> S. Cihangir,<sup>7</sup> A. G. Clark,<sup>23</sup> M. Cobal,<sup>23</sup> M. Contreras,<sup>5</sup> J. Cooper,<sup>7</sup> M. Cordelli,<sup>8</sup> D. P. Coupal,<sup>28</sup> D. Crane,<sup>7</sup> J. D. Cunningham,<sup>2</sup> T. Daniels,<sup>15</sup> F. DeJongh,<sup>7</sup> S. Dell'Agnello,<sup>23</sup> M. Dell'Orso,<sup>23</sup> L. Demortier,<sup>26</sup> B. Denby,<sup>7</sup> M. Deninno,<sup>3</sup> P. F. Derwent,<sup>16</sup> T. Devlin,<sup>27</sup> M. Dickson,<sup>25</sup> S. Donati,<sup>23</sup> J. P. Done,<sup>29</sup> R. B. Drucker,<sup>14</sup> A. Dunn,<sup>16</sup> K. Einsweiler,<sup>14</sup> J. E. Elias,<sup>7</sup> R. Ely,<sup>14</sup> E. Engels, Jr.,<sup>22</sup> S. Eno,<sup>5</sup> D. Errede,<sup>10</sup> S. Errede,<sup>10</sup> A. Etchegoyen,<sup>7a</sup> Q. Fan,<sup>25</sup> B. Farhat,<sup>15</sup> I. Fiori,<sup>3</sup> B. Flaughner,<sup>7</sup> G. W. Foster,<sup>7</sup> M. Franklin,<sup>9</sup> M. Frautschi,<sup>18</sup> J. Freeman,<sup>7</sup> J. Friedman,<sup>15</sup> H. Frisch,<sup>5</sup> A. Fry,<sup>28</sup> T. A. Fuess,<sup>28</sup> Y. Fukui,<sup>13</sup> S. Funaki,<sup>30</sup> G. Gagliardi,<sup>23</sup> M. Gallinaro,<sup>20</sup> A. F. Garfinkel,<sup>24</sup> S. Geer,<sup>7</sup> D. W. Gerdes,<sup>16</sup> P. Giannetti,<sup>23</sup> N. Giokaris,<sup>26</sup> P. Giromini,<sup>8</sup> L. Gladney,<sup>21</sup> D. Glenzinski,<sup>12</sup> M. Gold,<sup>18</sup> J. Gonzalez,<sup>21</sup> A. Gordon,<sup>9</sup> A. T. Goshaw,<sup>6</sup> K. Goulianos,<sup>26</sup> H. Grassmann,<sup>28</sup> A. Grewal,<sup>21</sup> G. Grieco,<sup>23</sup> L. Groer,<sup>27</sup> C. Grosso-Pilcher,<sup>5</sup> C. Haber,<sup>14</sup> S. R. Hahn,<sup>7</sup> R. Hamilton,<sup>9</sup> R. Handler,<sup>32</sup> R. M. Hans,<sup>33</sup> K. Hara,<sup>30</sup> B. Harral,<sup>21</sup> R. M. Harris,<sup>7</sup> S. A. Hauger,<sup>6</sup> J. Hauser,<sup>4</sup> C. Hawk,<sup>27</sup> J. Heinrich,<sup>21</sup> D. Hennessy,<sup>6</sup> R. Hollebeek,<sup>21</sup> L. Holloway,<sup>10</sup> A. Hölscher,<sup>11</sup> S. Hong,<sup>16</sup> G. Houk,<sup>21</sup> P. Hu,<sup>22</sup> B. T. Huffman,<sup>22</sup> R. Hughes,<sup>25</sup> P. Hurst,<sup>9</sup> J. Huston,<sup>17</sup> J. Huth,<sup>7</sup> J. Hylen,<sup>7</sup> M. Incagli,<sup>23</sup> J. Incandela,<sup>7</sup> H. Iso,<sup>30</sup> H. Jensen,<sup>7</sup> C. P. Jessop,<sup>9</sup> U. Joshi,<sup>7</sup> R. W. Kadel,<sup>14</sup> E. Kajfasz,<sup>7</sup> T. Kamon,<sup>29</sup> T. Kaneko,<sup>30</sup> D. A. Kardelis,<sup>10</sup> H. Kasha,<sup>33</sup> Y. Kato,<sup>19</sup> L. Keeble,<sup>29</sup> R. D. Kennedy,<sup>27</sup> R. Kephart,<sup>7</sup> P. Kesten,<sup>14</sup> D. Kestenbaum,<sup>9</sup> R. M. Keup,<sup>10</sup> H. Keutelian,<sup>7</sup> F. Keyvan,<sup>4</sup> D. H. Kim,<sup>7</sup> H. S. Kim,<sup>11</sup> S. B. Kim,<sup>16</sup> S. H. Kim,<sup>30</sup> Y. K. Kim,<sup>14</sup> L. Kirsch,<sup>2</sup> P. Koehn,<sup>25</sup> K. Kondo,<sup>30</sup> J. Konigsberg,<sup>9</sup> S. Kopp,<sup>5</sup> K. Kordas,<sup>11</sup> W. Koska,<sup>7</sup> E. Kovacs,<sup>7a</sup> M. Krasberg,<sup>16</sup> S. E. Kuhlmann,<sup>1</sup> E. Kuns,<sup>27</sup> A. T. Laasanen,<sup>24</sup> S. Lammel,<sup>4</sup> J. I. Lamoureux,<sup>32</sup> T. LeCompte,<sup>10</sup> S. Leone,<sup>23</sup> J. D. Lewis,<sup>7</sup> P. Limon,<sup>7</sup> M. Lindgren,<sup>4</sup> T. M. Liss,<sup>10</sup> N. Lockyer,<sup>21</sup> O. Long,<sup>21</sup> M. Loreti,<sup>20</sup> E. H. Low,<sup>21</sup> D. Lucchesi,<sup>23</sup> C. B. Luchini,<sup>10</sup> P. Lukens,<sup>7</sup> P. Maas,<sup>32</sup> K. Maeshima,<sup>7</sup> A. Maghakian,<sup>26</sup> M. Mangano,<sup>23</sup> J. Mansour,<sup>17</sup> M. Mariotti,<sup>23</sup> J. P. Marriner,<sup>7</sup> A. Martin,<sup>10</sup> J. A. J. Matthews,<sup>18</sup> R. Mattingly,<sup>2</sup> P. McIntyre,<sup>29</sup> P. Melese,<sup>26</sup> A. Menzione,<sup>23</sup> E. Meschi,<sup>23</sup> G. Michail,<sup>9</sup> S. Mikamo,<sup>13</sup> M. Miller,<sup>5</sup> T. Mimashi,<sup>30</sup> S. Miscetti,<sup>8</sup> M. Mishina,<sup>13</sup> H. Mitsushio,<sup>30</sup> S. Miyashita,<sup>30</sup> Y. Morita,<sup>13</sup> S. Moulding,<sup>26</sup> J. Mueller,<sup>27</sup> A. Mukherjee,<sup>7</sup> T. Muller,<sup>4</sup> L. F. Nakae,<sup>28</sup> I. Nakano,<sup>30</sup> C. Nelson,<sup>7</sup>



D. Neuberger,<sup>4</sup> C. Newman-Holmes,<sup>7</sup> L. Nodulman,<sup>1</sup> S. Ogawa,<sup>30</sup> K. E. Ohl,<sup>33</sup> R. Oishi,<sup>30</sup> T. Okusawa,<sup>19</sup> C. Pagliarone,<sup>23</sup> R. Paoletti,<sup>23</sup> V. Papadimitriou,<sup>7</sup> S. Park,<sup>7</sup> J. Patrick,<sup>7</sup> G. Pauletta,<sup>23</sup> L. Pescara,<sup>20</sup> M. D. Peters,<sup>14</sup> T. J. Phillips,<sup>6</sup> G. Piacentino,<sup>3</sup> M. Pillai,<sup>25</sup> R. Plunkett,<sup>7</sup> L. Pondrom,<sup>32</sup> N. Produit,<sup>14</sup> J. Proudfoot,<sup>1</sup> F. Ptohos,<sup>9</sup> G. Punzi,<sup>23</sup> K. Ragan,<sup>11</sup> F. Rimondi,<sup>3</sup> L. Ristori,<sup>23</sup> M. Roach-Bellino,<sup>31</sup> W. J. Robertson,<sup>6</sup> T. Rodrigo,<sup>7</sup> J. Romano,<sup>5</sup> L. Rosenson,<sup>15</sup> W. K. Sakumoto,<sup>25</sup> D. Saltzberg,<sup>5</sup> A. Sansoni,<sup>8</sup> V. Scarpine,<sup>29</sup> A. Schindler,<sup>14</sup> P. Schlabach,<sup>9</sup> E. E. Schmidt,<sup>7</sup> M. P. Schmidt,<sup>33</sup> O. Schneider,<sup>14</sup> G. F. Sciacca,<sup>23</sup> A. Scribano,<sup>23</sup> S. Segler,<sup>7</sup> S. Seidel,<sup>18</sup> Y. Seiya,<sup>30</sup> G. Sganos,<sup>11</sup> M. Shapiro,<sup>14</sup> N. M. Shaw,<sup>24</sup> Q. Shen,<sup>24</sup> P. F. Shepard,<sup>22</sup> M. Shimojima,<sup>30</sup> M. Shochet,<sup>5</sup> J. Siegrist,<sup>28</sup> A. Sill,<sup>7a</sup> P. Sinervo,<sup>11</sup> P. Singh,<sup>22</sup> J. Skarha,<sup>12</sup> K. Sliwa,<sup>31</sup> D. A. Smith,<sup>23</sup> F. D. Snider,<sup>12</sup> L. Song,<sup>7</sup> T. Song,<sup>16</sup> J. Spalding,<sup>7</sup> P. Sphicas,<sup>15</sup> A. Spies,<sup>12</sup> L. Stanco,<sup>20</sup> J. Steele,<sup>32</sup> A. Stefanini,<sup>23</sup> K. Strahl,<sup>11</sup> J. Strait,<sup>7</sup> G. Sullivan,<sup>5</sup> K. Sumorok,<sup>15</sup> R. L. Swartz, Jr.,<sup>10</sup> T. Takahashi,<sup>19</sup> K. Takikawa,<sup>30</sup> F. Tartarelli,<sup>23</sup> Y. Teramoto,<sup>19</sup> S. Tether,<sup>15</sup> D. Theriot,<sup>7</sup> J. Thomas,<sup>28</sup> R. Thun,<sup>16</sup> M. Timko,<sup>31</sup> P. Tipton,<sup>25</sup> A. Titov,<sup>26</sup> S. Tkaczyk,<sup>7</sup> A. Tollestrup,<sup>7</sup> J. Tonnison,<sup>24</sup> J. F. de Troconiz,<sup>9</sup> J. Tseng,<sup>12</sup> M. Turcotte,<sup>28</sup> N. Turini,<sup>3</sup> N. Uemura,<sup>30</sup> F. Ukegawa,<sup>21</sup> G. Unal,<sup>21</sup> S. Vejckik, III,<sup>16</sup> R. Vidal,<sup>7</sup> M. Vondracek,<sup>10</sup> R. G. Wagner,<sup>1</sup> R. L. Wagner,<sup>7</sup> N. Wainer,<sup>7</sup> R. C. Walker,<sup>25</sup> J. Wang,<sup>5</sup> Q. F. Wang,<sup>26</sup> A. Warburton,<sup>11</sup> G. Watts,<sup>25</sup> T. Watts,<sup>27</sup> R. Webb,<sup>29</sup> C. Wendt,<sup>32</sup> H. Wenzel,<sup>14</sup> W. C. Wester, III,<sup>14</sup> T. Westhusing,<sup>10</sup> A. B. Wicklund,<sup>1</sup> E. Wicklund,<sup>7</sup> R. Wilkinson,<sup>21</sup> H. H. Williams,<sup>21</sup> P. Wilson,<sup>5</sup> B. L. Winer,<sup>25</sup> J. Wolinski,<sup>29</sup> D. Y. Wu,<sup>16</sup> X. Wu,<sup>23</sup> J. Wyss,<sup>20</sup> A. Yagil,<sup>7</sup> W. Yao,<sup>14</sup> K. Yasuoka,<sup>30</sup> Y. Ye,<sup>11</sup> G. P. Yeh,<sup>7</sup> M. Yin,<sup>6</sup> J. Yoh,<sup>7</sup> T. Yoshida,<sup>19</sup> D. Yovanovitch,<sup>7</sup> I. Yu,<sup>33</sup> J. C. Yun,<sup>7</sup> A. Zanetti,<sup>23</sup> F. Zetti,<sup>23</sup> S. Zhang,<sup>15</sup> W. Zhang,<sup>21</sup> and S. Zucchelli<sup>3</sup>

(CDF Collaboration)

- <sup>1</sup> Argonne National Laboratory, Argonne, Illinois 60439
- <sup>2</sup> Brandeis University, Waltham, Massachusetts 02254
- <sup>3</sup> Istituto Nazionale di Fisica Nucleare, University of Bologna, I-40126 Bologna, Italy
- <sup>4</sup> University of California at Los Angeles, Los Angeles, California 90024
- <sup>5</sup> University of Chicago, Chicago, Illinois 60637
- <sup>6</sup> Duke University, Durham, North Carolina 27708
- <sup>7</sup> Fermi National Accelerator Laboratory, Batavia, Illinois 60510
- <sup>8</sup> Laboratori Nazionali di Frascati, Istituto Nazionale di Fisica Nucleare, I-00044 Frascati, Italy
- <sup>9</sup> Harvard University, Cambridge, Massachusetts 02138
- <sup>10</sup> University of Illinois, Urbana, Illinois 61801
- <sup>11</sup> Institute of Particle Physics, McGill University, Montreal H3A 2T8, and University of Toronto, Toronto M5S 1A7, Canada
- <sup>12</sup> The Johns Hopkins University, Baltimore, Maryland 21218
- <sup>13</sup> National Laboratory for High Energy Physics (KEK), Tsukuba, Ibaraki 305, Japan
- <sup>14</sup> Lawrence Berkeley Laboratory, Berkeley, California 94720
- <sup>15</sup> Massachusetts Institute of Technology, Cambridge, Massachusetts 02139



- 16 *University of Michigan, Ann Arbor, Michigan 48109*
- 17 *Michigan State University, East Lansing, Michigan 48824*
- 18 *University of New Mexico, Albuquerque, New Mexico 87131*
- 19 *Osaka City University, Osaka 588, Japan*
- 20 *Universita di Padova, Istituto Nazionale di Fisica Nucleare, Sezione di Padova, I-35131 Padova, Italy*
- 21 *University of Pennsylvania, Philadelphia, Pennsylvania 19104*
- 22 *University of Pittsburgh, Pittsburgh, Pennsylvania 15260*
- 23 *Istituto Nazionale di Fisica Nucleare, University and Scuola Normale Superiore of Pisa, I-56100 Pisa, Italy*
- 24 *Purdue University, West Lafayette, Indiana 47907*
- 25 *University of Rochester, Rochester, New York 14627*
- 26 *Rockefeller University, New York, New York 10021*
- 27 *Rutgers University, Piscataway, New Jersey 08854*
- 28 *Superconducting Super Collider Laboratory, Dallas, Texas 75237*
- 29 *Texas A&M University, College Station, Texas 77843*
- 30 *University of Tsukuba, Tsukuba, Ibaraki 305, Japan*
- 31 *Tufts University, Medford, Massachusetts 02155*
- 32 *University of Wisconsin, Madison, Wisconsin 53706*
- 33 *Yale University, New Haven, Connecticut 06511*

# Chapter 1

## Introduction

Particle physics deals with the study of the fundamental constituents of matter and the nature of the interactions between them. As of today, the Standard Model of particle physics [1] with three generations of quarks and leptons has provided a successful description of known quarks and leptons. Within this model, the quarks occupy 3 left-handed doublets and six right-handed singlets as shown below.

$$\begin{array}{lll} \left( \begin{array}{c} \nu_e \\ e^- \end{array} \right)_L & \left( \begin{array}{c} \nu_\mu \\ \mu^- \end{array} \right)_L & \left( \begin{array}{c} \nu_\tau \\ \tau^- \end{array} \right)_L & e_R^- & \mu_R^- & \tau_R^- & \nu_{eR} & \nu_{\mu R} & \nu_{\tau R} \\ \left( \begin{array}{c} u \\ d' \end{array} \right)_L & \left( \begin{array}{c} c \\ s' \end{array} \right)_L & \left( \begin{array}{c} t \\ b' \end{array} \right)_L & d_R' & s_R' & b_R' & u_R & c_R & t_R \end{array}$$

The Standard Model predicts the existence of the top quark, but direct searches in the collider experiments have so far failed to yield evidence for the top quark.

We can argue several questions about the top quark:

- Does the top quark really exist?
- How strong is the current evidence for the top quark?
- How do we detect the top quark?



It is reported that the top quark must be more massive than  $91 \text{ GeV}/c^2$ , at least 18 times heavier than any other quark mass<sup>1</sup>. The most interesting question is why the top quark is so heavy. But we have no idea why it is heavier.

This thesis describes an attempt to search for the top quark, performed on data taken by CDF collaboration during the 1992-93 collider run at Fermilab. The search is made by detecting two high  $P_t$  leptons in the event. The dilepton decay channel is the most promising one to detect top, since the backgrounds are relatively small. The emphasis is placed on how to separate the signal from backgrounds.

The remainder of Chapter 1 is devoted to an overview of theoretical prediction and current status of the top quark searches and to describing the production and decay mechanisms which the Standard Model top quark is anticipated to have. Chapter 2 briefly reviews the Tevatron and the CDF detector. In Chapter 3, we discuss the Monte Carlo data sets to evaluate the acceptance for the top quark and to study background processes. Event selection tools are described in Chapter 4. Based on these tools, dilepton event selection criteria to enhance the top signal is studied in Chapter 5. This section also describes the results of the search in our data sample. Chapter 6 is devoted to the determination of the detection efficiency for the top quark. Systematic uncertainties are also estimated. In Chapter 7 we estimate the background contribution to our selection criteria. In Chapter 8 we summarize the top quark search both in the high mass region and in the low mass region. We also derive a lower limit on the top quark mass. Chapter 9 concludes this analysis.

## 1.1 Theoretical indication for the top quark

The theoretical motivation the top quark must exist is that the complete families are required for the cancellation of anomalies in the current which couple to gauge fields. If the gauge current is anomalous, the gauge theory is not renormalizable. Hence the

---

<sup>1</sup>Recently, D0 collaboration extended the lower bound on the top mass to  $131 \text{ GeV}/c^2$  [2]



partner of the  $b, \tau$  and  $\nu_\tau$  must exist to complete the third family.

## 1.2 Indirect evidences for the existence of top quark

The top quark should exist in the framework of the Standard Model. Evidence for its existence is quite strong. Experimentally, there are four pieces of data which indicate the existence of an  $SU(2)$  partner of the bottom quark, *i.e.*, top quark.

They all come from measurement of the properties of  $b$  mesons.

### (1) Forward-backward asymmetry in $e^+e^- \rightarrow b\bar{b}$

In the Standard Model, the bottom quark is produced in  $e^+e^-$  annihilation with a forward-backward asymmetry which is given by

$$A_{FB}^b = \frac{\sigma(\theta < \pi/2) - \sigma(\theta > \pi/2)}{\sigma(\theta < \pi/2) + \sigma(\theta > \pi/2)} \simeq \frac{-3T_e^3 T_b^3 s / M_Z^2}{8 \sin^2 \theta_W \cos^2 \theta_W \cdot Q_b (s/M_Z^2 - 1)}$$

With  $T_e^3 = T_b^3 = -1/2$ ,  $Q_b = -1/3$  and the measured  $M_Z$  and  $\sin^2 \theta$ , one can expect an asymmetry of about -0.25 at a center of mass energy of  $\sqrt{s} \simeq 35$  GeV. The JADE collaboration has observed an asymmetry of  $-25.0 \pm 6.5$  % at the PETRA  $e^+e^-$  collider [8]. In the absence of a top quark, the bottom quark would be a singlet of weak isospin ( $T_b^3 = 0$ ) resulting in zero asymmetry.

### (2) Upper limit on the flavor changing decay $b \rightarrow \mu^+ \mu^- X$

At the time when only  $u, d, s$  quarks were known, Glashow, Iliopoulos and Maiani pointed out that the existence of a charm quark (in a same doublet with the  $s$  quark) would explain the experimentally observed extreme suppression of flavor changing neutral current (FCNC)  $s \rightarrow d$  transitions (GIM mechanism). It is natural to search for flavor-changing neutral currents in the weak decays of the  $b$  quark.

Some nonstandard models predict FCNC in the  $b$  decay. Kane and Peskin[13] showed that the ratio  $\Gamma(b \rightarrow l^+ l^- + X) / \Gamma(b \rightarrow l \nu X)$  must exceed 0.12, if there were no top quark and the bottom quark were a member of a left-handed-singlet. This corresponds to a branching ratio for  $b \rightarrow l^+ l^- X$  of greater than  $1.3 \times 10^{-2}$ . No positive evidence for FCNC

in the  $b$  decay has been observed. Upper limits on the branching ratio for  $b \rightarrow l^+ l^- + X$  have been set by several groups and the most stringent limit is  $1.2 \times 10^{-3}$  from a CLEO search[14], a factor of 10 below the Kane-Peskin limit.

### (3) Observed value of the $B^0 \bar{B}^0$ mixing

It was a surprising results that the observation of nonvanishing amount of  $B_d^0 \bar{B}_d^0$  mixing was made by the ARGUS collaboration [15]. While the UA1 collaboration [16] had already observed a positive signal of  $B^0 \bar{B}^0$  mixing the previous year, it could be ascribed to  $B_s$  mesons; the ARGUS signal was the first to point to mixing of  $B_d$  mesons.

The important contribution to mixing is via the box diagrams of Figure 1.1. The mixing is usually described by the mixing parameter  $r$  which is defined as the ratio of the probabilities that an initial  $B^0$  decay as a  $\bar{B}^0$  or as a  $B^0$ ,  $r = \text{prob}(B^0 \rightarrow \bar{B}^0) / \text{prob}(B^0 \rightarrow B^0)$ , where  $r=0$  means no mixing.

The mixing parameter  $r_d$  is given by [17]

$$r_d = \frac{(\Delta M / \Gamma)^2}{2 + (\Delta M / \Gamma)^2} = \frac{x^2}{2 + x^2},$$

where  $\Delta M$  is the mass difference between weak eigen states of  $B^0$  and  $\bar{B}^0$  and  $\Gamma$  is their lifetime.  $\Delta M$  calculated from the matrix element for the  $B_d$  transition assuming the box diagram with a virtual top quark exchange is given by [17]

$$\Delta M = 1/6\pi^2 G_F^2 B_b f_b m_{top}^2 m_b |V_{tb} V_{td}^*|^2.$$

Note that  $\Delta M$  is proportional to square of the top quark mass,  $m_{top}$ . The observed large  $B^0 \bar{B}^0$  mixing actually indicates that the top quark is heavy. ARGUS reported [15] that  $r_d = 0.22 \pm 0.08$ . This value suggests that the top quark mass is larger than about 50 GeV/c<sup>2</sup>.

### (4) Measurement of $Z \rightarrow b\bar{b}$ width

The last evidence for the existence of the top quark comes from the precision measure-



ment of  $Z \rightarrow b\bar{b}$  decay width at LEP by ALEPH and L3 [18] which give

$$\Gamma(Z \rightarrow b\bar{b}) = 350 \pm 50 \text{ MeV}.$$

One can calculate the width including the small QCD correction to be

$$\Gamma(Z \rightarrow b\bar{b}) = \frac{G_F M_Z^3}{\pi\sqrt{2}} \left(1 + \frac{\alpha_s}{\pi}\right) [(T_b^3 - Q_b \sin^2 \theta_W)^2 + (Q_b \sin^2 \theta_W)^2],$$

and gets

$$\begin{aligned} \Gamma(Z \rightarrow b\bar{b}) &= 381 \text{ MeV for } T_b^3 = -1/2; \\ &= 24 \text{ MeV for } T_b^3 = 0 \end{aligned}$$

corresponding to whether the  $b$  quark is accompanied by a SU(2) partner or not. The measured value clearly suggests the presence of a SU(2) partner of  $b$  -i.e. the top quark.

### 1.3 Indirect constraints on the top mass

A number of indirect constraints on the top mass is available.

The ratio of cross sections for W and Z production with subsequent decay into  $e\nu$  or  $ee$  is related to the W and Z total width through the formula,

$$R = \frac{\sigma_W Br(W \rightarrow e\nu)}{\sigma_Z Br(Z \rightarrow ee)} = \frac{\sigma_W}{\sigma_Z} \frac{\Gamma(W \rightarrow e\nu)}{\Gamma(Z \rightarrow ee)} \frac{\Gamma_Z}{\Gamma_W}$$

The measurement of the ratio R allows us to set a lower limit on the top mass, independent of its decay modes. The width of the W ( $\Gamma_W$ ), which depends on the top quark mass, can be extracted from the ratio. The first two terms are predicted by QCD, and a large fraction of the uncertainties cancel in taking the ratio of the cross section. The width of the Z is precisely measured by LEP. We find that  $M_{top} > 45(49) \text{ GeV}/c^2$  at 95(90) % confidence level [19].



Measurements of low-energy neutral current parameters and vector boson masses are sensitive to the top mass via one-loop radiative corrections in the Standard Model. The relation between the electroweak parameters can be expressed [20] as

$$\sin^2\theta_W = \frac{A^2}{M_W^2(1 - \Delta r)},$$

where  $A = (\pi\alpha/\sqrt{2}G_\mu)^{1/2}$ ,  $\sin^2\theta_W = 1 - M_W^2/M_Z^2$  and  $\Delta r$  is a radiative correction involving, among other parameters, the unknown top mass and the Higgs mass. The upper bound on the top mass is estimated to be 150-250 GeV/c<sup>2</sup> [9].

We can see that there are a number of parameters within the Standard Model which have some dependence on the top mass. Thus by combining all of the measurements with the theoretical analysis of their dependences on the top mass, it is possible to extract predictions for the allowable range and most likely value for this parameter. Several groups have reported the mass range and global fits to recent precision electroweak measurements yield a favored mass of  $M_{top} = 164_{-16-20}^{+17+18}$  GeV/c<sup>2</sup> [11]

## 1.4 Previous Searches

Direct searches in the collider experiments have so far failed to yield evidence for the top quark. We describe these searches at  $e^+e^-$  and  $p\bar{p}$  colliders.

### 1.4.1 Searches at $e^+e^-$ colliders

In  $e^+e^-$  colliders, charged particles of mass up to the energy of the beam can be produced in pairs. Thus we would expect to observe charged quarks with mass up to the highest energy available, until recently at LEP.

An electron and a positron annihilate into quark and antiquark pairs. The hadron cross section, relative to the  $\mu$ -pair cross section given by

$$R = \sigma(e^+e^- \rightarrow \text{hadrons})/\sigma(e^+e^- \rightarrow \mu\mu) = 3 \sum e_i^2,$$

where  $e_i$  are the charges of quarks and the factor of three comes from three colored quarks. This  $R$  value means just the sum of the squares of the quark charges times the number of colors in the final state. For the center of mass energy  $>10$  GeV, all the known quarks are included in the sum,

$$\begin{aligned} R &= 3 (e_u^2 + e_d^2 + e_s^2 + e_c^2 + e_b^2) \\ &= 3 (4/9 + 4/9 + 1/9 + 1/9 + 1/9) = 3.66 \end{aligned}$$

A plot of measured  $R$  value is shown in Figure 1.9. It is clear from this figure that the ratio is essentially constant in between thresholds for production of new heavy quarks.

An increase in the hadronic cross section at the threshold for production of a new generation of quarks: for top quarks,  $e_t = 2/3$  one should observe  $\Delta R = 4/3$ ;

The process  $Z \rightarrow t\bar{t}$  is an excellent way to look for the light top quark, and the large number of  $Z$ 's allows the LEP experiment to exclude a top quark mass less than  $46 \text{ GeV}/c^2$  at 95% confidence level with little dependence on the top decays.

### 1.4.2 Searches at $p\bar{p}$ colliders

The proton-antiproton collider experiments at CERN and Tevatron give us a unique opportunity and have played a major role to search for the top quark because of its large center of mass energy.

#### Searches at $Spp\bar{S}$

The first hadron collider search was made by UA1 at  $Spp\bar{S}$  [21]. UA1 explored a top quark mass range above  $40 \text{ GeV}/c^2$ , where  $p\bar{p} \rightarrow W \rightarrow t\bar{b}$  is more important than the strong production channel at  $\sqrt{s} = 630 \text{ GeV}$ . Top searches by UA1 have been performed using the  $\mu + \text{jets}$  and  $\mu\mu$  channels.

The  $\mu + \text{jets}$  selection applied on the 1988-1989 data required an isolated muon with transverse momentum  $P_T^\mu > 12 \text{ GeV}/c^2$  accompanied by at least two jets with transverse



energies  $E_T^{jet1} > 13$  GeV and  $E_T^{jet2} > 7$  GeV. A transverse mass <sup>2</sup> cut of  $M_T^{\mu\nu} < 60$  GeV/ $c^2$  is used to reject backgrounds from  $W \rightarrow \mu\nu$  produced in association with jets. After selection, the main backgrounds for top are muons from the semileptonic decays of heavy flavors in  $b\bar{b}$  and  $c\bar{c}$  events, and from the decay in flight of kaons and pions. Four variables are used to distinguish the top signal from from backgrounds. (i) An isolation variable,  $I \equiv \sqrt{(\sum E_T/3)^2 + (\sum P_T/2)^2}$ , where the sum runs over all calorimeter cells and tracks in a cone of radius  $R=0.7$  <sup>3</sup> surrounding the muon. (ii) The muon transverse momentum,  $P_T^\mu$ . (iii) The missing transverse energy,  $\cancel{E}_T$ . (iv) The azimuthal separation between the muon and the leading jet,  $\Delta\phi(\mu - jet1)$ .

Muons from  $b\bar{b}$  and  $c\bar{c}$  are produced inside or near jets and are not isolated while muons from very heavy quark decay are usually well separated from the jets and therefore isolated. No excess of isolated muons is observed in the UA1 data.

For improved sensitivity, all four variables are combined in a 'likelihood' variable :

$$L = \prod_{i=1}^4 P_{top}(X_i)/P_{bot}(X_i), \quad (1.1)$$

where  $P_{top}(X_i)$  and  $P_{bot}(X_i)$  are the probability density functions of the variable  $X_i$  for top signal events and for  $b\bar{b}$  and  $c\bar{c}$  background events, respectively. After a final cut of  $\ln(L) > 4$ , only 2 events remain in the data while  $2.8 \pm 0.8$  events are expected from  $b\bar{b}$ ,  $c\bar{c}$  and decays in flight. A total of 6.2 top events (4.1 from  $t\bar{b}$  and 2.1 from  $t\bar{t}$ ) are expected for  $M_{top} = 50$  GeV/ $c^2$ . From the  $\mu +$  jets analysis, a 95 % CL lower limit of  $M_{top} > 52$  GeV/ $c^2$  is obtained.

The UA1 search in the  $\mu\mu$  channel required one isolated muon with  $P_T^\mu > 8$  GeV/ $c$ , a second non-isolated muon with  $P_T^\mu > 3$  GeV/ $c$  and at least one jet with  $E_T^{jet} > 10$  GeV to search for  $W \rightarrow t\bar{b}$ . Again, no top signal was found and the data were consistent with

<sup>2</sup>The transverse mass variable is defined as  $M_T^{\mu\nu} = \sqrt{2P_T^\mu \cancel{E}_T (1 - \cos \Delta\phi_{\mu\nu})}$ , with  $\cancel{E}_T$  the missing transverse energy in the event, and  $\Delta\phi_{\mu\nu}$  the azimuthal separation between the muon and missing transverse energy vectors.

<sup>3</sup>R is a distance measured in pseudorapidity-azimuth space (radians).  $R \equiv \sqrt{(\Delta\eta)^2 + (\Delta\phi)^2}$ .  $\eta = -\ln(\tan(\theta/2))$ .  $\theta$  is the angle to the proton direction.



expected backgrounds, predominantly from b-quark and c-quark production and decays in flight. The  $\mu\mu$  channel alone excludes  $M_{top} > 46 \text{ GeV}/c^2$  at the 95 % CL.

UA1 has combined the 1988-1989 searches in the  $\mu + \text{jets}$  and  $\mu\mu$  channels with previous searches from 1983-1985 in the  $e + \text{jets}$ ,  $\mu + \text{jets}$ , and  $\mu\mu$  channels. The combined UA1 limit is  $M_{top} > 60 \text{ GeV}/c^2$  at the 90% CL.

The UA2 collaboration has looked for semileptonic decays of the top quark in the  $e + \text{jets}$  channel [4]. The UA2  $e + \text{jets}$  selection required an electron candidate with  $E_T^e > 12 \text{ GeV}$ , missing transverse energy  $\cancel{E}_T < 15 \text{ GeV}$ , and at least one jet with  $E_T^{jet} > 10 \text{ GeV}$ . To reduce misidentification backgrounds, events with the electron back-to-back to the leading jet were rejected. The major background after these cuts is from high  $P_T$   $W$  events produced in association with jets. The transverse mass of the electron-neutrino system

$$M_T^{e\nu} = \sqrt{2E_T^e \cancel{E}_T (1 - \cos \Delta\phi_{e\nu})}, \quad (1.2)$$

is used to distinguish a possible top signal from the  $W + \text{jets}$  background. The transverse mass distribution for the UA2 data was found to be consistent with expectations from  $W$  boson decay alone. The top quark would manifest itself as an excess of events in the low transverse mass region. The absence of such an excess in the UA2 data implies that  $M_{top} > 69 \text{ GeV}/c^2$  at the 95% CL.

### Previous searches at CDF

The first CDF top results came from searches in the  $e + \text{jets}$ [5] channel and in the  $e\mu$ [6] channel. The search in  $e + \text{jets}$ , similar to the UA2 analysis already described, employed the transverse mass variable to discriminate between top events and the dominant  $W + \text{jets}$  background. A limit of  $M_{top} > 77 \text{ GeV}/c^2$  was obtained. This method is no longer useful when  $M_{top}$  approaches  $M_W$ , in which case the transverse mass distributions are very similar.

The  $e\mu$  signature requires the presence of an electron and a muon with opposite electric charges, each with transverse momentum above the threshold  $P_T^{min} = 15 \text{ GeV}/c^2$ .



There is one event in the top quark signal region. Given one candidate event, a 95%-C.L. the lower bound on the top mass of  $72 \text{ GeV}/c^2$  was obtained.

A straightforward extension of the  $e\mu$  analysis is to also search for top in  $ee$  and  $\mu\mu$  events[7]. Dielectron and dimuon events were selected by requiring  $P_T > 15 \text{ GeV}/c^2$  for each lepton. A simple mass cut around the  $Z$  peak removes most of the background from  $Z$  decays. After the mass cut, the signal to background ratio is improved by requiring missing transverse energy  $\cancel{E}_T > 20 \text{ GeV}$ . Also, events with back-to-back or collinear dileptons are eliminated by requiring the azimuthal opening between the leptons to be in the region  $\Delta_{l+l-} < 160^\circ$ . After all cuts, there are no  $ee$  or  $\mu\mu$  events remaining in the data. With only one  $e\mu$  event observed, the limit from the  $e\mu$ ,  $ee$ , and  $\mu\mu$  channels together is  $M_{top} > 85 \text{ GeV}/c^2$ .

Finally, CDF has looked for additional low  $P_T$  muons in the  $e + \text{jets}$  and  $\mu + \text{jets}$  samples. The low  $P_T$  muon in the event is employed as a possible tag of the bottom quark in the chain  $t \rightarrow b \rightarrow \mu$ . No candidates were found. The result of the low  $P_T$  muon search combined with the previous dilepton searches extends the CDF top quark mass limit to  $M_{top} > 91 \text{ GeV}$  at the 95%-C.L.

## 1.5 Heavy quark production and decay

### 1.5.1 Production

The parton model describes successfully the hadronic cross section involving a large momentum transfer. We assume that any physically observed hadrons are made up of constituent particles, "partons", which we identify with quarks and gluons. At high energy, the masses of partons are negligible compared to the scale of  $Q$  of the hard scattering. A schematic view of a  $p\bar{p}$  collision is shown in Figure xx. In this picture the scattering occurs between partons that are treated as quasi free particles inside hadrons.

The parton model cross section is given by the formula

$$\sigma = \sum_{i,j} \int dx_1 dx_2 \hat{\sigma}_{ij}(\hat{s}) f_i(x_1, Q^2) f_j(x_2, Q^2)$$

The momentum distributions of the initial partons are represented by a set of parton distribution functions  $f_i$ , which gives the probability for finding a parton of type  $i$  inside the hadron carrying a fraction  $x$  of the hadron's total momentum. The subscript  $i$  and  $j$  indicate the type of the incoming parton. The sum extends over all parton cross sections  $\hat{\sigma}_{ij}$  contributing the process. The parton cross section is evaluated at the parton center of mass energy  $\sqrt{\hat{s}}$  through the relation  $\hat{s} = x_1 x_2 s$ . They are calculable with perturbative QCD and are expressed as an expansion in the coupling constant  $\alpha_s$ .

In the lowest order ( $\alpha_s^2$ ), the processes are quark-antiquark annihilation and gluon-gluon fusion:

$$\begin{aligned} g + g &\rightarrow Q + \bar{Q} \\ q + \bar{q} &\rightarrow Q + \bar{Q} \end{aligned} \tag{1.3}$$

The Feynman diagrams for these processes are shown in Figure 1.3. Two important kinematic consequences of the leading order processes are (1) the quark and antiquark are produced back-to-back in the parton-parton center of mass frame and remain back-to-back in the plane transverse to the colliding beam and (2) the heavy quarks are emitted with an average transverse momentum of about the half of the quark mass.

The issue of higher order QCD corrections is important in heavy quark production. The splitting of a final state gluon from  $gg \rightarrow gg$ , into a pair of heavy quark ( $g \rightarrow Q\bar{Q}$ ) occurs with only a small fraction of order  $\sim \alpha_s(m^2)$  of the time. However, given the large cross section of  $gg \rightarrow gg$ , it can be a competitive quark production process. This process ( $gg \rightarrow gQ\bar{Q}$ ) and other  $2 \rightarrow 3$  processes of order  $\alpha_s^3$ , as well as the  $\alpha_s^3$  part of the  $2 \rightarrow 2$  processes of 1.3 have been calculated by Nason, Dawson and Ellis [25]. The following parton subprocesses are included in the calculation up to order  $\alpha_s^3$ :



$$\begin{aligned}
q + \bar{q} &\rightarrow Q + \bar{Q} & \alpha_S^2, \alpha_S^3 \\
g + g &\rightarrow Q + \bar{Q} & \alpha_S^2, \alpha_S^3 \\
q + \bar{q} &\rightarrow Q + \bar{Q} + g & \alpha_S^3 \\
g + g &\rightarrow Q + \bar{Q} + g & \alpha_S^3 \\
g + q &\rightarrow Q + \bar{Q} + q & \alpha_S^3 \\
g + \bar{q} &\rightarrow Q + \bar{Q} + \bar{q} & \alpha_S^3
\end{aligned} \tag{1.4}$$

The theoretical cross sections depend on three different input quantities: parton distribution functions, choice of renormalization and factorization scale  $\mu$ , the choice of running coupling  $\alpha_S$  (or equivalently, the choice of the QCD parameter  $\Lambda$ , since  $\alpha_S$  is a function of  $\mu/\Lambda$ ), and the mass of the heavy quark.

The corrections affect the  $t\bar{t}$  production cross section. Due to the large uncertainties in the gluon structure function at small  $x$  together with contributions to the total cross section from gluon-gluon diagrams, total cross section is quite uncertain.

Since the top quark is now believed to be heavier than the  $W$ , a dominant production process is the  $t\bar{t}$  pair creation by gluon-gluon fusion and  $q\bar{q}$  annihilation. Above a top mass of about 100 GeV/c<sup>2</sup>,  $q\bar{q}$  annihilation is expected to be the dominant production source.

In order for the experiment to compute the number of  $t\bar{t}$  events expected, or to set the lower bound on the top mass, it is important to have a good central values for the production cross sections as well as estimation of systematic uncertainties. Cross sections have been calculated within QCD at the full NLO [25]. Recent work has extended those results with the inclusion of classes of higher-order diagrams dominated by the emission of multiple soft gluons[26].

### 1.5.2 Fragmentation of heavy quark

After a heavy quark is produced, it ‘fragments’ or ‘hadronizes’ into a hadron containing its flavor, and some softer, light-flavored hadrons.

The fragmentation function  $D_Q^H$  of a heavy quark  $Q$  into a  $Q$ -flavored hadron  $H$  describes the probability that the hadron carries away a fraction of the quark’s momentum between  $z = P_H/P_Q$  and  $z + dz$ . A softer fragmentation (i.e. the hadron carries away less of the quark’s momentum) will result in more accompanying hadrons with higher energies. Heavy quark fragmentation is modeled with the Peterson parametrization [33]:

$$D_Q^H = \frac{N}{z[1 - (1/z) - \epsilon_Q/(1 - z)]^2} \quad (1.5)$$

where  $N$  is a normalization constant and the Peterson parameter  $\epsilon$  is proportional to  $1/M_Q^2$ . The Peterson parametrization adequately describes existing  $c$  and  $b$  quark fragmentation data, as is seen in figure 1.6.

In the spectator approximation, the heavy quark contained in the hadron is assumed to decay independently of the other constituents, since the energy released by the quark is much bigger than the typical quark binding energies.

### 1.5.3 Decay of heavy quark

The experimental lower limit of  $91 \text{ GeV}/c^2$  on the top mass is valid so that the top quark decays into a bottom quark and a charged intermediate vector boson ( $t \rightarrow Wb$ )<sup>4</sup> in the minimal Standard Model. In the limit in which  $M_{top} > m_W$  the width is given by

$$\Gamma(t \rightarrow bW) = \frac{G_F M_{top}^3}{8\pi\sqrt{2}} |V_{tb}|^2 \approx 170 |V_{tb}|^2 \left(\frac{m_T}{m_W}\right)^3$$

MeV

<sup>4</sup>Decays into a strange quark or a down quark is possible:  $t \rightarrow Ws$  or  $Wd$ . But according to the Kobayashi-Maskawa theory, the top decay rate into these two quarks are too small to detect, because KM matrix elements  $V_{ts}$  ( $\Gamma_s \sim 0.0025$ ) and  $V_{td}$  ( $\Gamma_d \sim 10^{-4}$ ) are very small compared to  $V_{tb}$ , which is close to 1.



When the top quark is so heavy that the width becomes bigger than a typical hadronic scale. The top quark decays before its hadronization so that the mesons are never formed.

The two  $W$  bosons subsequently decay either to a lepton and a neutrino or a quark and an antiquark while the  $b$  quarks hadronize to a jet. The branching fractions for the different decay modes are listed in Table 1.1. The  $t\bar{t}$  decays can be characterized by the decay mode of the final state  $W^+W^-$  pair. The branching ratio is given by counting over the decay modes  $e\nu, \mu\nu$  and  $\tau\nu$  and three colors of  $u\bar{d}$  and  $c\bar{s}$ , with roughly equal probability for a total of nine possible final states. The branching ratio for each mode is thus  $1/9$ .

Most often both  $W$  bosons will decay to a quark-antiquark pair, leading to a fully hadronic final state. While this happens for about 44% ( $6/9 \times 6/9$ ) of  $t\bar{t}$  decays, there is a huge background from all other QCD multijet production processes, making separation of the  $t\bar{t}$  signal from the background extremely difficult. If one requires that at least one of the  $W^+W^-$  pair decay leptonically, the backgrounds are substantially reduced. Because of the difficulties associated with identifying  $\tau$  leptons, the backgrounds are reduced further if the lepton is restricted to be either an electron or a muon. When just one of the  $W$  bosons decays to an electron or muon, the final state includes a high transverse momentum charged lepton, a transverse momentum imbalance from the undetected neutrino, referred to as *missing*  $E_T$  or  $\cancel{E}_T$ , and four or more jets from the hadronized quarks. This 'lepton + jets' mode occurs about 30% ( $2/9 \times 6/9 \times 2$ ) of the time and the background comes predominantly from higher-order production of  $W$  bosons, where the  $W$  is recoiling against significant jet activity. The rate is about 2 to 10 times larger than the  $t\bar{t}$  rate, depending on the top mass and the jet selection requirements used.

Dilepton events with leptons coming directly from the decay of the  $W$  would have a probability of  $1/9 \times 1/9$ . Thus  $ee, \mu\mu$ , and  $\tau\tau$  all occur with the same rate. For an  $e\mu$  event, since there are two choices for which the  $W$  decays to  $e$  or  $\mu$ , a branching fraction is  $2/81$ . Hence, we would expect the branching ratio of dilepton events ( $ee, \mu\mu$  or  $e\mu$ ) is

Decay mode	Branching ratio
$t\bar{t} \rightarrow q\bar{q}l b q\bar{q}l\bar{b}$	36/81
$t\bar{t} \rightarrow q\bar{q}l b e \nu\bar{b}$	12/81
$t\bar{t} \rightarrow q\bar{q}l b \mu \nu\bar{b}$	12/81
$t\bar{t} \rightarrow q\bar{q}l b \tau \nu\bar{b}$	12/81
$t\bar{t} \rightarrow e \nu b \mu \nu\bar{b}$	2/81
$t\bar{t} \rightarrow e \nu b \tau \nu\bar{b}$	2/81
$t\bar{t} \rightarrow \mu \nu b \tau \nu\bar{b}$	2/81
$t\bar{t} \rightarrow e \nu b e \nu\bar{b}$	1/81
$t\bar{t} \rightarrow \mu \nu b \mu \nu\bar{b}$	1/81
$t\bar{t} \rightarrow \tau \nu b \tau \nu\bar{b}$	1/81

Table 1.1: Decay modes for a  $t\bar{t}$  pair and their branching ratios (to lowest order) assuming charged-current decays. The symbol  $q$  stands for a light quark:  $u, d, c, s$ .

about 5%.

#### 1.5.4 Signature

One expects event configurations consisting of two leptons, missing transverse energy and as many as two additional jets. The dilepton signal originates from  $WW$ ,  $Wb$ ,  $b\bar{b}$ ,  $W\tau$  and  $\tau\tau$ . Here  $b$  denotes both  $b$  and  $c$  quarks, and  $\tau$  denotes tau-daughters of a  $W$  decay. Most of the top acceptance, about 80 % for the top mass in the range of 90-160  $\text{GeV}/c^2$ , comes from the  $WW$  case. Contributions from other cases, with leptons coming from the decay of  $b$  or  $\tau$ -decays are also included in the acceptance.

Background contribution to the selected candidates is as follows:

- $b\bar{b}(c\bar{c})$  production followed by semi-leptonic decay of both  $b(c)$  quarks;
- $Z \rightarrow \tau\tau$ , followed by the decay of  $\tau$ 's into  $e$  or  $\mu$ ;
- Drell-Yan production of lepton pairs;
- diboson production;  $WW$  and  $WZ$
- lepton misidentification in generic multi-jet QCD events and in events containing  $W$ +jets, conversions and decays in flight.



## 1.6 Collider Run

The Fermilab Tevatron collider resumed operation on May 12, 1992, when it started delivering  $\bar{p}p$  collisions to the CDF detector. Commissioning the detector with beam lasted from May to August in 1992 and we showed that the detector was well on the way to achieving good quality data. With the start of the physics run in August 1992, the attention was turned to obtain the physics results, especially to search for the top quark. The 1992-93 collider run was successfully completed in July 1. During the run, the Fermilab Tevatron achieved a peak luminosity of  $9.22 \times 10^{30}$  (cm  $\cdot$  sec) which is nearly a factor of two larger than was planned for this run. For one year operation the Tevatron delivered an integrated luminosity of  $25 \text{ pb}^{-1}$ , with CDF recording  $21.4 \text{ pb}^{-1}$  on tape, more than 5 of the data sample from the last run. This was achieved with an average initial luminosity of around xx. The detector operated with almost 80% efficiency during the time.

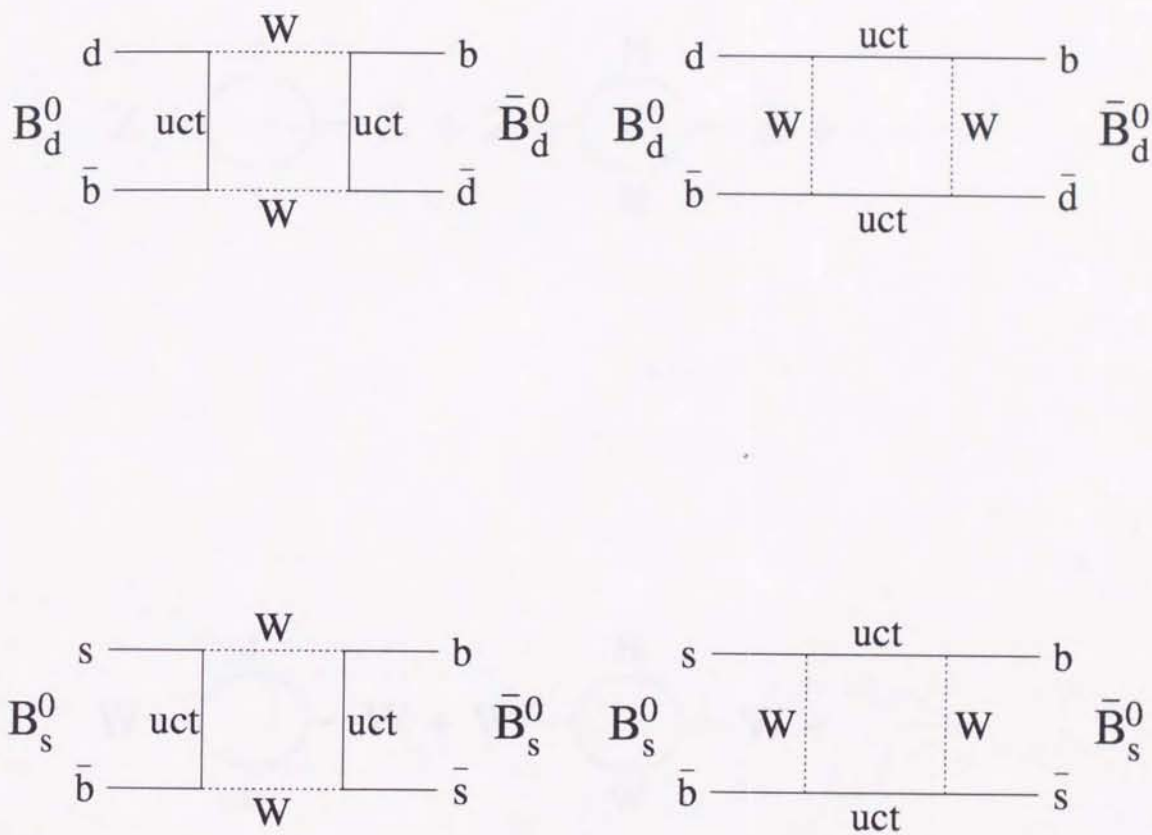


Figure 1.1: Box diagrams for a)  $B_d^0 \bar{B}_d^0$  and b)  $B_d^0 \bar{B}_d^0$  mixing.



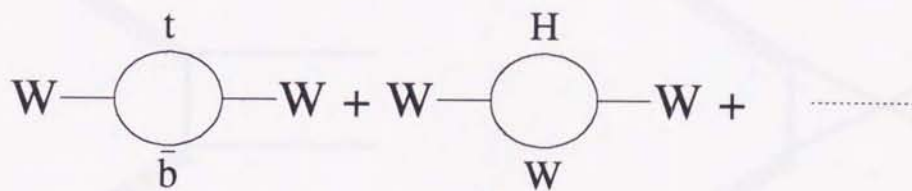
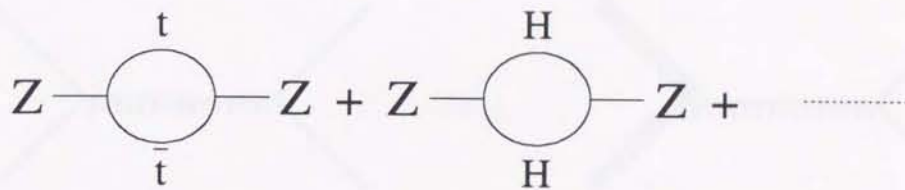


Figure 1.2: Diagrams for one-loop radiative corrections.

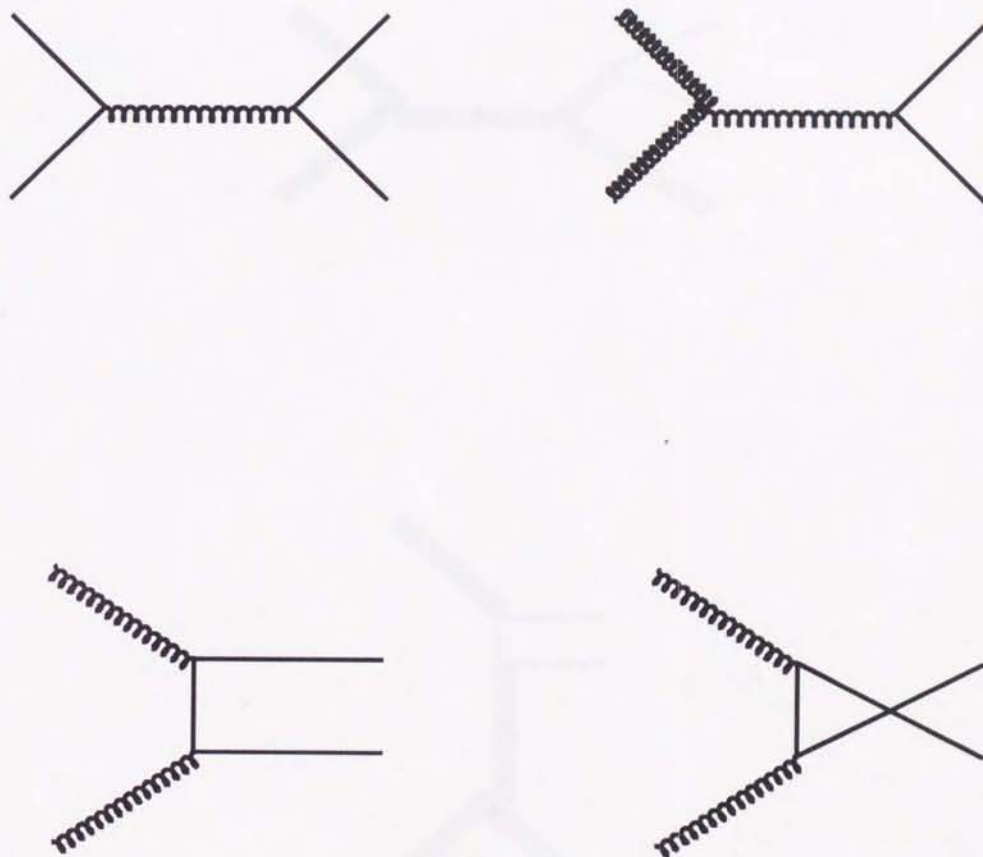


Figure 1.3: Lowest order Feynman diagrams for heavy quark production.



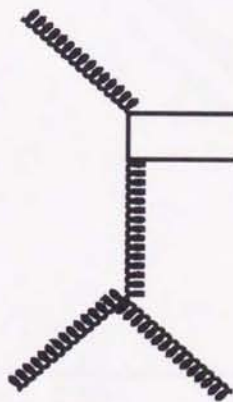
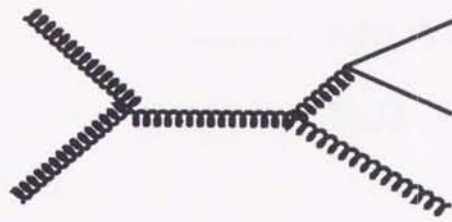


Figure 1.4: Feynman diagrams for a) gluon splitting and b) flavor excitation.

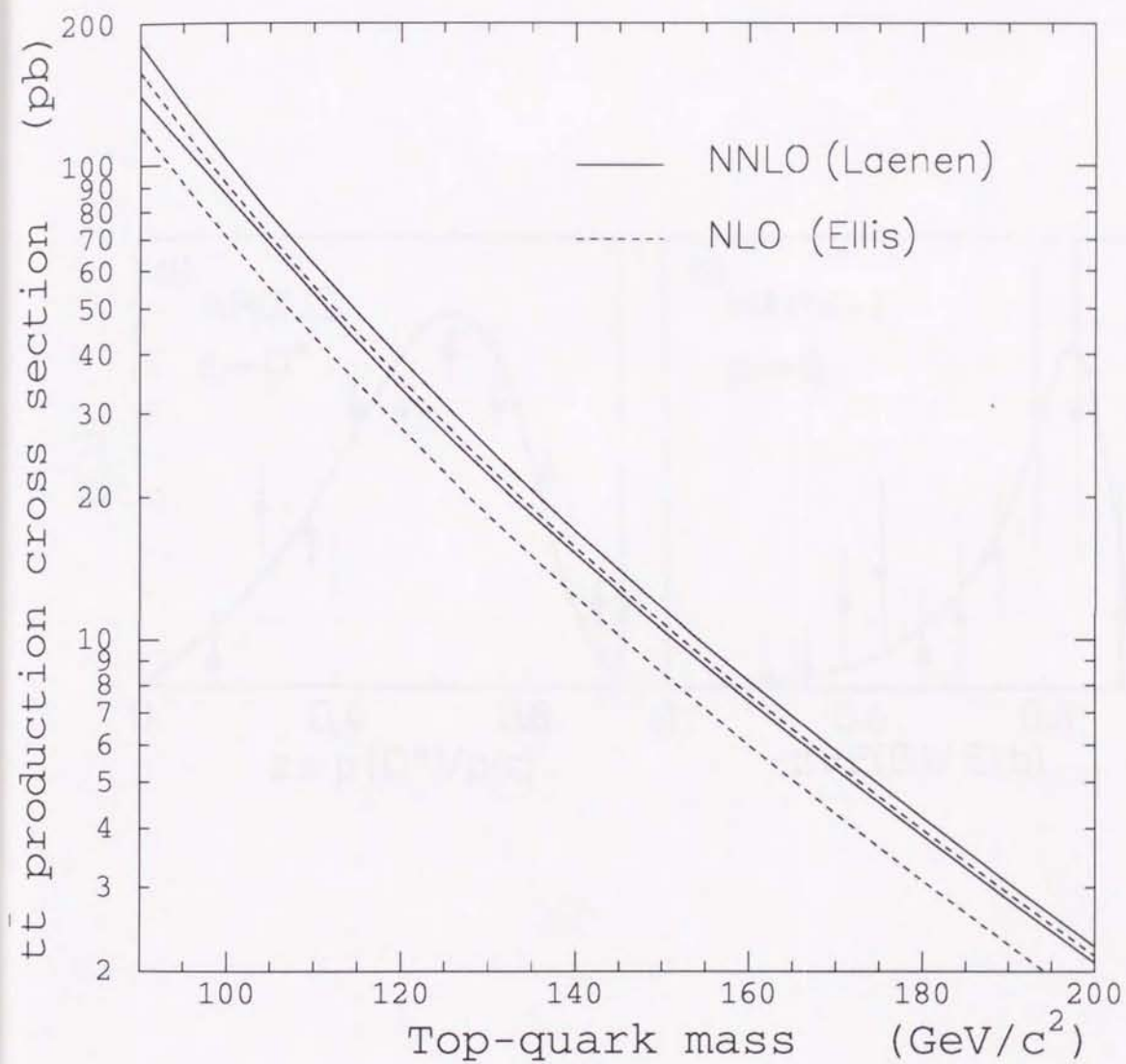


Figure 1.5: The  $t\bar{t}$  production cross section by Laenen et al.[26], based on the next-to-next-to-leading order calculation.



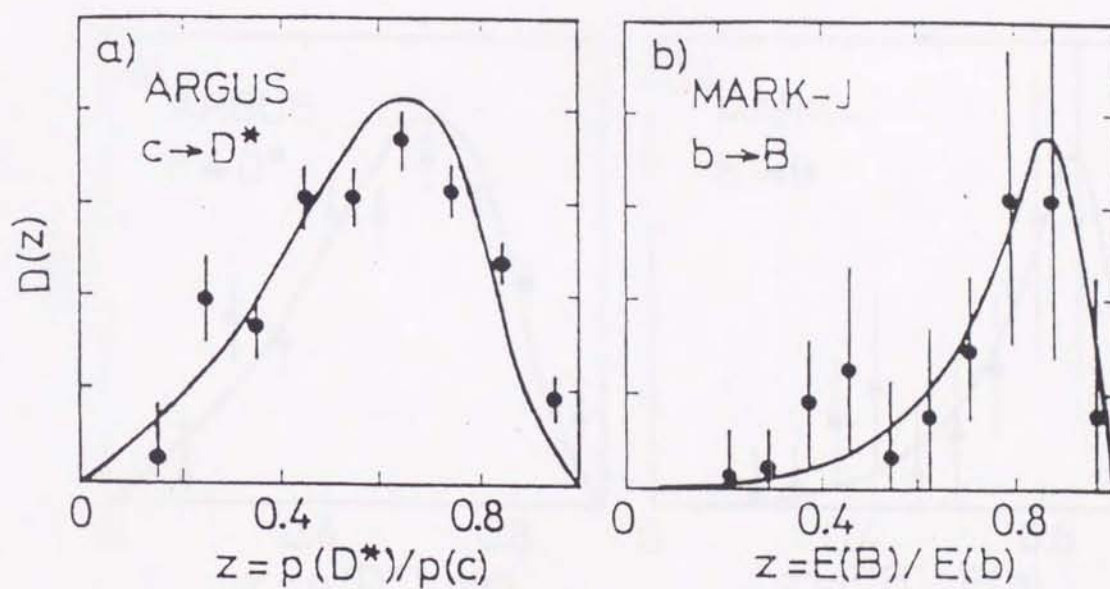


Figure 1.6: The fragmentation functions for  $c \rightarrow D^*$  and  $b \rightarrow B$  from Argus and Mark-J experiments, compared to Peterson model for  $\epsilon=0.18$  and  $\epsilon=0.018$ , respectively.

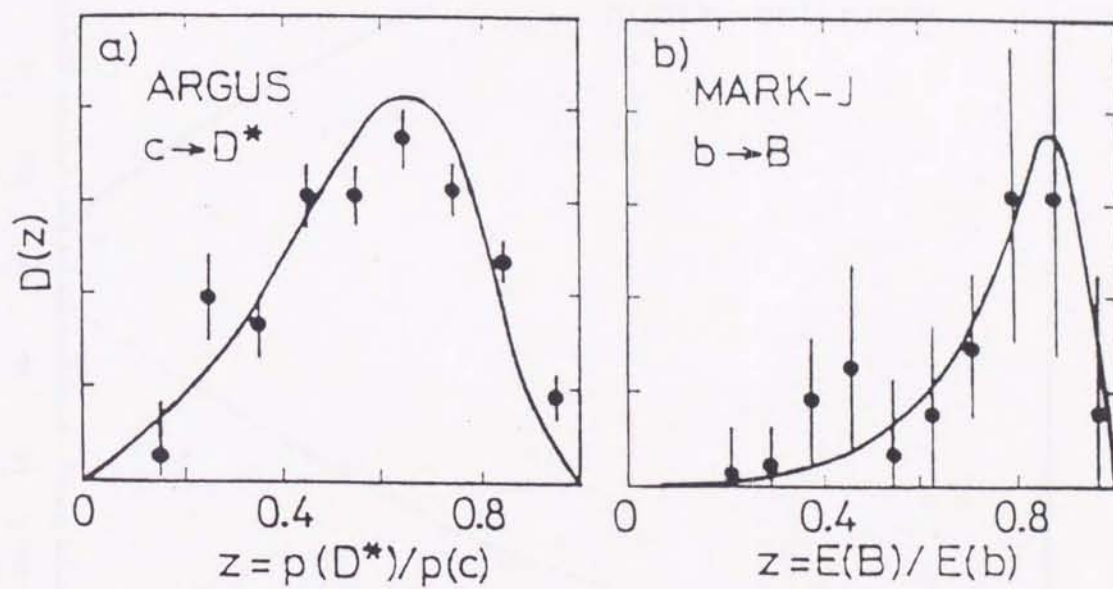


Figure 1.6: The fragmentation functions for  $c \rightarrow D^*$  and  $b \rightarrow B$  from Argus and Mark-J experiments, compared to Peterson model for  $\epsilon=0.18$  and  $\epsilon=0.018$ , respectively.



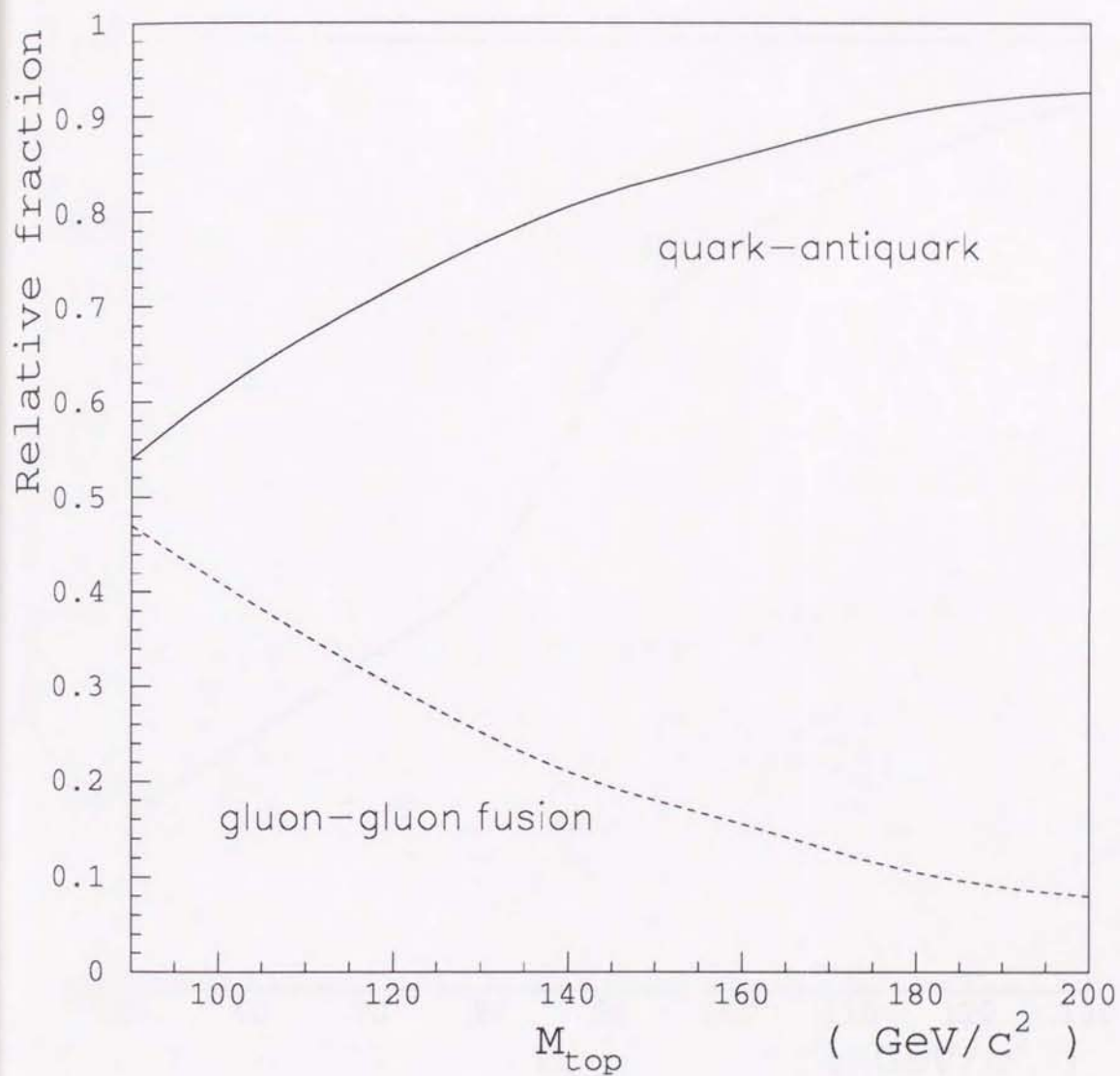


Figure 1.7: Fractions of  $q\bar{q}$  channel and  $gg$  channel contribution to total next-to-leading-order cross section as a function of the top quark mass at  $\sqrt{s}=1.8$  TeV.

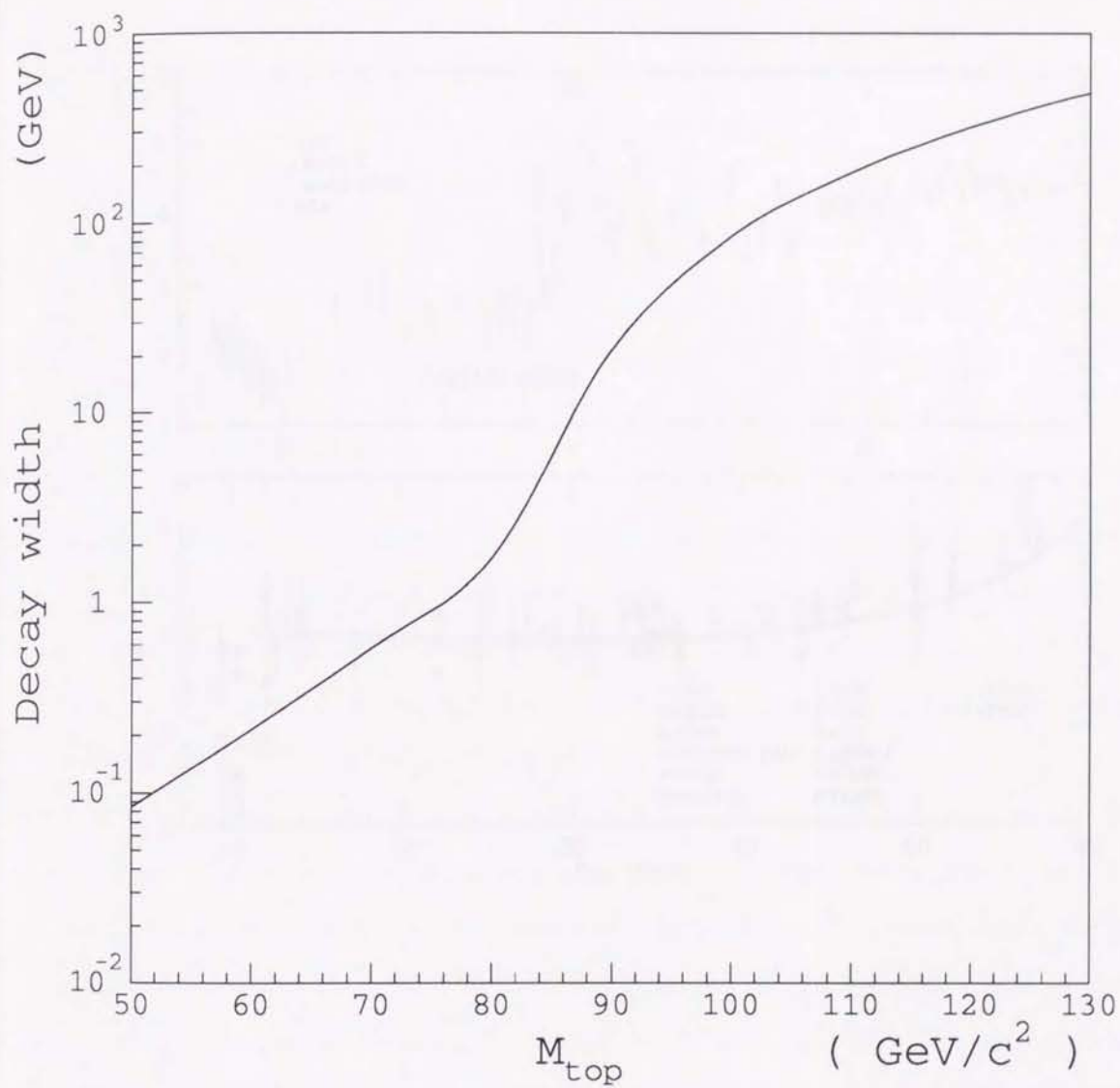


Figure 1.8: Decay width  $\Gamma_{top}$  for the top as a function of the top-quark mass.



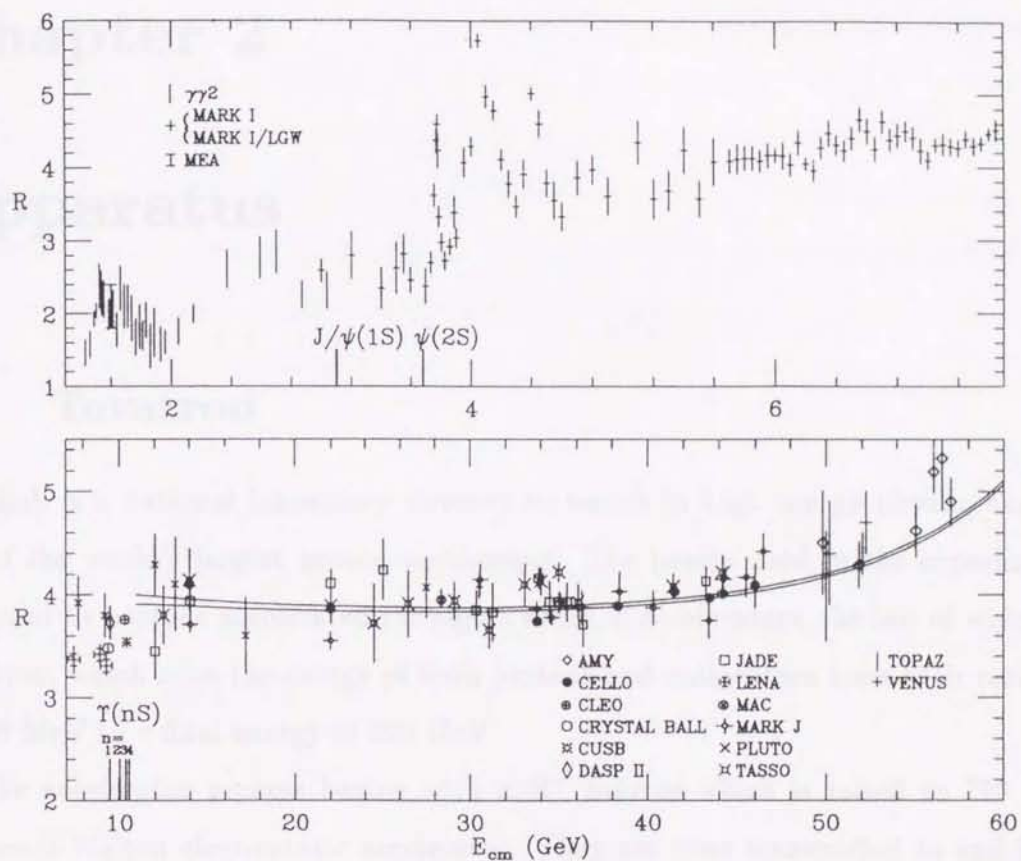


Figure 1.9: Measurements of  $R \equiv \sigma(e^+e^- \rightarrow \text{hadrons}) / \sigma(e^+e^- \rightarrow \mu^+\mu^-)$ .

## Chapter 2

# Apparatus

### 2.1 Tevatron

Fermilab is a national laboratory devoted to search in high energy physics and is the site of the world's largest proton accelerator. The beams used in the experiment are produced by protons accelerated through a series of accelerators, the last of which is the Tevatron, which raise the energy of both protons and antiprotons from their rest energy of 938 MeV to a final energy of 900 GeV.

The accelerator process begins with a  $H^-$  source which is raised to 750 keV by Cockcroft-Walton electrostatic accelerator. They are then transported to and injected into the Linac which increases the kinetic energy to 200 MeV. Upon entering the booster a thin foil is used to strip the two electrons from the  $H^-$  ion yielding a bare proton. The protons are then captured by the magnetic field of the booster. The booster is a rapid cycling (15 Hz) alternate gradient synchrotron which raise the proton kinetic energy to 8 GeV. From the Booster the 8 GeV protons are transported to the Main Ring where the energy is raised to 150 GeV total energy. The protons are coalesced into a bunch before they are extracted from the Main Ring and injected into the Tevatron. The Tevatron is a large (radius = 1km, the same as the Main Ring) (anti)proton accelerator constructed from superconducting magnets. A bunch of protons from the Main Ring is



injected into the Tevatron and stored there at 150 GeV.

150 GeV protons are focussed into a beryllium target to produce  $\bar{p}$ 's of approximately 8 GeV/c momentum. The  $\bar{p}$ 's are then focussed and collected into an Accumulator at a rate of  $2 \times 10^{10}$   $\bar{p}$ 's/hour and cooled to produce a typical monoenergetic  $\bar{p}$  stack of approximately  $2 \times 10^{11}$  particles. In successive main ring cycles, six proton and six anti-proton bunches are transferred to the Tevatron ring. Finally the bunches are simultaneously accelerated to 900 GeV in the Tevatron. The protons and anti-protons are collided at the B0 intersection. To observe processes with small production cross sections, a large number of  $\bar{p}p$  collisions must occur. A useful measure of collider performance is the luminosity  $L$  defined by the relation,

$$N = L\sigma,$$

where  $N$  is the number of events produced per second for some final state,  $\sigma$  is the cross section for a given reaction ( $cm^2$ ) and  $L$  is the luminosity in units of  $cm^{-2} \cdot sec^{-2}$ . The luminosity can be expressed in terms of the properties of the colliding proton and anti-proton bunches in the Tevatron.

$$L = f_r \frac{n_{bunch} N_p N_{\bar{p}}}{A},$$

where  $f_r$  is the revolution frequency of the beam,  $N_p$  ( $N_{\bar{p}}$ ) is the number of the protons (anti-protons) in each bunch,  $n$  is the number of bunches and  $A$  is the effective cross sectional area of beam overlap.

## 2.2 The CDF Detector

The collider detector is expected to perform a wide range of measurement. To begin with, we briefly describe the feature of the detector at the hadron collider. For a general purpose detector it is necessary to measure leptons and hadrons over a large range of

momenta. Quarks and gluons are observed as jets, and neutrinos, which escape detection, are measured as the missing energy. The nature of  $p\bar{p}$  collisions places general requirements on the detector design.

The detector should be a calorimetric detector. Good energy resolution, containment of particle showers and the absence of cracks are necessary to eliminate fake sources of missing energy.

The CDF is an azimuthally and forward-backward symmetric detector designed to study the physics of  $p\bar{p}$  collisions at the Fermi National Accelerator (FNAL) Tevatron. Event analysis is based on charged-particle tracking, magnetic-momentum analysis, and finely segmented calorimeters.

We expected the higher luminosity for the run, so the detector was upgraded to be able to tolerate the higher luminosity.

The CDF coordinate system is shown in figure . Its origin is at the center of the detector. The Z axis is defined as the same direction as motion of the proton beam, from West to East. The y-axis points vertically upward, and the x-axis points radially out of the Tevatron ring, so as to make a right handed coordinate system. The azimuthal angle  $\phi$  is set to be 0 on the positive x-axis and increases from positive x to positive y. The polar angle is measured from the proton beam direction. Instead of  $\theta$ , we use the pseudo-rapidity  $\eta = -\log(\tan(\theta/2))$ . The event vertex position can be shifted along the beam line and has *rms* width of approximately 30 cm. We will refer to both  $\eta$ 's which are detector pseudorapidity  $\eta_d$  for an origin chosen at the geometric center of the detector and event pseudorapidity  $\eta$  for an origin chosen at the event vertex.

### 2.2.1 Beam-beam counter

The beam-beam counters consist of two planes of scintillating plastic located in front and in back of the central calorimeters. Each plane of counters covered the angular region  $0.32^\circ < \theta < 4.47^\circ$ . This provides a monitor of the luminosity.



### 2.2.2 Tracking

The CDF tracking system covers the angular range  $\sim 8^\circ$  to  $\sim 172^\circ$  in polar angle ( $|\cos \theta| < 0.99$ ) and is contained within a 1.5 T axial magnetic field. Three dimensional track reconstruction is available in the range  $25^\circ$  to  $155^\circ$  in polar angle ( $|\cos \theta| < 0.91$ ). The tracking detectors consist of two separate systems: an inner radius system of

#### Vertex chamber

Due to space charge distortions in the drift region, the Vertex Time Projection Chamber operated during last run was inoperable at  $L > 3 \times 10^{30}$ , so it was replaced for this run to be able to withstand the higher luminosity and, in addition, to make space for the SVX. A vertex chamber (VTX) surrounds the beam pipe and extends  $\pm 1.4$  m along the beam line from the interaction point. This chamber measures charged particle tracks in the  $r - z$  plane to within  $3.5^\circ$  of the beam line. The interaction vertex of the  $p\bar{p}$  collisions is reconstructed with an rms resolution of 1 mm in the  $z$  direction. This vertex is used as the origin in computing the transverse energy ( $E_T = E_T \sin \theta$ ) deposited in each calorimeter cell. The distribution in  $z$  of reconstructed vertices in dilepton events is shown in Figure 2.4 and is well described as a gaussian mean -2.0 cm and width 29.5 cm. This spread in vertices reflects the convolution of the proton and antiproton bunches in the collider. The VTX is also used to detect photon conversions.

#### Central Tracking Chamber

The central tracking chamber (CTC) surrounds the VTX. The CTC was designed to measure charged particle tracks in the  $r - \phi$  plane to determine their curvature in the magnetic field and thus their momenta. The CTC has 84 layers of wires grouped together in nine "superlayers" as shown Figure 2.7. The nine superlayers are subdivided into measurement cells. Five superlayers have 12 sense wires per cell, parallel to the beam direction. These axial layers are used for the preliminary determination of the track curvature. In the other four superlayers, each cell has six sense wires within a  $3^\circ$  stereo angle to provide information necessary to determine the polar angle of the



tracks. The cells in all suerlayers are tilted at a  $45^\circ$  angle with respect to the radial direction to compensate for the Lorentz angle of electron drift in the magnetic field. This allows electrons to drift azimuthally(in the ideal case), simplifying the time-to-distance relationship.

The momentum resolution of the CTC is  $\delta p_T / p_T = 0.0011 p_T$  ( $p_T$  in GeV/c) for isolated tracks by requiring that a track intersect the beam at the beam position point (beam constraint). Complete tracking information is only available for  $40^\circ < \theta < 140^\circ$ . Tracks outside this angular region do not pass through all laayers of the chamber and consequently have a poorer momentum resolution.

### 2.2.3 Calorimetry

The CDF has three calorimeter systems: central, plug and forward regions over the region  $|\eta| < 4.2$ . Each section has a tower structure of an electromgnetic calorimeter and a hadronic calorimeter. In the central region ( $|\eta| < 1.1$ ) a lead-scintillator sampling calorimeter 18 radiation lengths deep provides electromagnetic shower detection. This central electromagnetic calorimeter (CEM) is segmented into  $15^\circ$  wedges in the azimuthal direction, with each wedge consisting of ten projective read out towers numbered from 0 to 9, where tower 0 is at  $90^\circ$  polaar angle. The size of a central tower is approximately  $\Delta\phi \times \Delta\eta = 15^\circ \times 0.11$ .

A set of proportional wire chambers is located in the CEM at a depth of six radiation lengths to meaasure the position and shape of electromagnetic showers. These central strip chambers (CES) have wire and cathode strip readout providing independent reconstruction off showers in the z and azimuthal views. The resolution on the position of shower centroids from 25 GeV/c electrons is  $\sim 2.5$  mm for both views.

Measurement of hadronic energy in the central region is provided by the central and end-wall hadronic calorimeters (CHA/WHA). The CHA/WHA has aapproximately the same geometry and segmentations as the CEM and covers the same region of pseudorapidity. The energy resolution is  $\sigma(E)/E = 80\%/\sqrt{E_T}$



In this analysis the central and plug calorimeters were used to identify electron and jets, and the missing transverse energy (which will be defined in Section 4.5) was computed using the full calorimeter out to  $|\eta| < 3.6$ .

System	$\eta$ range	Energy resolution
CEM	$ \eta  < 1.1$	$13.5\%/\sqrt{E_T} \oplus 2\%$
PEM	$1.1 <  \eta  < 2.4$	$28\%/\sqrt{E_T} \oplus 2\%$
FEM	$2.4 <  \eta  < 4.2$	$25\%/\sqrt{E_T} \oplus 2\%$
CHA	$ \eta  < 1.3$	$75\%/\sqrt{E_T} \oplus 3\%$
PHA	$1.3 <  \eta  < 2.4$	$90\%/\sqrt{E_T} \oplus 4\%$
FHA	$2.4 <  \eta  < 4.2$	$130\%/\sqrt{E_T} \oplus 4\%$

Table 2.1: Summary of calorimeter properties. CEM(CHA), PEM(PHA) and FEM(FHA) denote the central, plug and forward EM(HAD) calorimeters. The symbol  $\oplus$  signifies that the constant term is added in quadrature in the resolution.

## 2.2.4 Muon chamber

Muon chambers are located behind the central calorimeters at a radius of 3.47 m. there are approximately five hadronic absorption length of material between the muon chambers and the interaction point. The chamber covers the rapidity region  $|\eta| < 0.63$  ( $56^\circ < \theta < 124^\circ$ ). There is a gap between neighboring chambers at the boundary at  $\eta=0$  of about  $\delta\eta=0.05$ . A  $2.4^\circ$  gap in  $\phi$  between adjacent  $15^\circ$  calorimeter sections also is not covered. The four layers of drift cells in a muon chamber provide the three-dimensional reconstruction of tracks via single-hit time-to-digital converters (TDC's) in the transverse direction and charge division in the longitudinal direction. A drift resolution of  $250 \mu$  ( $\phi$ ) and a charge division resolution of 1.2 mm ( $z$ ) are determined from cosmic-ray studies.

### Central Muon Upgrade

The original CDF Central Muon detector(CMU), which covers the pseudorapidity re-

gion  $|\eta| < 0.6$ , has been complemented by the addition of the 4 layers of drift tubes behind 2 feet of steel resulting in a total of 8 absorption lengths. Only muon candidates with  $P_T$  above  $2.5 \text{ GeV}/c^2$  are expected to be able to reach the CMP chambers. As a result, hadronic punch-through backgrounds to the muon signal have been considerably reduced by requiring hits in the CMP chamber.

### Central Muon Extension (CMX)

We have added layers of drift tubes outside the calorimeter in the pseudorapidity region of  $0.6 < |\eta| < 1.0$ . The coverage in  $\phi$  is 80 % and the chambers are located behind 6 absorption length of calorimeter. This increases the muon coverage in CDF by 50 %.

## 2.3 Trigger

Events are selected in several stages. The first two levels are used to reduce the rate of events to a manageable level before writing to tape. Level 3 reduces the number of events to be reconstructed in order to economize on computing time.

The CDF trigger system has three levels of hardware triggers followed by a software (Level 3) trigger that utilizes a farm of processors running offline-like algorithms. These triggers require the presence of an inelastic  $\bar{p}p$  collision, signaled by a coincidence between two scintillator counters located along the beam pipe at the forward and backward regions.

Scintillation counter arranged in a rectangle around the beam pipe and covering the angular interval from  $0.3^\circ$  to  $4.5^\circ$  and from  $355.5^\circ$  to  $359.7^\circ$  provide a "minimum bias" trigger, which is satisfied if at least one scintillation counter on each side of the interaction region is above threshold within a 15-ns window centered on the beam-beam crossing time. Events satisfying this trigger are then considered by the higher level trigger logic.

At Level 1, a simple but fast decision to reject the majority of events are made



before the next beam crossing. For Level 2 a more complex decision based on identifying "physics" objects. The detector is dead for several crossing while this decision is being made. The Level 3 trigger is a software filter that is part of the online data decision path and runs a subset of the event reconstruction code and physics algorithms. Events that survive the Level 1 and Level 2 hardware triggeres are passed to Level 3 for a more detailed analysis before being accepted or rejected. The decision was made with Silicon Graphics processors using the UNIX operating system. The final stage after the trigger selection is the offline reconstruction.

Level 3 was running the equivalent of offline production, therefore all the information on electron objects(ELES) and muon objects (CMUO) are available at level 3. At Level 3, Detector is read out completely.

### 2.3.1 Electron trigger

The hardware trigger system is designed to use the projective nature of the calorimeter towers along with a fast two-dimensional hardware track finder, called the ceentral fast tracker (CFT). Trigger towers have a width of 0.2 in pseudorapidity and  $15^\circ$  in azimuth, mapping the detector into an array of 42 (in  $\eta$ ) by 24 (in  $\phi$ ) in both electromagnetic and hadronic calorimeters. Electron candidates are triggered on using calorimeter information that requires a significant localized deposite of energy in the electromagnetic calorimeter with little leakage into the hadron compartment behind it. Further rejection can be obtained by requiring a stiff track pointing at the cluster.

#### Level 1

The first level trigger used information exclusively from the calorimeters and required a single trigger tower with  $E_T$  more than 6 GeV for the CEM, or  $E_T$  more than 8 GeV in any region of the calorimeter.

#### Level 2

The central electron trigger requires an energy cluster with  $E_T > 9.2$  GeV, together with an aassociated CTC track with transverse momentum  $P_T > 9.2$  GeV/c as measured by

the CFT. The plug electron trigger simply requires either an energy cluster with  $E_T > 20$  GeV or  $E_T > 15$  GeV and  $\cancel{E}_T > 15$  GeV. The ratio of hadronic to electromagnetic energy in the cluster (HAD/EM) is required to be less than 0.125.

### Level 3

The central electron trigger at level 3 requires that the reconstructed cluster energy  $E_T$  be above 18 GeV and that there be a reconstructed track with  $P_T > 13$  GeV/c pointing to the cluster. The plug trigger requires the reconstructed  $E_T$  is required to be above 20 GeV with  $\cancel{E}_T > 20$  GeV.

## 2.3.2 Muon trigger

### Level 1

The level 1 trigger was based solely on the muon chamber information. condition requires that hits from a track form coincidence in two of the four layers of the chamber within a time window determined by the  $P_T$  threshold, as shown in the following equation:  $Min(|t_4 - t_2|, |t_3 - t_1|) < t_{max}$ , where  $|t_4 - t_2|$  and  $|t_3 - t_1|$  are the time difference equivalent to the  $P_T$  threshold preset. The  $P_T$  is measured by using the constraint that the track had to originate at the beam line and knowing the line integral of the magnetic field traversed by the particle.  $P_T$  of the muon track segment in the CMU with  $P_T > 6$  GeV/c in coincidence with hits in the CMP was required.

### Level 2

The level 2 trigger condition is that a match between a CFT track in the  $r - \phi$  plane with  $P_T > 9.2$  GeV/c and a track segment in the muon chambers which is defined as a level 1 trigger. The hits in the CMP chambers is used to confirm a trigger in the CMU chambers if the CMP chambers are available.

### Level 3

The level 3 muon requires a match better than 10 cm in  $r - \phi$  between a reconstructed track with  $P_T > 18$  GeV/c which is extrapolated to the radius of the muon chambers and a track segment in those chambers. In addition, the energy deposited in the associated



CHA tower must be less than 6 GeV.

### 2.3.3 Offline reconstruction

Since the last run(1988-89), all of CDF's offline reconstruction codes was ported to UNIX(both Silicon Graphics and IBM), enabling us to run the offline code as part of the level 3 trigger.

Large fraction of the 1992 code is new for new detectors and many changes to the reconstruction code for existing detectors were made based on the data collected in the last run. A data compression scheme is introduced to accomodate the laarge size of the data set.

Full reconstruction of all CDF data is completed within two days of data taking, using 1000 MIPS from a Silicon Graphics farm , while approximately 5-10 % of the data, including the most interesting events, are reconstructed and available within a few hours of data taking.

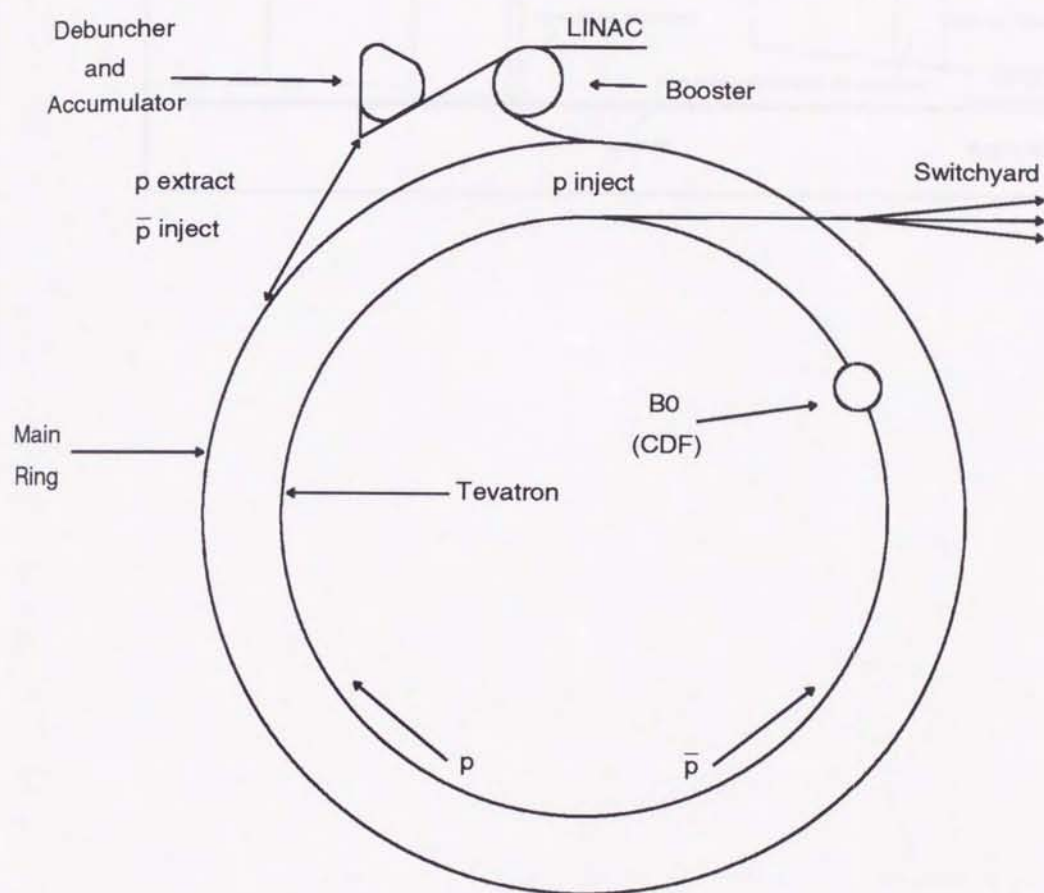


Figure 2.1: The Fermilab accelerator complex



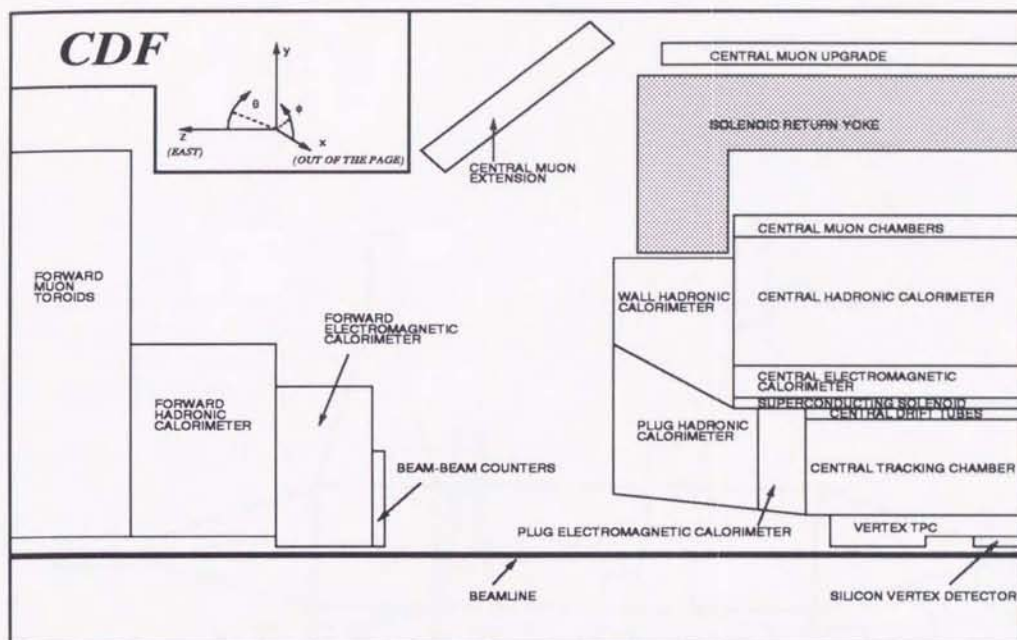


Figure 2.2: A cut-away view of one quadrant of the CDF detector. The detector is forward-backward symmetric about the interaction point.

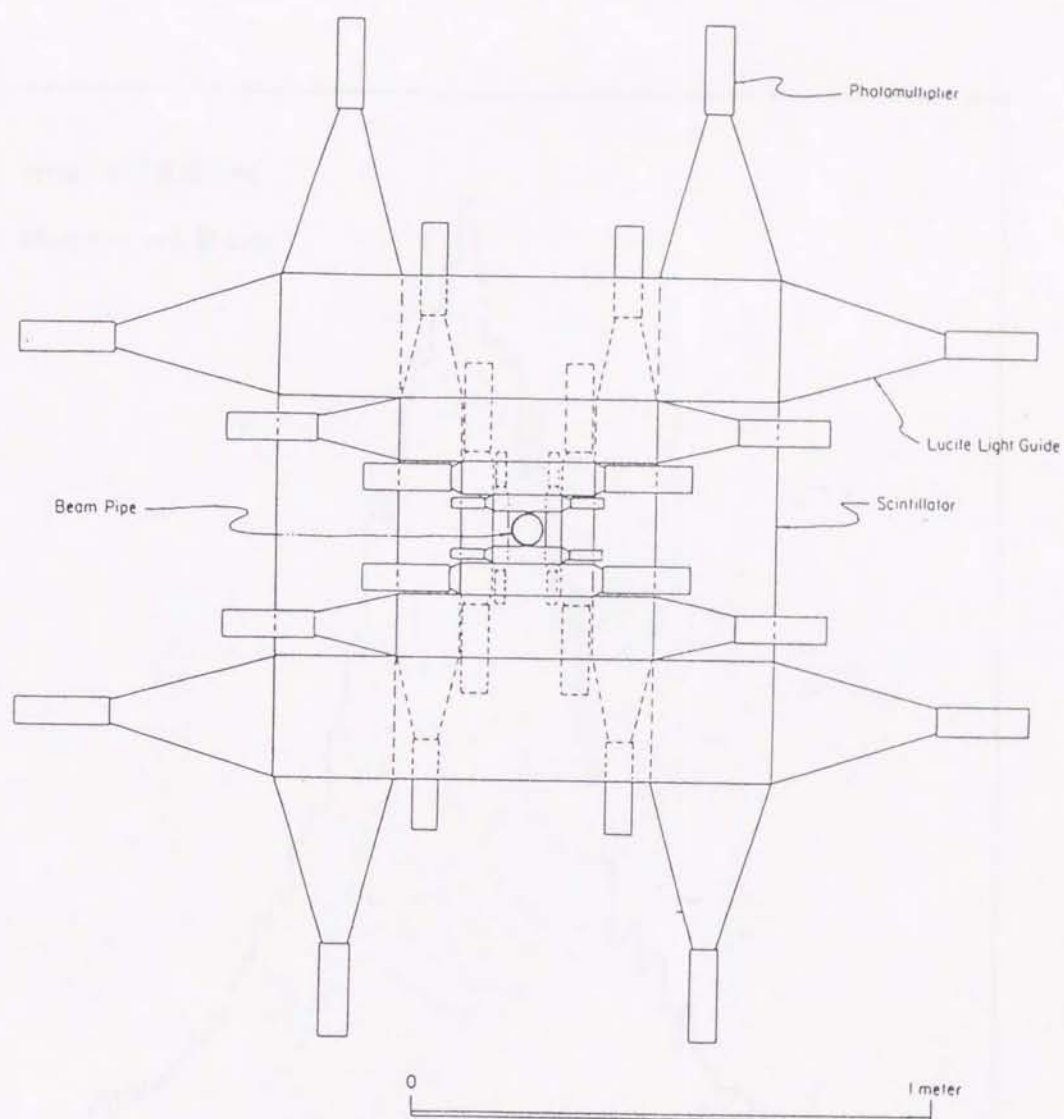


Figure 2.3: One of plane of beam-beam counters viewed from the beam-line



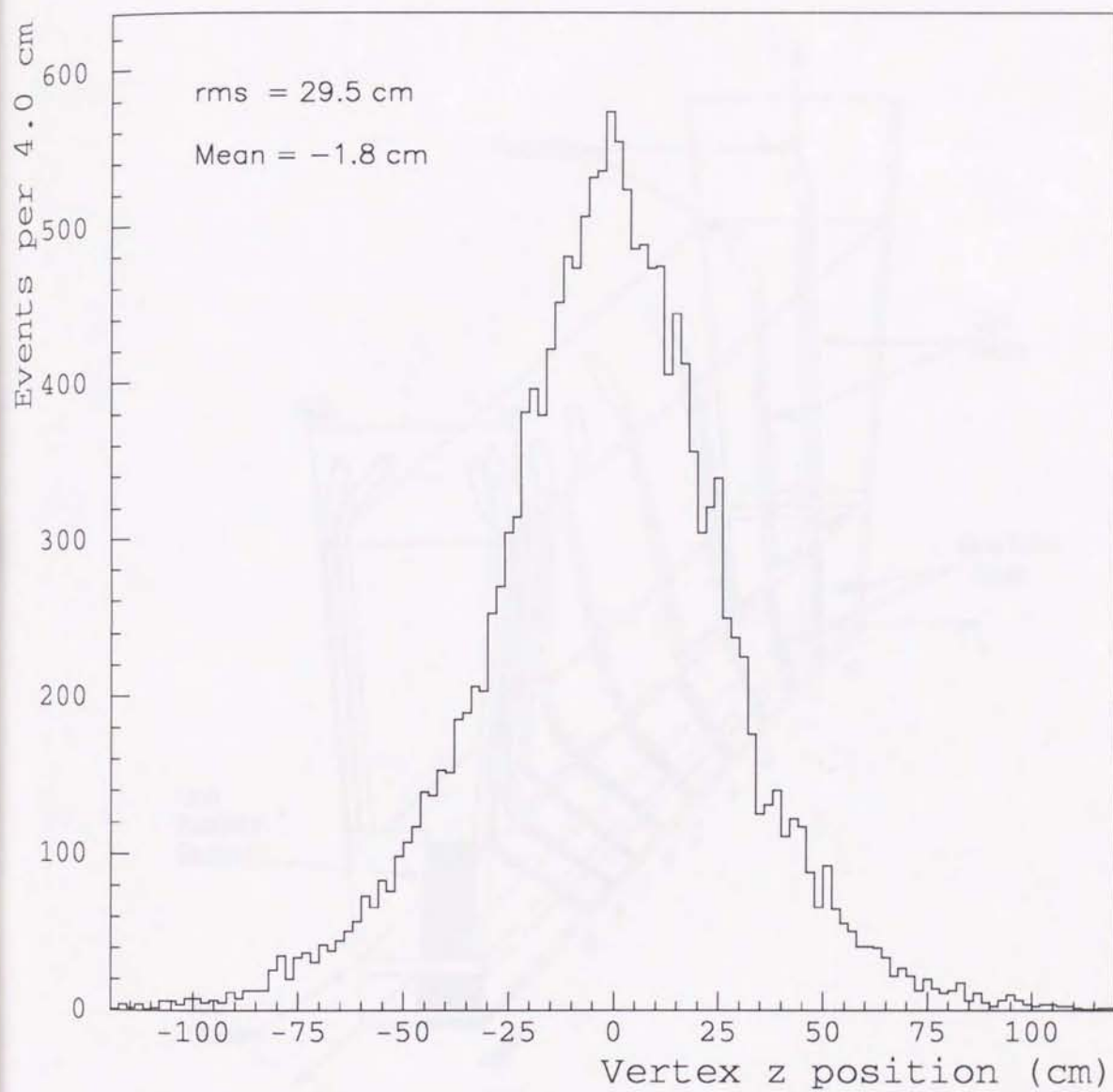


Figure 2.4: Event vertex distributions along the beam line for the high  $P_T$  dilepton events.

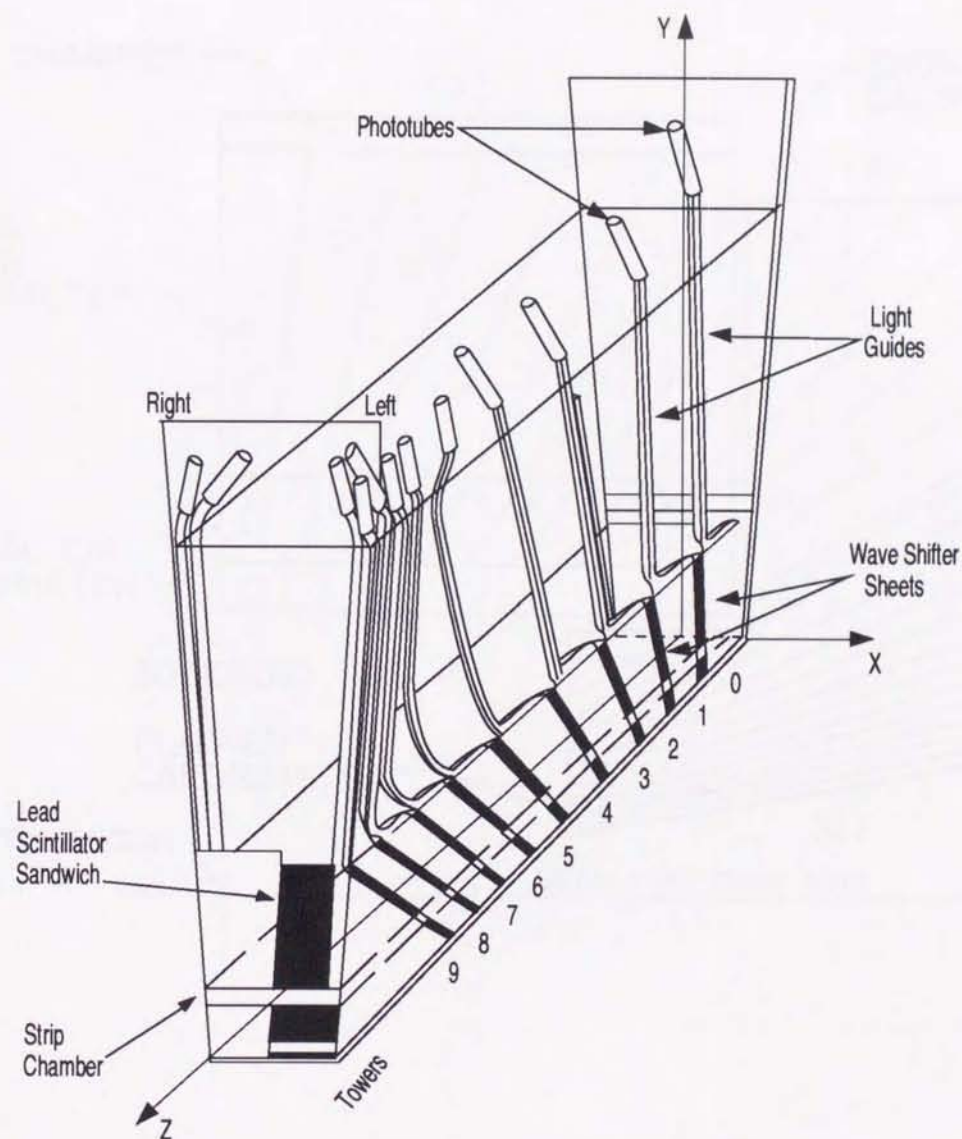


Figure 2.5: Cutaway view of a central electromagnetic calorimeter module. The wavelength shifters collect the light from the layers of scintillators and indicate the cell structure in  $\eta$ . Each wedge subtends  $15^\circ$  in  $\phi$ .



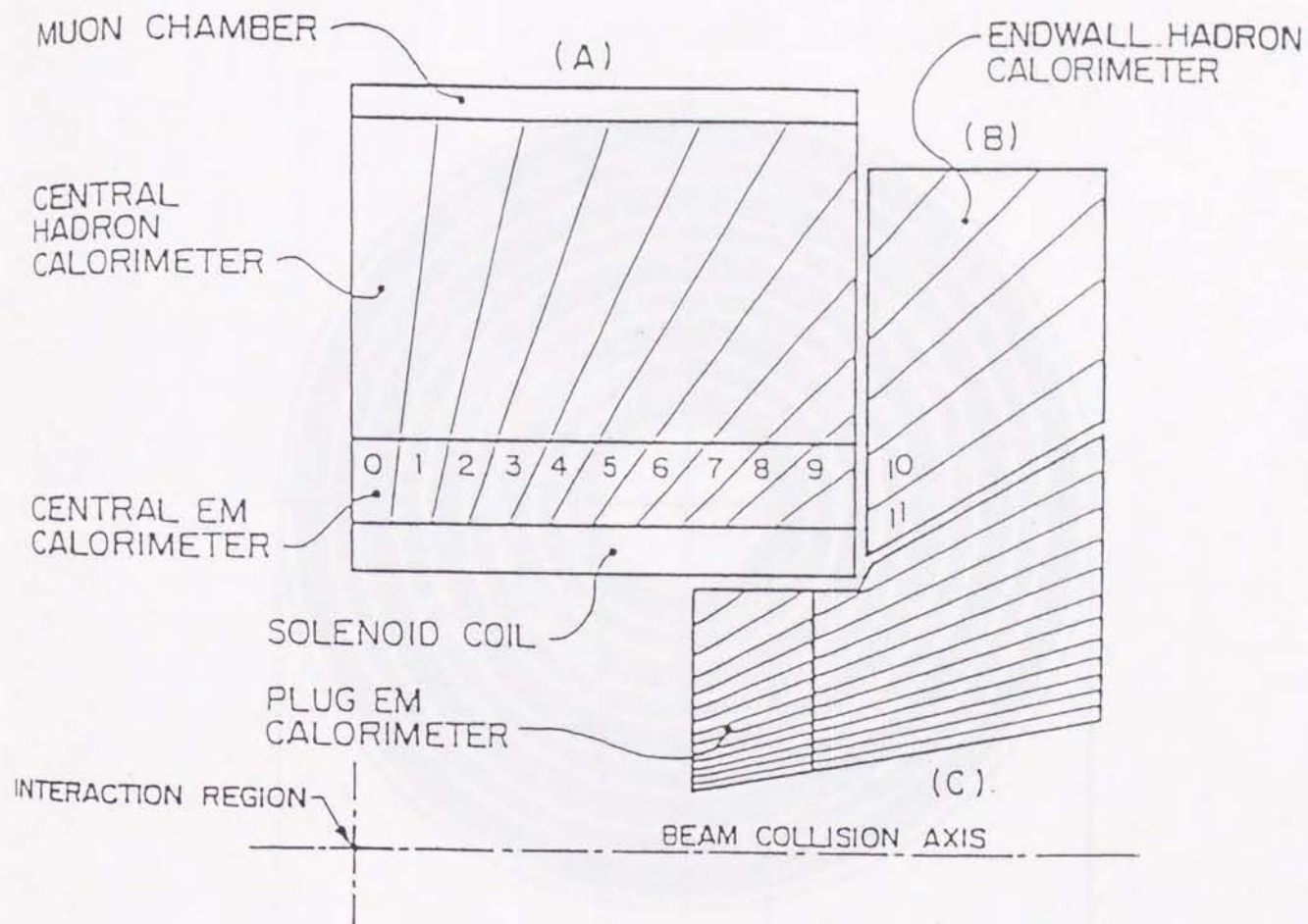


Figure 2.6: Quadrant of the calorimeter where A, B and C show the central, endwall and plug, respectively.

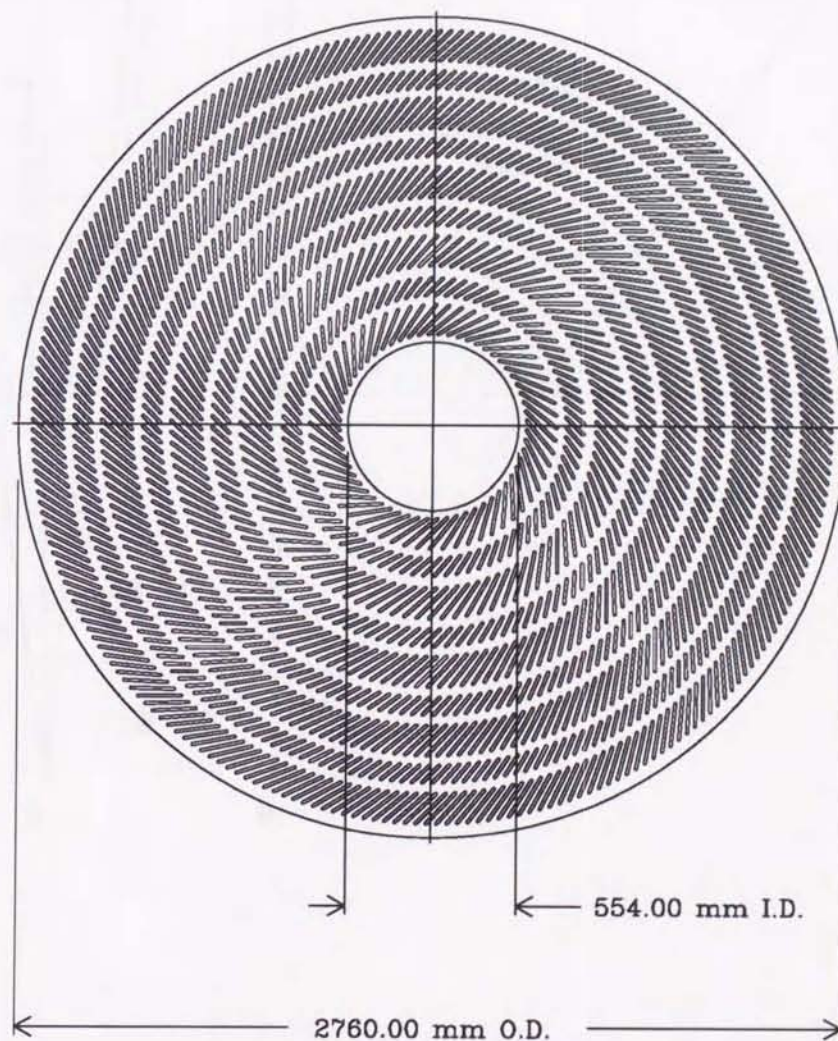


Figure 2.7: Layout of wires at the end of the central tracking chamber (CTC) showing the disposition of the superlayers and cells within the superlayers.



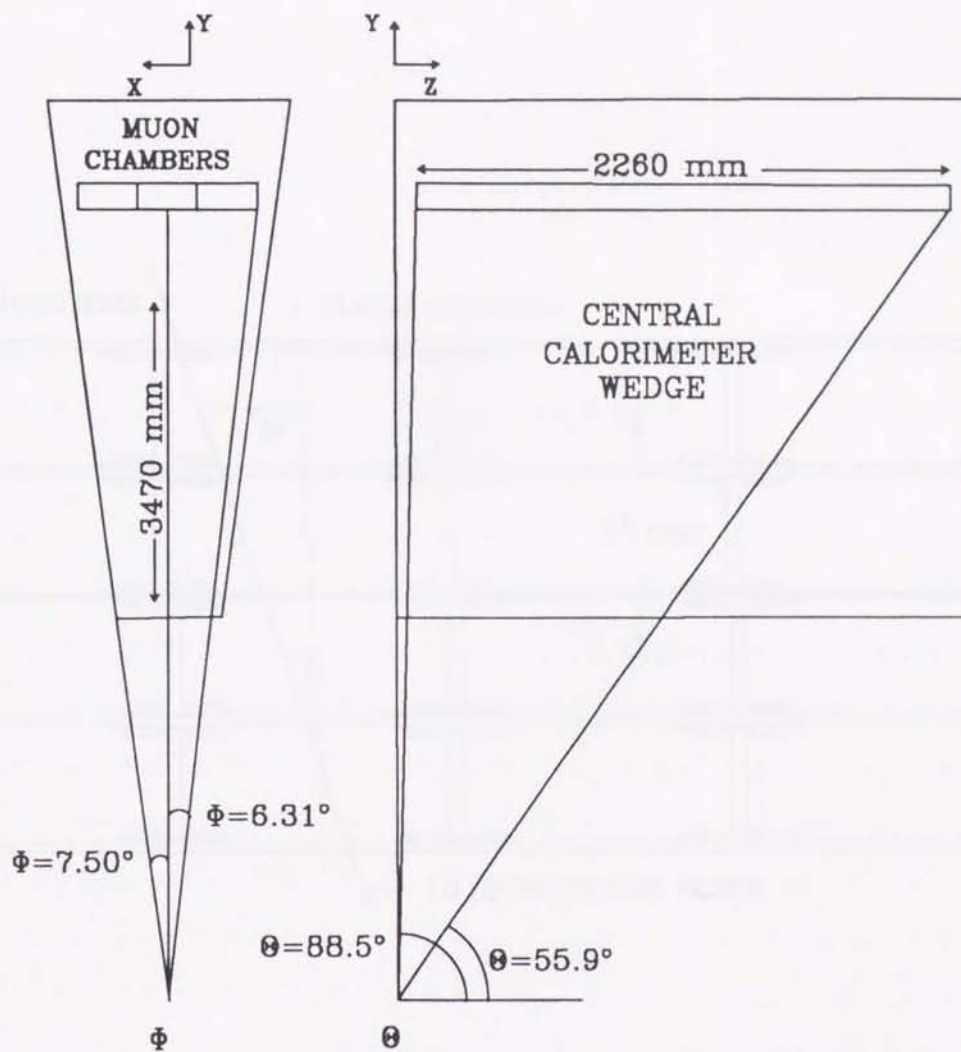


Figure 2.8: Central muon chamber location with respect to a central calorimeter wedge.

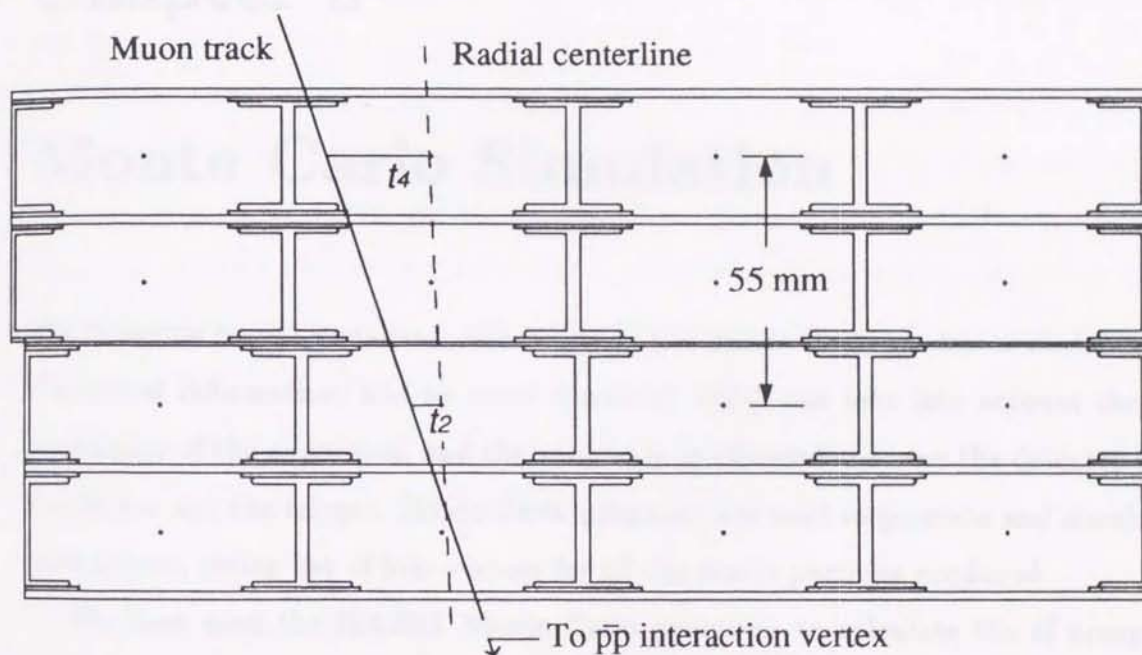


Figure 2.9: The arrangement of the four plates of central muon chambers in a view along the beam direction. The drift times  $t_2$  and  $t_4$  are used at the trigger level to determine a muon momentum cutoff.



## Chapter 3

### Monte Carlo Simulation

The  $t\bar{t}$  events must be analyzed with a help of the Monte Carlo generator containing the theoretical information, and an event simulator which can take into account the finite acceptance of the apparatus, and the variations in efficiencies across the detector due to the device and the trigger. Monte Carlo programs are used to generate and simulate  $p\bar{p}$  interactions, giving list of four-vectors for all the stable particles produced.

We have used the ISAJET Monte Carlo generator to calculate the  $t\bar{t}$  acceptance in experiment. This is also used to estimate backgrounds to top signals, for example, the background from bottom and charm. The momenta of the partons which enter the hard scattering interaction are determined by the structure function(EHLQ set 1 parameterization[31]). The matrix element for the hard scattering is calculated to  $O(\alpha_s^2)$ , taking  $Q^2 = 2\hat{s}\hat{t}\hat{u}/(\hat{s}^2 + \hat{t}^2 + \hat{u}^2)$ . QCD radiation is then included using the branching approximation[32]. QCD radiation from the incoming and outgoing partons is simulated iteratively, so that parton showers are generated. The partons which originate from the hard scattering diagram are generally off-shell. At each branching point, the partons move closer to their on-shell masses. A cut-off parameter is used to truncate the shower development; for instance, for gluons, the branching process is stopped when the virtual mass of the gluon falls below  $6 \text{ GeV}/c^2$ .

Following the QCD shower simulation, the outgoing heavy quarks are fragmented inde-

pendently, using the Peterson parameterization [33] with  $\epsilon_c=0.08$  for charm and  $\epsilon_b=0.5$  for bottom. For top, the Peterson variable is scaled according to  $1/M_{top}^2$ , giving a very hard fragmentation function. Light partons are fragmented using a purely phenomenological parametrization. The unstable particles produced in the fragmentation process are decayed based on the measured branching ratios if possible and estimated branching ratios otherwise.

The “underlying event”, all the particles unrelated to the hard scattering process, are low  $P_T$  hadrons which are approximately uniformly distributed in rapidity and azimuth. In ISAJET program, the underlying has two components: (1) QCD radiation from incoming partons described above, and (2) beam-jet fragmentations simulated using a phenomenological model. The average level activity from the underlying event is adjusted so as to match the measurement.

In addition to simulating QCD-induced heavy flavor production as described, ISAJET can generate a variety of process such as Drell-Yan and W processes.

### 3.1 Monte Carlo Data Sets

This section describes the Monte Carlo data sets to which we will refer in subsequent sections. The primary Monte Carlo generator used to evaluate acceptance and backgrounds is ISAJET<sup>1</sup>. All Monte Carlo events were passed through a simulation of the CDF detector. The detector simulation program extrapolates the final-state particle trajectories through the magnetic field to the calorimeter cells. The average calorimeter responses and resolutions for charged pions, photons, electrons, and muons have been parameterized and tuned to reproduce (1) test-beam measurements for particles with momenta from a few GeV/c up to about 200 GeV/c, and (2) isolated track data collected with a minimum-bias trigger at low  $P_T$ . The simulation also includes effects of response across boundaries between calorimeter cells, zero response in uninstrumented regions, photon

<sup>1</sup>Unless otherwise stated, we used version 6.43 of ISAJET Monte Carlo program.



conversions and the observed distribution of vertex positions about the mean position at the center of the detector. After simulation, the events were passed through the offline reconstruction in the same way as the CDF data. The effects on the trigger efficiencies and small differences of lepton detection efficiencies between data and Monte Carlo reconstruction were corrected. Corrections were also applied for muon acceptance, since some of CMU wedges have been completely dead, throughout the run so far.

We have checked the validities of the Monte Carlo simulation, especially on the lepton identification, isolation variables and the missing  $E_T$ .

- $t\bar{t}$

The ISAJET Monte Carlo program was used to generate  $t\bar{t}$  events for the top quark masses of 100, 120, 140, 160 and 180 GeV/c<sup>2</sup>. The integrated luminosity of these generated samples were 1127, 2953, 6780, 14194 and 27768 pb<sup>-1</sup>, respectively. We have used the  $t\bar{t}$  production cross section calculated by Laenen et al. [26] which was used for the normalization of the expected  $t\bar{t}$  events.

- $b\bar{b}$  and  $c\bar{c}$

ISAJET program was also used to generate a sample of  $b\bar{b}$  and  $c\bar{c}$  events. Production of  $b$  quarks via the mechanisms of (a) direct  $b\bar{b}$  production ( $gg \rightarrow b\bar{b}$ ), (b) gluon splitting ( $gg \rightarrow gg, g \rightarrow b\bar{b}$ ), and (c) flavor excitation ( $gb \rightarrow gb$ ) are included in the calculation. We have required that there was at least one  $b$  quark with  $P_T$  more than 25 GeV/c<sup>2</sup>. This  $P_T$  threshold was chosen to keep 90 % of the daughter leptons with  $P_T$  more than 15 GeV/c<sup>2</sup>. The sample was then passed through the CLEO Monte Carlo to decay  $b$  quarks. It is known from the CLEO and CDF experiences that the CLEO program models them better than that in the naive ISAJET program. This changes the average charged particle multiplicity and the energy flow around the lepton.

- WW and WZ

ISAJET was also used to model WW and WZ backgrounds. The integrated luminosity of WW and WZ samples are  $16790 \text{ pb}^{-1}$  and  $94100 \text{ pb}^{-1}$ , respectively. The ISAJET predicts WW cross section to be 6 pb, but we use the theoretical predictions of 9.5 pb calculated by Ohnemus[47].

- $Z \rightarrow \tau\tau$

We used  $Z \rightarrow e^+e^-$  in data to make  $Z \rightarrow \tau\tau$  simulation sample. The two electrons in the  $Z \rightarrow e^+e^-$  event were removed and then replace each electron with a tau. The tau is then allowed to decay semileptonically and simulated with the full simulation of the CDF detector. The reconstructed tau's were merged to the original event. In order to get much statistics, we have repeated this process 80 times for every Z event.



## Chapter 4

### Event Selection

The top-quark search in this analysis is based on a signature with high transverse momentum leptons, large missing transverse energy, and jets. We begin with the techniques for lepton detection in the hadron collider environment in section 4.1 and 4.2, respectively. Each section presents a set of lepton identification variables used in the analysis. Leptons coming from the top-decays are expected to be isolated, and we present the lepton isolation in the following section. The last two sections of the chapter explain jet reconstruction and the neutrino detection in CDF.

#### 4.1 Electron Identification in CDF

This section describes the electron variables used to identify electrons and gives the cut values used.

##### 4.1.1 Offline clustering

The electron identification algorithms begin with the formation of electromagnetic clusters using an array of seed towers with transverse electromagnetic energy  $>3.0$  GeV. Neighboring towers with  $E_T > 0.1$  GeV are added to the cluster until the maximum cluster size is reached. The maximum cluster size is limited to three towers in pseudorapidity

( $\delta\eta \approx 0.3$ ) by 1 tower in azimuth ( $\delta\phi=15^\circ$  in the central region, and 5 towers in pseudorapidity ( $\delta\eta \approx 0.5$ ) by 5 towers in azimuth ( $\delta\phi=25^\circ$  in the plug region. The cluster size used for the different calorimeters reflect the variation of shower size and cell size in  $\eta$ . For clustering purposes, we define the transverse energy  $E_T \equiv E \sin \theta$  using the measured energy  $E$  in the calorimeter and the polar angle  $\theta$  given by the tower center position in the detector and the event vertex. As a cluster candidate, offline software threshold is required that the electromagnetic  $E_T$  of the cluster be  $>5.0$  GeV and that the ratio of hadronic  $E_T$  (for towers in the electromagnetic cluster) to electromagnetic  $E_T$  ( $HAD/EM$ ) be less than 0.125.

#### 4.1.2 Electron response corrections

All central calorimeter modules were calibrated in a test beam. These calibrations were maintained with radioactive sources and light flushers. However, the ultimate calibration of the electromagnetic detector was performed using the CDF data itself. First, the energy deposited in the calorimeter was compared to the momentum measured in the central tracking chamber for a large sample of low energy electrons. This  $E/p$  measurement was used to set the relative calibration of the individual calorimeter modules (tower-to-tower response). Then, the overall energy scale was determined by requiring that the  $E/p$  as measured using electrons in  $W \rightarrow e\nu$  events agree with the predictions of a radiative  $W$  Monte Carlo [35].

#### 4.1.3 Central Electron Identification Variables

After the trigger selections, a sample contains significant backgrounds from  $\pi^0, \pi^\pm$  overlap, early showering charged pions, conversions, and Dalitz pairs. At CDF, electron identification requires both calorimeter and tracking information. We have used the following variables to define electrons [36]:

##### Track momentum

We require the three-dimensional track associated to the EM cluster to distinguish elec-



trons from photons. This track is used to determine the electron's three momentum vector. The direction is much better determined using this track than using calorimeter variables which has a coarse granularity.

### HAD/EM

There must be minimal shower "leakage" into the hadronic calorimeter. We define the ratio between the hadronic and electromagnetic energy in the cluster. The electron/pion separation has been studied in the test beam and verified taken at the collider using an unbiased sample of electrons, i.e., the  $W \rightarrow e\nu$  sample obtained by triggering on the neutrino. The offline analysis required a missing  $E_T > 30$  GeV in the event, and a central EM cluster with  $E_T > 30$  GeV matched to a reconstructed track; thus this sample provides an unbiased electron sample. Figure 4.2 shows the hadronic fraction distribution for the electron candidate cluster. Test beam data for electrons and pions are shown, as well as electrons from the sample mentioned above. Both distributions agree fairly well and HAD/EM has good pion rejection.

### Lateral shower profile

The shower development in the electromagnetic calorimeter must be characteristic of an electromagnetic process. We define the Lshare variable, which is a chisquare-like lateral shower profile measuring the energy deposition in towers adjacent to the seed tower of the electromagnetic cluster. The lateral shower profile in the calorimeter is equivalent to a local isolation requirement of electron candidates, since the EM cluster is essentially 100 % contained in a single tower. This variable is defined as

$$Lshr = 0.14 \sum_k \frac{M_k - P_k}{\sqrt{0.14^2 E + (\Delta P_K)^2}}$$

where the sum is over the towers adjacent to the seed tower,  $M_k$  is the measured energy in the adjacent tower,  $P_k$  is the expected energy in the adjacent tower predicted using the impact point  $z$  in the proportional chamber(CES), the event vertex and a shower profile parametrization obtained from testbeam measurements,  $E$  is the electromagnetic

energy in the 3-tower segment and  $\delta P_k$  is the error in  $P$  associated with a 1 cm variation in the impact point. The factor  $0.14 \sqrt{E}$  is chosen to normalize the energy difference  $M_k - P_k$  relative to the statistical fluctuation inherent in the energy measurement of electromagnetic showers. For most events  $\delta P_k$  is small since the CEM has full containment (>99%) for showers more than 2 cm away from a boundary.

### Strip chamber variables

As described in section 2.2.3, a gas proportional chamber (CES) is located close to shower maximum in the central electromagnetic calorimeter. This chamber is used to determine the shower center and to quantify the cleanliness of the electron signal. The shower profiles across the strips and across the wires are separately fitted to parameterizations derived from 50 GeV/c testbeam electron data[37]. In the strip view for instance, the fitting procedure obtains the  $z$ -coordinate of the shower center,  $Z_{CES}$ , and the strip cluster energy  $E_s$  by minimizing the function:

$$X^2(z, E) \stackrel{\text{def}}{=} \sum_{i=1}^n \frac{(E_i^{\text{meas}} - E q_i^{\text{pred}}(z))^2}{\sigma_i^2(z)} \quad (4.1)$$

where the sum extends over  $n = 11$  channels. The  $E_i^{\text{meas}}$  represent measured channel energies, whereas the  $q_i^{\text{pred}}(z)$  are predicted energies normalized to 1 and corresponding to a given  $z$ -coordinate of the shower center. Fluctuations in a single channel response are taken as

$$\sigma_i^2(z) = (0.026)^2 + (0.096)^2 q_i^{\text{pred}}(z) \quad (4.2)$$

Equation 4.2 has been obtained from 10 GeV/c testbeam electron data. Since shower fluctuations and the location of shower maximum both vary with energy, the variance of a channel response can also be expected to depend on energy. However, this dependence is common to all channels and hence does not affect the fitting.

To test a single electron or single photon hypothesis, one introduces the variable:

$$\chi_{\text{Strips}}^2 \stackrel{\text{def}}{=} \frac{1}{4} \left( \frac{E_{\text{CEM}}}{10} \right)^{0.747} \sum_{i=1}^n \frac{(q_i^{\text{meas}} - q_i^{\text{pred}}(Z_{\text{CES}}))^2}{\sigma_i^2(Z_{\text{CES}})} \quad (4.3)$$



where  $\{q_i^{meas}\}_{i=1}^n$  is the measured strip profile normalized to 1. The  $E_{CEM}$ -dependent factor in front of the sum sign compensates for the aforementioned energy dependence of  $\sigma_i^2$  ( $E_{CEM}$  is the electron energy measured from the CEM cluster, which has better resolution than the CES measurement  $E_s$ ).

The treatment of the wire view is entirely analogous to that of the strip view and consists in calculating the local  $x$ -coordinate  $X_{CES}$  of the shower center and the corresponding goodness of fit variable  $\chi_{Wires}^2$ . A plot of the average CES chisquare  $(\chi_{Strips}^2 + \chi_{Wires}^2)/2$  is shown in figure 4.2 for 50 GeV testbeam electrons and pions, and for electrons from  $W \rightarrow e\nu$ . The  $\chi^2$  cut is made to remove a potential contamination from pion overlap backgrounds in a sample.

We also require a match between the EM cluster position as measured by the strip chambers and the extrapolated track coordinates.

$$\Delta X = X_{extrap} - X_{CES} \quad (4.4)$$

$$\Delta Z = Z_{extrap} - Z_{CES} \quad (4.5)$$

where  $X_{extrap}$  and  $Z_{extrap}$  are the coordinates of the electron track extrapolated to the radius of the strip chamber. These variables help reject fake electron signals caused by a charged pion track which overlaps with a neutral pion showering in the electromagnetic calorimeter.

### Energy-momentum ratio

Electrons are expected to have a good agreement between the electromagnetic energy and a track in the central tracking chamber. We use the ratio of the calorimeter energy to the electron track momentum of the highest momentum track associated with the EM cluster,  $E/P = E_T/P_T$ , in order to verify the matching between the EM cluster and the CTC measurement of the electron energy. This ratio is calculated from the corrected energy and beam constrained momentum.

The presence of a small tail at higher  $E/p$  due to hard synchrotron radiation which

lowers the value of the momentum( $p$ ) detected in the central tracking chamber, while having a smaller effect on the energy  $E$  because most of the radiated energy is deposited in the same calorimeter cell with the electron shower.

Because high energy electrons tend to radiate in the detector, and since the CTC only measures the charged track momenta whereas the calorimeter captures most of the radiated energy, we expect the mean of the  $E/p$  distribution to be slightly above 1.

Variable	Tight	Loose
$E_T$	$> 20 \text{ GeV}$	$> 20 \text{ GeV}$
$P_T$	$> 10 \text{ GeV}/c$	$> 10 \text{ GeV}/c$
HAD/EM	$< 0.05$	$< 0.055 + 0.045 E_T/100$
$E/P$	$< 1.5$	$< 4.0$
$L_{shr}$	$< 0.2$	$< 0.2$
$\Delta_x$	$< 1.5 \text{ cm}$	$< 1.5 \text{ cm}$
$\Delta_z$	$< 3.0 \text{ cm}$	$< 3.0 \text{ cm}$
$\chi^2_{strip}$	$< 15$	

Table 4.1: Central electron selection requirement

### Isolation

We require that an absence of additional particles around the electron, since electrons coming from the top-decay are expected to be isolated. We require that at least one central lepton in the event be isolated in the central tracking chamber. This will be described in section 4.3 of this chapter.

Table 4.1 summarizes the central electron selection criteria. The distributions of the identification variables before cuts are shown in Figure 4.3, 4.4, 4.5, 4.6, 4.7, and 4.8 for electrons from a sample of  $Z \rightarrow ee$  events. In the same figures, we also show the distribution for electrons coming from  $W^-$  and  $b$ -decays from top Monte Carlo. The central electron detection efficiency determined from  $Z \rightarrow ee$  events is 87% and 94%,



respectively for the tight and loose selection cuts, as we see in Section 6.2.1.

#### Conversion removal

We reject electrons from photon conversions and  $\pi^0$  decays by requiring that the electron candidate has a VTX track and that the second oppositely charged track forming an effective  $e^-e^+$  mass less than 0.5 GeV is not present. The number of nonconversion electrons mistakenly rejected by the algorithm depends on the density of tracks near the electron. It is estimated that approximately 4 % of prompt electrons are rejected by these requirement. We have taken into this correction in the acceptance calculations.

#### Fiducial cuts

The following regions are excluded in order to ensure the quality of electrons.

- The seed tower of the electron cluster must be one of towers 0-8 of the central electromagnetic calorimeter. The tower 9 has a different shape from other central calorimeter towers and the electron response varies significantly with the  $z$  position in the tower.
- The shower position in the strip chamber must be at least 9 cm away from the  $Z=0$  plane in order to exclude the  $90^\circ$  crack region.
- The extrapolated track position at the strip chamber(=184 cm) must be at least 2.5 cm away from azimuthal boundaries between central calorimeter wedges( $15^\circ$  boundaries).

### 4.1.4 Plug Electron Identification Variables

The plug electrons must satisfy the following requirement:

#### HAD/EM

We use the same quantity as the central electron's as stated above.

#### Lateral shower shape: $\chi_{3 \times 3}^2$

A lateral shower distribution variable ( $\chi_{3 \times 3}^2$ ) measures the deviation of the shower from

the predicted shower shape obtained from test beam. We use a  $3 \times 3$  array of calorimeter cell, since most of electron shower is confined in this size.

#### VTX hit occupancy

We use the position information in the VTX, which gives good position in the  $\theta$  coordinate, but poor position resolution in  $\phi$ . Given the cluster position and the event vertex, we define a road where we would expect the electron go through the VTX active region and look for hits on the wires along this road. The fraction of actual hits to expected hits is used to distinguish electrons from photons and required to be greter than 0.5.

Table 4.2: Plug electron selection requirement

Variable	Cut
$E_T$	$> 20 \text{ GeV}$
HAD/EM	$< 0.05$
$\chi^2_{3 \times 3}$	$< 3.0$
$\chi^2_{depth}$	$< 15.0$
$N_{VTX}$	$> 0.5$
Track	one and only one CTC track
$N_{axialsuperlayer}$	$> 3$
Isolation	$< 0.1$

#### Track requirement

One and only one track associated to the EM cluster is required to be well reconstructed in three CTC by demanding a minimum number of hits above 3. There must be no additional three-dimensional track with  $P_T > 1.5 \text{ GeV}/c$  within a cone of radius 0.25 around the electron track. This is required because we see some plug electrons with a bunch of tracks pointing to an EM cluster, which identifies to be a jet. Figure 4.11 shows the track finding efficiencies which satisfy track quality cuts. In the region  $1.2 < |\eta| < 1.4$  fewer CTC layers are available for pattern recognition as shown in Figure 4.11.

#### Isolation

$I \equiv (E_C - E_T)/E_T$ , where  $E_C$  is the total transverse energy within a cone of radius 0.4



in  $\eta - \phi$  space centered on the cluster and require  $I < 0.1$ .

### Fiducial region

- The position of the seed tower of the electron cluster must not be in three outer tower annuli nor in two inner tower annuli. This means that it should be within a pseudo-rapidity range of  $1.32 < \eta_d < 2.22$ .
- The position of the cluster centroid must be at least  $5^\circ$  away from azimuthal boundaries between the quadrants.

Table 4.2 summarizes the plug electron selection cuts. The efficiency of these requirements are calculated from  $Z \rightarrow ee$  events and it is 85% (See Section 6.2.1).

## 4.2 Muon Identification in CDF

Muons are identified by their ability to penetrate many hadronic interaction lengths of absorber with minimal energy loss. Both calorimeter and tracking information are used to identify muons by requiring that the tower to which a track extrapolates has energy deposition consistent with that of a minimum ionizing particle. This requirement suppresses backgrounds from hadrons that interact in the calorimeters. High  $P_T$  muons can be efficiently found in the rapidity region  $|\eta| < 1.2$ , covered by the central and endwall calorimeters, and where the tracking information is available from the CTC. If the track goes into the region  $|\eta| < 1.0$  where the muon chambers are instrumented, a match between the CTC track and the muon chamber segment can be used to reject backgrounds. The confirmation by additional CMP chambers also makes possible to reduce the backgrounds. The presence of a muon chamber segment is also useful for online-triggering of muons. If the muon has no associated muon segment track, the isolation cut is imposed in order to reject backgrounds instead of using the muon segment information. We call muons with and without a muon chamber track as CMUOs

(central muon objects) and CMIOs (central minimum ionizing objects), respectively.

### **Fiducial Region**

To ensure the energy deposited is well measured, fiducial cuts are imposed. The same fiducial cuts defined for electrons are applied on CMIOs to avoid cracks between calorimeter modules. No explicit fiducial cuts are applied on the muon-chamber muons, since tracks going through cracks are naturally avoided. This requirement defines a muon fiducial volume that covers 85 % of solid angle for  $|\eta| < 1.2$ .

## **4.2.1 Identification variables**

We describe the parameters which characterize muons in this section.

### **Minimum ionization requirement**

We demand that the energy deposited to calorimeter be consistent with that of a minimum-ionizing particle. Energy deposited of the muon to the calorimeter tower must be less than 2.0 GeV in the EM compartments and less than 6 GeV in the hadronic compartments. We also require that a sum of EM and hadronic energy deposited must be above 0.1 GeV. Figure 4.12 shows energy deposited to the EM and HAD compartments for 57 GeV/c test-beam muons. On the average a minimum ionizing particle deposits 0.3 GeV in the EM and 2 GeV in the HAD calorimeters.

### **Track requirement**

The CTC track for the muon candidate must have an impact parameter  $|d_0| < 0.3$  cm where  $|d_0|$  is the distance of the extrapolated track trajectory from the beam axis at the point of closest approach. A match between the CTC track and the primary vertex along the beamline must also be less than 5 cm. These cuts are placed to reject occasional tracks from cosmic rays and from muons coming from decays in flight of kaons and pions. In addition, we require at least 3 axial and 2 superlayers and the sum of both be greater or equal to 6 to ensure the quality of tracks.



### Match between the CTC track and the muon chamber track

For the CMUO, an additional requirement of matching between CTC track and muon segment track in  $R - \phi$  plane( $\Delta x$ ) is imposed. Muons must satisfy either of  $\Delta x(CMU) < 10$  cm or  $\Delta x(CMP) < 20$  cm or  $\Delta x(CMX) < 20$  cm.

### Isolation

We require that at least one central lepton in the event be isolated in the central tracking chamber. This will be described in section 5.3. We require the absence of additional particles around CMIOs. The transverse energy in the towers within a cone of 0.4 excluding the muon energy must be less than 5 GeV.

Table 4.3: Central muon selection requirement

Variable	CMUO cuts	CMIO cuts
$P_T$	$> 20$ GeV	$> 20$ GeV
$\eta$ range	$< 1.0$	$< 1.2$
EM energy	$< 2$ GeV	$< 2$ GeV
HAD energy	$< 6$ GeV	$< 6$ GeV
Impact parameter	$< 3$ mm	$< 3$ mm
Z-vertex match	$< 5$ cm	$< 5$ cm
$\Delta x$ (CMU)	$< 10$ cm	
$\Delta x$ (CMP)	$< 20$ cm	
$\Delta x$ (CMX)	$< 20$ cm	

### Cosmic ray removal

The cosmic ray events have tracks which are back-to-back in three dimensions in the central tracking chamber. Also, they do not normally pass close to the interaction region, hence their impact parameter distribution is relatively flat. Reconstruction of the cosmic ray tracks as it goes towards the CTC center is generally worse than for tracks emanating from the center, because the time-of-flight corrections are wrong. By looking for a poor quality tracks back-to-back with the muon candidate rejects the majority of cosmic rays.

We classify CMUOs into two classes: 'tight' and 'loose' muons. The difference between them is that tight muons are required to match to a CMU or CMP track segment, while loose ones are allowed to that the muon type is CMU or CMP or CMX.

### 4.3 Lepton Isolation

The energy surrounding a lepton depends on the lepton source. Leptons coming from Drell-Yan process, W's and Z's are said to be isolated in contrast to the nonisolated leptons coming from the decay of charm and bottom hadrons which are accompanied by quark hadronization and decay products. Leptons from the decay of top quark are expected to be isolated. In the semi-leptonic decay of a W from a top quark will be emitted at a large angle with respect to the other decay and hadronization products. Lepton isolation is a powerful tool in detecting leptons from top quark decay in the presence of bottom and charm leptonic decays. We define a measure to quantify the absence of the additional particles around the lepton. In the CDF detector the activity around leptons can be measured both in calorimeter and in the central tracking chamber, namely calorimeter isolation and track isolation.

In the following we show that a track isolation cut will be more efficient for top and at least as good at rejecting background.

Looking at  $t\bar{t}$  Monte Carlo with  $M_{top}=120$  GeV/ $c^2$ , we see that the calorimeter isolation cut keeps 89% of 'direct' ( $t \rightarrow W \rightarrow e$ ) 20 GeV central electrons which pass the standard set of electron identification requirement (figure 4.17 (c)). A track isolation cut, requiring less than 3 GeV of  $P_T$  in a cone of 0.25 about the electron does better, keeping 94% of the 'direct' electrons (figure 4.17 (a)). These are efficiencies per lepton. Requiring both legs in the event to be isolated will double the inefficiency.

Looking at the same Monte Carlo, we can also find the efficiency for all the electrons in the event, direct or indirect. Figure 4.17 (b) shows the sum  $P_T$  of CTC tracks inside a cone of 0.25 for central electrons, and Figure 4.17 (b) shows the calorimeter  $E_T$  in a



cone of 0.4 for all central electrons in the  $t\bar{t}$  events. In both cases, the lepton energy is excluded from the sum. Cutting on calorimeter isolation on a single electron keeps 85% of them, cutting on track isolation keeps 91%.

Electrons passing tight cuts, selected inclusively from the high- $P_T$  dilepton sample (very loose selection cuts on the second lepton), are enriched in  $b \rightarrow e$  decays and also contain fakes and, to a much lesser extent, electrons from Drell-Yan and  $Z$ . Looking at these electrons, we see that the calorimeter isolation cut rejects 39% of the central electron with  $E_T$  above 20 GeV which pass a set of tight electron cuts, while the track isolation cut rejects 51% of them. This gives us some indication of how well the two cuts reject background. The track isolation cut is favorable over the isolation cut. Alternatively, we can look at EM clusters which have HAD/EM greater than 6%, so that we know we are looking at 'junk', and we see that the calorimeter isolation cut rejects 82% and the track isolation cut rejects 83%.

Cut	Cone	$t \rightarrow W \rightarrow e$	$t \rightarrow X \rightarrow e$	'good' EM cluster	HAD/EM > 0.06
$E_T < 5$	0.40	.89	.85	.39	.82
$P_T < 3$	0.20	.96	.93	.49	.80
$P_T < 3$	0.25	.94	.91	.51	.83
$P_T < 3$	0.30	.92	.88	.53	.84

Table 4.4: Comparison of tracking and calorimeter isolation variables. The efficiencies in first two columns are from Monte Carlo. The second two, are from data. See text for details.

We also checked that the cuts did not throw away good electrons by looking at  $Z \rightarrow ee$ . Putting tight cuts listed in Table 4.1 on both legs of the  $Z$  leaves us with 415 central-central events, or 830 electrons. The track isolation cut keeps 828/830 electrons, while the calorimeter isolation cut keeps 822/830.

Finally, we varied the cone size for the track isolation cut. A summary is given in table 4.4. The numbers are fractions of electrons with  $E_T > 20$  GeV which passed the isolation cut of given cone size.

We use sum of track  $P_T$  in a cone of  $R=0.25$  around the muon, excluding the muon

track,  $<3.0 \text{ GeV}/c$  (See Section 5.3).

## 4.4 Jets

Jets are characterized by an extended cluster of hadronic and electromagnetic deposition. Jets are reconstructed using an algorithm which forms clusters from the recorded energies deposited in the calorimeter towers. In CDF it is an iterative fixed cone algorithm that begins by looking for contiguous clumps of energy, called "pre-clusters", and then gathers all the energy within a fixed distance from these pre-clusters. The pre-clustering stage begins by combining contiguous towers with  $E_t > 1 \text{ GeV}$ . This relatively high tower threshold is designed to eliminate clusters formed from fluctuations in the soft underlying event. Any pre-cluster with  $E_t > 3 \text{ GeV}$  is considered a "seed" for the cluster finder. A circle in  $\eta$ - $\phi$  space is drawn around each seed. The radius of this circle is a parameter of the algorithm; the default is 0.7. Now, all towers inside the circle and with  $E_t$  above 100 MeV are included in the cluster. (Once a good seed has been found, a lower threshold is used to allow the algorithm to gather the maximum fraction of the jet energy and therefore have the best possible energy resolution. The 100 MeV threshold is well above the electronic noise level for the calorimeter in CDF.) The position of each cluster is recalculated using the  $E_t$  weighted centroid of all towers in the cluster. A new circle is iterated until stable. If two clusters have more than 75 % of their towers in common, the clusters are merged. When a tower is shared by two unmerged clusters, it is uniquely assigned to the cluster that is closest in  $\eta - \phi$  space.

From the towers associated with the cluster, the quantities  $(p_x, p_y, p_z, E)$  are calculated. The electromagnetic and hadronic compartments of each tower are assigned massless four-vector with magnitude equal to the energy deposited in the tower and with the direction defined by a unit vector pointing from the event origin to the center of the face of the calorimeter tower (calculated at the depth that corresponds to shower maximum).  $E$  is the scalar sum of tower energies;  $p_x$  is the sum of  $p_{x,i}$  where  $i$  is the



tower index. The transverse energy is defined as  $E_T \equiv E \sin \theta$ .

## 4.5 Missing transverse energy

Decays of  $t\bar{t}$  events produces neutrinos. Since these particles can not be detected directly, their presence must be inferred by the presence of a large momentum imbalance in the event. The missing transverse energy ( $\cancel{E}_T$ ) is defined to be the negative of the vector sum of the transverse energy in all calorimeter towers with  $|\eta| < 3.6$ .

$$\cancel{E}_T = - \left| \sum_{|\eta| < 3.6} \vec{E} \right|$$

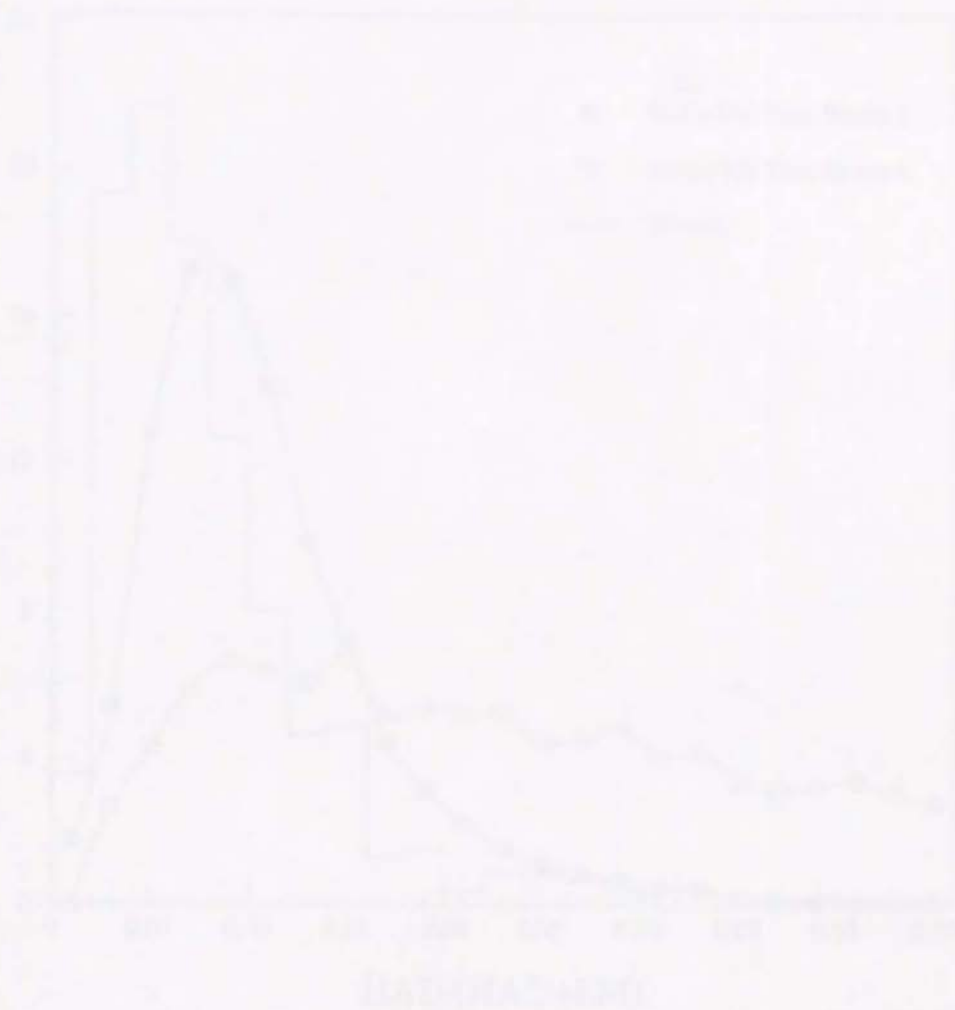
The  $\eta$  range is restricted because the low- $\beta$  quadrupoles of the Tevatron cover part of the azimuthal regions for  $3.6 < \eta < 4.2$ . To be included in the sum, towers must pass an energy threshold requirement of 0.1 GeV for all the calorimeters (This is the same threshold as the one used for the jet clustering). Missing  $E_T$  measurement is sensitive all types of detector imperfections. Mismeasurement of jets due to finite detector resolution, loss of energy in cracks and loss of jet down the beamline is the primary source of the missing  $E_T$ .

We compute the missing  $E_T$  from the 'raw' missing transverse energy  $\vec{\cancel{E}}_{T,\text{uncorrected}}$  as

$$\vec{\cancel{E}}_T = \vec{\cancel{E}}_{T,\text{uncorrected}} + \sum_{\text{muons}} (\vec{E}_T^{\text{muon-tower}} - \vec{p}_T^\mu) + \sum_{\text{jets}} (\vec{E}_{T,\text{uncorrected}}^{\text{jet}} - \vec{E}_{T,\text{corrected}}^{\text{jet}}), \quad (4.6)$$

where  $\vec{p}_T^\mu$  is the transverse component of the muon momentum vector,  $\vec{E}_T^{\text{muon-tower}}$  is the transverse energy measured in the calorimeter tower crossed by the muon. Note that we also correct the missing  $E_T$  for jets with observed  $E_T > 10$  GeV and  $|\eta| < 2.4$ . The second sum on the right-hand side is the difference between the corrected jet  $E_T$  ( $\vec{E}_{T,\text{corrected}}^{\text{jet}}$ ) and the observed(uncorrected) jet  $E_T$  ( $\vec{E}_{T,\text{uncorrected}}^{\text{jet}}$ ). We will show that the missing  $E_T$  corrected for jet energy scale has a better rejection for the backgrounds than using uncorrected quantity in Section 5.6.

The resolution on the  $\cancel{E}_T$  measurement depends on the amount of energy in the event. For minimum-bias events, the resolution for the two components  $\cancel{E}_{Tx}$  and  $\cancel{E}_{Ty}$  of the  $\cancel{E}_T$  vector can be parametrized as  $\sigma(\cancel{E}_T) = 0.47\sqrt{\sum E_T}$ , where





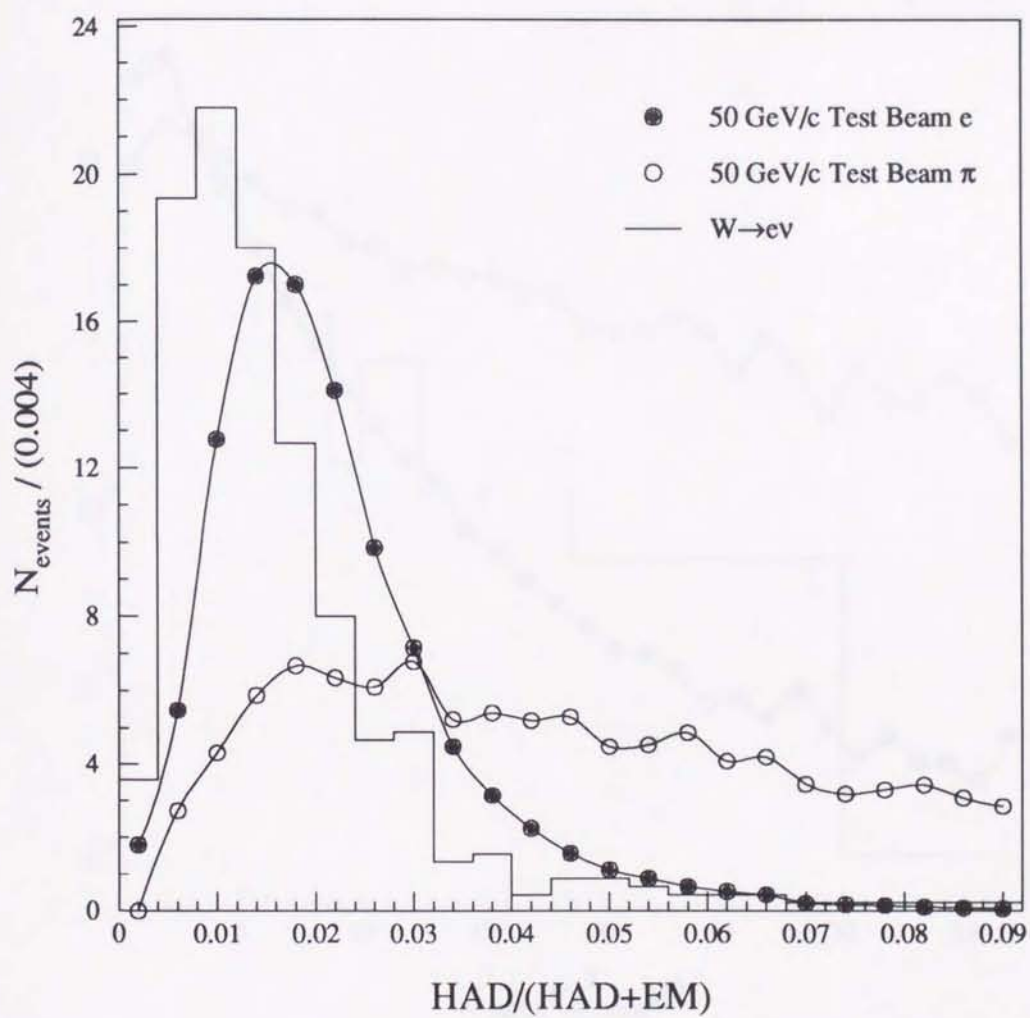


Figure 4.1: The  $\text{HAD}/(\text{HAD}+\text{EM})$  distribution for 50 GeV testbeam electrons and for electrons from  $W$  decays. From

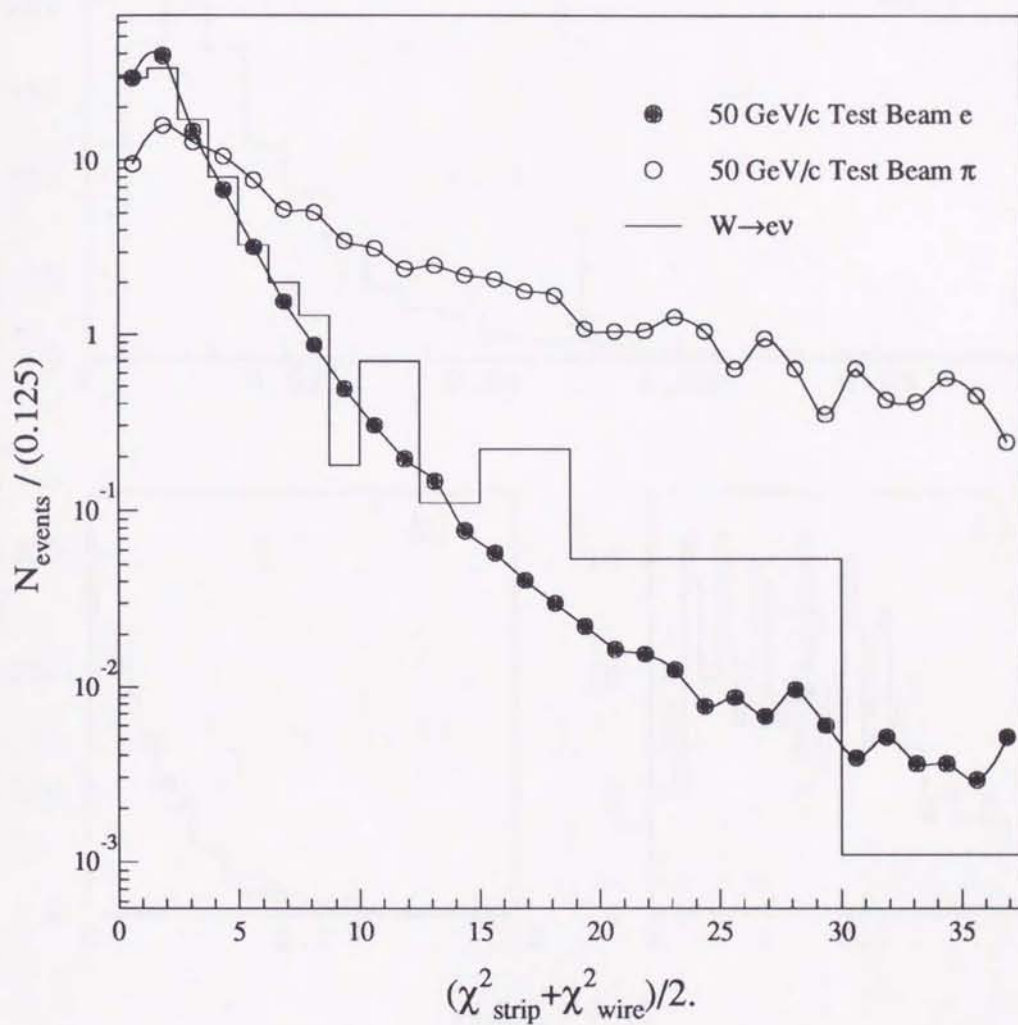


Figure 4.2: The average CES chisquare distribution for 50 GeV testbeam electrons and charged pions, and for electrons from W decays. From



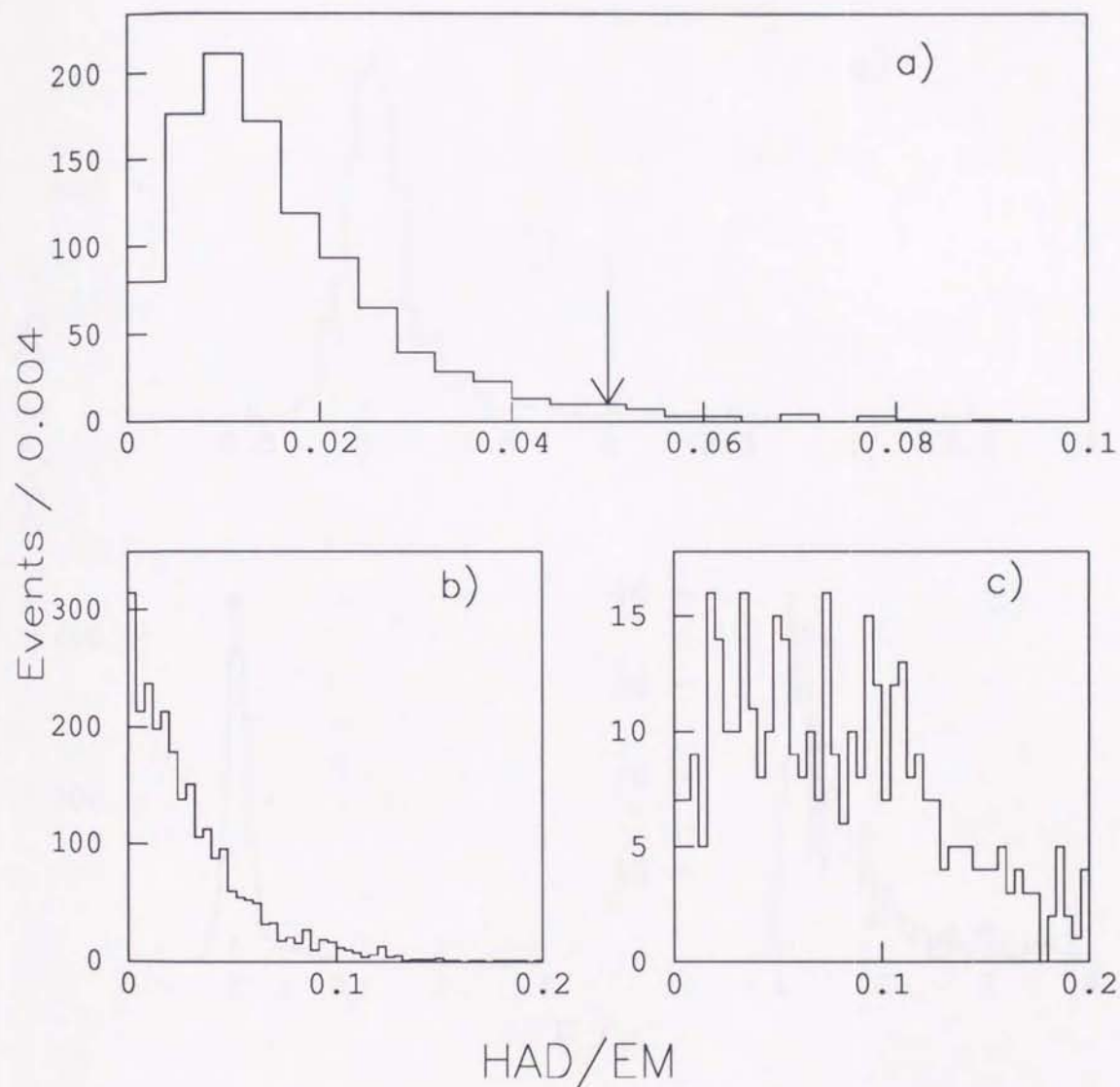


Figure 4.3: Ratio of hadronic and electromagnetic energy deposition (HAD/EM) for electrons from a)  $Z \rightarrow ee$  decays. Also shown are the values of the cuts for the selection in the dilepton analysis. b) and c) are the same variables for electrons from the decays of  $W$  and from the decays of  $b$ , respectively from the  $t\bar{t}$  Monte Carlo.

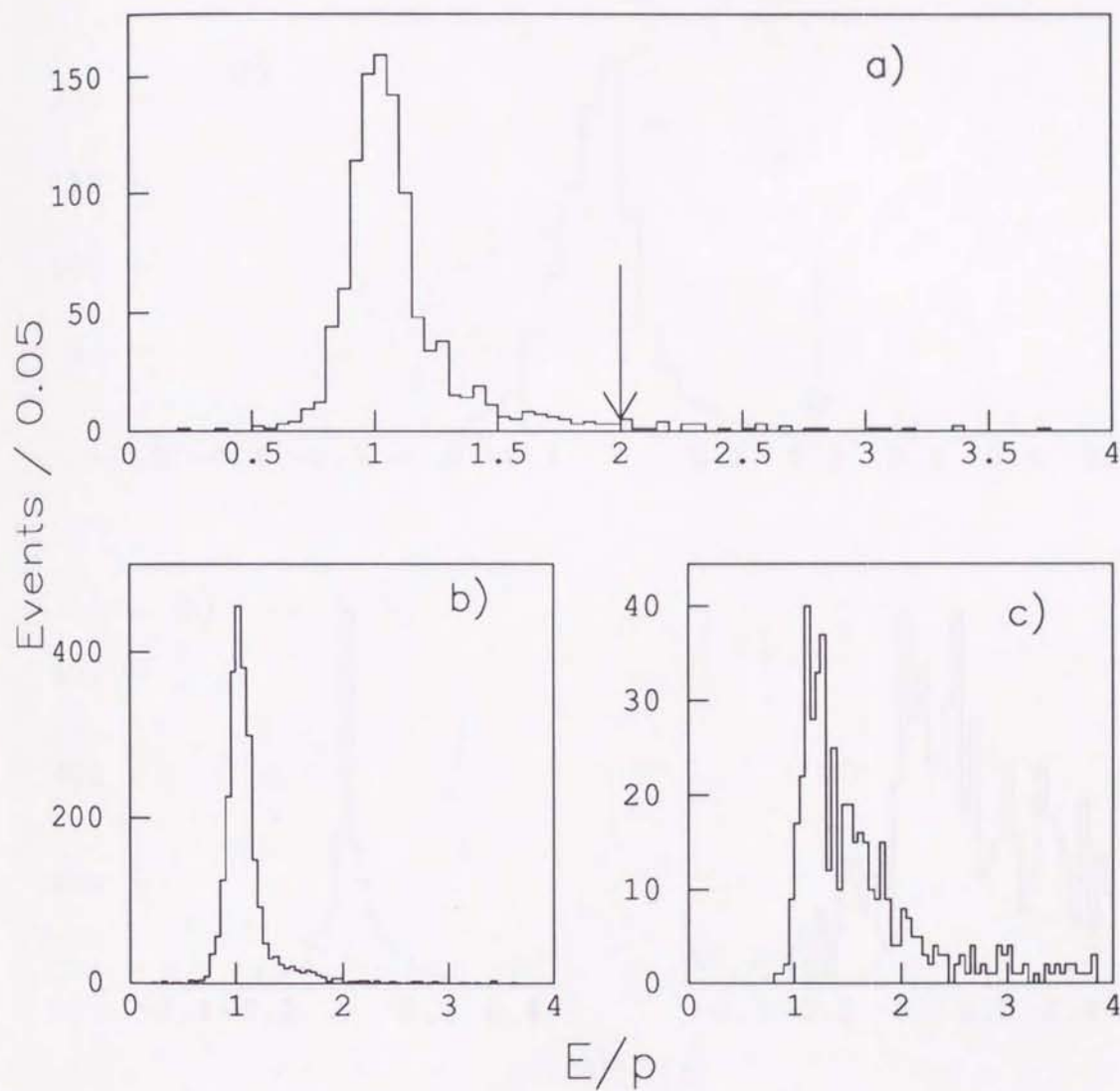


Figure 4.4: Ratio of calorimeter energy and momentum for electrons from a)  $Z \rightarrow ee$  decays. Also shown are the values of the cuts for the selection in the dilepton analysis. b) and c) are the HAD/EM distributions for electrons from the decays of  $W$  and from the decays of  $b$ , respectively in the Monte Carlo  $t\bar{t}$  events.



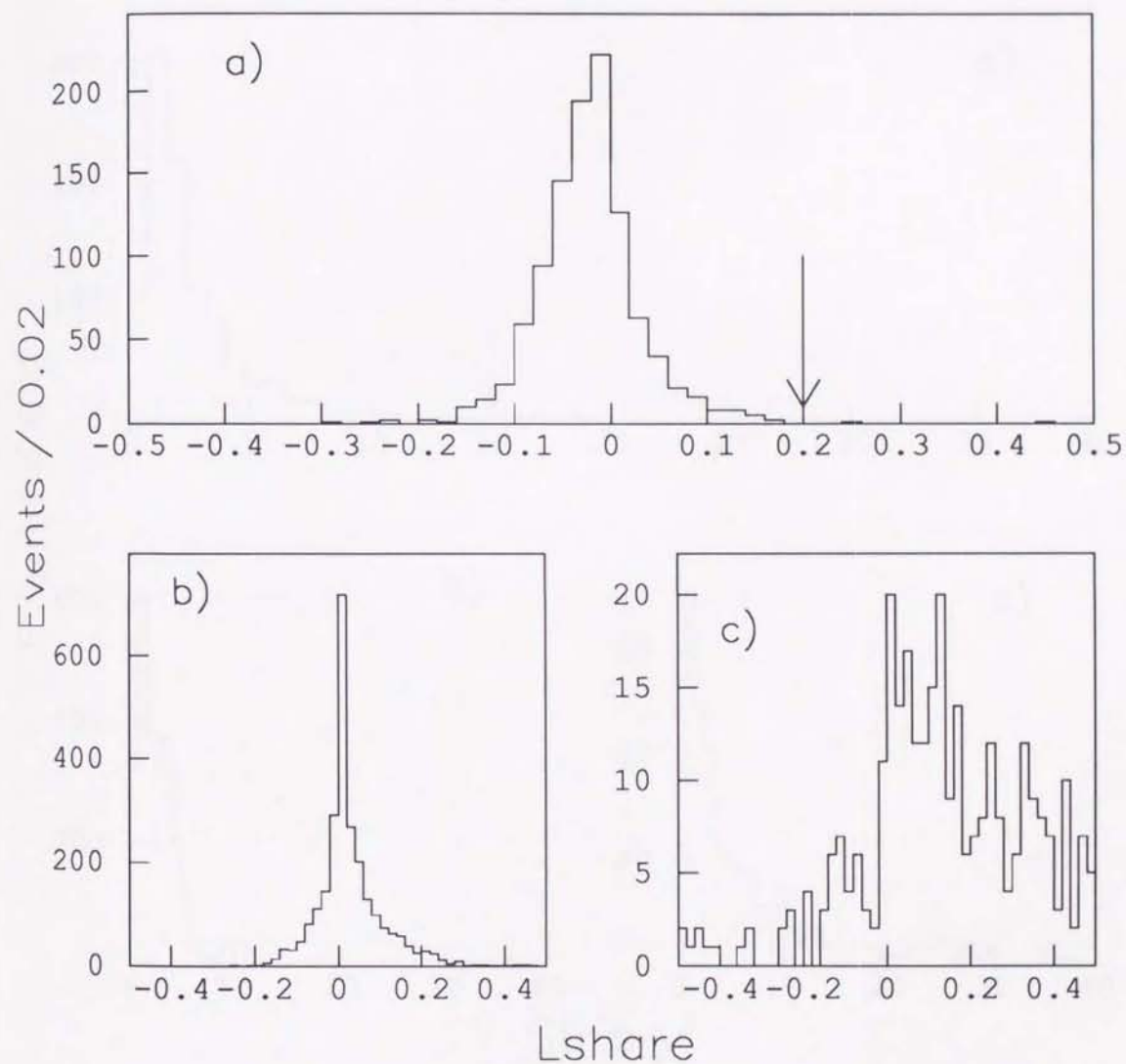


Figure 4.5: Lateral shower profile for electrons from a)  $Z \rightarrow ee$  decays. Also shown are the values of the cuts for the selection in the dilepton analysis. b) and c) are the same variable for electrons from the decays of  $W$  and from the decays of  $b$ , respectively in the Monte Carlo  $t\bar{t}$  events.

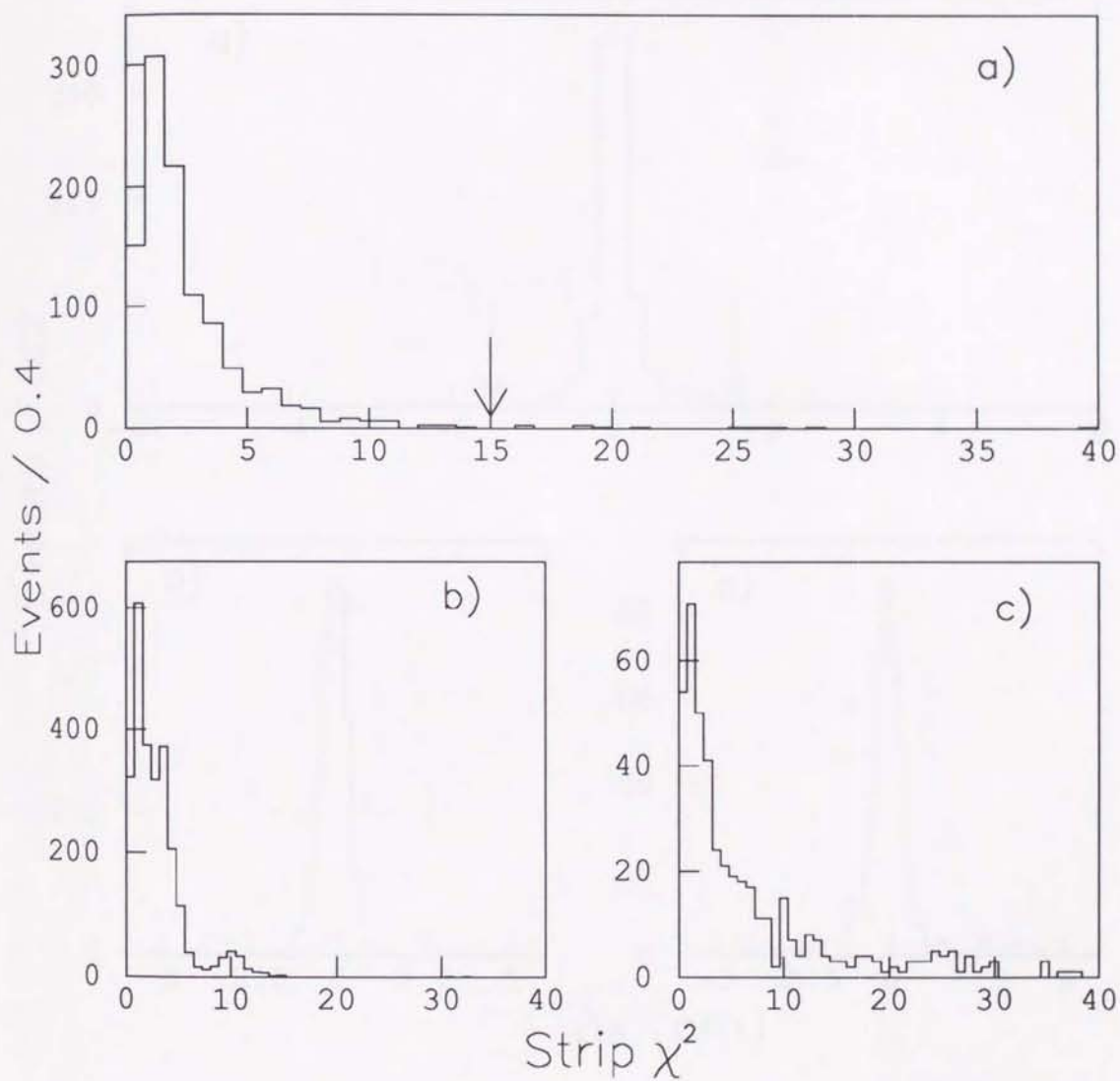


Figure 4.6: Distribution of  $\chi^2_{strip}$  for a)  $Z \rightarrow ee$  events. Also shown are the values of the cuts for the selection in the dilepton analysis. b) and c) are the same distributions for electrons from the decays of  $W$  and from the decays of  $b$ , respectively in the Monte Carlo  $t\bar{t}$  events.



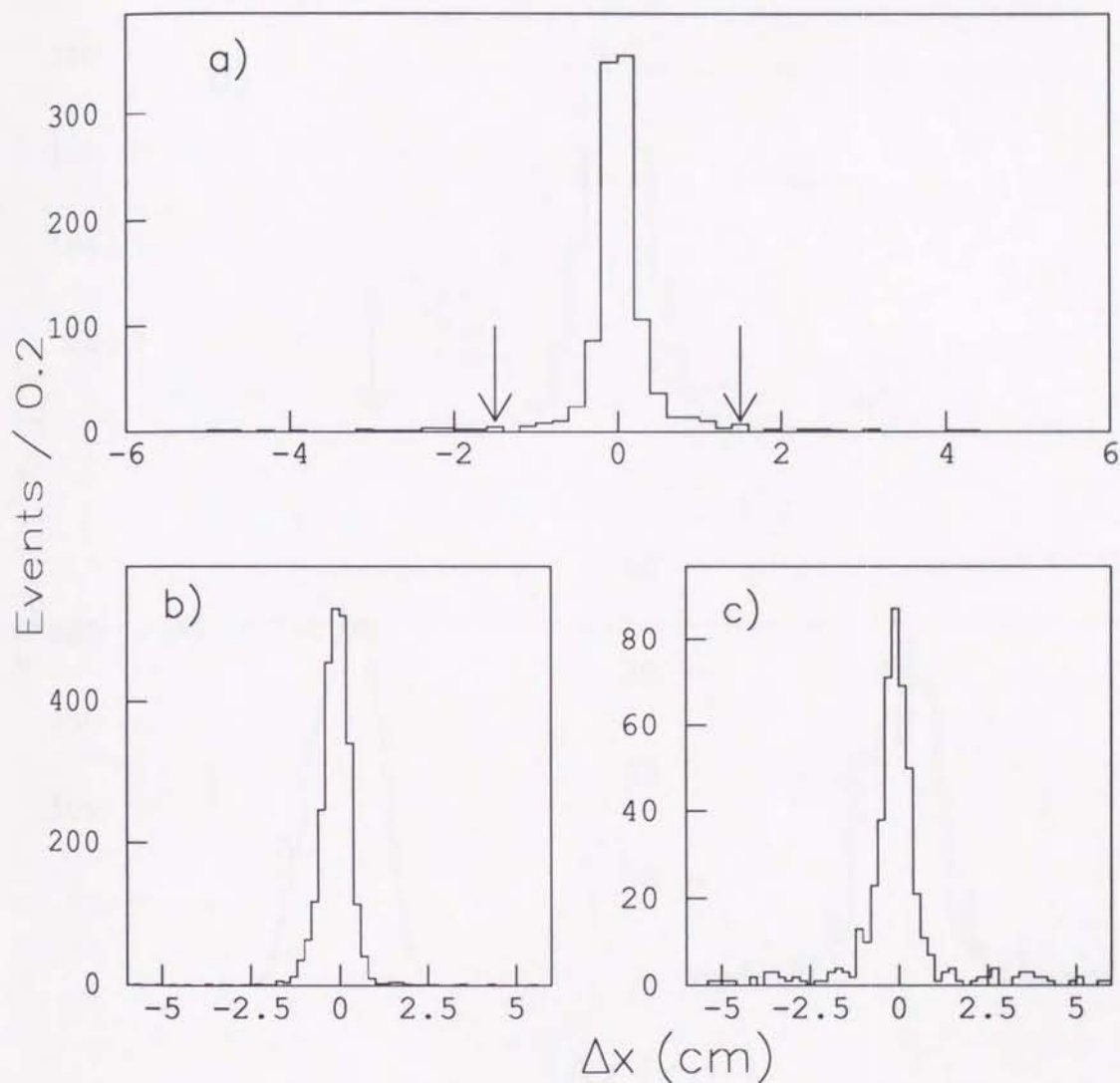


Figure 4.7: Distribution of match in the  $R - \phi$  view between the track and the shower position as measured in the strip chambers for a)  $Z \rightarrow ee$  events. Also shown are the values of the cuts for the selection in the dilepton analysis. b) and c) are the same distributions for electrons from the decays of  $W$  and from the decays of  $b$ , respectively in the Monte Carlo  $t\bar{t}$  events.

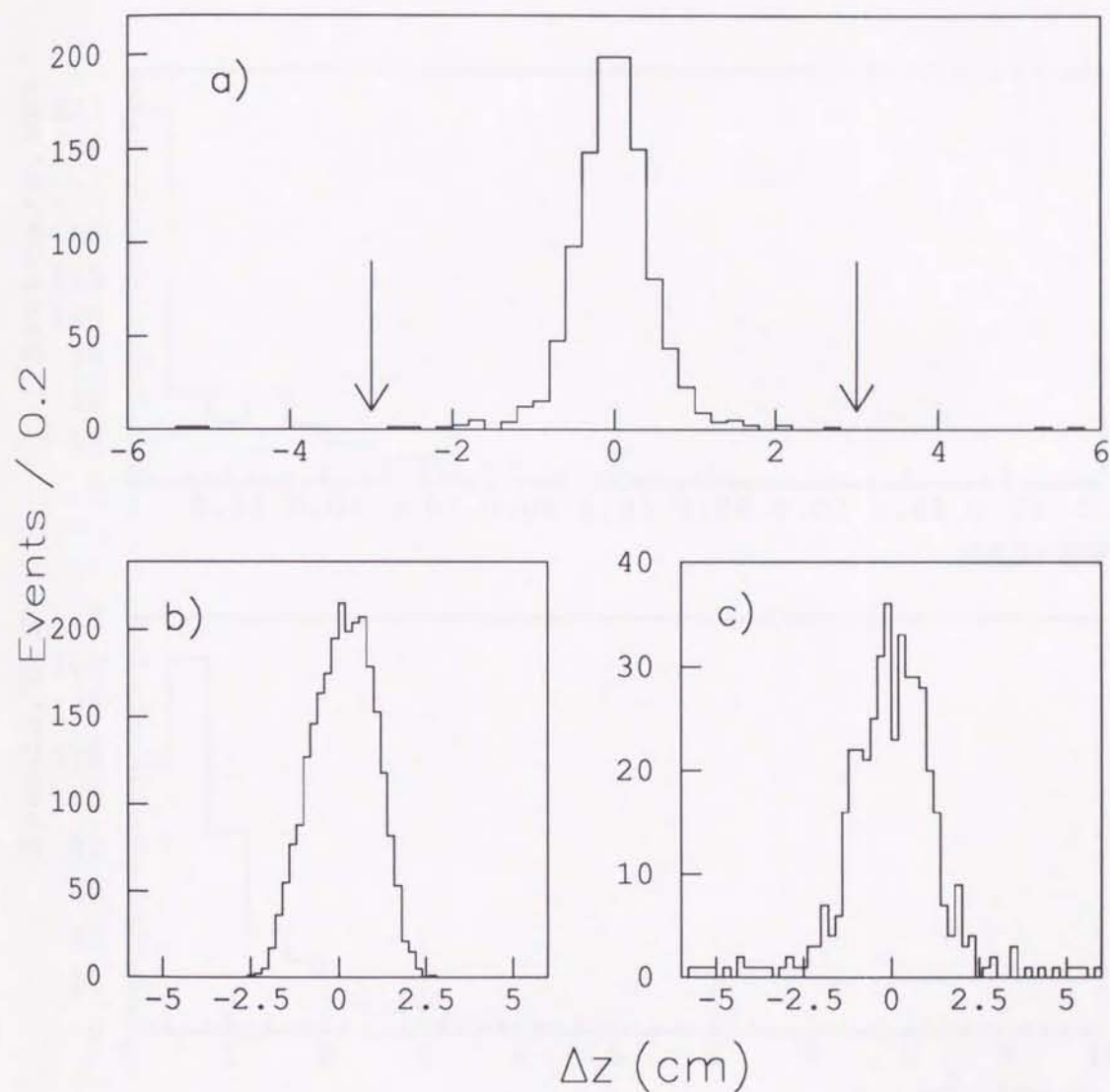


Figure 4.8: Distribution of match in the  $z$  view between the track and the shower position as measured in the strip chambers for a)  $Z \rightarrow ee$  events. Also shown are the values of the cuts for the selection in the dilepton analysis. b) and c) are the same distributions for electrons from the decays of  $W$  and from the decays of  $b$ , respectively in the Monte Carlo  $t\bar{t}$  events.



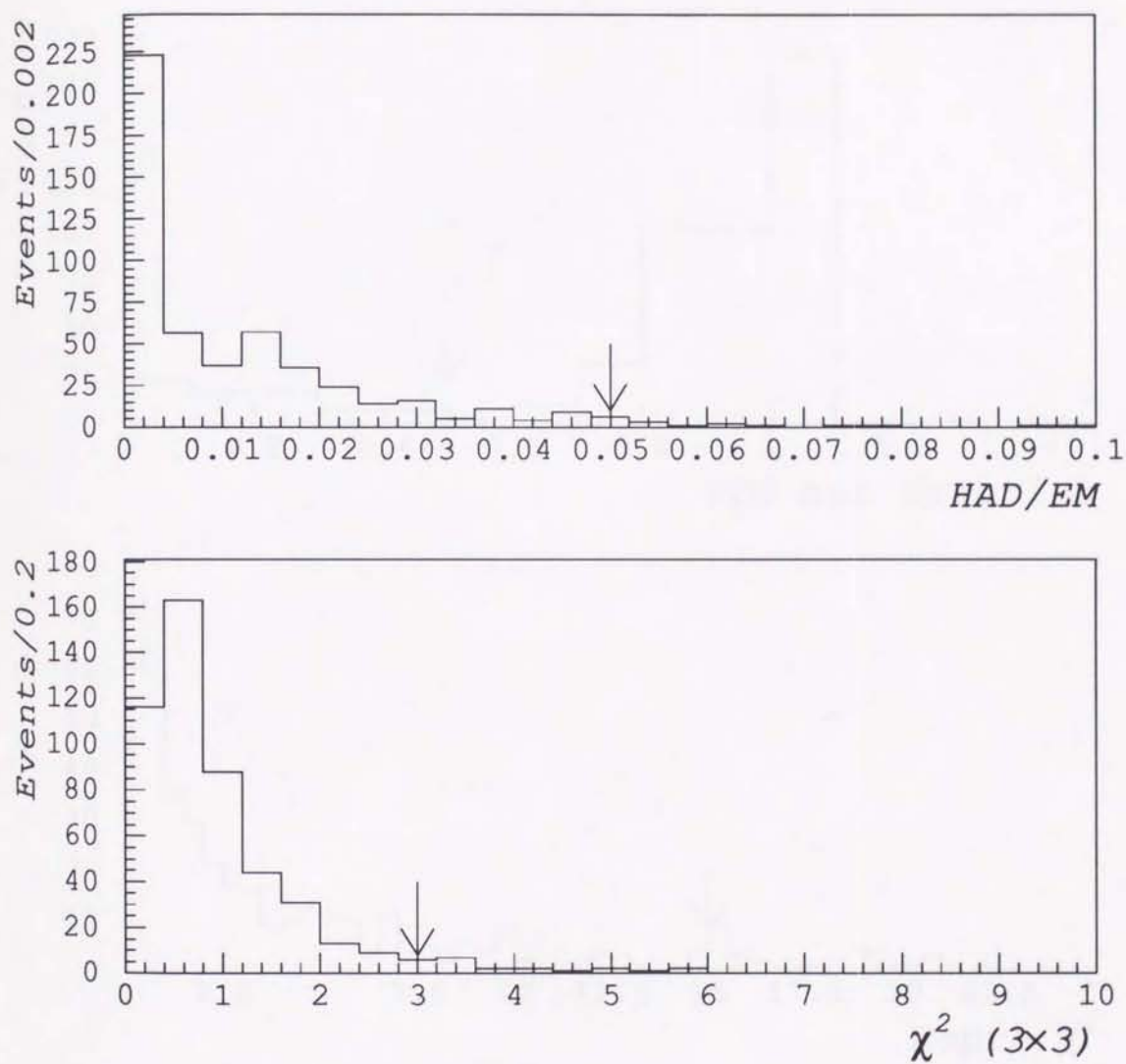


Figure 4.9: Plug electron quality variables for  $Z \rightarrow ee$  events. Also shown are the values of the cuts for the selection in the dilepton analysis.

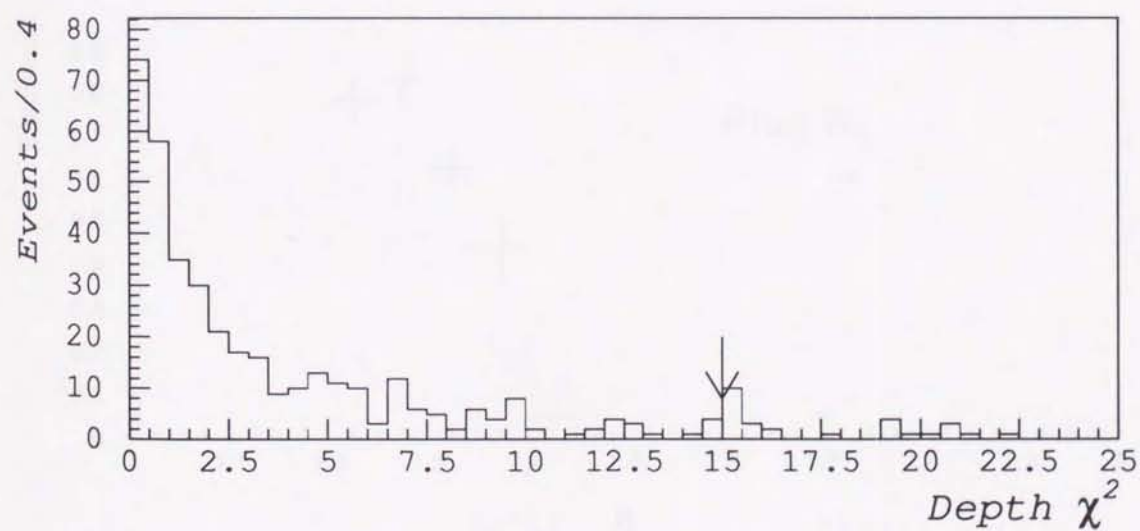
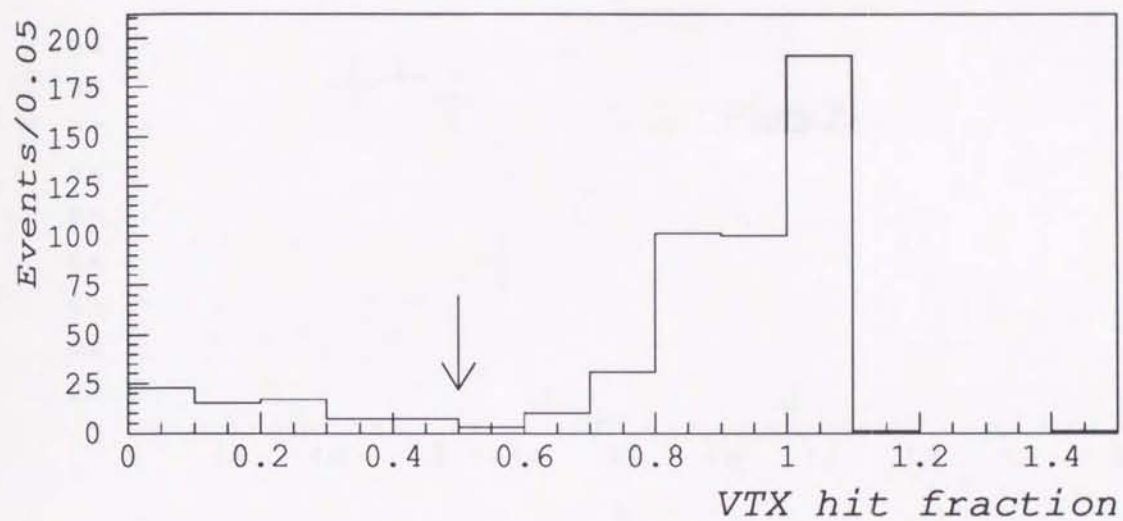


Figure 4.10: Plug electron quality variables for  $Z \rightarrow ee$  events. Also shown are the values of the cuts for the selection in the dilepton analysis.



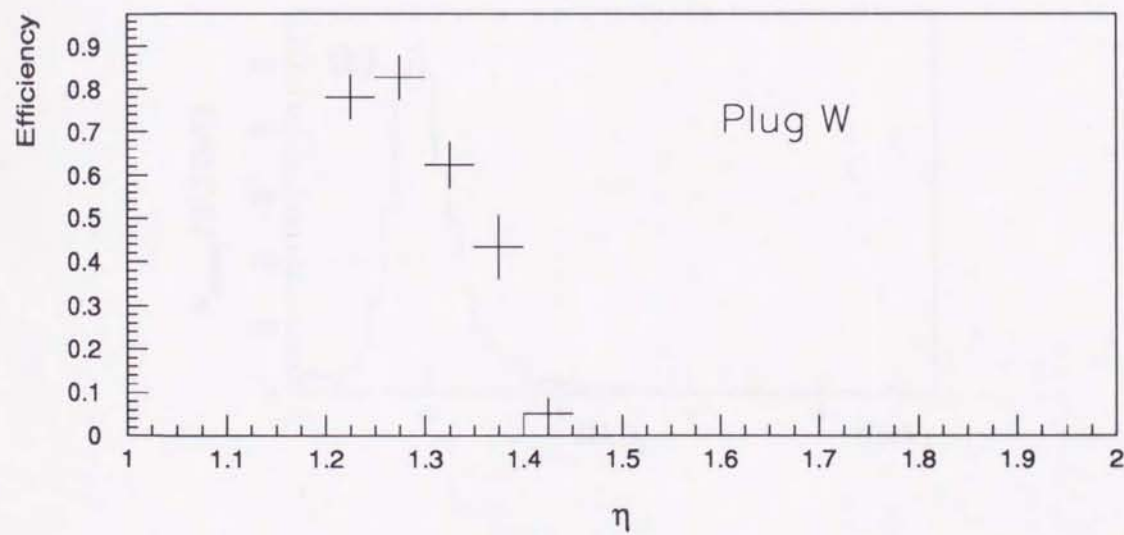
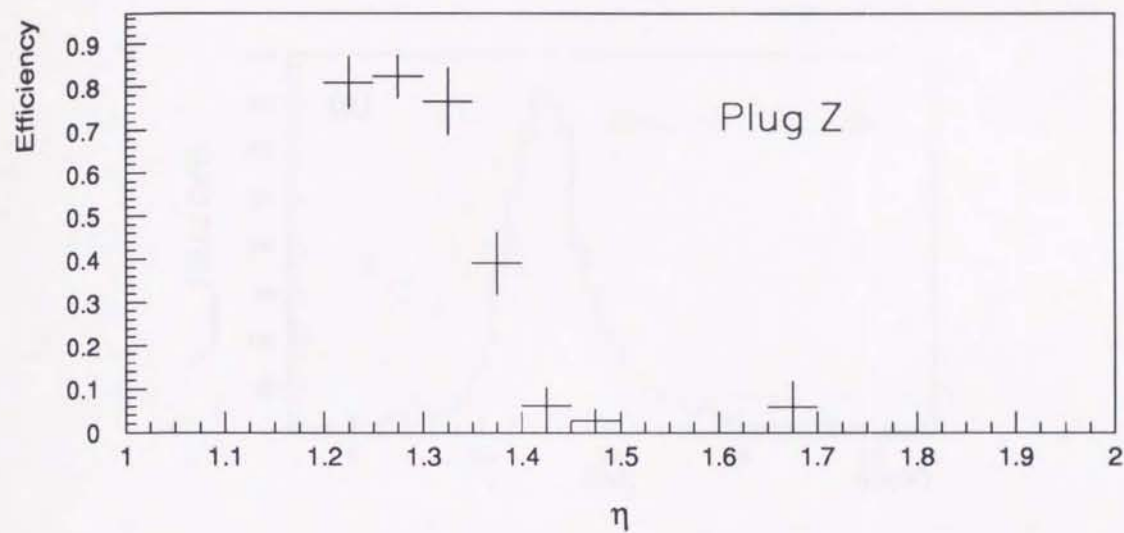


Figure 4.11: Efficiency for track requirement on plug electrons as a function of pseudo-rapidity ( $\eta$ ) measured using plug electrons from (a) Z decays and (b) W decays.

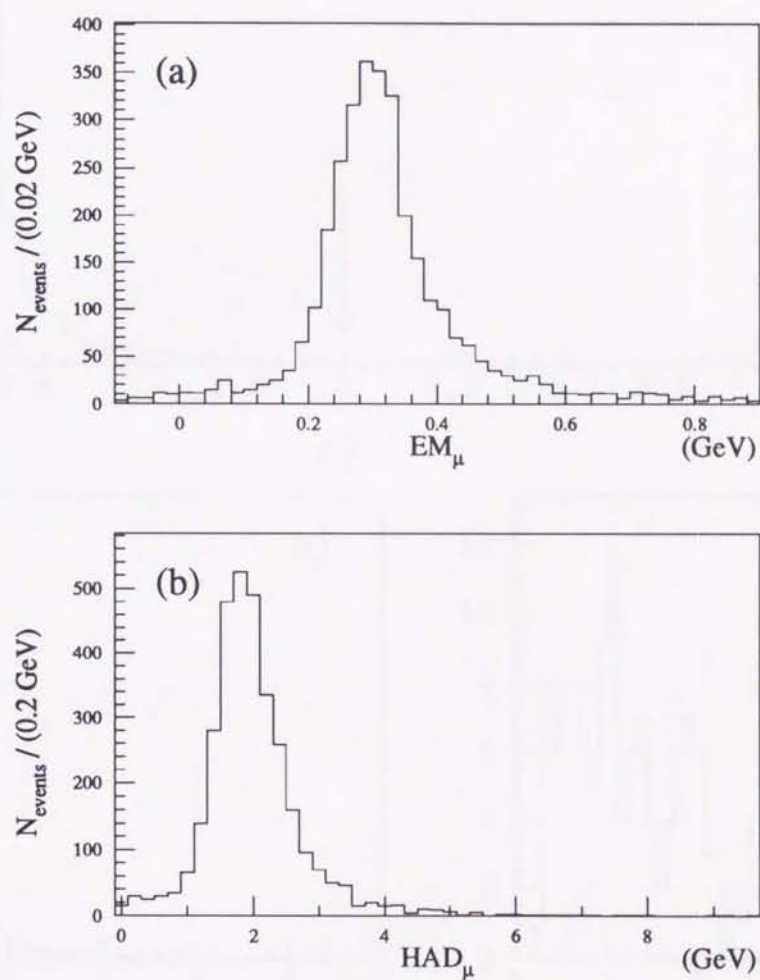


Figure 4.12: Energy deposited in the calorimeter by test-beam muons: a) electromagnetic calorimeter and b) hadronic calorimeter.



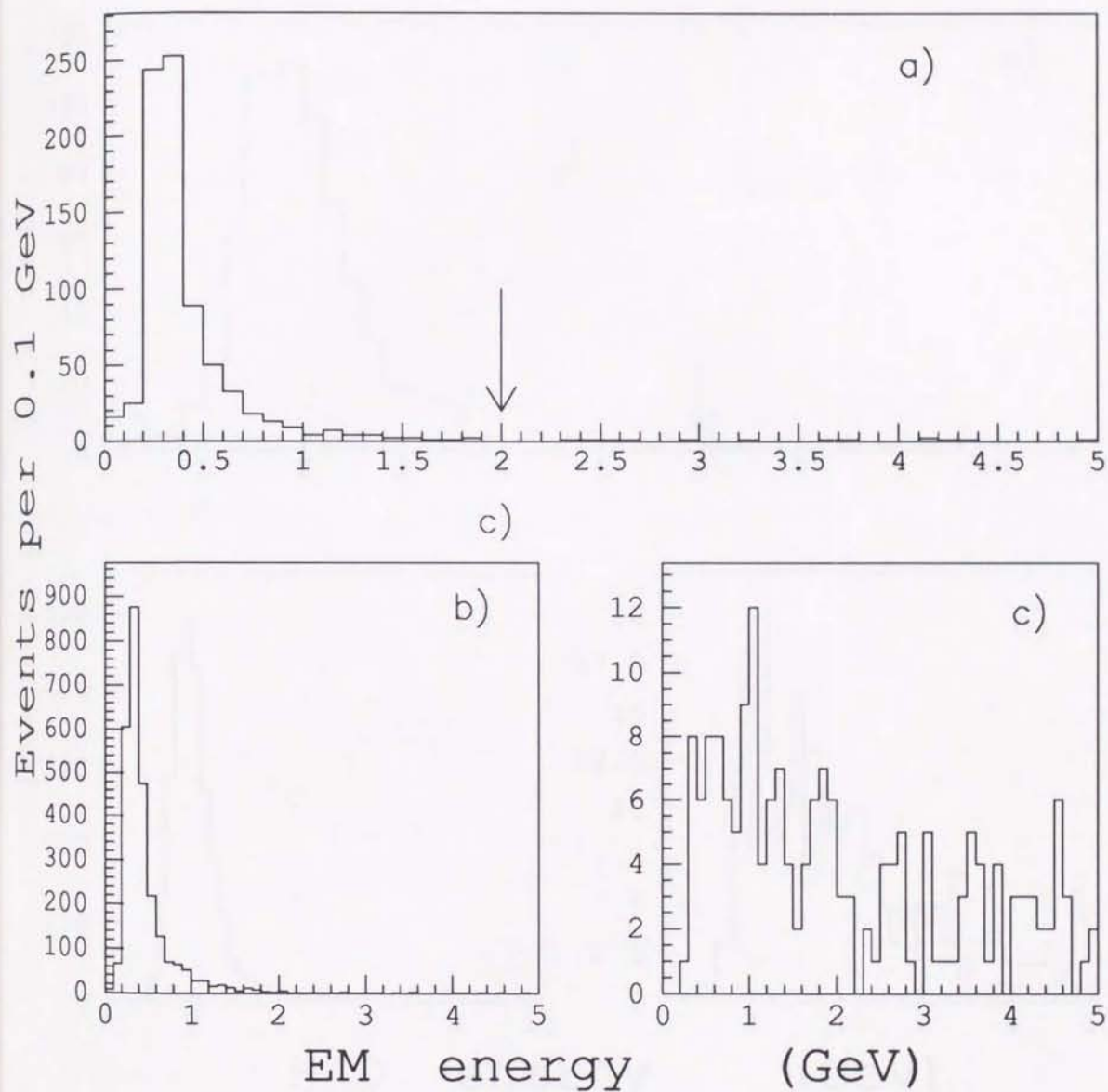


Figure 4.13: Energy deposited in the electromagnetic calorimeter by muons for a)  $Z \rightarrow \mu\mu$  events. Also shown are the values of the cuts for the selection in the dilepton analysis. b) and c) are the same distributions for muons from the decays of W and from the decays of b, respectively in the Monte Carlo  $t\bar{t}$  events.

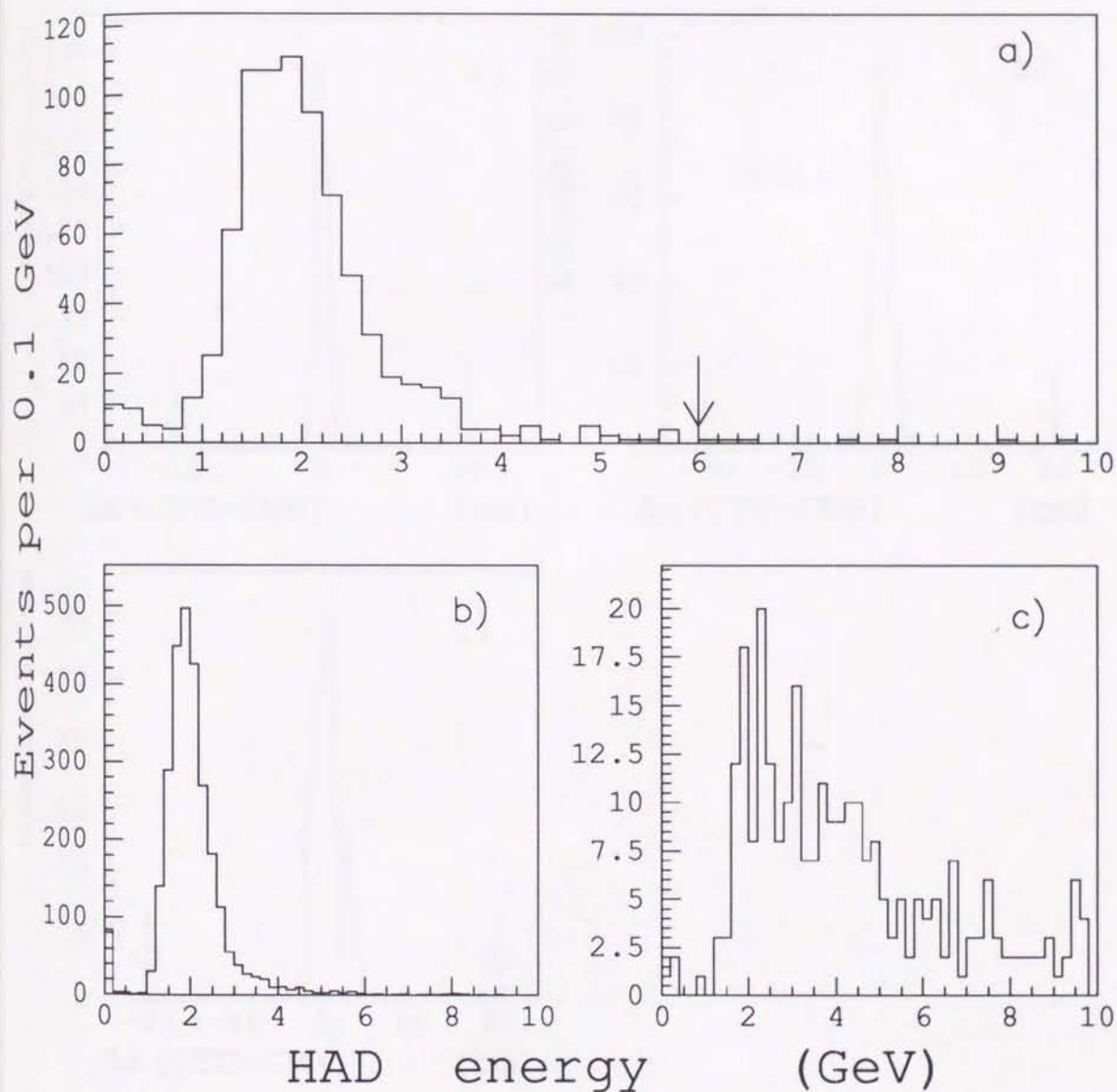


Figure 4.14: Energy deposited in the hadronic calorimeter by muons for a)  $Z \rightarrow \mu\mu$  events. Also shown are the values of the cuts for the selection in the dilepton analysis. b) and c) are the same distributions for muons from the decays of W and from the decays of b, respectively in the Monte Carlo  $t\bar{t}$  events.



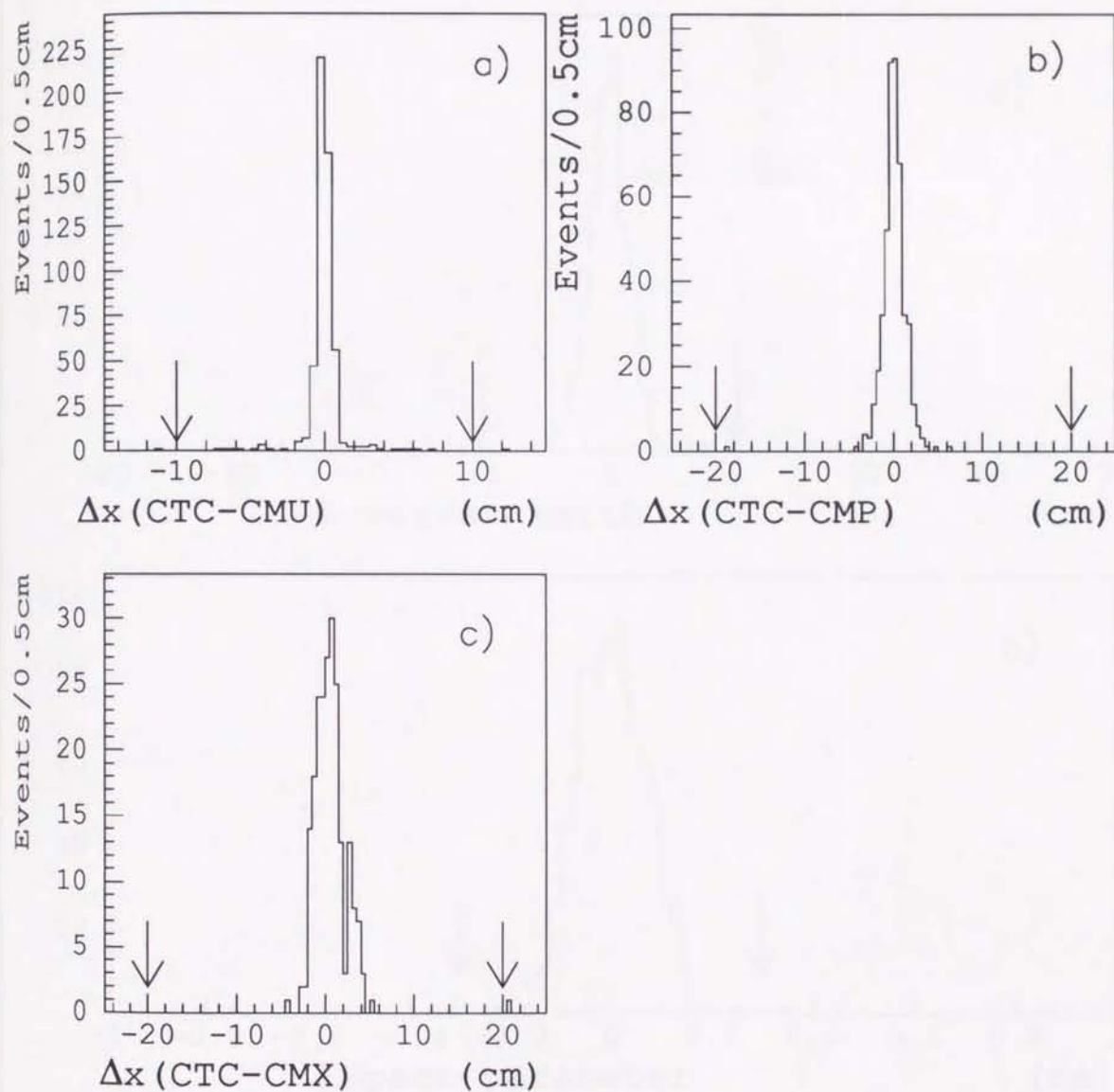


Figure 4.15: Match ( $\Delta x$ ) between the CTC track extrapolated to the lowest wire plane of the muon chambers and the muon chamber track for a sample of muons from Z decays of  $P_T > 20$  GeV/c.

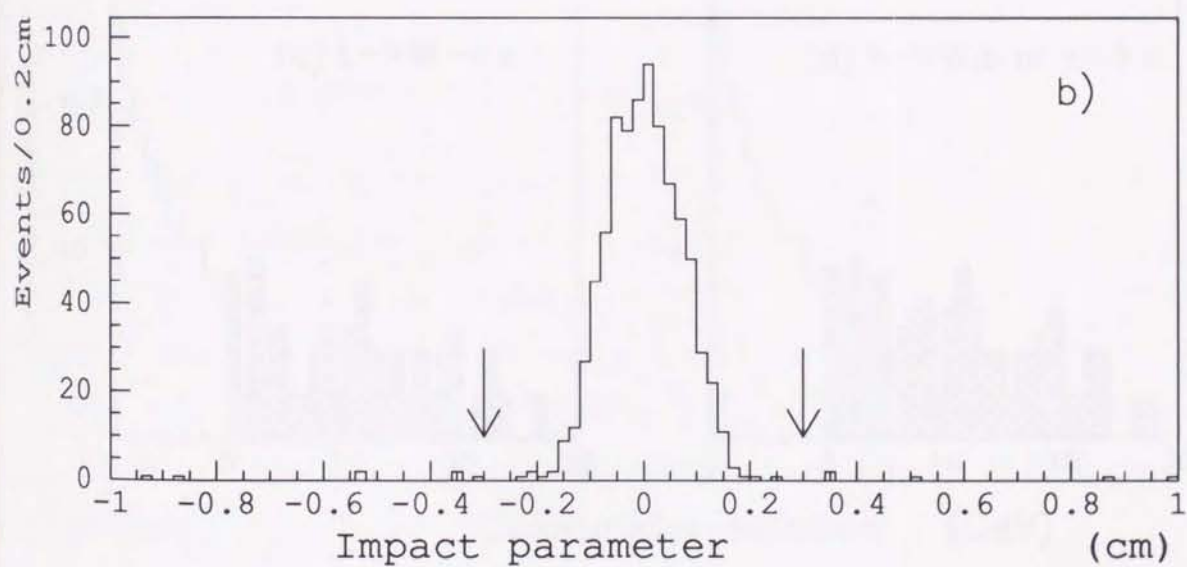
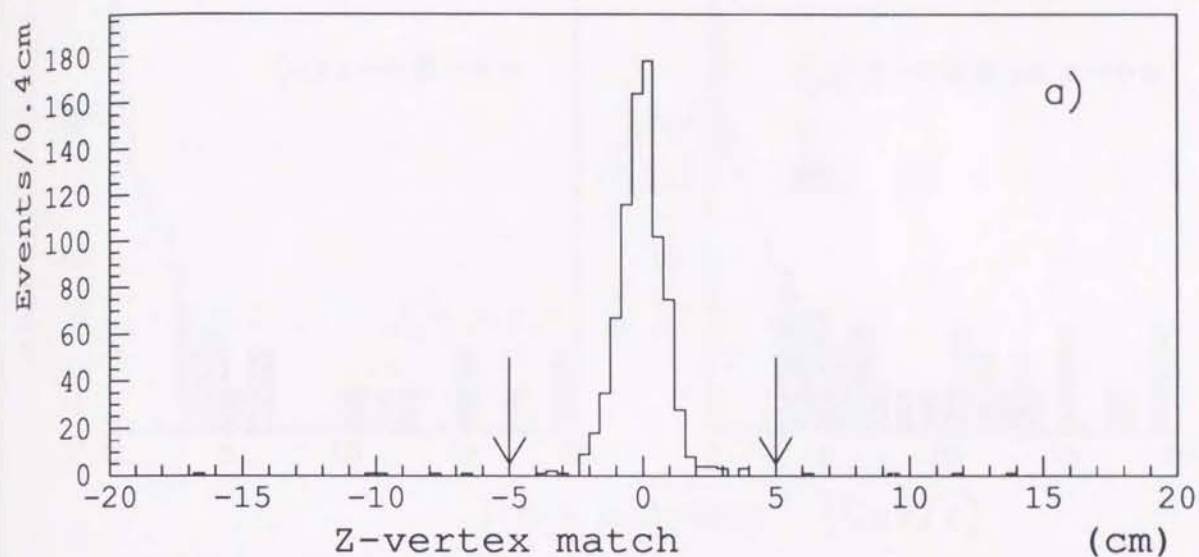


Figure 4.16: Variables for track quality cuts: a) the track-to-vertex distance along the beamline ( $Z_{\text{track}} - Z_{\text{vertex}}$ ) for muon tracks from the decays of  $Z$ . b) the impact parameter for muon tracks from the decays of  $Z$  of  $P_T > 20$  GeV/c.



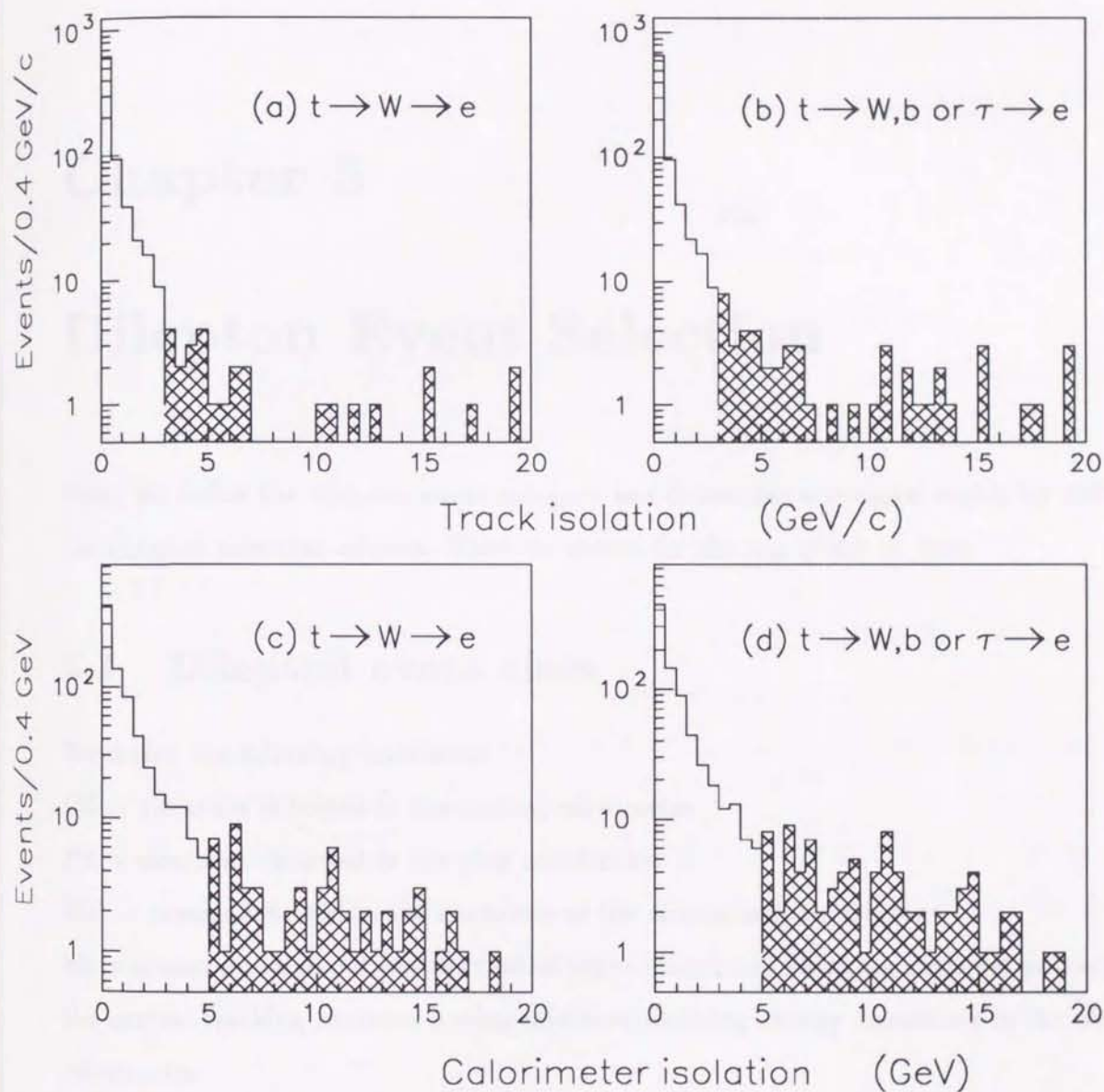


Figure 4.17: Isolations for electrons: (a)(b) track isolations and (c)(d) calorimeter isolation. Lepton identification cuts are already applied.

## Chapter 5

### Dilepton Event Selection

First, we define the dilepton event category and determine our signal region by defining the dilepton selection criteria. Then we search for the top quark in data.

#### 5.1 Dilepton event class

We define the following notations:

CE = electrons detected in the central calorimeter

PE = electrons detected in the plug calorimeter

MU = muons detected in the chambers of the central muon detector

MI = muons directed outside the central muon chambers, which are detected as tracks in the central tracking chamber having minimum-ionizing energy deposition in the central calorimeter

Out of 10 possible classes of dilepton events, we consider 8 classes:

- CE-CE    Tight central electron - Loose central electron
- CE-PE    Tight central electron - Plug electron
- MU-MU    Tight central muon - Loose central muon
- MU-MI    Tight central muon - Minimum ionizing track (CMIO)



- CE-MU    Tight central electron - Loose central muon
- MU-CE    Tight central muon - Loose central electron
- CE-MI    Tight central electron - Minimum ionizing track (CMIO)
- PE-MU    Plug electron - Loose central muon
- PE-MI    Plug electron - Minimum ionizing track (CMIO)

We require that there be at least one lepton in the central region, as a dilepton candidate. Dilepton events consisting of two CMIO's (MI-MI) are not directly triggered on and hence are not used. PE-PE has not been include in the analysis, because a fraction of having both electrons in the plug region is very small for  $t\bar{t}$  events. ( $<1\%$  for  $M_{top}=140\text{ GeV}/c^2$ .)

A trigger path was not explicitly required when events were selected, however we have checked that volunteers, which do not trigger on with the central or plug electron or central muon paths, are amount to  $\sim 1\%$  of the dilepton events after the  $P_T$  cuts. Futhermore, we observed two candidate events in the signal region and verified that they came in the proper trigger path.

In the following section, we define the signal region. The selection cuts we will use are lepton  $P_T$ , isolation cut, event topological cuts of the mass, missing  $E_T$ , and the two-jet cut. We also require two leptons in the event must be oppositly-charged dilepton.

## 5.2 Lepton $P_T$ cut

We require that the transverse momentum ( $P_T$ ) of both leptons be greater than 20 GeV/c. Large  $P_T$  leptons provide a good signature, because a high  $P_T$  threshold separates the  $t\bar{t}$  signal from  $b\bar{b}$ ,  $Z \rightarrow \tau\tau$ , which concentrate at lower  $P_T$  and also can separate from the fake lepton backgrounds. This can be seen from Figure 5.1. The acceptance due to geometrical and  $P_T$  cuts varies from 34 to 63 % for a top quark mass from 100 to 160 GeV/ $c^2$ .

### 5.3 Lepton track isolation

For top decay ( $t \rightarrow Wb \rightarrow l\nu b$ ), the large top mass results in a large separation between the lepton and the bottom quark, yielding an isolated lepton. On the other hand, in bottom decay ( $b \rightarrow l\nu c$ ), the lepton is much closer to the charm quark and thus less isolated. The  $b\bar{b}$  and fake lepton backgrounds are rejected by an isolation requirement.

As we saw in section 4.3, the track isolation variable has a better background rejection and preserves much more  $t\bar{t}$  events than using the calorimeter isolation variable.

We define the lepton track isolation to be the sum of all the CTC track transverse momenta within a cone of radius  $\Delta R = (\Delta\eta^2 + \Delta\phi^2)^{1/2} = 0.25$  around the lepton track, excluding the lepton track itself. Here,  $\eta$  is the pseudo-rapidity and  $\phi$  is the azimuthal angle measured in radians.

To keep more  $t\bar{t}$  events, we always require at least one central lepton ( $e$  or  $\mu$ ) and this lepton must have a stiff isolated track pointing to cluster. We always impose calorimeter isolation cut on PE and CMIO. In other words,

- 1) If there are two central leptons, where central is CE, MU or MI, then we require at least one of them (any one of them) to pass track isolation.
- 2) For PE+(CE, MU, or MI) we require the CE, MU, or MI to pass track isolation.

The efficiency of this requirement is about 95 %, independently of top mass.

### 5.4 Oppositely charged leptons

The same-sign charged lepton pairs from  $t\bar{t}$  must include one lepton from the decay of  $b$ 's. Since these leptons tend to be non-isolated (accompanied by nearby particles from the  $b$  hadronization and decay), they are less likely to pass lepton identification cuts. The two leptons in the events are required to have opposite charges. This cut reduces backgrounds from lepton misidentification by a factor of two and  $b\bar{b}$  by 30 %, while this cut loses 3 to 6 % of top signals.



$M_{\text{top}}$ (GeV/ $c^2$ )	120	160
1) (W <sup>+</sup> W <sup>-</sup> )	81.9 ± 1.4	75.9 ± 1.5
2a) (Wb) (b $\bar{b}$ ) ( $\tau^+\bar{b}$ ) (Opposite sign)	4.2 ± 0.8	6.5 ± 0.9
2b) (Wb) (b $\bar{b}$ ) ( $\tau^- b$ ) (Same sign)	3.4 ± 0.7	5.7 ± 0.8
3) ( $\tau^+\tau^-$ ) (W <sup>+</sup> $\tau^-$ ) (W <sup>-</sup> $\tau^+$ )	10.4 ± 1.1	11.7 ± 1.1

Table 5.1: The fractions of  $t\bar{t} \rightarrow ll + X$  having 1) both leptons coming directly from the top quark decay, 2) at least one lepton coming from the decay of a bottom or charm quark, and 3) one or both leptons coming from a  $\tau$  decays. In category 2), fractions of both opposite and same sign events are shown. Lepton identification cuts are imposed. All numbers are percentages.

## 5.5 $Z^0$ removal

Events containing a  $Z^0$  decaying into an  $e^+e^-$  ( $\mu^+\mu^-$ ) pair give rise to high  $P_T$  electrons (muons), thereby contributing to the background to the top signal. We explicitly removed events that contain a lepton pair with a mass between 75 and 105 GeV/ $c^2$ . The efficiency for top events is 80% for  $M_{\text{top}}=140$  GeV/ $c^2$ .

## 5.6 Missing transverse energy

The remaining backgrounds are  $b\bar{b}$ ,  $Z \rightarrow \tau\tau$  and lepton misidentification for  $e\mu$  channel, and  $ee$  and  $\mu\mu$  events are expected to be dominated by the Drell-Yan events. None of these events are expected to have significant missing  $E_T$ , while  $t\bar{t}$  events contain at least two energetic neutrinos, which results in large missing transverse energy. Figure 5.4 shows the missing  $E_T$  distribution for  $t\bar{t}$  events together with background processes of  $b\bar{b}$ ,  $Z \rightarrow \tau\tau$ , and WW. We require that candidate events must have a missing transverse energy greater 25 GeV.

Note that we compute the missing  $E_T$  after correcting the jet energy scale, as discussed in section 4.5. The motivation is that the corrected missing  $E_T$  reject Drell-Yan events better than using uncorrected missing  $E_T$  as shown in Figure 5.5(a). For  $t\bar{t}$  events,

no change was observed as shown in Figure 5.5(b).

In addition to the cut on the magnitude of the missing transverse energy, the Drell-Yan and  $Z \rightarrow \tau\tau$  backgrounds are further reduced by cuts on the direction of the missing transverse energy.

In principle no neutrinos are involved in the Drell-Yan events so that the missing  $E_T$  in the event is expected to be small. The significant missing  $E_T$  arises from jets when a large fluctuation in the calorimeter measurement occurs. In this case, the direction of missing  $E_T$  tends to lie along that of the jet. Figure 5.7 illustrates one of examples for these events. The missing  $E_T$  of this event is 50 GeV, but it can be seen that the missing  $E_T$  is observed along a jet with a large  $E_T$  of 83 GeV. The missing  $E_T$  is considered to be arising from mismeasurement of the jet. Hence, no energetic jets must be detected in the direction of the missing transverse energy for candidate events. We show a plot of the azimuthal difference between a missing  $E_T$  and a closest jet) versus a missing  $E_T$  in Figure 5.8. We require that the missing  $E_T$  direction be more than  $20^\circ$  away from the closest jet. The cut value is chosen to achieve good rejection in a Drell-Yan control sample of  $Z + \text{jets}$  events<sup>1</sup>.

A similar cut is imposed to minimize the background from  $Z \rightarrow \tau\tau$ . For  $Z \rightarrow \tau\tau$  events the missing transverse energy originates from neutrinos, which are often aligned with the charged leptons. Because of the large mass of the top quark, neutrinos from top decay are produced isotropic and are not aligned with the charged leptons. The backgrounds from  $Z \rightarrow \tau\tau$  are minimized by requiring that no energetic lepton be detected in the direction of the missing transverse energy. Figure 5.8 shows the azimuthal difference between a missing  $E_T$  and a closest lepton versus a missing  $E_T$ . We demand that the missing  $E_T$  direction be more than  $20^\circ$  away from the closest lepton.

In summary, we require that  $\Delta\phi(\cancel{E}_T, \text{lepton}) > 20^\circ$  and  $\Delta\phi(\cancel{E}_T, \text{jet}) > 20^\circ$ , if  $\cancel{E}_T < 50$  GeV. Note that the cut is imposed in case that the missing  $E_T$  be less than 50

<sup>1</sup>We estimate the background from Drell-Yan continuum using  $Z$  events in CDF data as we will discuss in Section 7.1



GeV, otherwise the cut is not imposed. This condition is added in order to preserve more  $t\bar{t}$  events, since Monte Carlo study shows that these background events are less likely to have a large missing  $E_T$  greater than 50 GeV, as illustrated in Figure 5.6. We also show in Figure 5.10 the azimuthal separation between the missing  $E_T$  and a closest jet or lepton versus the missing  $E_T$ .

The efficiency of this requirement for top events is 76% for  $M_{top}=140$  GeV/ $c^2$

## 5.7 Two jet cut for higher mass top search

In searching for the higher mass top quark, it is difficult to achieve a good signal-to-background separation, because  $t\bar{t}$  production cross section becomes significantly smaller, and also because the background from WW production becomes comparable with the  $t\bar{t}$  signal for a top mass above 150 GeV/ $c^2$ . As a result, we must rely on additional details of the top signature to improve the signal-to-background ratio. One of methods is to require the presence of jets in the events. This can be seen in Figure 5.11 which shows the distribution of the jet multiplicity for WW and top Monte Carlo.

Figure 5.12 shows the leading and second leading jet  $E_T$  for the top masses of 100, 140 and 160 GeV/ $c^2$ . For the top mass not much larger than the W mass, the b quark from the top decay has a rather soft  $P_T$  spectrum and the efficiency for reconstructing b jets in the detector is low. For higher mass top, above 120 GeV/ $c^2$ , however, the two b quarks in the decay of the  $t\bar{t}$  pair can have significant energy and are detected with good efficiency as hadronic jets in the calorimeter. An additional two-jet requirement preserves most of the  $t\bar{t}$  signal for high mass top and reduces backgrounds, which contain occasionally observed hadronic jets only through higher order processes. The  $Z \rightarrow \tau\tau$ , WW and WZ backgrounds can be reduced by a factor of about 6 by requiring two jets. The efficiency for the two-jet requirement depends on the observed jet  $E_T$  and on the top mass. We have investigated the fraction of events which pass the two-jet cut for  $t\bar{t}$  and WW events by varying the jet  $E_T$  threshold. We used three set of cuts:  $E_T^{jet1}, E_T^{jet2}$

$>(10,10)$ ,  $(15,15)$  and  $(20,10)$  GeV. The fractions are tabulated in Table 5.2. Figure 5.14 illustrates the two-jet cut efficiencies for the top quark as a function of its mass, together with those for WW events.

For  $t\bar{t}$  events with mass above  $120 \text{ GeV}/c^2$ , the efficiency is more than 63 %, while 13 % of WW events survives the cut by requiring two or more jets with observed  $E_T > 10 \text{ GeV}$ .

In the case, we require two or more jets with observed transverse energy greater than 10 GeV. A cluster cone radius of 0.4 is used. Furthermore, because the pseudorapidity distribution of jets from  $t\bar{t}$  production is narrower than that from other background events, we require the jets to have  $|\eta| < 2.4$ . This cut was made on the pseudorapidity of the jet as determined from the center of the detector to ensure that the jets are contained in the central or plug calorimeter, rather than the event origin.

$M_{\text{top}} (\text{GeV}/c^2)$	100	120	140	160	WW
$E_T^{\text{jet}} > (10,10) \text{ GeV}$	$33.0 \pm 1.4\%$	$63.0 \pm 1.3\%$	$75.1 \pm 1.0\%$	$83.9 \pm 0.9\%$	$13.7 \pm 1.1$
$E_T^{\text{jet}} > (15,15) \text{ GeV}$	$22.2 \pm 1.3\%$	$45.9 \pm 1.4\%$	$62.3 \pm 1.2\%$	$74.5 \pm 1.0\%$	$5.5 \pm 0.7$
$E_T^{\text{jet}} > (20,10) \text{ GeV}$	$26.2 \pm 1.4\%$	$54.9 \pm 1.3\%$	$72.0 \pm 1.1\%$	$82.4 \pm 0.9\%$	$10.9 \pm 1.0$

Table 5.2: The efficiency of the two-jet cut of different jet  $E_T$  thresholds for top and WW Monte Carlo events.

Table 5.3: Summary of dilepton selection criteria

At least one central lepton isolated in the tracking chamber
Reject same sign dilepton events
$\cancel{E}_T > 25 \text{ GeV}$
Reject $75 < M_{ll} < 105 \text{ GeV}/c^2$ for $ee$ and $\mu\mu$
$\Delta\phi(\cancel{E}_T, \text{jet}) > 20^\circ$ and $\Delta\phi(\cancel{E}_T, \text{lepton}) > 20^\circ$ if $\cancel{E}_T < 50 \text{ GeV}$
Two or more jets with observed $E_T > 10 \text{ GeV}$



## 5.8 Data Analysis

In our data sample, 5  $e\mu$ , 685  $ee$  and 571  $\mu\mu$  events are left after the Lepton  $P_T$ , lepton identification, isolation, and opposite charge cuts.

### 5.8.1 $e\mu$

The lepton  $P_T$  transverse momenta for the five electron-muon events are shown in Fig. 5.15, together with the prediction from  $t\bar{t}$  Monte Carlo. The azimuthal angle difference between the missing transverse energy and the closest lepton or jet for is plotted in Fig. 5.16 against the missing transverse energy. Two  $e\mu$  events survive the final missing  $E_T$  cut, both its magnitude and direction cuts. The one of candidates has an isolated central electron with  $E_T^e$  of 22.2 GeV and an opposite-sign muon with  $P_T^\mu$  of 47.7 GeV/c with a dilepton azimuthal opening angle of  $18^\circ$ . There are two large calorimeter clusters in the central region with observed transverse-energy depositions of 108 and 44 GeV, one cluster of 18 GeV in the forward region. Other characteristics of the event include the presence of a second muon candidate with transverse momentum of 8.8 GeV/c in the highest  $E_T$  jet. Another event contains an isolated central electron with  $E_T^e$  of 50.6 GeV and an isolated opposite-sign muon in the CMX chamber with  $P_T^\mu$  of 37.3 GeV/c with three calorimeter clusters with observed  $E_T$  of 67, 14 and 11 GeV.

In these events, no energetic lepton or jet is detected in the direction of the missing  $E_T$ . Figure 5.20 - 5.23 show a tracking chamber and calorimeter displays for the candidates. Some properties of two events are summarized in Table 5.5.

### 5.8.2 $ee$ and $\mu\mu$

The dielectron and dimuon invariant masses are shown in Figure 5.17 and 5.18 for 685 dielectron events and 571 dimuon events, respectively. Also shown in the plots are the Monte Carlo predictions from ISAJET program. By removing the majority of  $Z^0$  backgrounds, the data sample is reduced to 58  $ee$  and 62  $\mu\mu$  events. The distribution in

the missing  $E_T$ -  $\Delta\phi(\cancel{E}_T, \text{lepton or jet})$  plane is shown in Figure 5.19 for CDF data. After imposing the missing  $E_T$  requirement, no dielectron or dimuon events were observed.

A summary of the numbers of events surviving different stage of cuts is shown in Table 5.4.

In the following two sections, we will determine the detection efficiency for the selection criteria stated above, and estimate the expected number of backgrounds.

Cut	$ee$	$\mu\mu$	$e\mu$
$P_T$	702	588	8
Opposite-Charge	695	583	6
Isolation	685	571	5
Invariant Mass	58	62	5
$\cancel{E}_T$	0	1	2
$\cancel{E}_T$ direction	0	0	2
Two-jet	0	0	2

Table 5.4: Numbers of data events surviving various consecutive cuts.



	Event I				Event II			
	Charge	$P_T$ (GeV/c)	$\eta$	$\phi$ (deg)	Charge	$P_T$ (GeV/c)	$\eta$	$\phi$ (deg)
electron	—	22.2	0.84	32	+	50.6	0.93	25
muon	+	47.7	0.17	14	—	37.3	—0.74	4
muon	+	8.8	0.18	352				
Jet 1		107.9	0.11	352		67.0	0.64	218
Jet 2		44.3	—0.54	215		13.6	—3.31	344
Jet 3		18.0	—2.94	112		10.7	1.34	344
Missing $E_T$		136.4		179		59.6		149
$\Delta\phi(\cancel{E}_T, \ell)$				147				124
$\Delta\phi(\cancel{E}_T, j)$				36				68

Table 5.5: Characteristics of the top-quark candidate events. Observed calorimeter  $E_T$  is used for jet clusters.

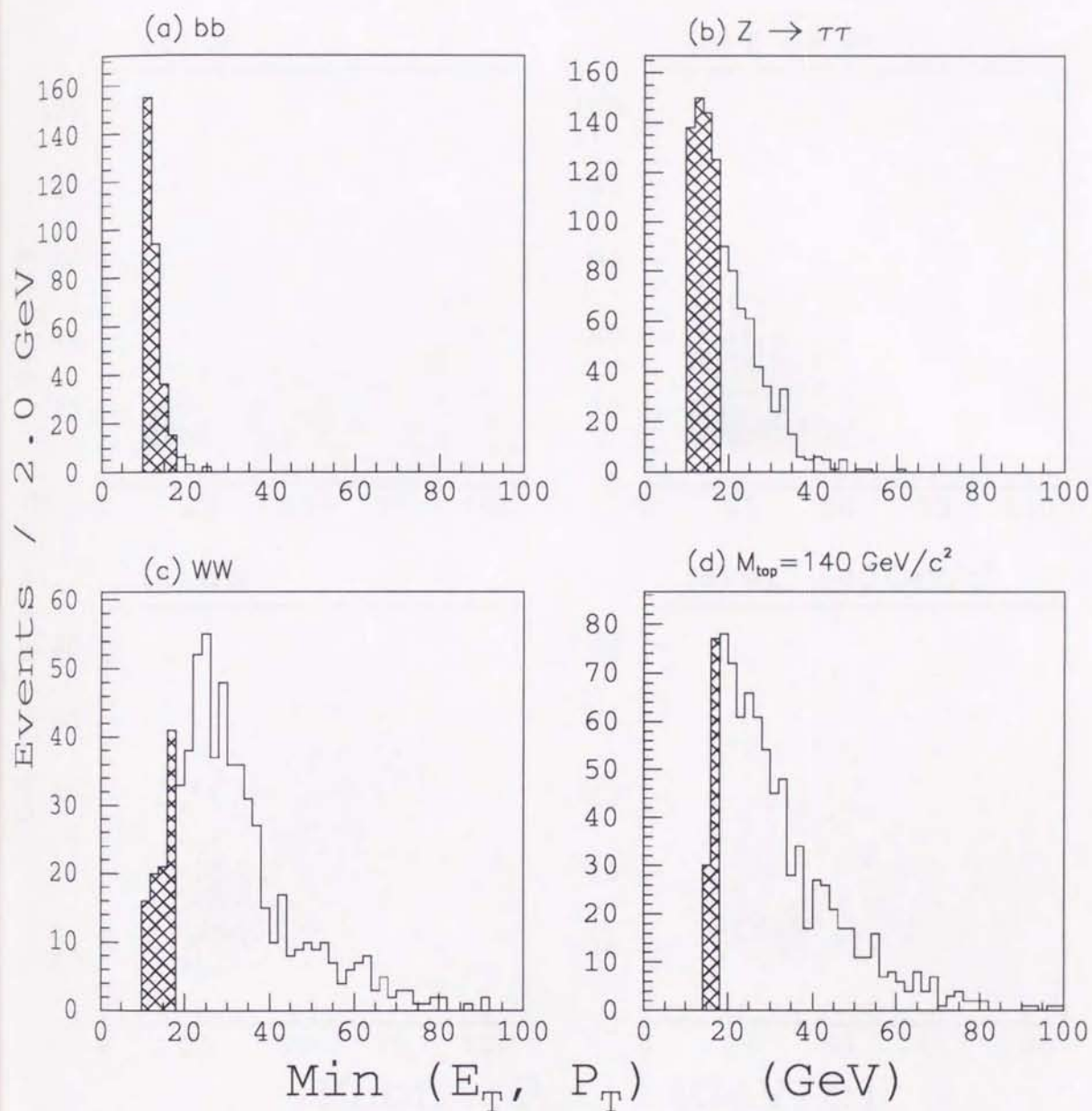


Figure 5.1: Minimum of  $E_T^e$  and  $P_T^\mu$  for (a)  $b\bar{b}$ , (b)  $Z \rightarrow \tau\tau$ , (c)  $WW$ , and (d)  $t\bar{t}$  Monte Carlo data ( $M_{top}=140 \text{ GeV}/c^2$ )  $P_T > 10 \text{ GeV}$  is imposed on the Monte Carlo samples. For the  $t\bar{t}$  events,  $P_T > 15 \text{ GeV}$  is imposed. The hatched area is rejected.



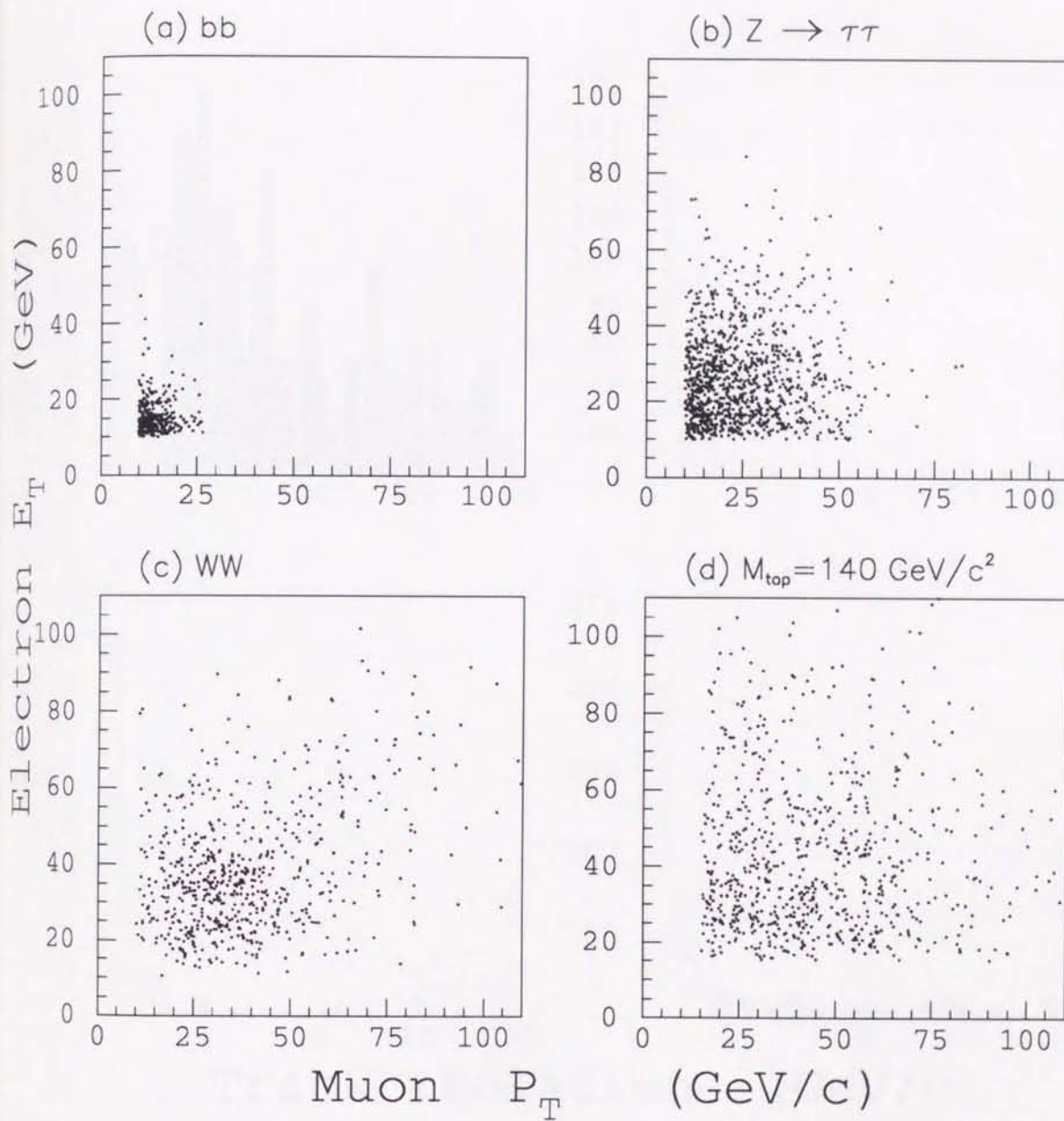


Figure 5.2:  $E_T^e$  versus  $P_T^\mu$  for (a)  $b\bar{b}$ , (b)  $Z \rightarrow \tau\tau$ , (c)  $WW$ , and (d)  $t\bar{t}$  Monte Carlo data ( $M_{\text{top}} = 140 \text{ GeV}/c^2$ ).  $E_T^e(P_T^\mu) > 10 \text{ GeV}/c$  is imposed except for  $t\bar{t}$  events.

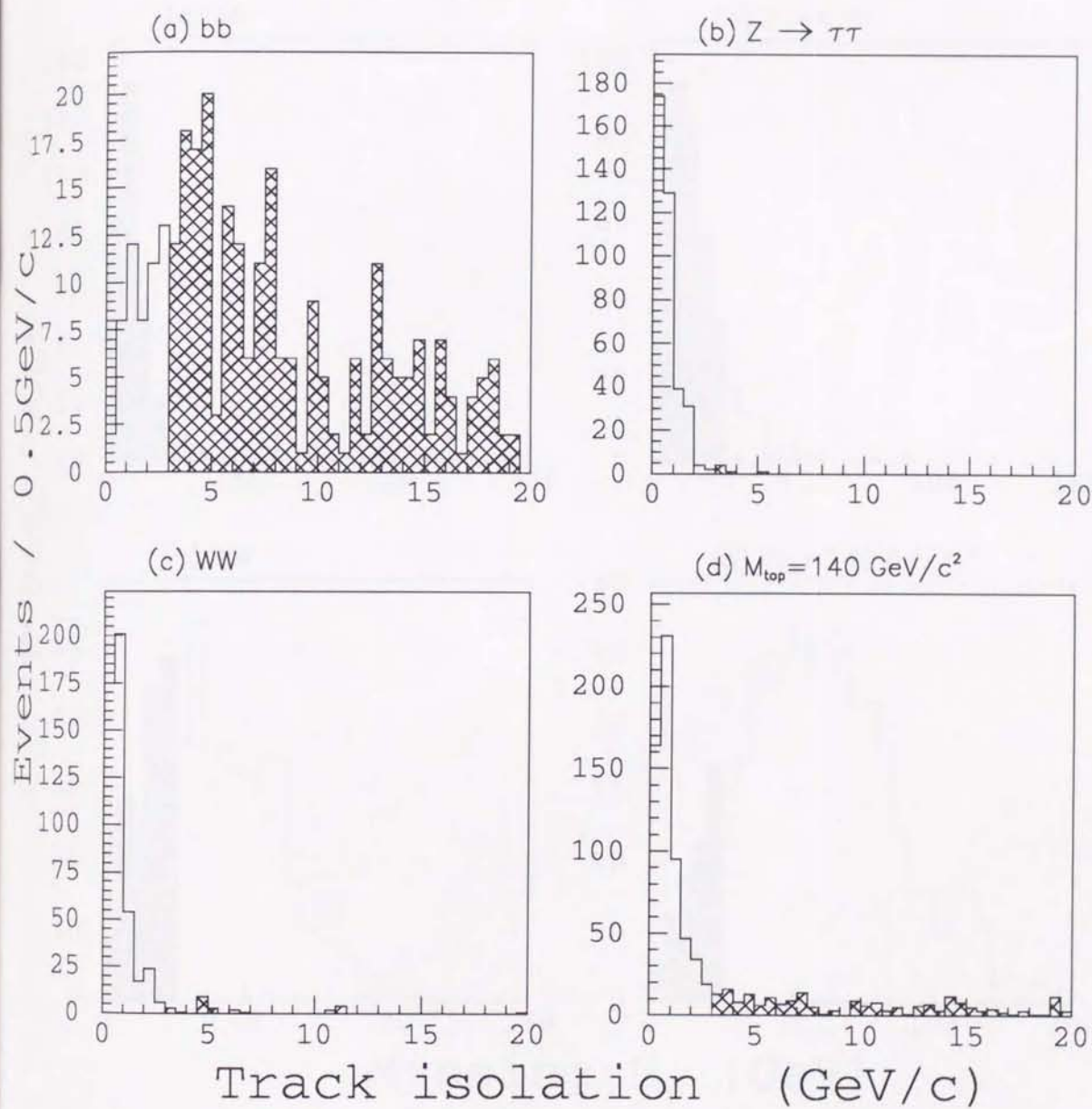


Figure 5.3: Track isolation of  $E_T^e$  and  $P_T^\mu$  for (a)  $b\bar{b}$ , (b)  $Z \rightarrow \tau\tau$ , (c)  $WW$ , and (d)  $t\bar{t}$  Monte Carlo data ( $M_{top}=140 \text{ GeV}/c^2$ ). The hatched area is rejected.



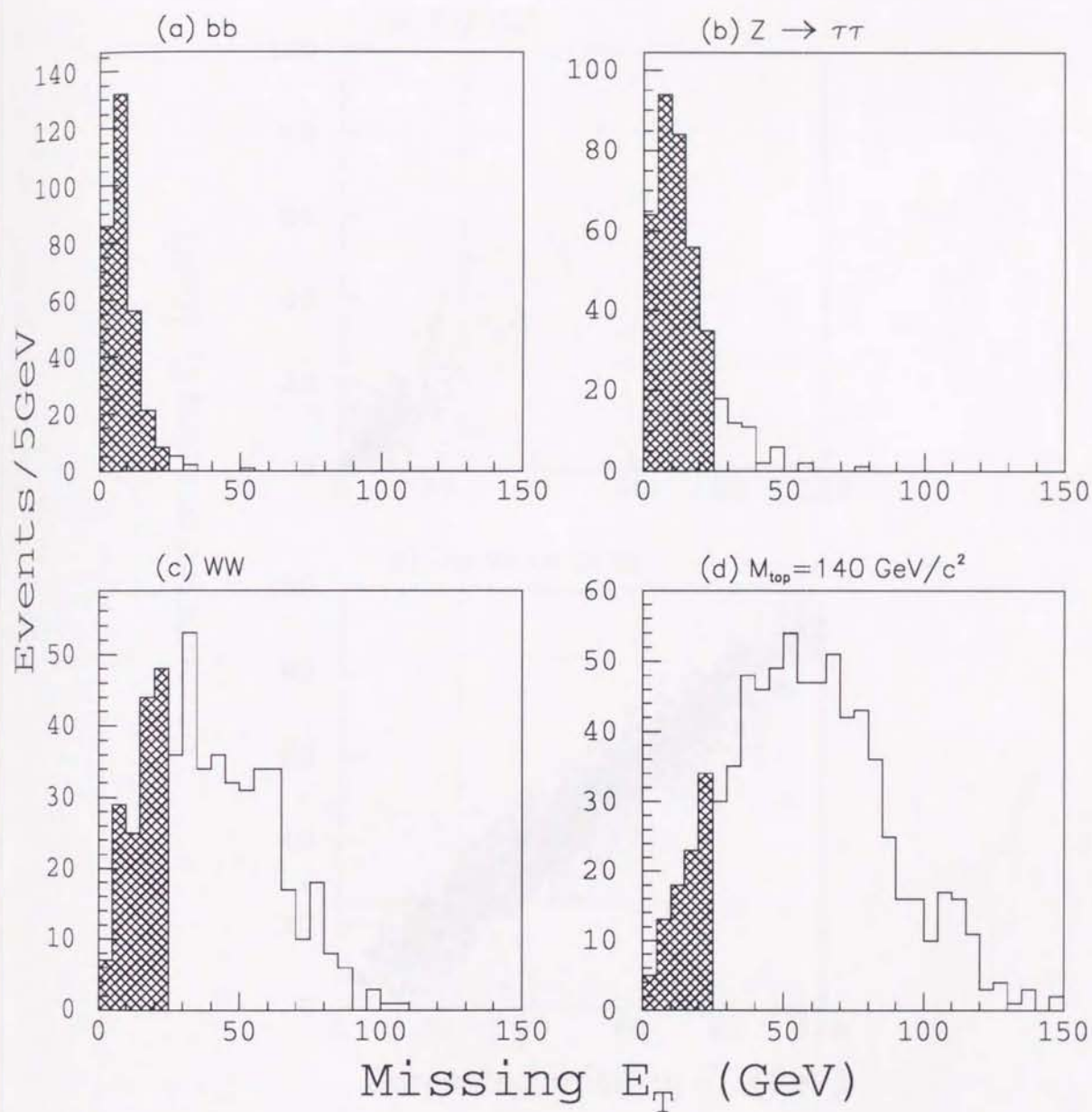


Figure 5.4: Missing transverse energy for (a)  $b\bar{b}$ , (b)  $Z \rightarrow \tau\tau$ , (c)  $W\bar{W}$ , and (d)  $t\bar{t}$  Monte Carlo data ( $M_{top}=140 \text{ GeV}/c^2$ ). The hatched area is rejected. The hatched area is rejected.

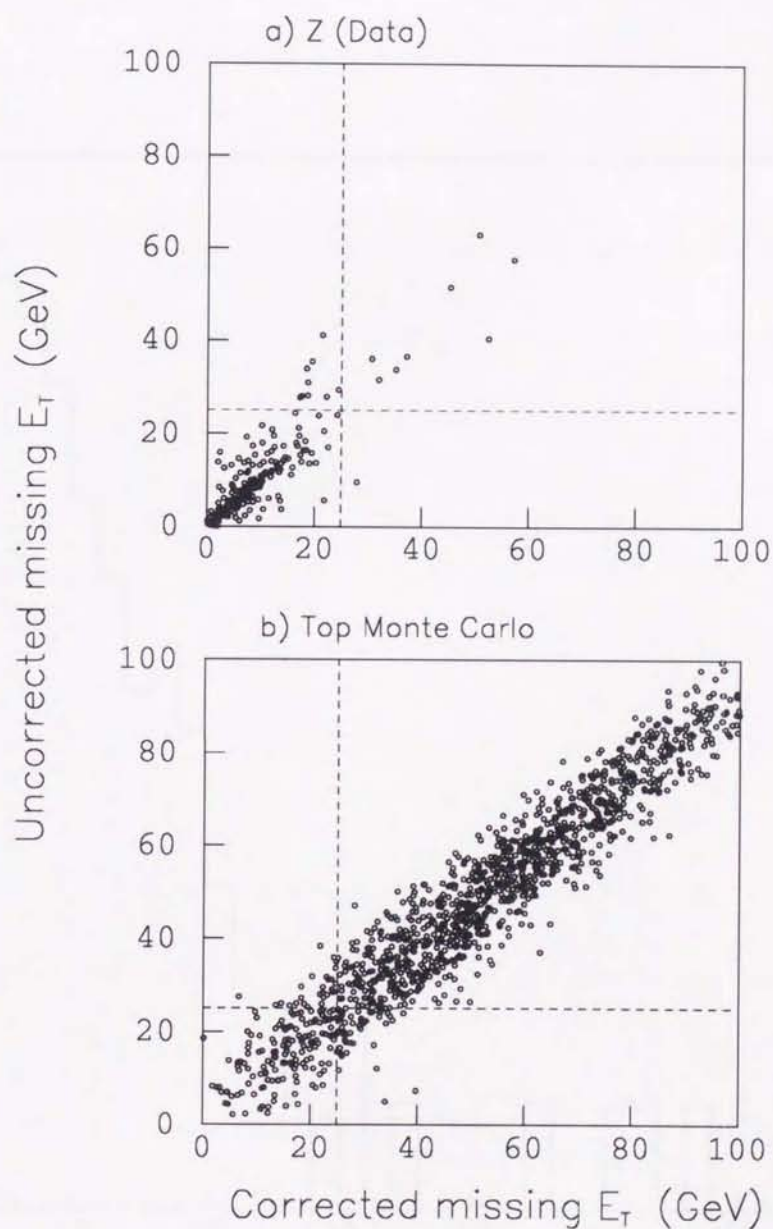


Figure 5.5: Raw missing  $E_T$  versus missing  $E_T$  corrected for jet energy scale a) for events from the Z decays, and b) top Monte Carlo of 140 GeV/c<sup>2</sup>. Note that the corrected quantity has better background rejection near the missing  $E_T$  threshold.



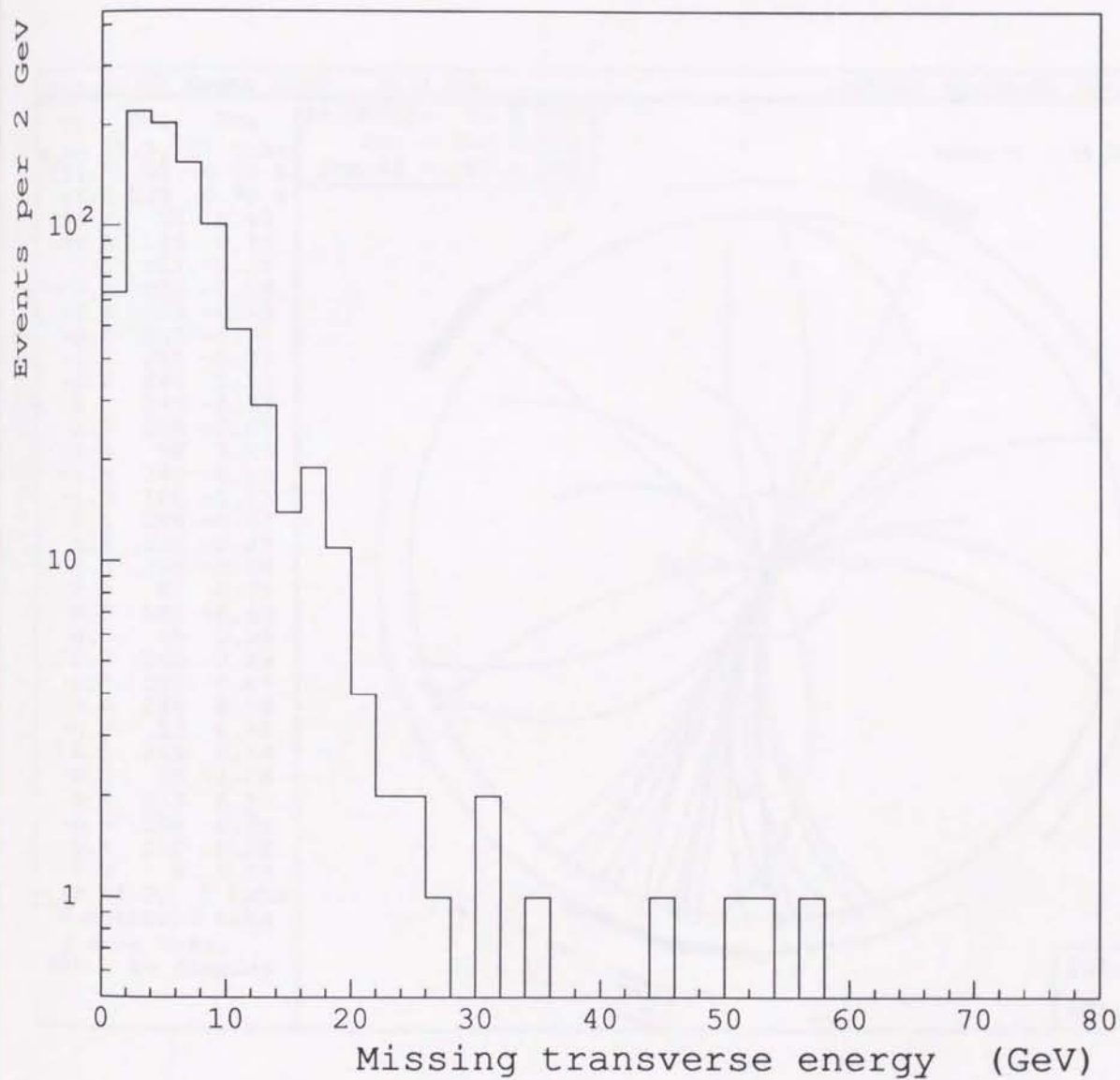


Figure 5.6: Missing  $E_T$  distribution for  $Z \rightarrow ll$  decays from CDF data.

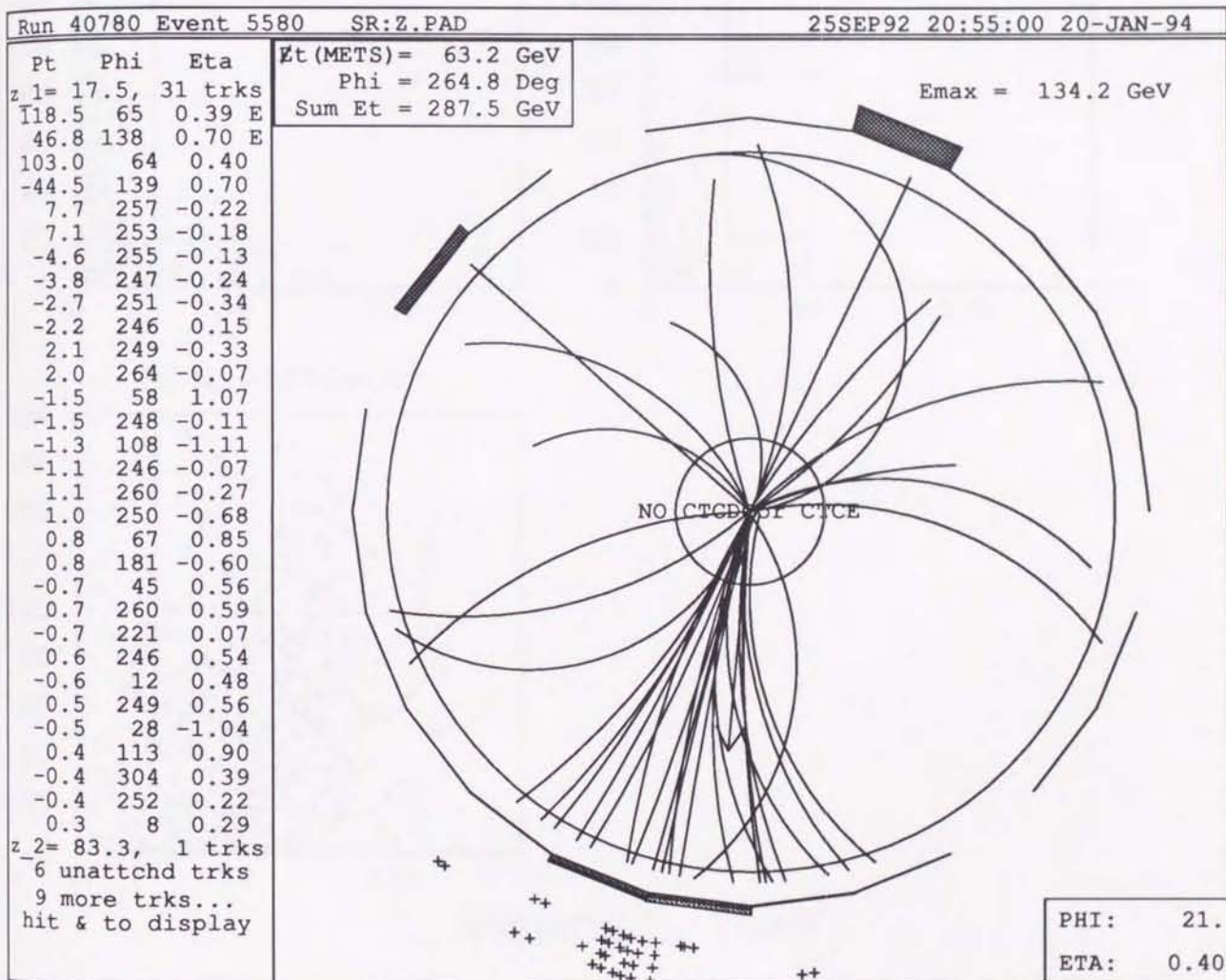


Figure 5.7: One event from  $Z \rightarrow ee$  decays with the large missing  $E_T$ . The large missing  $E_T$  arises from jet mismeasurement.



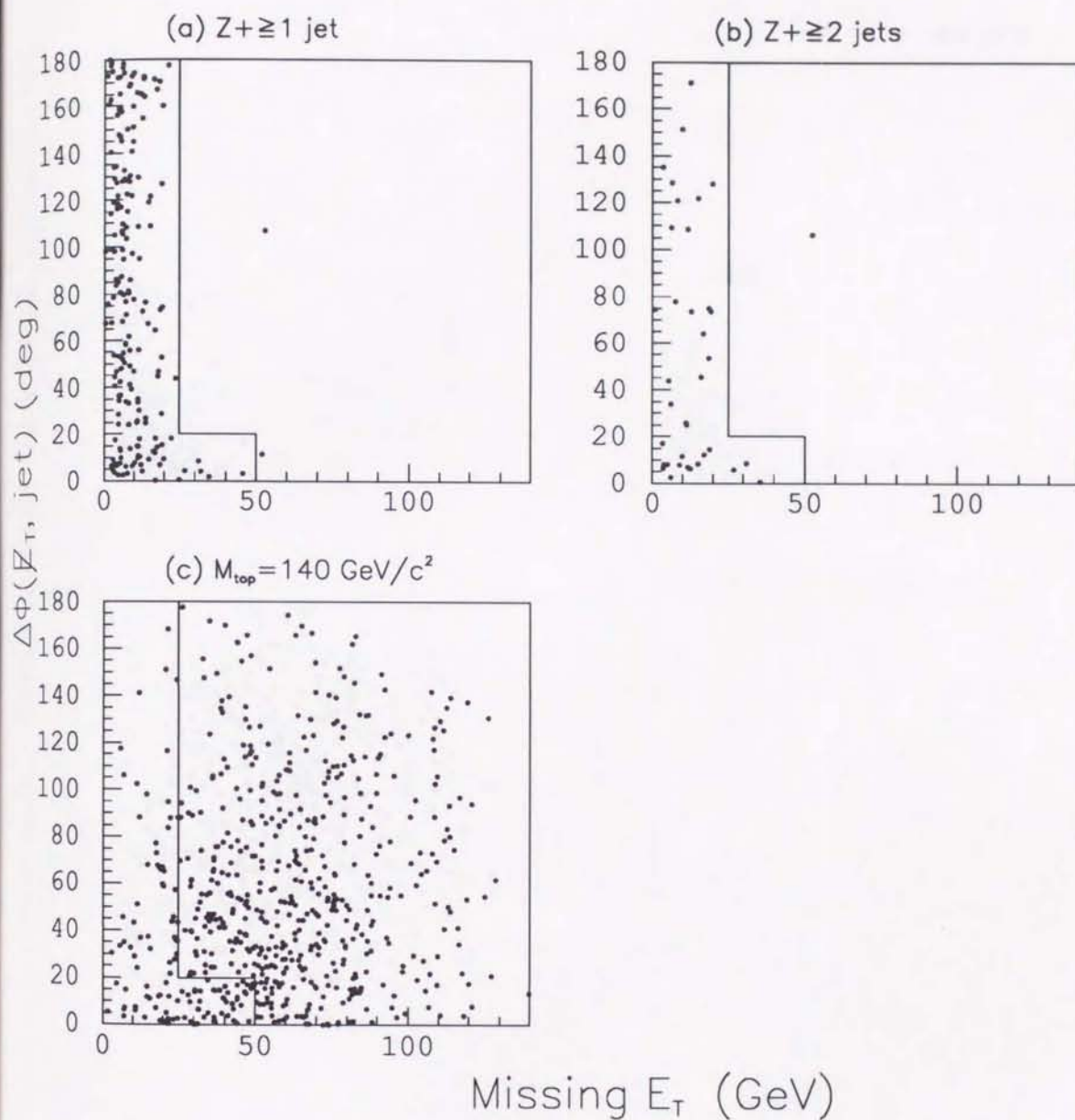


Figure 5.8: Azimuthal angle difference between the missing  $E_T$  and the closest lepton versus the missing  $E_T$  : dielectron and dimuon data from a Drell-Yan control sample of a)  $Z + \geq 1$  jet and b)  $Z + \geq 2$  jets. c) top Monte Carlo of  $140 \text{ GeV}/c^2$ .

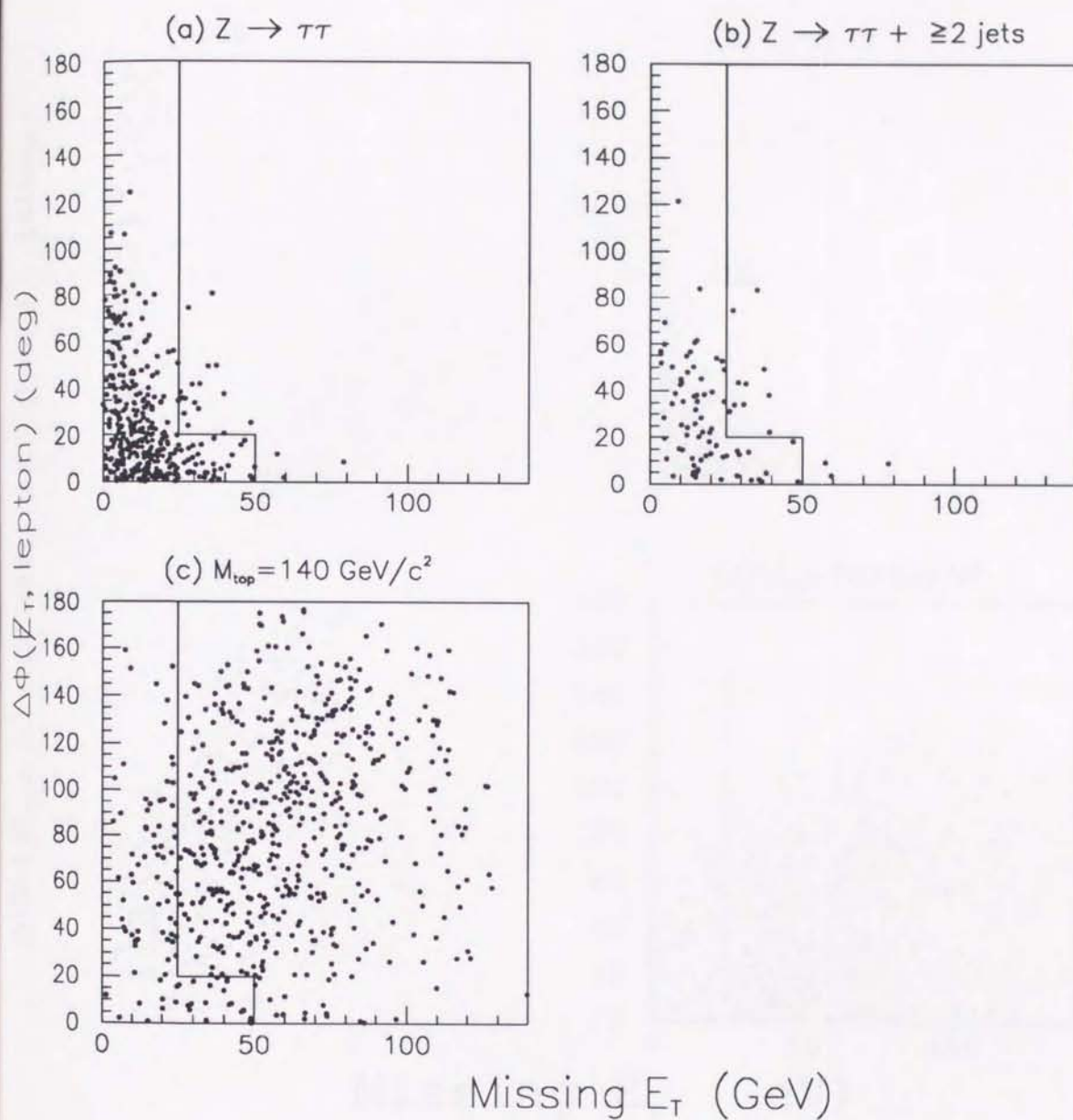


Figure 5.9: Azimuthal angle difference between the missing  $E_T$  and the closest jet versus the missing  $E_T$ . a)  $Z \rightarrow \tau\tau$  simulation, b)  $Z \rightarrow \tau\tau$  simulation with two-jet cut, and c) top Monte Carlo of  $140 \text{ GeV}/c^2$ .



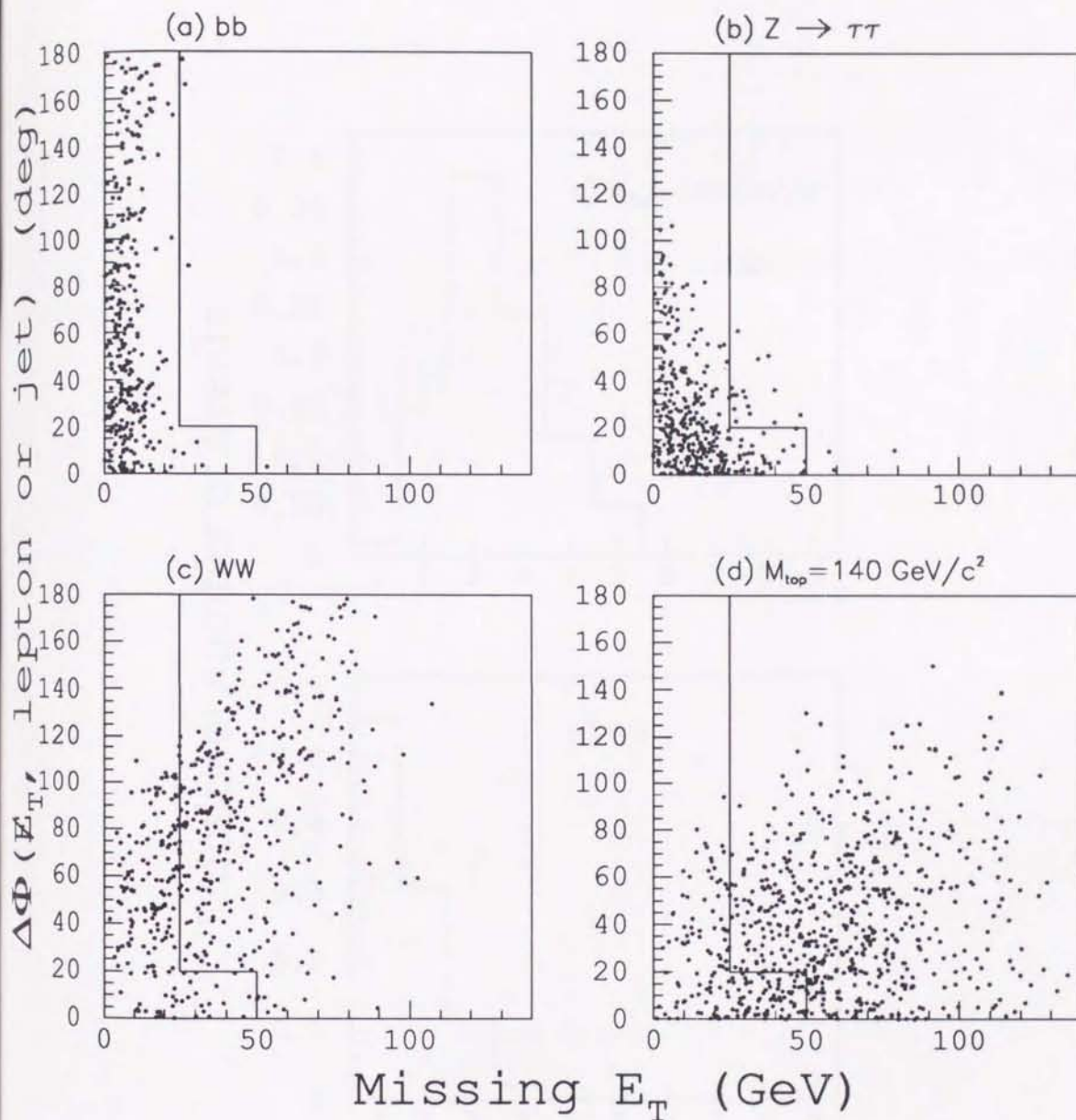


Figure 5.10: Azimuthal difference between the missing transverse energy and a closest lepton or jet for (a)  $b\bar{b}$ , (b)  $Z \rightarrow \tau\tau$ , (c)  $WW$ , and (d)  $t\bar{t}$  Monte Carlo data ( $M_{top}=140 \text{ GeV}/c^2$ )

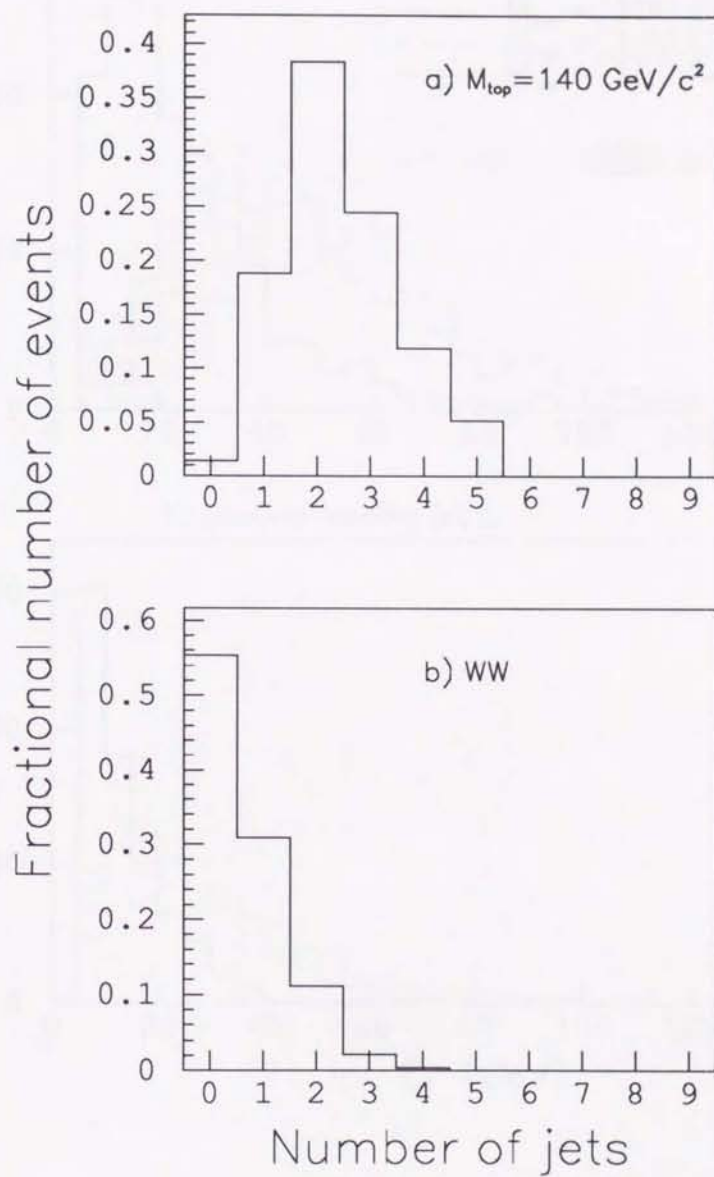


Figure 5.11: The number of jets for a) top Monte Carlo of  $140 \text{ GeV}/c^2$  and b) WW events. The numbers are normalized by the total number of events.



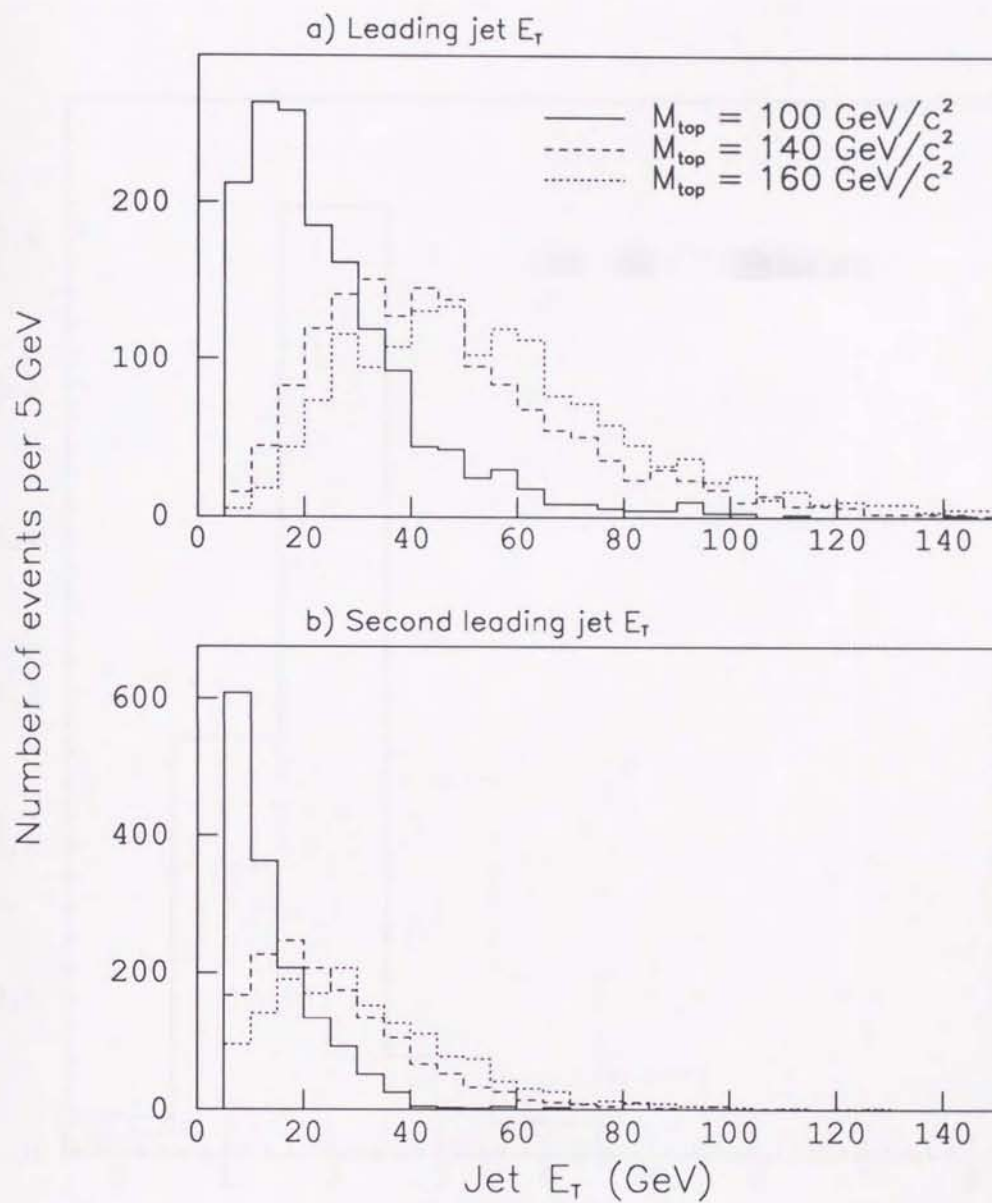


Figure 5.12: Jet  $E_T$  distribution for top Monte Carlo events: a) leading jet  $E_T$  and b) next-to-leading jet  $E_T$ . Distributions are normalized to unity.

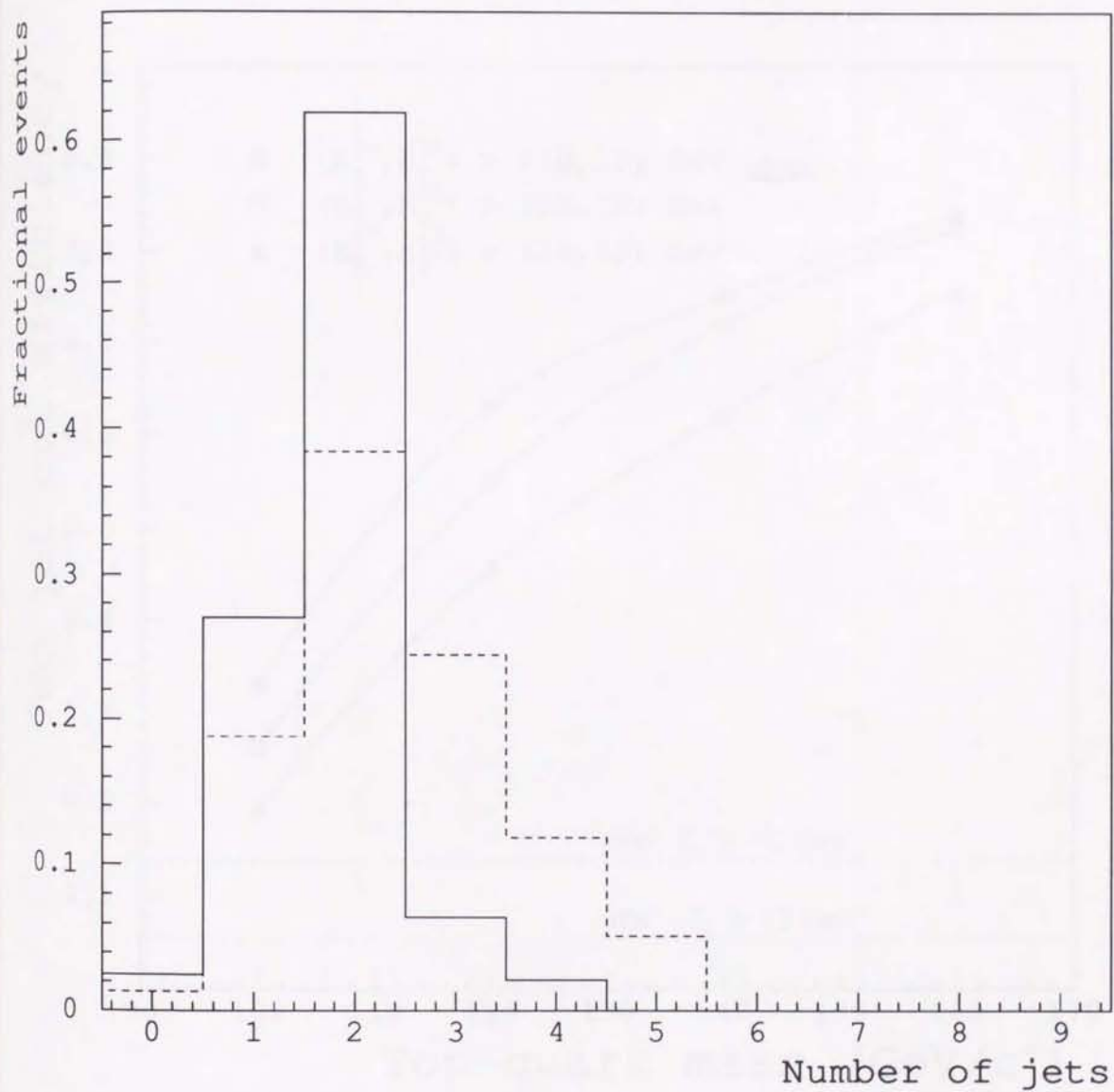


Figure 5.13: The number of jets for top Monte Carlo of 140 GeV/c<sup>2</sup> with gluon radiation (dashed line) and without gluon radiation (solid line). The numbers are normalized by the total number of events.



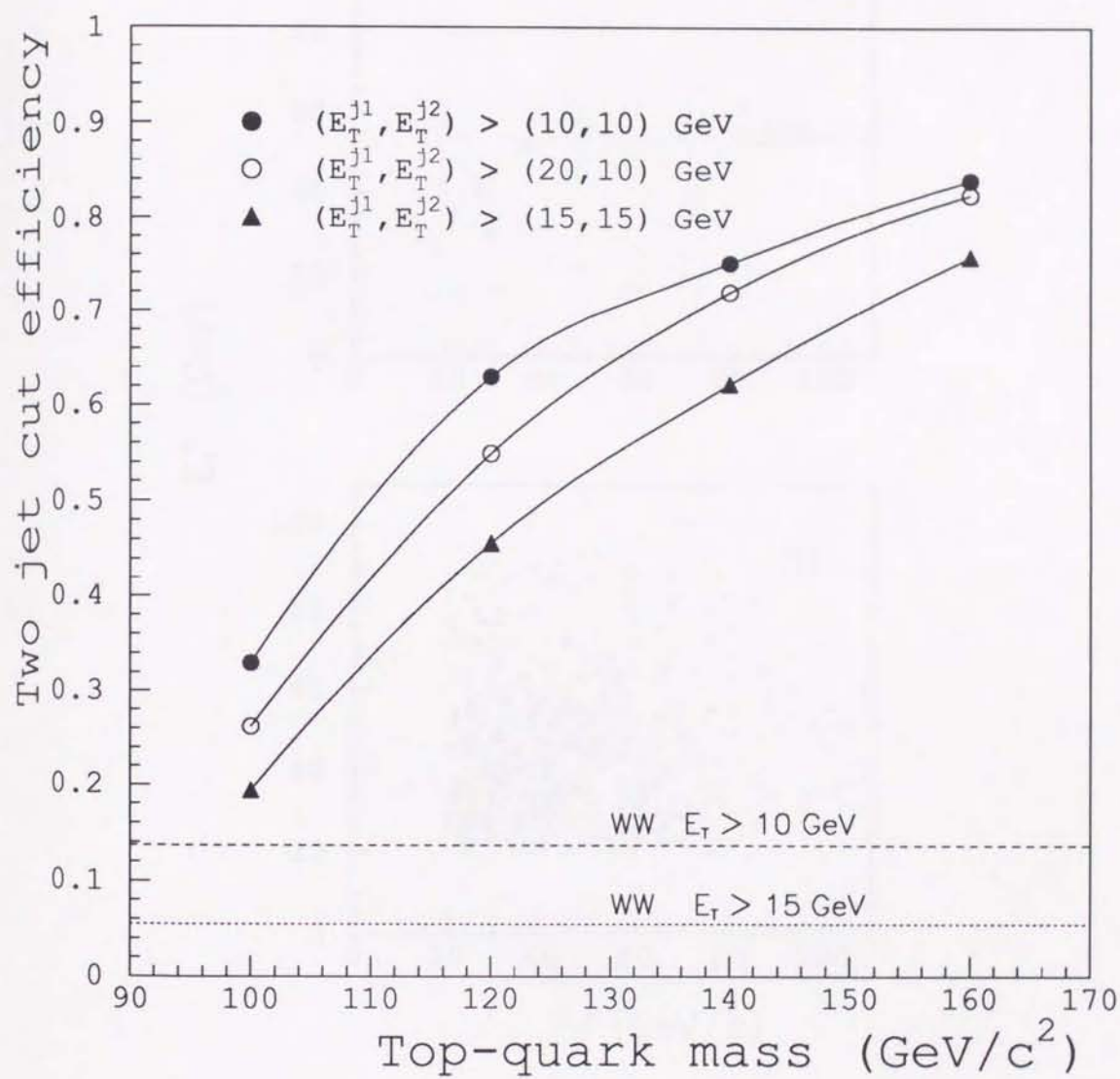


Figure 5.14: Two-jet cut efficiency for  $t\bar{t}$  events as a function of a top-quark mass. Also shown are the efficiencies for WW Monte Carlo events with both  $E_T > 10$  and 15 GeV

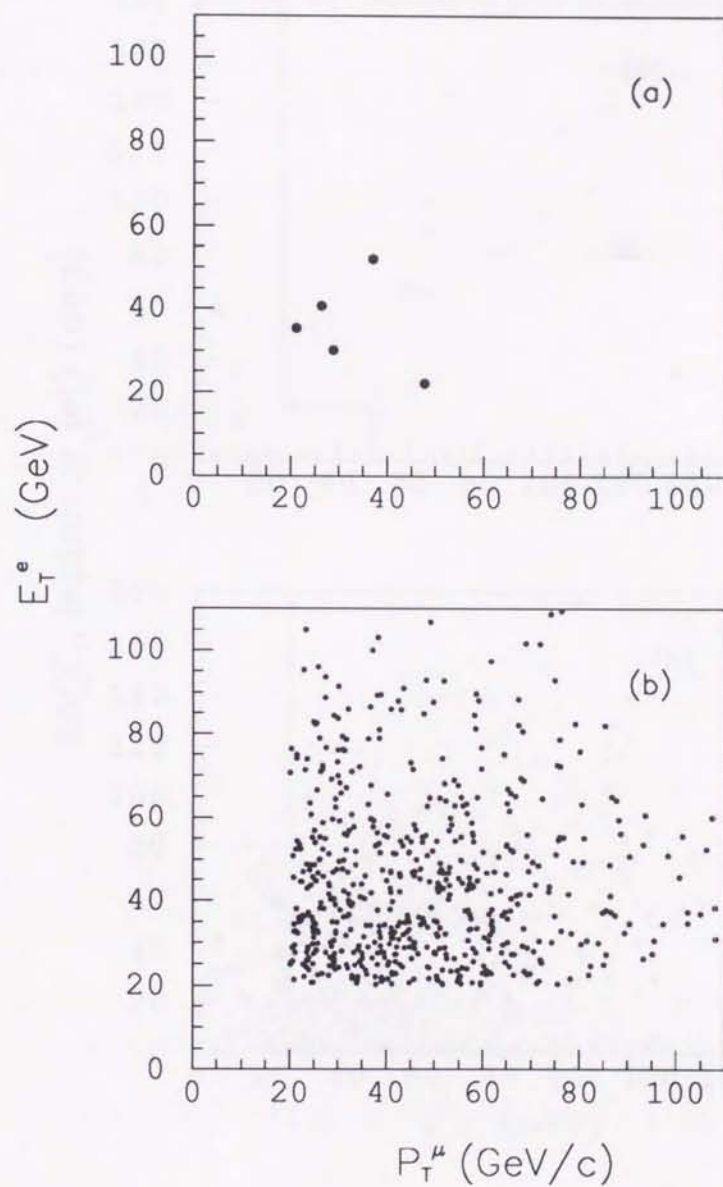


Figure 5.15: Electron transverse energy versus muon transverse momentum in CDF electron-muon data with integrated luminosity of  $21.4 \text{ pb}^{-1}$ , together with b)  $t\bar{t}$  prediction ( $M_{top}=140 \text{ GeV}/c^2$ ).



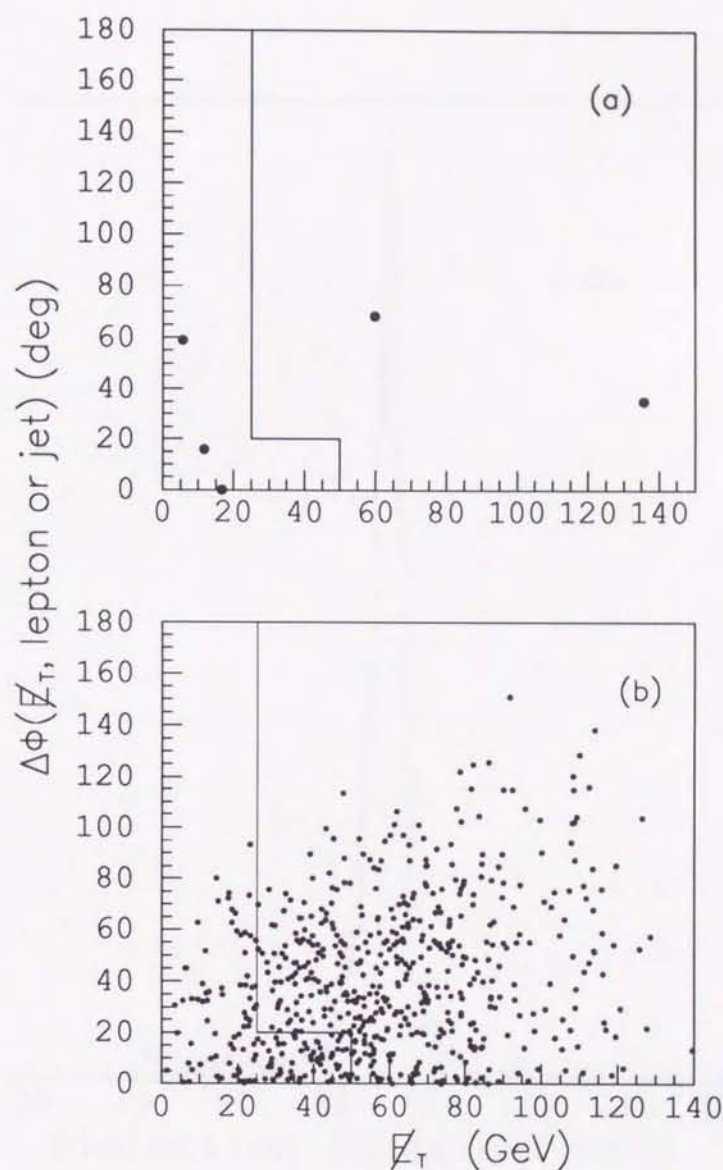


Figure 5.16: Azimuthal angle difference between missing  $E_T$  and the closest lepton or jet in CDF electron-muon data with integrated luminosity of  $21.4 \text{ pb}^{-1}$ , together with b)  $t\bar{t}$  prediction ( $M_{top}=140 \text{ GeV}/c^2$ ). The region to the left of the solid line is excluded by the missing  $E_T$  requirement.

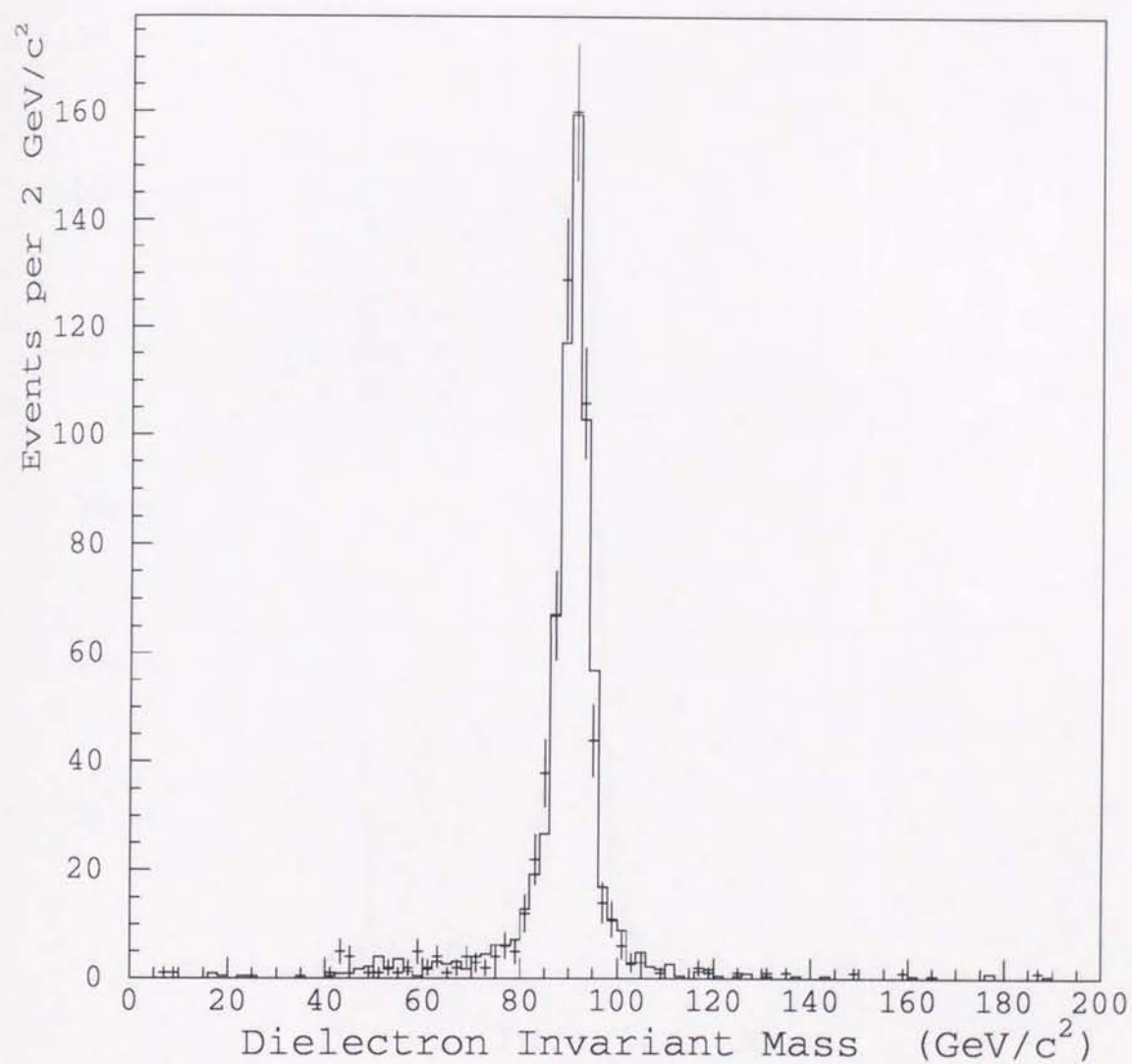


Figure 5.17: Dielectron invariant-mass distribution of CDF data with integrated luminosity of  $21.4 \text{ pb}^{-1}$  (plotted). The histogram is a Monte Carlo Dreall-Yan prediction normalized to data.



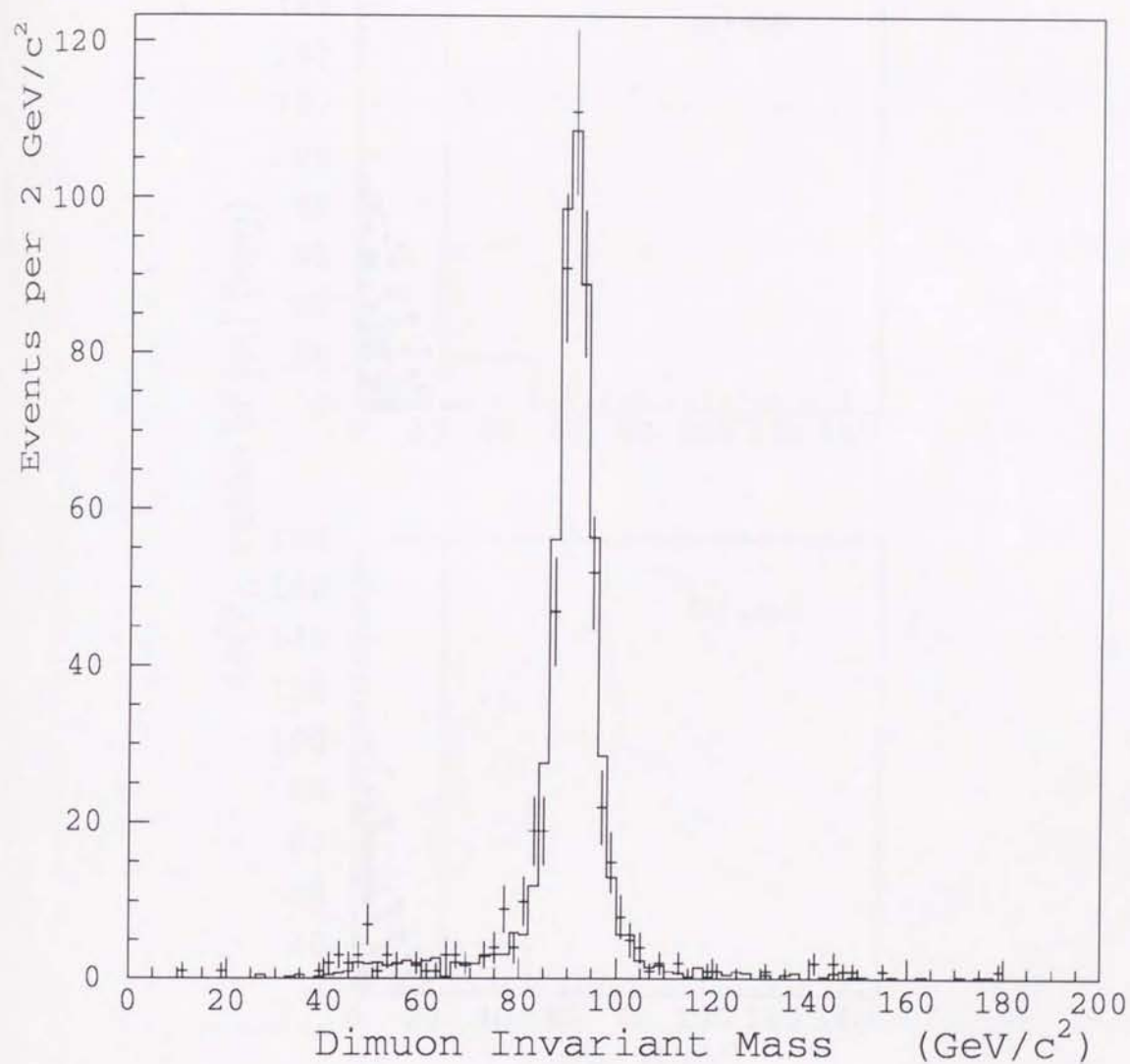


Figure 5.18: Dimuon invariant-mass distribution of CDF data with integrated luminosity of  $21.4 \text{ pb}^{-1}$  (plotted). The histogram is a Monte Carlo Dreall-Yan prediction normalized to data.

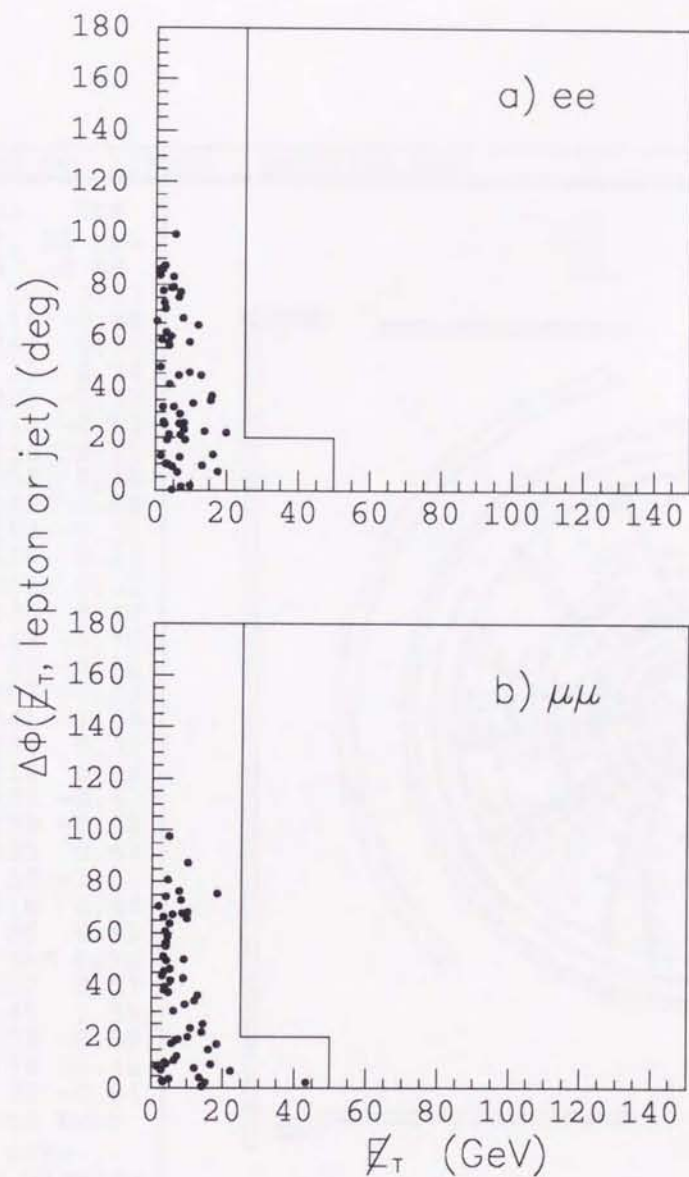


Figure 5.19: Distribution in the  $\Delta\phi(\cancel{E}_T, \text{lepton or jet})$ - $\cancel{E}_T$  plane for CDF data with integrated luminosity of  $21.4 \text{ pb}^{-1}$ . The solid line indicate the event topology cuts: a) dielectron and b) dimuon events. Events with dilepton masses in the range  $75 < M_{ll} < 105$  are not included in the figure.



Run 41540 Evt 127085 EMU41540.DST 29OCT92 3:33:20 21-JAN

Pt	Phi	Eta
z <sub>1</sub> = -4.7, 25 trk		
-22.2	32	0.84
56.5	14	0.17
30.0	216	-0.58
-22.4	352	0.18
-21.6	33	0.84
16.1	222	-0.53
-12.7	212	-0.53
9.3	356	0.11
8.9	352	0.19
-5.0	348	0.08
-4.1	214	-0.51
-3.1	350	0.11
-2.8	352	0.13
2.0	330	0.10
-1.6	148	-0.70
-1.4	81	0.82
1.3	357	-0.09
1.0	341	1.49
-1.0	334	0.33
-0.9	314	0.86
0.8	227	-0.67
0.8	159	-0.98
0.7	235	0.67
0.7	50	-1.02
-0.7	210	-0.44
0.4	28	0.61
8 unattchd trks		
4.5	352	0.07
-2.0	145	1.59
1.4	203	-0.58
1.3	174	-0.44
1.2	97	-0.94
3 rejectd trks		
6 more trks...		
hit & to display		

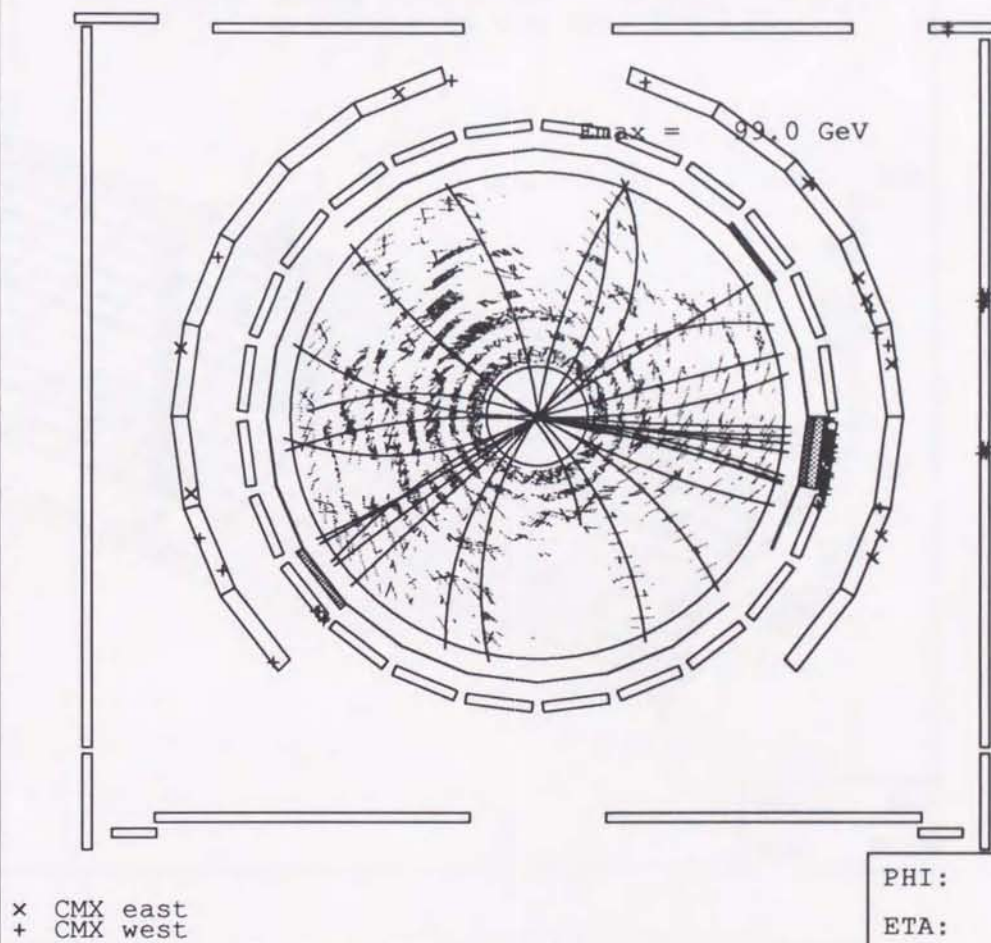


Figure 5.20: A display of the candidate events: Run 41540 Event 127085 view of the tracking chamber in the transverse plane

Run 41540 Evt 127085 EMU41540.DST 29OCT92 3:33:20 21-JAN-9

DAIS E transverse Eta-Phi LEGO Plot  
 Max tower E= 72.4 Min tower E= 0.50 N clusters  
 METS: Ettotal = 723.1 GeV, Et(scalar)= 235.3  
 Et(miss)= 80.4 at Phi= 175.3 Deg.

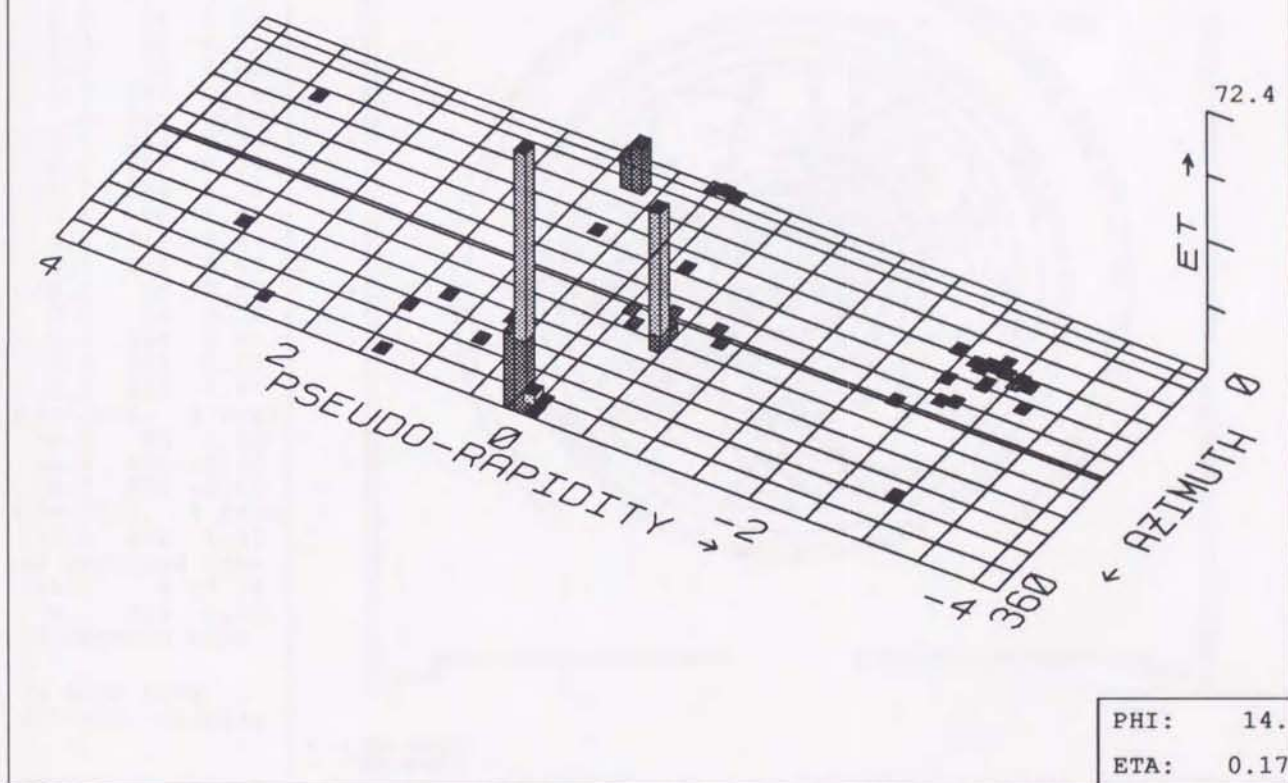


Figure 5.21: A display of the candidate events: Run 41540 Event 127085 The cylindrical calorimeter has been "unrolled" such that the axes of the grid the azimuthal angle around the beam line, and the pseudorapidity, defined as  $\eta = -\log(\tan(\theta/2))$ , where  $\theta$  is the polar angle with respect to the beam line. The height of each cell is proportional to its transverse energy  $E_T = E \sin \theta$ .



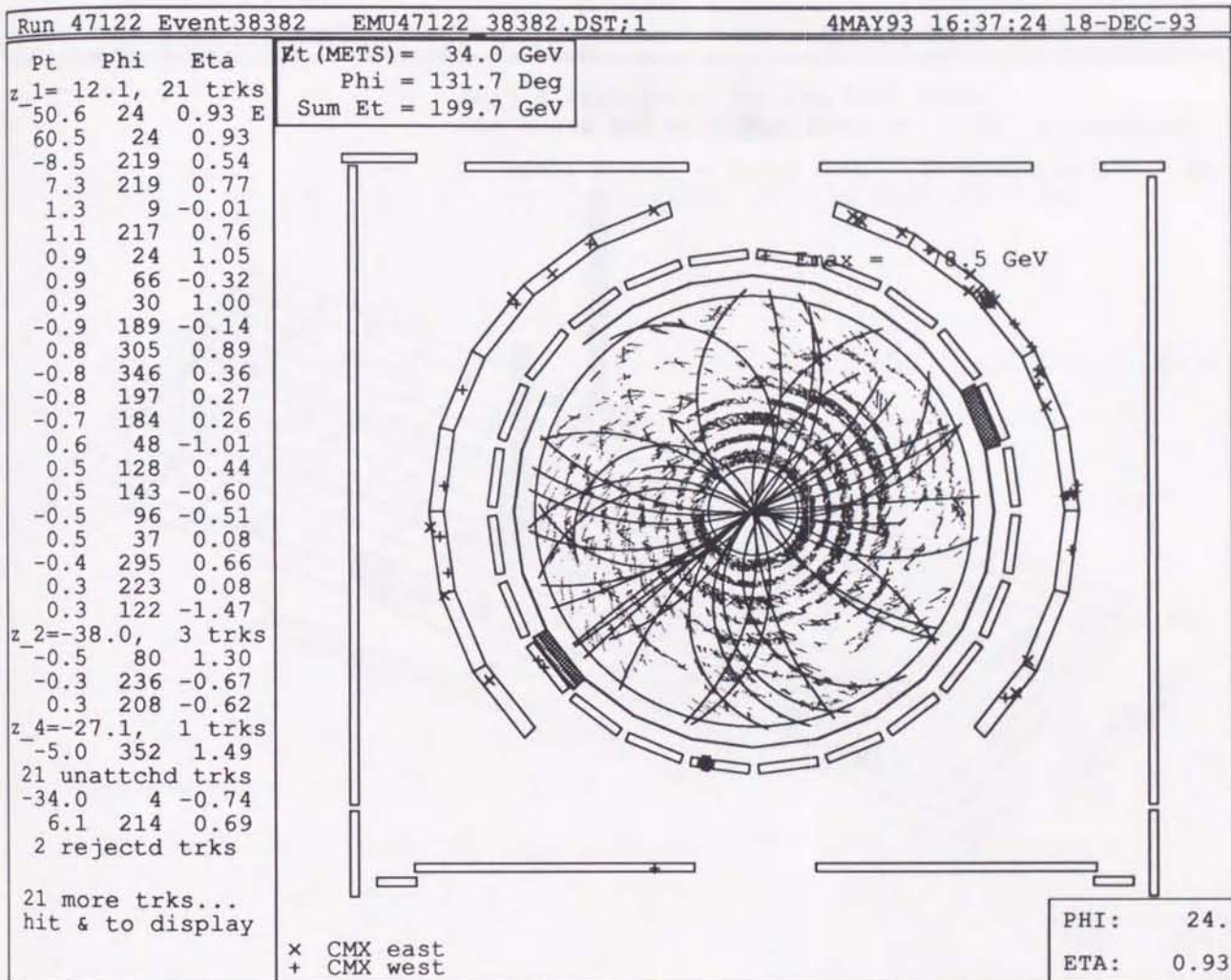


Figure 5.22: A display of the candidate events: Run 47122 Event 38382 view of the tracking chamber in the transverse plane

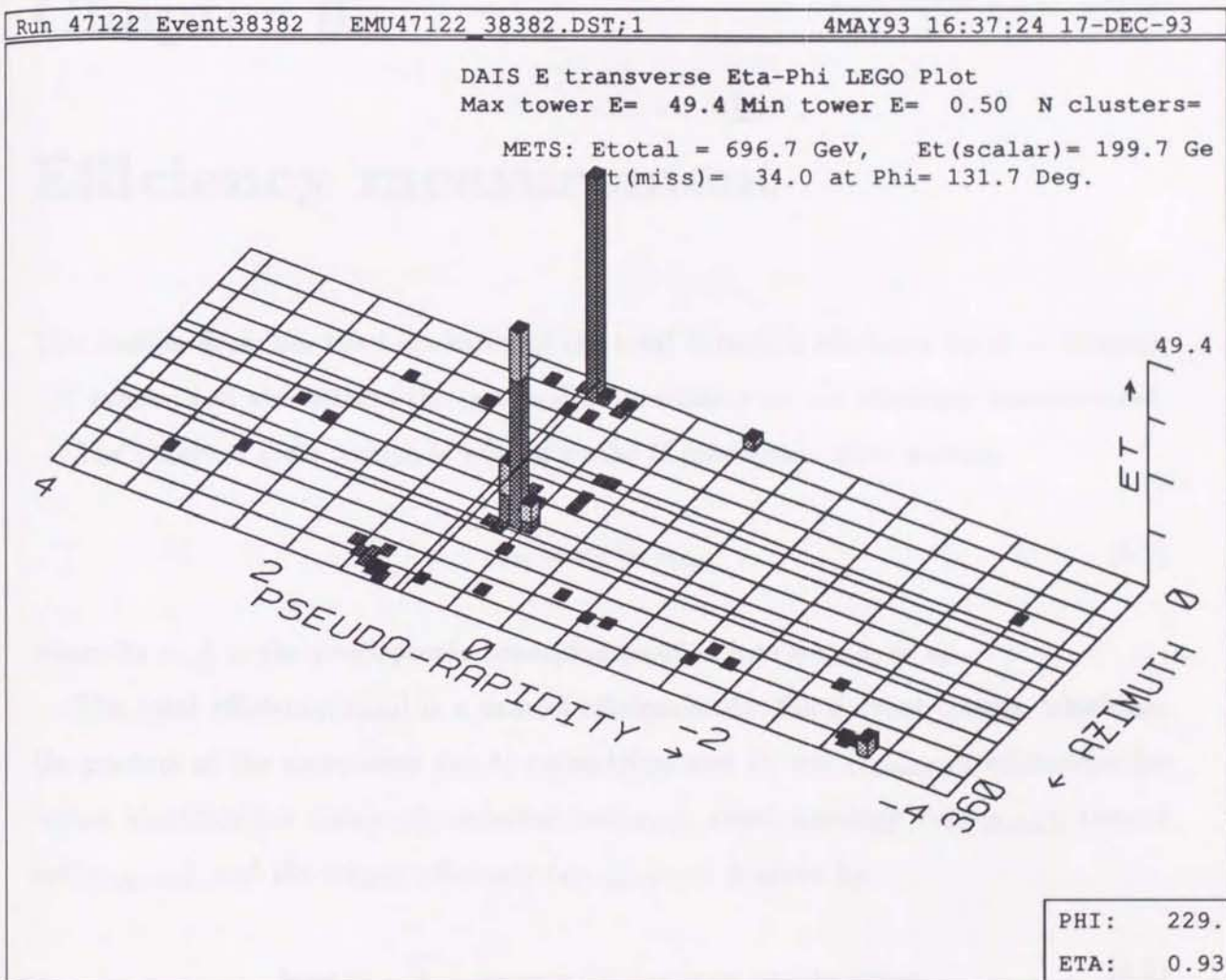


Figure 5.23: A display of the candidate events: Run 47122 Event 38382



## Chapter 6

### Efficiency measurement

This section describes the calculation of the total detection efficiency for  $t\bar{t} \rightarrow$  dilepton  $+X$  events, and also discuss the systematic uncertainty on the efficiency measurement.

The observed cross section is related to the  $t\bar{t}$  production cross section:

$$\sigma_{\text{obs}} = \sigma_{t\bar{t}} \text{Br } \epsilon_{\text{total}} \quad (6.1)$$

where  $\text{Br} = \frac{4}{81}$  is the semileptonic branching fraction into  $e\bar{e}$ ,  $\mu\bar{\mu}$ , or  $e\mu$ .

The total efficiency ( $\epsilon_{\text{total}}$ ) is a sum of efficiencies for the 8 event classes, which are the product of the acceptance due to geometrical and  $P_T$  cut ( $\epsilon_{\text{geom} \cdot P_T}$ ), efficiencies for lepton identification cuts ( $\epsilon_{ID}$ ), isolation cut ( $\epsilon_{\text{isol}}$ ), event topology cut ( $\epsilon_{\text{Event}}$ ), two-jet cut ( $\epsilon_{\text{Two-jet}}$ ), and the trigger efficiency ( $\epsilon_{\text{Trigger}}$ ) and is given by

$$\epsilon_{\text{total}} = \sum_{\text{event class}} \epsilon_{\text{geom} \cdot P_T} \epsilon_{ID} \epsilon_{\text{isol}} \epsilon_{\text{Event}} \epsilon_{\text{two-jet}} \epsilon_{\text{trigger}} \quad (6.2)$$

The arrangement of the factors on the right-hand side of equation (6.2) is meant to define an order in our set of selection cuts. According to this order, the efficiency of a given cut is determined relative to a sample on which all the preceding cuts have already been applied.

In the following sections, we will describe the efficiency calculation for individual

cuts. We use the ISAJET Monte Carlo generator and a simulation of the CDF detector to determine the geometric and kinematic acceptance and the efficiencies for lepton identification cuts, lepton isolation cuts, the combined efficiency of the dilepton charge, invariant mass and missing  $E_T$  cuts, and the efficiency for the two-jet cut. The trigger efficiencies are determined using data collected by independent triggers.

## 6.1 Geometric and kinematic acceptance

The acceptance due to geometrical and  $P_T$  cut is the fraction of  $t\bar{t} \rightarrow \text{dilepton} + X$  events (normalized to the double semi-leptonic branching ratio of  $4/81$ ) inside the fiducial volume of the detector and passing the  $P_T$  cuts. It should be noted that this definition in principle allows efficiencies larger than 1.0. The double semi-leptonic decay of a  $t\bar{t}$  pair with an assumed branching ratio of  $4/81$ , i.e., a lepton pair from WW, contributes most of the signal, but the remaining contributions from sequential decays of a daughter  $b$  or  $c$  quark or  $\tau$  lepton are also taken into account. Hence, the effective branching ratio is larger than  $4/81$ . In Table 6.1, we show the contributions to the signal from the following lepton sources: (1) both leptons come directly from the W decay; (2) at least one lepton comes from the  $b$  decay<sup>1</sup>; and (3) leptons coming from the decay of a tau (but no events such as  $b - \tau$ , since these events are counted in the category (2)). This is evaluated using ISAJET Monte Carlo generator and the CDF detector simulation. Leptons from top quarks at the ISAJET generator level are related to the simulated lepton candidates by examining the matching in  $\eta - \phi$  space between both leptons. We looked at the distributions of the distance between them and required to be less than 0.04. Figure 6.1 illustrates the matching distribution for electrons coming from the decays of W and of bottom. The efficiency of passing the matching cut is about 95 %.

After testing the matching cut, we counted the number of events which passes the lepton  $P_T$  and fiducial cuts described in section 4.1 and 4.2. In the calculation, track re-

<sup>1</sup>We also include the charm decay. By  $b$ , we mean both  $b$  and  $c$  quarks.



		100	120	140	160
1)	$W^+W^-$	$82.2 \pm 1.5$	$68.1 \pm 1.6$	$55.0 \pm 1.5$	$46.7 \pm 1.4$
2)	$Wb, \tau b$	$9.2 \pm 1.1$	$23.7 \pm 1.5$	$38.4 \pm 1.7$	$46.2 \pm 1.6$
3)	$\tau\tau, W\tau$	$8.7 \pm 1.1$	$7.9 \pm 0.9$	$6.4 \pm 0.8$	$6.7 \pm 0.7$

Table 6.1: Fractions of  $t\bar{t} \rightarrow ll + X$  having 1) both leptons coming directly from the top quark decay, 2) at least one lepton coming from the decay of a bottom or charm quark, and 3) leptons coming from other decays except 1) and 2). This was calculated at the parton level using ISAJET Monte Carlo program.

$M_{top}$	100	120	140	160
CE-CE	$0.064 \pm 0.003$	$0.085 \pm 0.004$	$0.112 \pm 0.004$	$0.114 \pm 0.005$
CE-MU	$0.131 \pm 0.005$	$0.175 \pm 0.005$	$0.218 \pm 0.006$	$0.279 \pm 0.006$
CE-MI	$0.039 \pm 0.003$	$0.042 \pm 0.003$	$0.054 \pm 0.003$	$0.053 \pm 0.003$
CE-PE	$0.011 \pm 0.001$	$0.013 \pm 0.002$	$0.014 \pm 0.002$	$0.013 \pm 0.002$
MU-MU	$0.055 \pm 0.003$	$0.066 \pm 0.004$	$0.089 \pm 0.004$	$0.114 \pm 0.005$
MU-MI	$0.019 \pm 0.002$	$0.022 \pm 0.002$	$0.038 \pm 0.003$	$0.037 \pm 0.003$
MU-PE	$0.013 \pm 0.002$	$0.012 \pm 0.002$	$0.017 \pm 0.002$	$0.018 \pm 0.002$
PE-MI	$0.004 \pm 0.001$	$0.004 \pm 0.001$	$0.004 \pm 0.001$	$0.003 \pm 0.001$
Total	$0.337 \pm 0.012$	$0.419 \pm 0.011$	$0.547 \pm 0.010$	$0.632 \pm 0.009$

Table 6.2: Geometric and kinematic acceptances for the top mass from 100- 160 GeV/c<sup>2</sup>.

quirement on the plug electron is imposed. For the dimuon class, at least one triggerable muon is required.

Table 6.2 summarizes the geometric and kinematic acceptance. The acceptance is increasing with the top mass (34 - 63 %) because the leptons are more likely to be in the central region and have large  $P_T$  at higher top mass, and also because the contribution to the acceptance from events with one or more leptons from the decay of  $b$  is increasing, from 24 % at  $M_{top}=120$  GeV/ $c^2$  to 46 % at  $M_{top}=160$  GeV/ $c^2$ . However, note that the contribution of leptons coming from  $b$  quarks are suppressed because they are less isolated, and less likely to pass implicit isolation cuts such as HAD/EM and Lshr, than the leptons directly coming from  $W$ , as we will see in the next section.

## 6.2 Lepton Identification

There are 3 sources of top dileptons, as we have discussed in previous section. Leptons in  $t\bar{t}$  events have widely varying isolation characteristic, depending on whether their parent particle is  $W$ , bottom(charm) or tau, as shown in Figure 6.2. It is evident that leptons from the decay of  $W$ 's and  $\tau$ 's are well isolated but ones from the decay of  $b$  are less isolated. Hence the efficiencies for lepton identification cuts are expected to vary according to parentage. It also should be noted that the presence of jet activity in the  $t\bar{t}$  events makes the detection efficiency less efficient than in  $Z^0$  events. It can be seen in the same figure (Figure 6.2 (d)) that leptons from  $Z$  decays are more isolated than those from  $W$ -decays. It is not realistic to estimate the lepton detection efficiency using leptons from the  $Z$  decay. Therefore, the efficiencies are extracted from the  $t\bar{t}$  Monte Carlo. Before measuring the efficiency, it is important to check how well Monte Carlo simulates the lepton identification variables. From Figure 6.3 to 6.5, comparisons of electron variables between data and Monte Carlo are made using central electrons from the decay of  $Z$ . We have also included a small correction factor which account for the difference of identification efficiencies between Monte Carlo and data using  $Z$  events.



The correction ensures that the efficiencies for leptons from Z-decay measured in the data agree with those of simulated Z-decay leptons.

We compute the lepton selection efficiency as

$$\epsilon_{ID} = \sum_{i,j} f_{i,j} \epsilon_i \frac{\epsilon_Z^{Data}}{\epsilon_Z^{MC}}, \quad (6.3)$$

(  $i$  = lepton parentage, and  $j$  = lepton class ).

This is the weighted average where  $f_{i,j}$  is the fraction of leptons passing the  $P_T$  cut at the ISAJET generator level<sup>2</sup> and  $\epsilon_i$  is the efficiencies for leptons extracted from top Monte Carlo. The summation runs over  $i$ 's, three lepton origins which are  $W$ ,  $b$  and  $\tau$  and over  $j$ 's, five lepton classes which are tight CE, loose CE, PE, MU and MI. The last term ( $\epsilon_Z^{Data}/\epsilon_Z^{MC}$ ) is a correction factor to account for the difference between data and Monte Carlo reconstruction. This ratio is determined from the Z decays to dileptons for both data and Monte Carlo events.

### 6.2.1 Lepton identification efficiency from Z events

First, we determine the lepton selection efficiency ( $\epsilon_Z^{Data}$ ) using a sample of leptons from  $Z^0$  decays in data. We select the sample of  $Z^0$  events by requiring a lepton candidate passing the selection criteria and another cluster (or track for a muon) such that the lepton pair form a mass between  $75 \text{ GeV}/c^2$  and  $105 \text{ GeV}/c^2$ . The efficiency is measured by looking at whether the second lepton passes the cuts or not and the efficiency ratio is defined as  $r = (\text{number of electrons passed cut}) / (\text{number of electron tested})$ . For events with two central electrons (CE-CE) and with two CMUO's (MU-MU), in order to properly take into account the combinatorics, the efficiency is  $\epsilon = 2r/(1 + r)$  as describe below, wheres we have simply  $\epsilon = r$  for the plug electron and the MI's.

The following efficiency calculations rely on a simple probability argument that lep-

<sup>2</sup>Strictly speaking, we took the matching in  $\eta - \phi$  of particles between ISAJET generator level and simulated particle as mentioned in the previous section, but no lepton identification cuts were imposed.

tons have two chances to pass the cuts, since real  $Z \rightarrow l_1 l_2$  decays have two leptons. For a cut efficiency of  $\epsilon$ , then there are four cases:

- probability of both leptons pass the cut  $= \epsilon^2$
- probability of  $l_1$  passes and  $l_2$  fails the cut  $= \epsilon(1 - \epsilon)$
- probability of  $l_1$  fails and  $l_2$  passes the cut  $= \epsilon(1 - \epsilon)$
- probability of neither lepton passes the cut  $= (1 - \epsilon)^2$

Let  $N$  be the number of events inside the mass window with at least one tight electron,  $N_1$  the number of events with both leptons passing the tight cuts,  $N_i$  the number of events in which both leptons pass the cut  $i$ . The number of  $Z$  events in the sample is denoted by  $N_Z$ , which is unknown. We can express,

$$N = N_Z \epsilon (2 - \epsilon) \quad (6.4)$$

$$N_1 = N_Z \epsilon^2 \quad (6.5)$$

$$N = N_Z \epsilon (2\epsilon_i - \epsilon) \quad (6.6)$$

Solving these equations<sup>3</sup>,

The efficiency for the individual cuts are

$$\epsilon_i = \frac{N_1 + N_i}{N + N_1}$$

and the overall efficiency is

$$\epsilon_{all} = \frac{2N_1}{N + N_1}.$$

<sup>3</sup>Eq. (1.6) can be obtained as follows. The efficiency that a positron passes the individual cut  $i$  is expressed as  $\epsilon_i \epsilon N_Z$  and the efficiency for an electron is  $\epsilon_i \epsilon N_Z$  in the same way. Here we should note that the events which pass both electron and positron pass the cut  $i$  are counted twice ( $= \epsilon^2 N$ ). Thus, we obtain  $(2 \times \epsilon_i \epsilon - \epsilon^2) N_Z$ .



The statistical error on this efficiency, given by binominal statistics, is

$$\delta\epsilon^i = \sqrt{\frac{\epsilon^i(1-\epsilon^i)}{N+N_1}}.$$

The efficiencies for the loose selection cuts are calculated similarly. Of course, the individual cut efficiencies remain the same if the cut is the same.; only the total efficiencies change.

### Central electrons

The efficiency is determined from a data sample of  $Z^0 \rightarrow ee$ . The event must contain one tight central electron which passes the electron identification cuts listed in Table 4.1 and be in side the fiducial region. In addition, a second central cluster is required to pass cuts:  $E_T > 20$  GeV and a track pointing to it with  $P_T > 10$  GeV/c. There remains 509 events. The sample contains 394 events which both electrons pass the tight cuts, and of the type tight-tight and 450 events which one pass tight and the other pass our loose selection cuts. The central electron identification efficiencies for the different selections are summarized in Table 6.3. They are measured to be  $87.3 \pm 1.1$  % and  $93.8 \pm 0.8$  % for the tight and loose selection criteria, excluding about 4% loss of electrons associated with the conversion removal.

### Plug electrons PE

The plug electron ID efficiency was measured using  $Z^0 \rightarrow ee$ , where one electron is in the central region satisfying with the tight selection criteria and the other in the plug satisfying  $E_T > 20$  GeV and the isolation measured in the calorimeter is less than 0.1. Our sample consists of 115 tight-loose  $Z$ 's. For this sample, a three-dimensional track requirement on plug electrons was imposed. Only about 1/3 of the total CE-PE  $Z$  events pass this requirement. The track requirement is taken as a fiducial cut, and absorbed as part of the geometrical acceptance in the calculation of the top detection efficiency.

Cut	$N_i$	$\epsilon_{Data}$	$\epsilon_{MC}$
(tight cut)			
HAD/EM < 0.05	484	$0.972 \pm 0.005$	0.837
E/P < 2.0	478	$0.966 \pm 0.006$	0.983
$\Delta x < 1.5$ cm	466	$0.952 \pm 0.007$	0.990
$\Delta z < 3.0$ cm	500	$0.990 \pm 0.003$	0.988
$\chi^2(\text{Strip}) < 15.$	489	$0.978 \pm 0.005$	0.994
$L_{shr} < 0.2$	504	$0.994 \pm 0.002$	1.000
Total (tight)	394	$0.873 \pm 0.011$	0.802
(loose cut)			
HAD/EM < $0.055 + 0.045E_T/100$	504	$0.994 \pm 0.002$	0.936
E/P < 4.0	509	$1.000 \pm 0.000$	0.998
$\Delta x < 1.5$ cm	466	$0.952 \pm 0.007$	0.998
$\Delta z < 3.0$ cm	500	$0.990 \pm 0.003$	0.988
$L_{shr} < 0.2$	504	$0.994 \pm 0.002$	1.000
Total (loose)	450	$0.938 \pm 0.008$	0.909

Table 6.3: Central electron selection efficiency from  $Z \rightarrow ee$  in data. Both tight and loose selection efficiencies are listed. Efficiencies calculated from Z Monte Carlo are also shown in the last column



The plug electron isolation efficiency for the top quark is estimated from the  $t\bar{t}$  Monte Carlo. The efficiencies are summarized in Table 6.4 and the overall efficiency is found to be  $85.2 \pm 0.03 \%$ .

	Cut	Npass	$\epsilon$		
HAD/EM	$< 0.05$	113	0.983	$\pm$	0.012
$\chi^2(3 \times 3)$	$< 3.$	111	0.965	$\pm$	0.017
N(VTPC)	$> 0.5$	109	0.948	$\pm$	0.021
$\chi^2(\text{depth})$	$< 15.$	109	0.948	$\pm$	0.021
Combined		98	0.852	$\pm$	0.033

Table 6.4: Plug electron selection efficiency

### Central muons MU

From a sample of  $Z^0 \rightarrow \mu\mu$  events, the efficiencies for the minimum ionizing and a match between the CTC track and the muon chamber track was determined. The number of events in the sample is 394 events. The efficiency is summarised in Table 6.5 and the overall selection efficiency is estimated to be  $92.6 \pm 0.1\%$ . The efficiency of the track quality requirement is measured to be  $0.99 \pm 0.1\%$  using a sample of electron tracks from  $W \rightarrow e\nu$  decays. Since the matching between a CTC track and a muon segment track is quite efficient ( $> 0.99$ ), the selection efficiency for CMIO is almost equal to the one for CMUOs. The CMIO efficiency can be obtained from table 6.5 by removing the  $\Delta x$  cut.

We also calculated the muon selection efficiency for Monte Carlo events and results are shown in Table 6.5.

### 6.2.2 Efficiency calculation from top Monte Carlo

At this point we calculated the lepton selection efficiencies using Z events. We can compute the correction factor in eq. 6.3. Next step is to extract lepton identification

cut	$N_i$	$\epsilon_{Data}$	$\epsilon_{MC}$
EM	368	$0.965 \pm 0.007$	0.996
HAD	385	$0.993 \pm 0.005$	0.982
EM+HAD	392	$0.997 \pm 0.002$	1.000
dX	393	$0.999 \pm 0.001$	1.000
	340	$0.926 \pm 0.010$	0.977

Table 6.5: Central muon selection efficiency from  $Z \rightarrow \mu\mu$ . Efficiencies from Z Monte Carlo are also shown.

efficiencies from the top Monte Carlo events. Distributions for identification variables were shown in Figure 4.3 - 4.8.

	$\epsilon_W$	$\epsilon_b$	$\epsilon_\tau$	$\epsilon_{total}$
CE(tight)	$0.794 \pm 0.009$	$0.114 \pm 0.016$	$0.822 \pm 0.036$	$0.670 \pm 0.014$
CE(loose)	$0.872 \pm 0.006$	$0.156 \pm 0.017$	$0.854 \pm 0.028$	$0.739 \pm 0.014$
PE	$0.627 \pm 0.022$	$0.092 \pm 0.051$	$0.454 \pm 0.122$	$0.520 \pm 0.022$
MU	$0.924 \pm 0.003$	$0.213 \pm 0.020$	$0.885 \pm 0.020$	$0.775 \pm 0.015$
MI	$0.893 \pm 0.010$	$0.131 \pm 0.043$	$0.829 \pm 0.064$	$0.732 \pm 0.018$

Table 6.6: Single lepton identification efficiency extracted from top Monte Carlo. Errors are statistical only.

In Table 6.6 we give the single lepton efficiencies ( $\epsilon_i$  in Eq. 6.3) of the 3 sources and 5 classes of leptons<sup>4</sup> for  $M_{top}=140$  GeV/c<sup>2</sup> for instance to illustrate how the efficiencies are calculated. The fractions  $f_W$ ,  $f_b$  and  $f_\tau$  depend slightly on the top mass and on the rapidity of the leptons considered. For  $M_{top} = 140$  GeV/c<sup>2</sup> and for central electrons, the fractions are  $f_W=0.767\pm0.013$ ,  $f_b=0.185\pm0.012$ , and  $f_\tau=0.049\pm0.007$ . The efficiency for the single central electron is calculated using these fractions and the first row in

<sup>4</sup>Correction factors to account for the difference between Monte Carlo and real data are already included in these numbers.



Table 6.6 as follows:

$$\begin{aligned}
 & f_W \epsilon_W + f_b \epsilon_b + f_\tau \epsilon_\tau \\
 = & 0.767 \times 0.794 + 0.207 \times 0.114 + 0.049 \times 0.822 \\
 = & 0.670
 \end{aligned}$$

Similarly, the fractions for the muons are  $f_W=0.746\pm0.013$ ,  $f_b=0.207\pm0.012$ , and  $f_\tau=0.048\pm0.007$ .

The efficiencies  $\epsilon(\text{class}, W)$ ,  $\epsilon(\text{class}, b)$  and  $\epsilon(\text{class}, \tau)$  include a small correction factor which accounts for the difference between real data and Monte Carlo. We find the ratios ( $\epsilon_Z^{\text{Data}}/\epsilon_Z^{\text{MC}}$ ) to be 1.04, 0.99, 1.08, and 0.95 for the tight CE, loose CE, PE, and MU/MI lepton classes, respectively. In addition, central electron efficiencies have been degraded by 4% to account for losses due to the conversion cuts.

The total lepton identification efficiency in dilepton events is obtained by summing over the eight dilepton categories. It is given in table 6.7. The entries in table 6.7 are products of the single lepton efficiencies of table 6.6, except for the CE-CE case where the formula  $\epsilon = \epsilon_{\text{tight}} (2 \epsilon_{\text{loose}} - \epsilon_{\text{tight}})$  was used to take into account correlations between tight and loose central electron cuts. Figure 6.7 shows the plot of the lepton identification efficiency as a function of top mass. It can be seen that the efficiency is constant, as we expect, if we count only leptons coming from the decay of W. The efficiency is decreasing, if we count all the lepton contributions to the efficiency, because the fraction of having leptons from  $b$ -decays is increasing as a function of the top mass, and also because leptons from  $b$ -decay are less likely to pass identification cuts.

In table 6.6, the MI efficiency is low by two sigma (4%) compared with the muon(MU), although these efficiencies are expected to be equal. We believe this could be a statistical fluctuation, with negligible effect in the overall detection efficiency.

$M_{\text{top}}$	$\epsilon_{\text{ID}}$			
	100	120	140	160
CE-CE	$0.625 \pm 0.017$	$0.577 \pm 0.019$	$0.494 \pm 0.014$	$0.441 \pm 0.013$
CE-MU	$0.657 \pm 0.017$	$0.612 \pm 0.019$	$0.519 \pm 0.015$	$0.463 \pm 0.013$
CE-MI	$0.631 \pm 0.018$	$0.596 \pm 0.022$	$0.490 \pm 0.016$	$0.451 \pm 0.014$
CE-PE	$0.451 \pm 0.020$	$0.438 \pm 0.027$	$0.341 \pm 0.016$	$0.333 \pm 0.016$
MU-MU	$0.782 \pm 0.018$	$0.724 \pm 0.019$	$0.601 \pm 0.016$	$0.550 \pm 0.014$
MU-MI	$0.751 \pm 0.020$	$0.705 \pm 0.023$	$0.568 \pm 0.018$	$0.536 \pm 0.016$
MU-PE	$0.537 \pm 0.023$	$0.518 \pm 0.031$	$0.394 \pm 0.019$	$0.396 \pm 0.019$
PE-MI	$0.516 \pm 0.023$	$0.505 \pm 0.032$	$0.372 \pm 0.019$	$0.386 \pm 0.019$

Table 6.7: The lepton selection efficiency for the top mass from 100-160 GeV/c<sup>2</sup>. Errors are statistical only.

### 6.3 Isolation

The dilepton isolation efficiencies shown in table 6.8, are the fractions of dilepton events passing the  $P_T$  and lepton ID cuts, which also pass the isolation cuts. The isolation cut is very efficient because we require only one central isolated lepton in the tracking chamber for the CECE,CEMU,MUMU categories, which account for 82% of the acceptance for  $M_{\text{top}} = 140$  GeV/c<sup>2</sup>. In addition to requiring at least one CE, MU or MI isolated in the tracking chamber, for the CE-MI, CE-PE, MU-MI, MU-PE, and PE-MI categories (18% of the acceptance), the PE or MI leg is required to be isolated in the calorimeter, resulting in a lower isolation efficiency for these categories.

### 6.4 Event topology cuts

The efficiency for event topology cuts ( $\epsilon_{\text{event}}$ ) is the fraction of dilepton events passing the  $P_T$  and isolation cuts which also pass the following cuts combined: opposite-sign, invariant mass, and missing  $E_T$  (both magnitude and direction). See table 6.9. For  $M_{\text{top}} = 160$  GeV/c<sup>2</sup>, the efficiencies of the opposite-sign and missing  $E_T$  cuts are 94% and



$M_{top}$	$\epsilon_{Isol}$			
	100	120	140	160
CE-CE	$0.989 \pm 0.008$	$0.973 \pm 0.011$	$0.984 \pm 0.008$	$0.988 \pm 0.007$
CE-MU	$0.989 \pm 0.005$	$0.986 \pm 0.005$	$0.980 \pm 0.006$	$0.975 \pm 0.006$
CE-MI	$0.812 \pm 0.036$	$0.830 \pm 0.032$	$0.839 \pm 0.030$	$0.782 \pm 0.033$
CE-PE	$0.889 \pm 0.105$	$1.000 \pm 0.000$	$0.867 \pm 0.088$	$0.842 \pm 0.084$
MU-MU	$0.979 \pm 0.009$	$0.982 \pm 0.008$	$0.980 \pm 0.008$	$0.988 \pm 0.006$
MU-MI	$0.880 \pm 0.036$	$0.856 \pm 0.037$	$0.875 \pm 0.029$	$0.831 \pm 0.035$
MU-PE	$0.955 \pm 0.044$	$0.824 \pm 0.092$	$0.704 \pm 0.088$	$0.926 \pm 0.050$
PE-MI	$0.875 \pm 0.117$	$1.000 \pm 0.000$	$0.875 \pm 0.117$	$1.000 \pm 0.000$
Total	$0.959 \pm 0.006$	$0.955 \pm 0.006$	$0.951 \pm 0.006$	$0.947 \pm 0.006$

Table 6.8: Isolation cut efficiency for the top masses:100-160 GeV/c<sup>2</sup>. Errors are statistical only.

76%, respectively. The invariant mass cut applied in the  $ee$  and  $\mu\mu$  channels is 80% efficient. The combined efficiency of the three cuts on dileptons is  $\epsilon_{event} = 69\%$ .

## 6.5 Two-jet cut

We investigated the efficiency for the two-jet cut in section 5.7 to determine the jet  $E_T$  thresholds. The result was tabulated in Table 5.2. Jet multiplicity and  $E_T$  spectrum are affected by Monte Carlo assumptions about gluon radiation. ISAJET  $t\bar{t}$  Monte Carlo generator includes radiation of gluons from the initial- and final-state partons. Emissions of these gluons increases the jet multiplicity and therefore increases the efficiency of the number-of-jets requirement. For  $M_{top}=120$  GeVc<sup>2</sup>, approximately 30 % of the jets passing the selection cuts are due to gluon radiation.

To get around the problem of the poorly known effects due to the gluon radiation, we calculated the efficiency ( $\epsilon_{Two-jet}$ ) listed in Table 5.2 in the following manner.

$$\epsilon_{Two-jet} = 1/2 (\epsilon_{Two-jet}^{ON} + \epsilon_{Two-jet}^{OFF}), \quad (6.7)$$

	100	120	140	160
CE-CE	$0.52 \pm 0.04$	$0.55 \pm 0.03$	$0.59 \pm 0.03$	$0.57 \pm 0.03$
CE-MU	$0.73 \pm 0.02$	$0.71 \pm 0.02$	$0.75 \pm 0.02$	$0.75 \pm 0.02$
CE-MI	$0.71 \pm 0.05$	$0.67 \pm 0.04$	$0.78 \pm 0.03$	$0.71 \pm 0.04$
CE-PE	$0.50 \pm 0.18$	$0.59 \pm 0.12$	$0.69 \pm 0.13$	$0.50 \pm 0.13$
MU-MU	$0.61 \pm 0.03$	$0.61 \pm 0.03$	$0.54 \pm 0.03$	$0.58 \pm 0.03$
MU-MI	$0.60 \pm 0.06$	$0.58 \pm 0.06$	$0.50 \pm 0.05$	$0.55 \pm 0.05$
MU-PE	$0.71 \pm 0.10$	$0.64 \pm 0.13$	$0.89 \pm 0.07$	$0.76 \pm 0.09$
PE-MI	$0.71 \pm 0.17$	$0.86 \pm 0.13$	$0.86 \pm 0.13$	$1.0 \pm 0.00$
Total	$0.659 \pm 0.014$	$0.662 \pm 0.013$	$0.690 \pm 0.012$	$0.688 \pm 0.012$

Table 6.9: The combined efficiency of the dilepton charge, invariant mass, and missing  $E_T$  cuts for top masses from 100-160 GeV/c<sup>2</sup>. Errors are statistical only.

where  $\epsilon_{\text{Two-jet}}^{\text{ON}}$  is the two-jet cut efficiency with the default ISAJET, and  $\epsilon_{\text{Two-jet}}^{\text{OFF}}$  is computed by disabling gluon radiation in ISAJET. Thus, we define the efficiency as a mean value of both numbers. We have also checked the jet multiplicity using HERWIG Monte Carlo generator [49] and found that  $73.9 \pm 2.8$  % of top Monte Carlo events of 140 GeV/c<sup>2</sup> were satisfied with the two-jet requirement. This result is consistent with the ISAJET average of  $75.1 \pm 1.0$  %.

## 6.6 Trigger

Efficiencies of single electron or muon triggers are calculated as shown in Table 6.10 from data using independent triggers [42].

Trigger	Electron	Muon
Level 1	$99.2 \pm 0.08$	$94.99^{+0.74}_{-0.82}$
Level 2	$93.5 \pm 0.3$	$93.68^{+1.27}_{-1.52}$
Level 3	$97.4 \pm 0.2$	$97.7 \pm 0.6$

Table 6.10: Single lepton trigger efficiency at each trigger level



Dilepton events are collected with two of any high  $P_T$  single lepton triggers. The trigger efficiency for dilepton events is evaluated using the trigger efficiency for inclusive lepton trigger. The trigger efficiency for the dilepton events is calculated as is  $1 - f_1 \cdot f_2$ , where  $f_1$  and  $f_2$  are the separate probabilities for failing the first and second triggers, respectively. In case of having no trigger for one of two leptons, for instance for CMIO,  $f$  is set to be 1. A summary of dilepton trigger efficiencies is shown in Table 6.11.

$M_{\text{top}}$	$\epsilon_{\text{trigger}}$			
	100	120	140	160
CE-CE	0.993	0.993	0.993	0.993
CE-MU	0.989	0.989	0.989	0.989
CE-MI	0.916	0.916	0.916	0.916
CE-PE	0.983	0.983	0.979	0.983
MU-MU	0.983	0.983	0.983	0.983
MU-MI	0.869	0.869	0.869	0.869
MU-PE	0.973	0.974	0.967	0.973
PE-MI	0.797	0.803	0.745	0.797
Total	0.972	0.974	0.972	0.976

Table 6.11: Trigger efficiency

## 6.7 Total detection efficiency

Table 6.12 shows the detection efficiency as a function of top mass for each dilepton category. The sums over dilepton categories are also provided. Efficiency plots before a) the two-jet cut, and b) after the additional two-jet cut, are shown in Figures 6.10 and 6.11. respectively. In table 6.13 a rundown is given of all the individual efficiencies which contribute to the total detection efficiency for a top mass of  $140 \text{ GeV}/c^2$ .

The total detection efficiency as a function of the top mass remains relatively constant as the top mass increases because the decrease in the the lepton detection efficiency with mass is compensated by the rising acceptance due to geometrical and  $P_T$  cuts.

$M_{\text{top}}$	$\epsilon_{\text{total}}$				
	100	120	140	160	180
CE-CE	0.007	0.016	0.024	0.024	0.028
CE-MU	0.020	0.047	0.062	0.078	0.080
CE-MI	0.004	0.008	0.012	0.010	0.011
CE-PE	0.001	0.002	0.002	0.002	0.002
MU-MU	0.008	0.018	0.021	0.029	0.032
MU-MI	0.002	0.004	0.006	0.007	0.010
MU-PE	0.002	0.002	0.003	0.004	0.005
PE-MI	0.000	0.001	0.001	0.001	0.001
Total	0.044	0.098	0.132	0.154	0.169
Total(no jet cut)	0.135	0.156	0.175	0.184	0.192

Table 6.12: Total efficiency

	$\epsilon_{\text{geom-P}_T}$	$\epsilon_{\text{ID}}$	$\epsilon_{\text{Isol}}$	$\epsilon_{\text{event}}$	$\epsilon_{\text{two-jet}}$	$\epsilon_{\text{Trigger}}$	$\epsilon_{\text{total}}$
CE-CE	11.2	54.1	98.8	59.1	75.1	99.3	2.6
CE-MU	21.8	51.9	98.3	75.1	75.1	98.9	6.2
CE-MI	5.4	49.0	84.6	78.3	75.1	91.6	1.2
CE-PE	1.4	34.1	85.7	66.7	75.1	97.9	0.2
MU-MU	8.9	60.1	98.4	54.0	75.1	98.3	2.1
MU-MI	3.8	56.8	87.7	50.2	75.1	86.9	0.6
MU-PE	1.7	39.4	79.5	87.1	75.1	96.7	0.3
PE-MI	0.4	37.2	91.7	90.9	75.1	74.5	0.1
Total (%)	54.7	52.8	95.4	69.4	75.1	97.3	13.4

Table 6.13: Dilepton efficiency for a top mass of 140 GeV/c<sup>2</sup>



## 6.8 Systematic uncertainties

We describe systematic uncertainties of the dilepton analysis in this section. The basic idea to estimate these errors are to compare the different generator or simulator and to measure the variation by changing the parameters.

### Acceptance due to geometrical and $P_T$ cuts

Here, one source of systematic uncertainty is the modeling of initial state radiation. Initial state radiation affects the motion of the  $t\bar{t}$  system and hence the rapidity and transverse momentum distributions of the top quark decay products. This effect can be studied by turning on and off gluon radiation in ISAJET. Another systematic uncertainty results from the choice of structure functions. Our estimate is 3% for the total systematic uncertainty on the geometrical and kinematical acceptance.

### Lepton identification

We extracted the lepton identification efficiencies from the  $t\bar{t}$  Monte Carlo, together with  $Z$  events in data to correct for the difference between data and Monte Carlo. Uncertainties depend largely on how the Monte Carlo models the  $t\bar{t}$  production and decay. Detector simulation affects lepton identification. Here, we take half the difference between the result obtained from two different simulations of the CDF detector; this is 5%. The modeling of gluon radiation affects the isolation properties of the leptons, and hence their identification efficiency. We studied this effect by turning on and off gluon radiation in ISAJET, and taking half the difference in the corresponding lepton identification efficiencies as systematic uncertainty. This gives 2.4%. Since these two contributions are clearly independent, the systematic uncertainty on lepton identification is  $2.4\% \oplus 5\% = 6\%$ .

### Isolation

The technique for determining the systematic uncertainty on lepton isolation is the same as for lepton identification. The effect due to gluon radiation and detector simulation are both 1 %. Hence the combined systematic uncertainty is conservatively  $1\% \oplus 1\% = 2\%$ . We have also investigated the uncertainty due to the fragmentation model ISAJET

fragments quarks according to the Peterson fragmentation function:

$$D(z) = 1/z \times (1 - 1/z - \epsilon/(1 - z))^{-2}$$

where  $z$  is the fraction of the quark momentum carried by the particle (usually a meson) that contains the quark. The parameter  $\epsilon$  for top quark in ISAJET defaults to 0.5. We have changed  $\epsilon$  to 0.2 and 1.5 and generated samples of top Monte Carlo with  $M_{top}=140$  GeV/c<sup>2</sup>. As a result, no significant change was observed.

### Trigger

Errors of each single lepton trigger efficiency are propagated to the total detection efficiency, which result in observation of less than 1%.

### Jet

In case of requiring the two-jet cut, we have to take into account systematic uncertainty due to jets and this arises the largest contribution.

Uncertainties in the understanding of the jet energy scale and the gluon radiation are reflected in an uncertainty in the total detection efficiency in case of requiring the two-jet cuts in the analysis, where we require that there are at least two jets with  $E_T > 10$  GeV. The energy scale is estimated to be  $\pm 10\%$  for jets of  $E_T$  near 10 GeV. A  $\pm 10\%$  uncertainty in the jet energy scale, which depends on  $M_{top}$ , results in the change of detection efficiency by  $\pm 1.3(M_{top}=160 \text{ GeV}^2) - 5.0(M_{top}=100 \text{ GeV}^2)$ .

The ISAJET Monte Carlo generator includes radiation of gluons from the initial- and final state-partons. These radiations increases the jet multiplicity, which results in increasing the efficiency of the number-of-jet requirement. We estimate that  $\sim 20 - 30\%$  of jets in the  $t\bar{t}$  events coming from gluon radiation. Disabling gluon radiation in ISAJET decreases the efficiency of the jet multiplicity requirement by 6.4% for  $M_{top}=140 \text{ GeV}^2$ .

### Others

To measure some of the efficiencies, we depend much on Monte Carlo. This is about 3%.

We also take the 10% uncertainty in luminosity measurement.



Table 6.14: Summary of uncertainties in the acceptance calculation.

Uncertainty source	No jet cut
Geometrical and $P_T$ cuts	3%
Lepton detection	
(a) gluon radiation	2.4%
(b) simulation	5 %
Isolation	
(a) gluon radiation	1 %
(b) simulation	1 %
Calorimeter(jet) energy scale	2 %
on the missing $E_T$	
MC statistics	3%

To obtain the error in the expected number of events we have added the statistical error in quadrature with the systematic error. A systematic error of 13% is used except for the calculation of the two jet efficiency cut. The later systematic error depends on two factors the gluon radiation and the jet energy scale. The error due to gluon radiation is obtained by turning off the gluon radiation in ISAJET. We use half the difference between on and off as the sigma for the gluon radiation. By changing the jet energy scale by  $\pm 10\%$  we determine the systematic error in the jet energy scale. The systematic error is a function of the top quark mass and is given in table 6.15.

Systematic error in $\epsilon_{\text{total}}$ (%)				
13% error in quadrature with error on jets				
$M_{\text{top}}$	100	120	140	160
Gluon radiation	36.3	12.1	6.4	2.9
Energy scale	5.0	3.6	2.2	1.3
Other from table above	8	8	8	8
total	38	15	10	9

Table 6.15: Systematic uncertainty in the two-jet cut



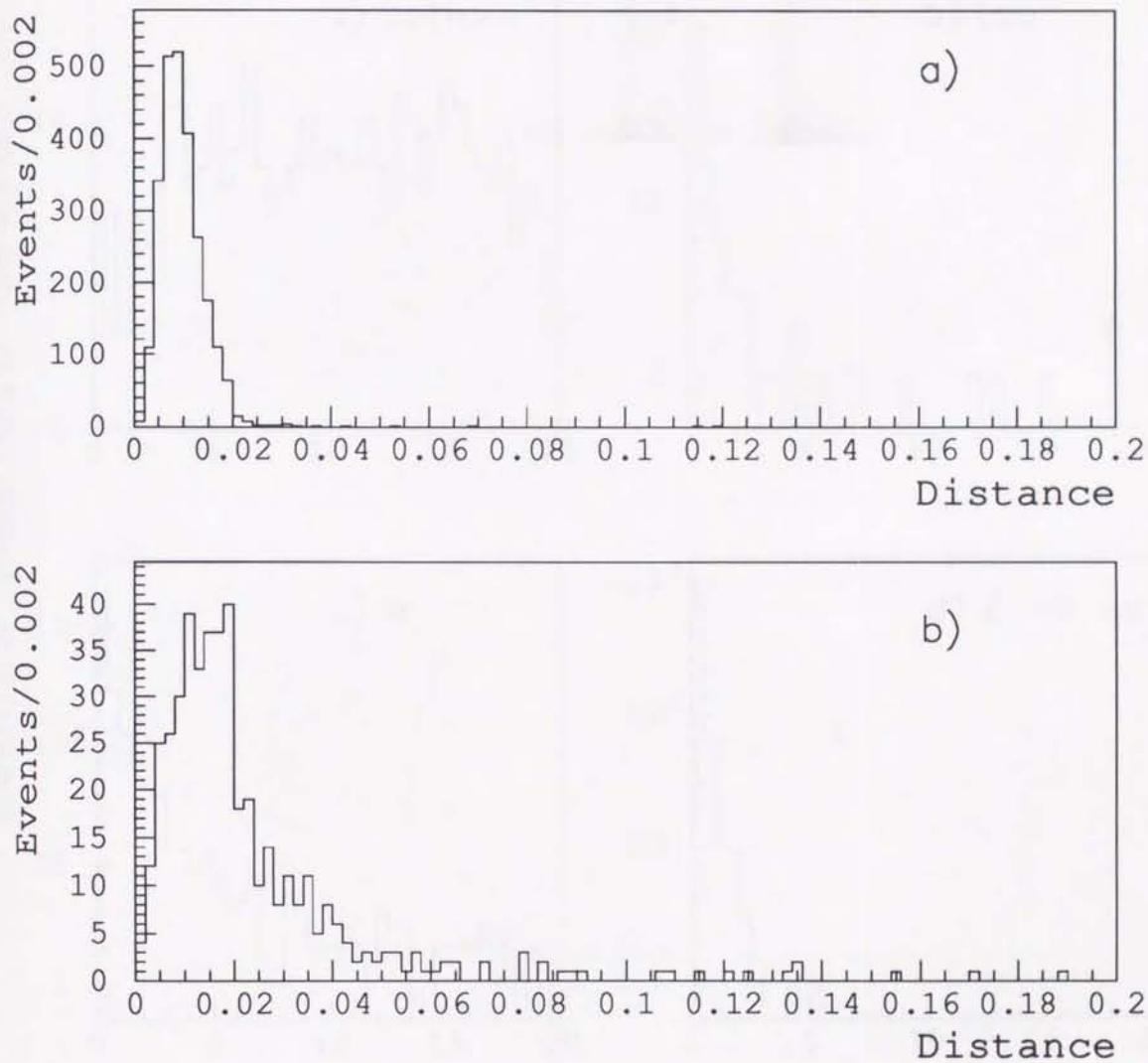


Figure 6.1: A matching in  $\eta - \phi$  between reconstructed electron and electron before simulation. Electrons from a) W decays and b) bottom decays in  $t\bar{t}$  events. The top mass is 140 GeV

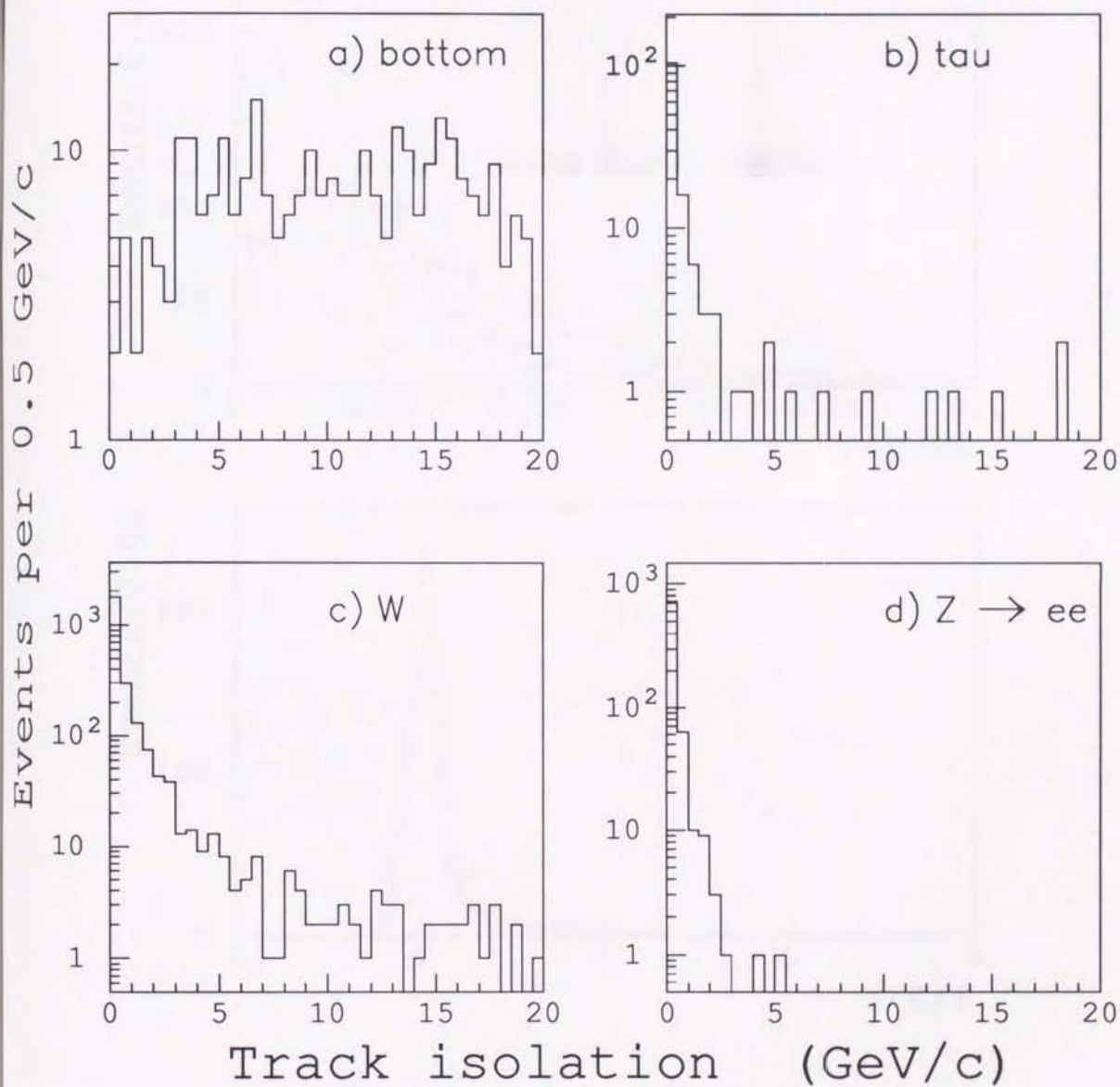


Figure 6.2: Track isolation distributions from top Monte Carlo ( $M_{top} = 140 \text{ GeV}/c^2$ ) for leptons from a)  $b$  decays, b)  $\tau$  decays, and c)  $W$  decays. Also shown in d) is the track isolation for electrons from  $Z$  decays.



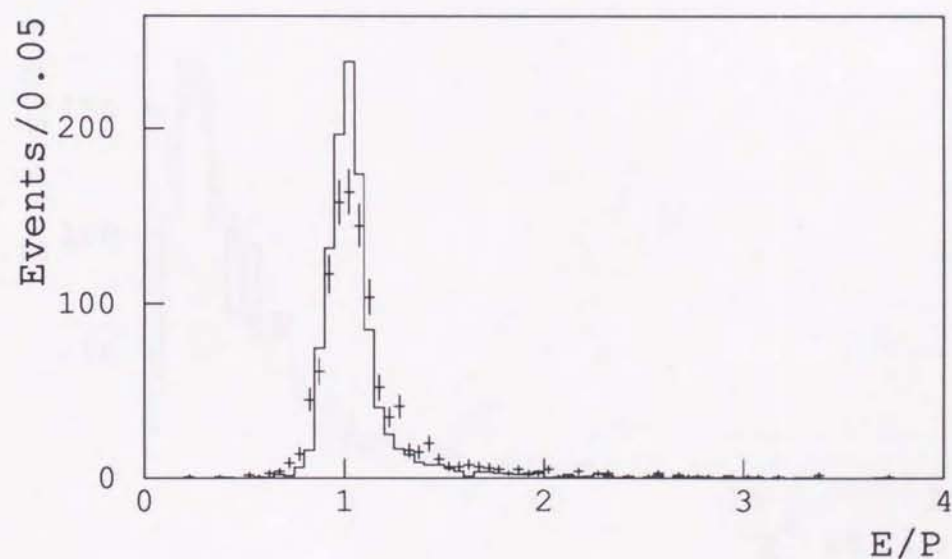
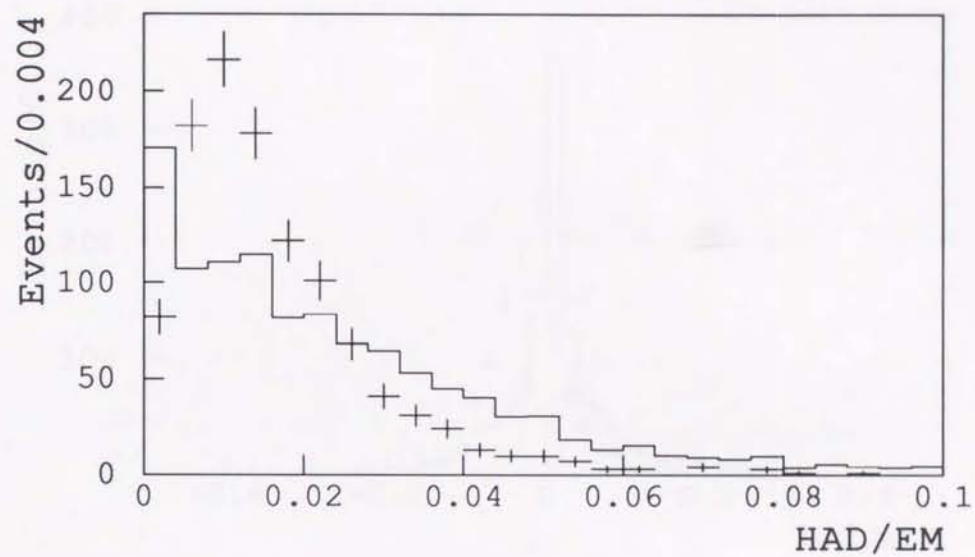


Figure 6.3: Central electron quality variables: HAD/EM and E/p. The full histogram corresponds to the distribution from ISAJET Monte Carlo  $Z \rightarrow ee$  events, and points for  $Z \rightarrow ee$  events from CDF data.

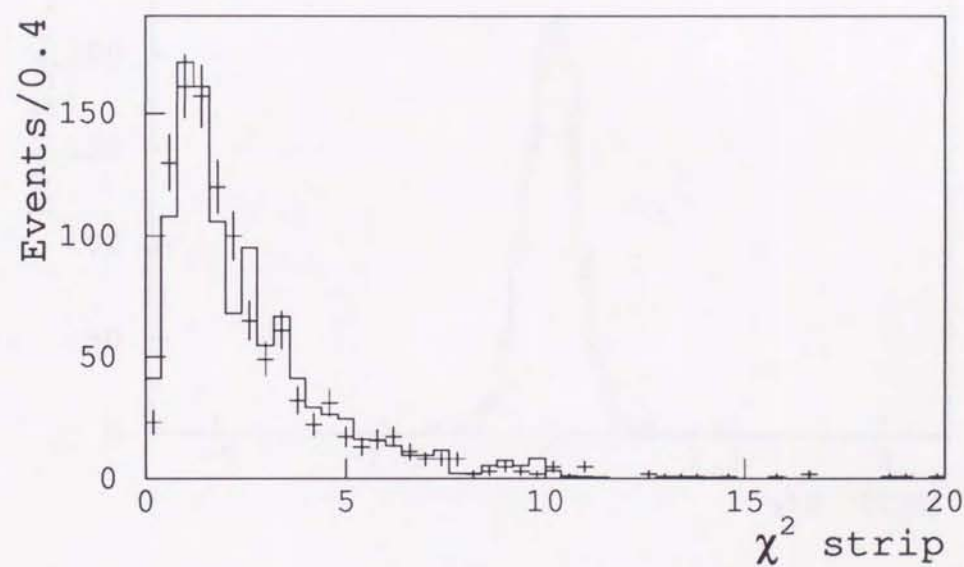
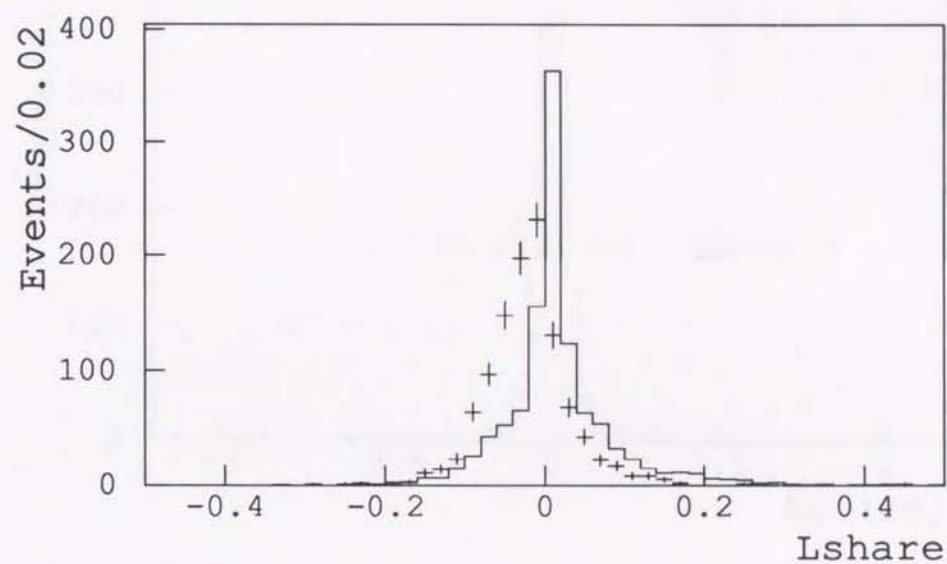


Figure 6.4: Central electron quality variables:  $L_{share}$  and  $\chi^2$ . The full histogram corresponds to the distribution from ISAJET Monte Carlo  $Z \rightarrow ee$  events, and points for  $Z \rightarrow ee$  events from CDF data.



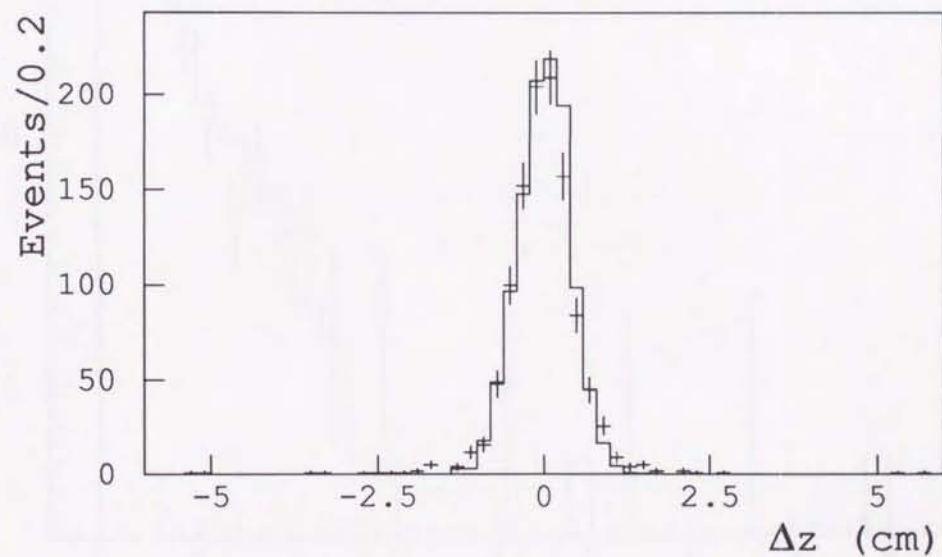
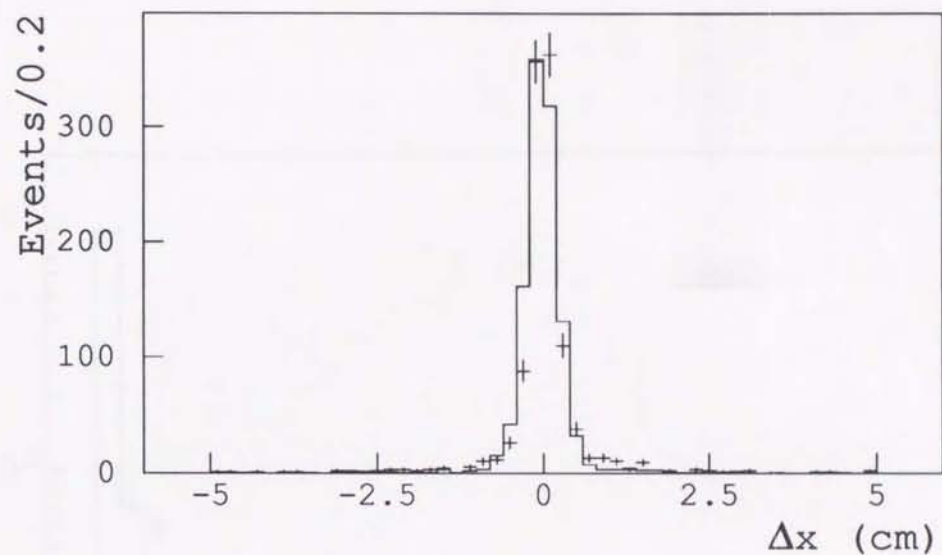


Figure 6.5: Central electron quality variables: a) match in the  $R\phi$  view between the track and the shower position as measured in the strip chamber and b) match in the  $z$  view between the track and the shower position as measured in the strip chamber. The full histogram corresponds to the distribution from ISAJET Monte Carlo  $Z \rightarrow ee$  events, and points for  $Z \rightarrow ee$  events from CDF data.

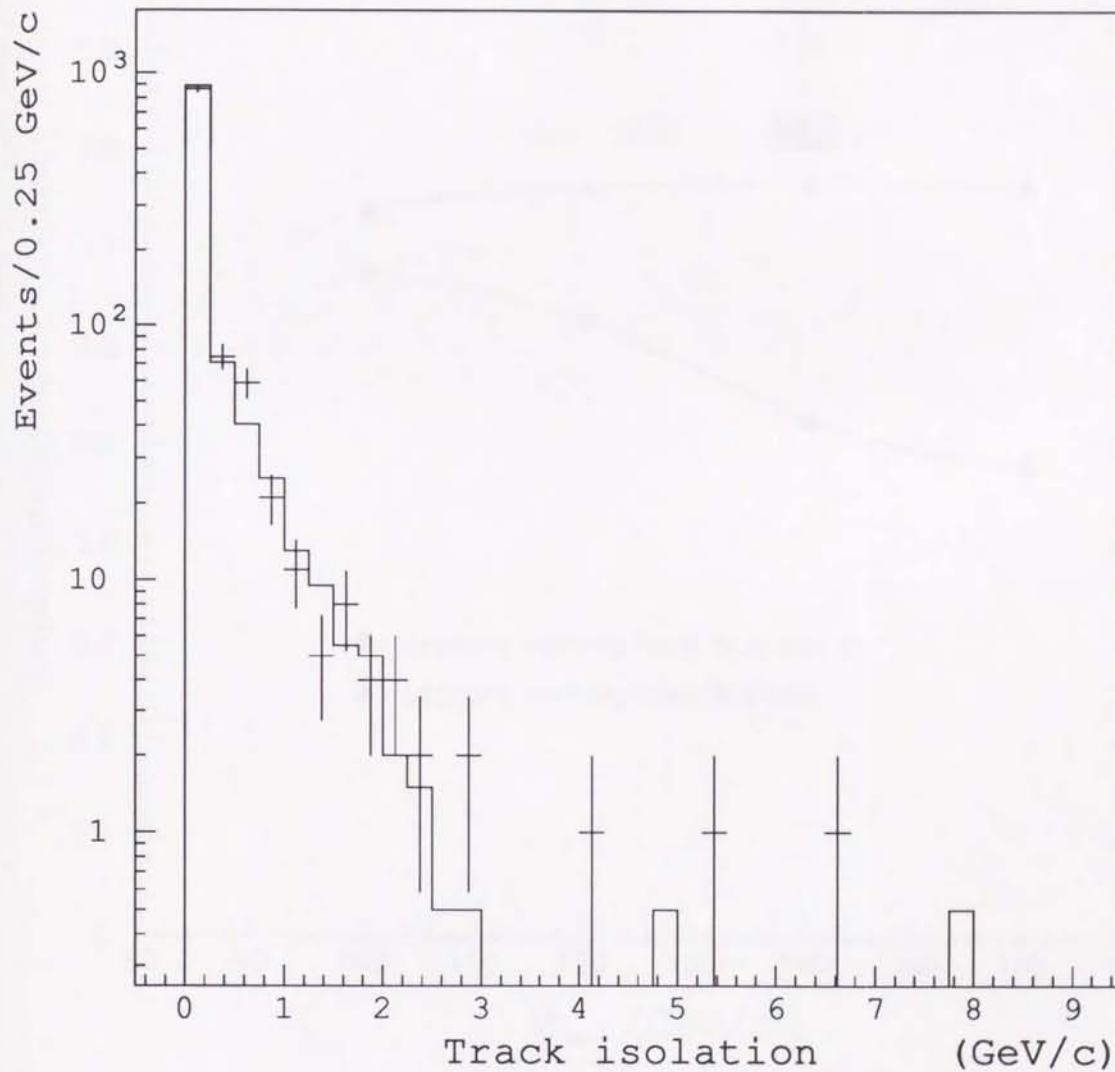


Figure 6.6: Track isolation distribution of the Z decay into  $ee$  from CDF data is shown (points), and the histogram corresponds to track isolation distribution from ISAJET Monte Carlo, together with a simulation of the CDF detector.



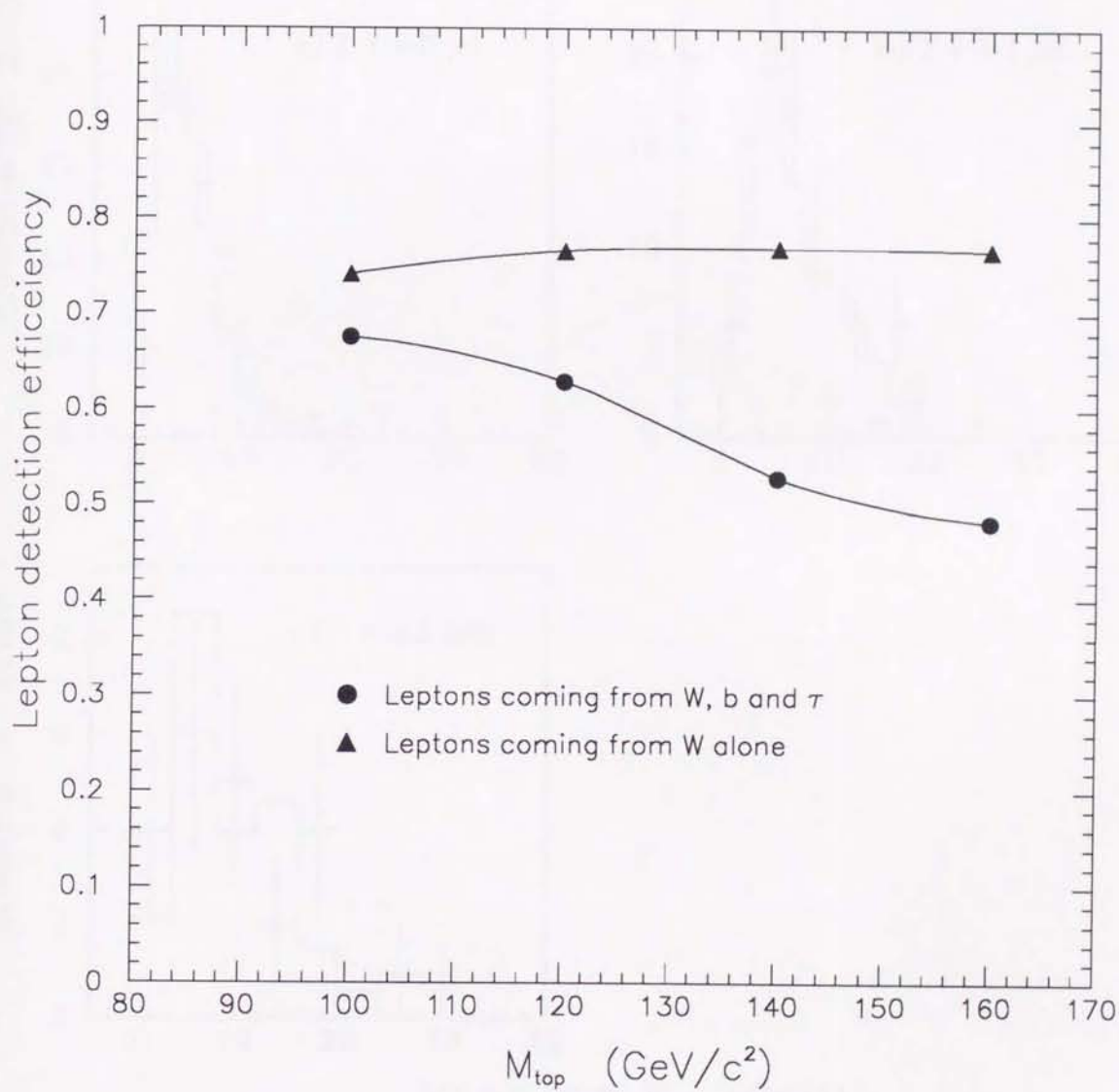


Figure 6.7: Lepton detection efficiency as a function of top quark mass. Two curves shows efficiencies of leptons coming from WW only and all the lepton contribution from W, bottom or  $\tau$ .

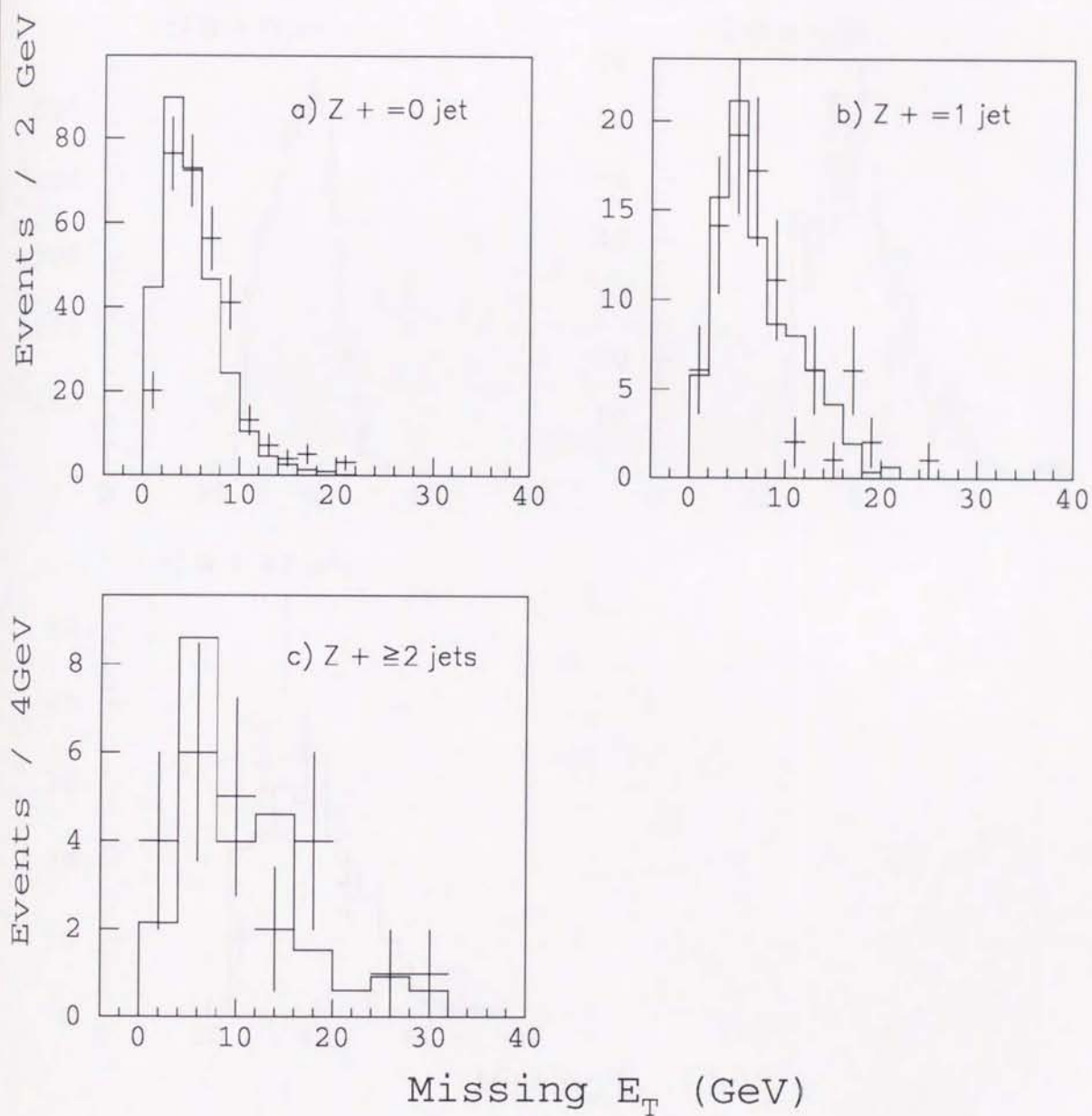


Figure 6.8: Distributions of the missing transverse energy of  $Z \rightarrow ee$  events. The histogram is the Monte Carlo prediction and the overlay is from data: a)  $Z + 0$  jet, b)  $Z + 1$  jet and c)  $Z + \geq 2$  jets.



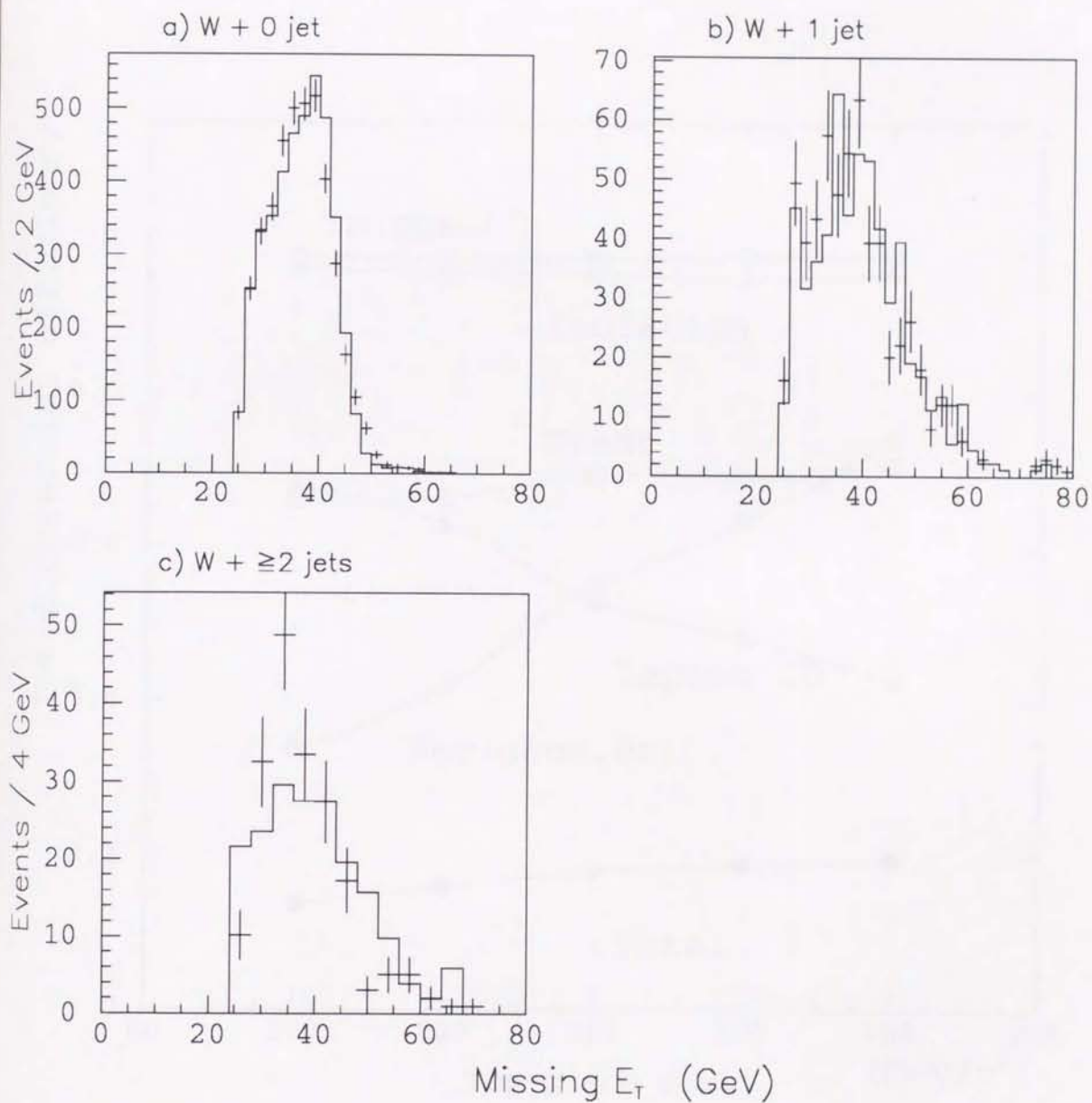


Figure 6.9: Distributions of the missing transverse energy of  $W \rightarrow e\nu$  events. The histogram is the Monte Carlo prediction and the overlay is from data: a)  $W + 0$  jet, b)  $W + 1$  jet, c)  $W + \geq 2$  jets.

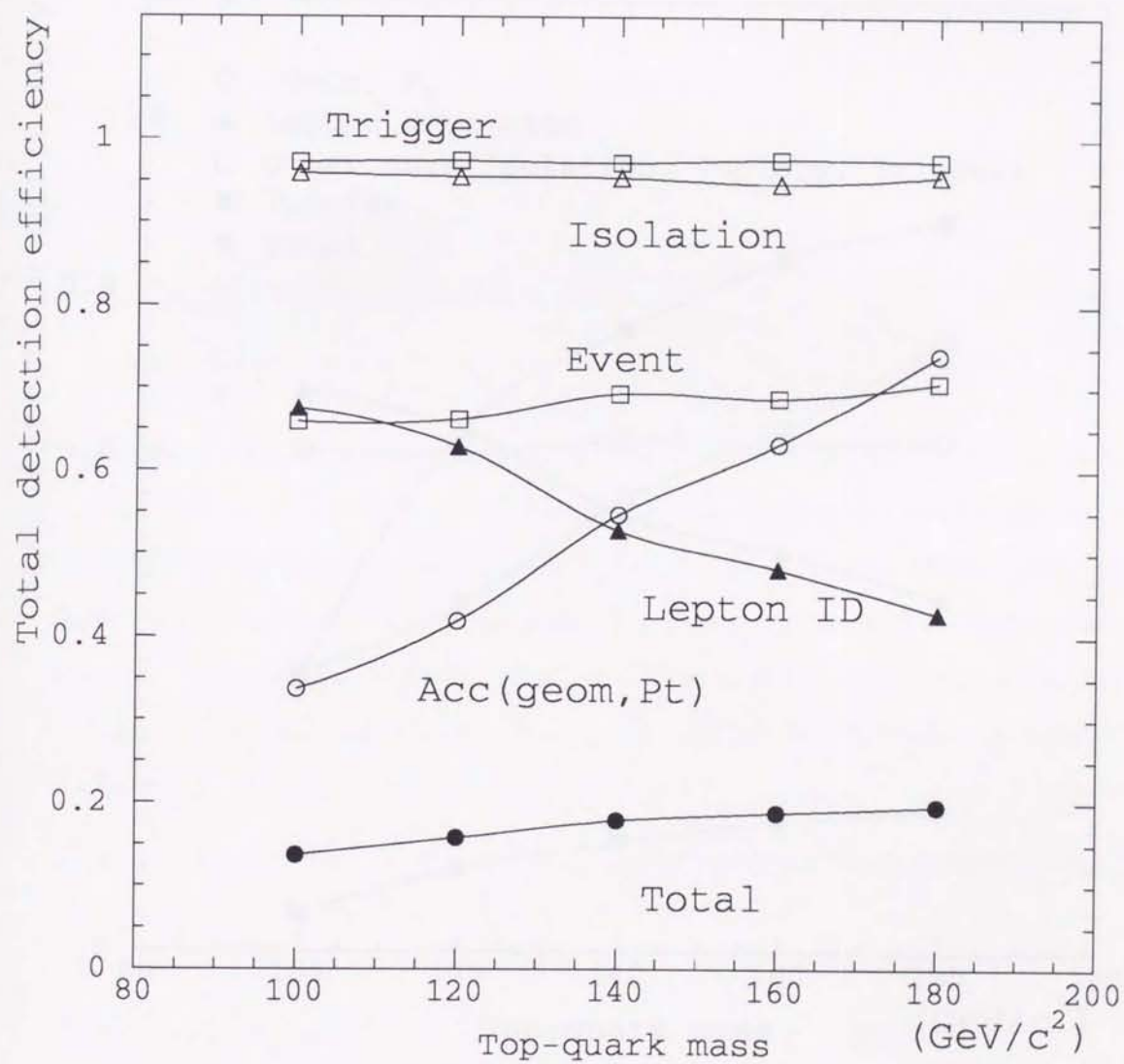


Figure 6.10: Dilepton efficiency as a function of top quark mass without the two-jet cut



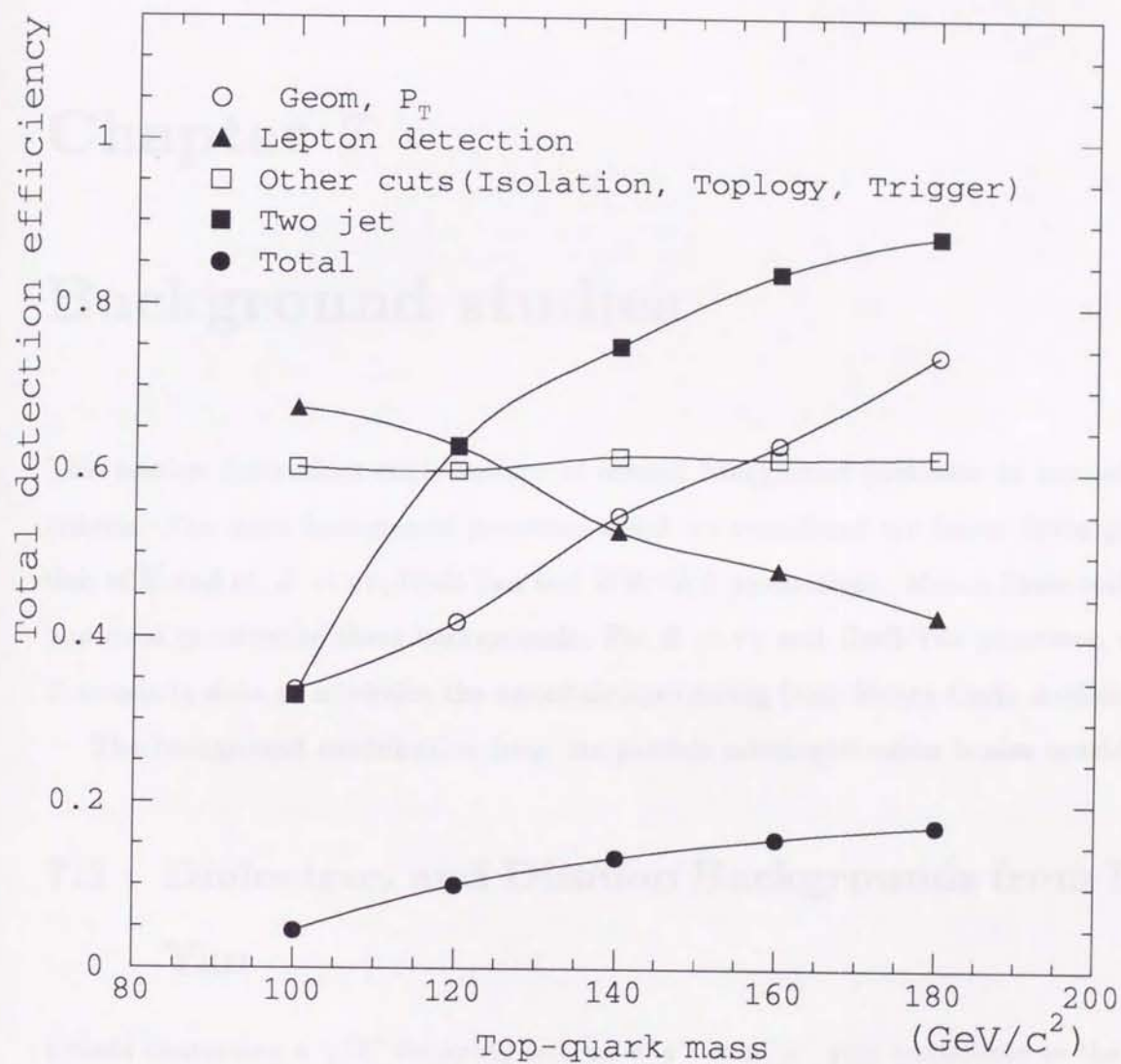


Figure 6.11: Dilepton efficiency as a function of top quark mass with the two-jet cut. The efficiencies for isolation, event topology cut and trigger are combined in the plot.

## Chapter 7

### Background studies

This section determines contributions of several background processes to our selection criteria. The main background processes which we considered are heavy flavor production of  $b\bar{b}$  and  $c\bar{c}$ ,  $Z \rightarrow \tau\tau$ , Drell-Yan and WW/WZ productions. Monte Carlo technique was used to estimate these backgrounds. For  $Z \rightarrow \tau\tau$  and Drell-Yan processes, we use  $Z$  events in data to minimize the uncertainties coming from Monte Carlo modeling.

The background contribution from the particle misidentification is also considered.

#### 7.1 Dielectron and Dimuon Backgrounds from Drell-Yan

Events containing a  $\gamma/Z^0$  decaying into an  $e^+e^-$  or  $\mu^+\mu^-$  pair contribute to the background to the top signal. Although events in the  $Z$  mass window between 75 and 105 GeV/ $c^2$  are explicitly removed from the signal region, Drell-Yan continuum events outside the window are potential backgrounds.

We use the observed  $Z^0 \rightarrow ee$ , and  $\mu\mu$  distributions to estimate the background from the continuum. Since the modeling of the tail of the  $P_T$  distribution is important, it is desirable to be independent of the Monte Carlo prediction. Our initial assumption is that the  $P_T^{\gamma, Z^0}$  distributions inside and near the  $Z^0$  region are similar. Figure 7.1 shows



Cut	Number of Events	Fraction
a) Z events	1151	100%
b) $E_T$ (uncorr) > 20GeV	32	2.8%
c) $E_T$ (corr) > 20GeV	27	2.3%
d) $E_T$ (uncorr) > 25GeV	16	1.4%
e) $E_T$ (corr) > 25GeV	9	0.8%
f) e) + $\Delta\phi(E_T, \text{jet})$ cut	4	0.3%
g) f) + $\Delta\phi(E_T, l)$ cut	3	0.3%
h) g) + 1 or more jets w/ $E_T > 10$	3	0.3%
i) g) + 2 or more jets w/ $E_T > 10$	1	0.1%

Table 7.1: Cut rejections. Each line is an independent cut.

the  $P_T^{\gamma, Z^0}$  distribution from ISAJET Monte Carlo<sup>1</sup> for near Z mass peak ( $75 < M_{l+l-}$  or  $105 < M_{l+l-}$ ) and inside Z mass region. ISAJET Monte Carlo predicts that there is a slight stiffening with increasing mass in the  $P_T^{\gamma, Z}$  which could lead to an overestimate of the background. When looking at  $P_T^{\gamma, Z}$  in data, it turns out that the  $P_T^{\gamma, Z}$  distribution has no mass dependence inside and outside Z mass region as shown in Figure 7.2, and our assumption is verified. We also note that the ISAJET Monte Carlo does not reproduce the jet multiplicity in Z events as shown in Figure 7.3. For these reasons, Drell-Yan background is estimated from Z events in data rather than using Monte Carlo. The method consists of (1) the determination of the rejection factors, which are applied to the Drell-Yan events outside the Z-window, for the missing  $E_T$  and jet cuts obtained from Z events; followed by (2) applying a small Monte Carlo correction to account for the mass dependence of the  $P_T$  and jet activity.

We exploited in section 5.6 that both the magnitude and direction of the missing  $E_T$  are the useful variables. We require that the missing  $E_T$  must be greater than 25 GeV, and also that the direction of the missing  $E_T$  must be separated from a jet by more than  $20^\circ$ , if the missing  $E_T$  is less than 50 GeV. Table 7.1 summarizes how the events inside Z mass region (1151 events) are reduced by each selection cut. In the table, fraction

<sup>1</sup>We have used version 6.36 of ISAJET Monte Carlo to generate the Drell-Yan process.

$M^H(\text{GeV})$	$P_T > 15\text{GeV}$ ( $\times 10^{-2}$ )	$P_T > 20\text{GeV}$ ( $\times 10^{-2}$ )	$P_T > 30\text{GeV}$ ( $\times 10^{-3}$ )
40.0	1.832	0.992	2.824
60.0	2.500	1.184	3.947
80.0	3.133	1.533	5.533
100.0	3.333	1.594	5.217
120.0	3.889	1.944	5.833
200.0	5.6		
300.0	8.5		

Table 7.2: Efficiencies of having two or more jets with different parton  $P_T$  threshold with Drell-Yan masses.

of passing different missing  $E_T$  cuts are shown and the missing  $E_T$  corrected for jets gives better rejection by a factor of two in case of the missing  $E_T > 25$  GeV. The latter cut helps reduce Drell-Yan background since the large missing  $E_T$  often arises from mismeasurement of hadronic jets.. The definition of the cut was chosen from looking at Figure 5.9 (a) and (b) for  $Z + 1$  jet events. Also shown in the table is the rejection factor for the jet requirement.

Next, the missing  $E_T$  and jet rejection factors obtained from  $Z$  events are corrected for mass dependence due to small changes in  $P_T$  and jet activity. We use two-jet cut efficiencies as a function of mass from a boson+2 jet matrix element Monte Carlo [43]. Table 7.2 tabulates the fraction of  $\gamma/Z^0$  events with two jets of  $P_T$  larger than the indicated value. Note that these are parton  $P_T$ 's. The 15 GeV column corresponds to 10 GeV jets before correction. We find that for our cuts, using the jet activity from  $Z^0$  events and assigning it to events outside the  $Z^0$  mass window requires a correction factor<sup>2</sup> of 0.87. Even though we only use the mass dependence, and not the absolute prediction of Mangano's boson + 2 jet matrix element Monte Carlo, it is interesting to

<sup>2</sup>Using the first column of Table 7.2, we calculate the correction factor as follows. For a 20 GeV lepton  $P_T$  cut, 88 events have a mass less than 75 GeV and the average mass for these events is 56 GeV which corresponds to  $\epsilon_1 = 2.35\%$ , 35 events have a mass above 105 GeV and the average mass for these events is 133 GeV which corresponds to  $\epsilon_3 = 4.1\%$ , and events inside  $Z$  mass region correspond to  $\epsilon_2 = 3.2\%$ . So  $\epsilon_1 : \epsilon_2 : \epsilon_3 = 0.7 : 1.0 : 1.3$  and the correction is  $(88 \times 0.7 + 35 \times 1.3)/(88 + 35) = 0.87$ .



Lepton $P_T$ cut	Before two-jet	$E_T^{jet} > 10$ GeV
(15,15)	$0.46 \pm 0.27$	$0.15 \pm 0.15$
(20,20)	$0.28 \pm 0.17$	$0.10 \pm 0.10$

Table 7.3: Number of events expected from Drell-Yan background.

note that the values predicted are somewhat low. In fact, only about 3.2% of  $Z$  events are predicted to have two jets with  $P_T > 15$  GeV at the generator level. After simulation and reconstruction this would translate into 2% or less for an uncorrected jet threshold of 10 GeV, to be compared with  $4.1 \pm 0.6\%$  in  $Z$  data.

The backgrounds before the two-jet cut are based on the three events left in our selection criteria. Only one of these events satisfies the two-jet requirement. The numbers of events expected from the Drell-Yan background in  $21.4 \text{ pb}^{-1}$  are listed in Table 7.3. for different choices of  $P_T$  cut and two-jet cut. The correction factor is applied.

After the signal cuts, including the two-jet cut, there is one event in the  $Z$ -region. When scaled back, this gives a background expectation of  $0.10 \pm 0.10$  events in the top dilepton signal region.

## 7.2 $Z^0 \rightarrow \tau\tau$

Rather than using a Monte Carlo to estimate the  $Z^0 \rightarrow \tau\tau$  background, we have used our data sample of 1113  $\gamma/Z^0 \rightarrow ee$  events. A sample of  $Z \rightarrow \tau\tau$  [44] was simulated as follows: In each event we remove the two electrons from the event and then replace each electron with a  $\tau$  which has the same momenta and energy as the electron removed. The  $\tau$ 's are then decayed semileptonically and simulated with the CDF detector simulation. Finally we merge the reconstructed  $\tau$ 's to the underlying event which is the original event with the two electron removed. We repeated this procedure 80 times for 1113 events to get a better statistics.

ISAJET Monte Carlo together with a simulation of the CDF detector was used to

Cut	Mass window	$\cancel{E}_T$	Two-jet
Our sample	0.89	0.15	0.31
ISAJET QTW=0	0.97	0.11	0.67
ISAJET QTW=3-200	0.93	0.06	0.67
ISAJET QTW=7-200	0.96	0.11	0.69

Table 7.4: Event topology cut efficiencies for the  $Z^0 \rightarrow \tau\tau$  background with a (20,20)  $P_T$  cut.

Lepton $P_T$	$E_T^{\text{jet}}$	$e\mu$	$ee, \mu\mu$	Total
20 GeV		$0.22 \pm 0.04$	$0.20 \pm 0.04$	$0.42 \pm 0.08$
20 GeV	>10 GeV	$0.07 \pm 0.02$	$0.06 \pm 0.02$	$0.13 \pm 0.04$
15 GeV		$0.56 \pm 0.08$	$0.55 \pm 0.07$	$1.11 \pm 0.15$
15 GeV	>10 GeV	$0.17 \pm 0.04$	$0.17 \pm 0.04$	$0.34 \pm 0.07$

Table 7.5: Number of events expected from the  $Z \rightarrow \tau\tau$  background in  $21.4 \text{ pb}^{-1}$  with different lepton  $P_T$ , and with and without the two-jet requirement. Errors are statistical only.



generate three set of samples with different values of the ISAJET parameter QTW<sup>3</sup> which governs the transverse momentum of the Z. These samples were used for comparison with our results.

The event topology cut efficiencies extracted from these simulation sample are given in table 7.4. In order to reduce the  $Z \rightarrow \tau\tau$  background, we have developed the similar cut as used for the Drell-Yan process. As discussed in Section 5.6, the missing  $E_T$  direction must be more than  $20^\circ$  away from a lepton, since it is expected to be aligned with one of leptons as illustrated in Figure 5.9 (a) and (b). In addition, if we require two or more jets, this background can be further reduced by a factor of three or more. The fractions are shown in Table 7.4.

The overall yields were normalized by taking the  $Z \rightarrow \tau\tau$  cross section to be equal to the  $Z \rightarrow ee$  cross section measured at CDF [45], and a branching fraction of the  $\tau$  pair into dileptons  $B = (0.178 \times 2)^2 = 0.127$ . The number of events we expect in  $21.4 \text{ pb}^{-1}$  is given in table 7.5.

### 7.3 Background from WW and WZ

The detection efficiency was calculated in the same way as was done for the  $t\bar{t}$  signal, which is described in Chapter 6. As before, ISAJET Monte Carlo generator together with a simulation of CDF detector was used to determine the geometrical and kinematical acceptance, the efficiency of the lepton isolation cuts, and the efficiency of the combined missing  $E_T$ , invariant mass, and two-jet cuts. We used lepton identification efficiencies from Z and trigger efficiencies measured in data collected with independent triggers. These efficiencies are shown in Table 7.6

The cross sections used to normalize the diboson expectations are taken from Ref-

<sup>3</sup>The ISAJET parameter QTW selects Z Pt limits for Z and  $\gamma$ . A choice of QTW equal to 0 would select lowest order Drell Yan process with the parent  $\gamma$  or Z Pt originating from initial state radiation. A choice of a non-zero QTW select next-to-leading order Drell-Yan processes to generate the parent  $\gamma$  or Z  $P_T$ .

Efficiency (%)	Geom. $P_T$	ID	Isol	Event	Two-jet	Trigger	Total( $\epsilon_{\text{Total}}$ )
WW	26.3	98.9	76.3	60.5	13.1	97.1	$1.5 \pm 0.6$
WZ	25.3	99.4	76.3	13.2	13.1	97.3	$1.3 \pm 0.5$

Table 7.6: Detection efficiency for WW and WZ with a two-jet requirement

Lepton $P_T$ thresh.	Jet $E_T$ thresh.	$e\mu$	$ee, \mu\mu$	Total
20 GeV	None	$0.74 \pm 0.22$	$0.43 \pm 0.13$	$1.17 \pm 0.35$
20 GeV	10 GeV	$0.097 \pm 0.041$	$0.057 \pm 0.024$	$0.15 \pm 0.06$
15 GeV	None	$0.86 \pm 0.26$	$0.51 \pm 0.15$	$1.37 \pm 0.41$
15 GeV	10 GeV	$0.11 \pm 0.05$	$0.07 \pm 0.03$	$0.18 \pm 0.08$

Table 7.7: Number of WW events expected in  $21.4 \text{ pb}^{-1}$ .

erence [47]: 9.5 pb for WW and 2.5 for WZ. We assigned a 30% of uncertainty due to theoretical uncertainties in the cross section. The cross section of background events,  $\sigma_{\text{obs}}$ , is given by:

$$\sigma_{\text{obs}} = \sigma_{\text{Theory}} \times Br \times \epsilon_{\text{Total}},$$

where  $\sigma_{\text{Theory}}$  is the theoretical cross section and  $\epsilon_{\text{Total}}$  is the total detection efficiency listed in Table 7.6.

Contributions of WW background to the selection criteria are  $1.17 \pm 0.35$  and  $0.15 \pm 0.06$  events before and after the two-jet requirement. The number of WW background events expected for different lepton  $P_T$  and the jet  $E_T$  is summarized in Table 7.7.

Our estimation using ISAJET Monte Carlo predicts that the 13 % of WW events contain two or more jets with the observed  $E_T$  with 10 GeV. Since the ISAJET prescription for gluon radiation is essentially unconfirmed, we checked the two-jet rejection factor by examining a matrix element Monte Carlo [43], as was done for the Drell-Yan background. It can be seen from Table 7.2 that the efficiency of the two-jet requirement should be approximately 2.7 times higher at typical WW subprocess energies of 300 GeV than at subprocess energies of 90 GeV. We can use this Monte Carlo shape for the mass



variation and we can use Z data at 90 GeV for calibration. The data show that  $4.1 \pm 0.6$  % of Z events have two jets above 10 GeV. Therefore the two-jet cut efficiency for WW can be estimated as  $2.7 \times 4.1\% = 11\%$ . Since the agreement between this estimate and ISAJET is good, we simply use the ISAJET two-jet cut efficiency and assign a 30% systematic uncertainty on it.

## 7.4 Background from heavy flavor production ( $b\bar{b}$ )

Heavy flavor backgrounds, mostly  $b\bar{b}$ , have been studied using ISAJET Monte Carlo program to model the production processes, together with the CLEO Monte Carlo to model  $b$  quark decays, as briefly described in section 3.1. An integrated luminosity of  $67.5 \text{ pb}^{-1}$  of  $b\bar{b}$  Monte Carlo samples have been generated for studies of high  $P_T$  leptons from B decays as a background in top searches [46]. Basic idea to estimate  $b\bar{b}$  backgrounds is that we obtain the rejection factor due to event topology and two jet requirement using a sample of dilepton events with  $P_T > 15 \text{ GeV}/c$ , which has a higher statistics, and that the number of events with  $P_T > 20 \text{ GeV}/c$  is used to determine the normalization.

The reduction factors for each cuts was determined as follows. At first, the reduction factor for the missing  $E_T$  requirement ( $> 25 \text{ GeV}$ ) is  $0.14 \pm 0.06$ . The correlation between  $\cancel{E}_T$  and lepton  $P_T$  was checked by varying the  $P_T$  of one of the leptons to 17, 19, and 21  $\text{GeV}/c$ . A 30% change was observed and this contributes the major part of the uncertainty assigned to the rejection factor for  $\cancel{E}_T$ . The azimuthal angle requirement reduce the events further by  $0.56 \pm 0.12$ . No strong correlation was observed between the lepton  $P_T$  and the azimuthal angle separation between the missing  $E_T$  and a closest lepton (or jet). Another additional rejection was obtained by requiring two or more jets in the events and this was  $0.43 \pm 0.10$ .

To determine the number for  $21.4 \text{ pb}^{-1}$  of data, we choose to normalize the number of  $e\mu$  events that pass the (15, 5) cuts with no isolation requirement in  $16.3 \text{ pb}^{-1}$  of Monte Carlo and  $13.1 \text{ pb}^{-1}$  of data. Such data are dominated by  $e\mu$  events from  $b\bar{b}$

sources and hence they provide a better normalization than using the Monte Carlo cross sections. In doing this Monte Carlo to data luminosity normalization, we are taking into account possible effects not considered by the Monte Carlo, such as trigger efficiencies. The uncertainty on lepton ID efficiencies is reduced to variations of data to Monte Carlo ratio as a function of lepton  $P_T$ . There are 184  $e\mu$  events found in  $13.1 \text{ pb}^{-1}$  of data and 196 events in  $16.3 \text{ pb}^{-1}$  of Monte Carlo. In last run's low  $P_T$   $e\mu$  analysis, background in the data was determined to be  $20 \pm 10\%$ . At higher  $P_T$ , the background fraction should be lower since QCD process in general have a softer  $P_T$  spectrum than heavyflavor production. To be conservative, we use a background fraction of  $20 \pm 20\%$  in this study. The normalization factor is therefore  $0.94 \pm 0.19$ . This factor must be divided by 90% to account for the inefficiency of the cut in the Monte Carlo generation on b quark  $P_T$  of 25 GeV, which keeps 90% of the daughter leptons with  $P_T \geq 15 \text{ GeV}$ . Combining this with the above background estimate, we obtain the background expected in  $21.4 \text{ pb}^{-1}$  of data as given in the following tables.

The number of background events expected in our data sample is given in table 7.8.

	$P_T$ cut at (15,15)	$P_T$ cut at (20,20)
$P_T$ , Iso, Opp-Sgn Cuts	$24 \pm 5$	$2.8 \pm 0.6$
Additional Missing $E_T$ Cut	$1.91 \pm 0.96$	$0.22 \pm 0.12$
Additional Two-Jet Cut	$0.83 \pm 0.43$	$0.10 \pm 0.05$

Table 7.8: Number of events expected from  $b\bar{b}$  background for a run of  $21.4 \text{ pb}^{-1}$ .

## 7.5 $Z^0 \rightarrow b\bar{b}$

ISAJET Monte Carlo generator together with the CDF detector simulation was used to estimate the  $Z^0 \rightarrow b\bar{b}$  background. The total of 740 K were generated corresponding to an integrated luminosity of  $841 \text{ pb}^{-1}$ . No events were found in the signal region when



the nominal cuts (no two jet cut) were applied. This gives a limit of less than 0.025 events for a run of  $21.4 \text{ pb}^{-1}$ . If the two jet cut reduces this by a factor of 3, as it does for  $Z^0 \rightarrow \tau\tau^4$ , then this background is less than 0.01 events. We therefore do not consider this background further.

## 7.6 $Wb\bar{b}, Wc\bar{c}$

We have looked at the background from production of W's in association with heavy quark pairs ( $Wb\bar{b}, Wc\bar{c}$ ) via the gluon splitting processes. An integrated luminosity of  $3700 \text{ pb}^{-1}$  of events were generated with the leading-order matrix element calculation described in [48] and the HERWIG Monte Carlo generator [49] together with the CDF detector simulation. This sample was used to compute the contribution of these events to the signal region. The cross section, according to ref [48], is 5.4pb. Figure 7.5 shows the lepton  $P_T$  distribution from the  $Wb\bar{b}$  events. It is obvious that a leading  $P_T$  lepton comes from the decay of W and that a second one with soft  $P_T$  comes from the decay of  $b$ . Most of  $Wb\bar{b}$  backgrounds are rejected using large  $P_T$ .

No events survived our selection cuts without the two jet cut. This gives us the limit of the number of events expected in  $21.4 \text{ pb}^{-1}$  and it is less than 0.006. The sample contains only events with the decay of W into the central electron. So, we need to take into account events of the W decay into plug electrons and muons. Using W Monte Carlo, the ratios of W decaying into central electron(CE), plug electron(PE) and muon(MU) were calculated to be  $\text{CE} : \text{PE} : \text{MU} = 1 : 0.07 : 0.80$ . Thus we would expect less than 0.011  $Wb\bar{b}$  events ( $= 0.006 \times (1+0.07+0.80)$ ) We conclude that this background contribution to the signal region is negligibly small.

---

<sup>4</sup>31% of events have two or more jets as seen in section 7.2

## 7.7 Fake dilepton background

We consider the "fake dilepton" background: (1) events from ordinary QCD jet or  $W$ +jets with at least one misidentified lepton<sup>5</sup>, (2) conversion electron, and (3) muon from hadronic decay in flight. These events may also have large missing  $E_T$ , and maybe difficult to distinguish kinematically from top events. The procedure employed for estimating the background is to a) estimate the probability of a jet to fake a lepton, b) find how many events with lepton+jet would be in the signal region if the jet faked a lepton, and c) multiply the number of events found in b) by the fake rates found in a).

The "fake probability" per lepton is obtained from a background sample of events collected with a jet trigger with an  $E_T$  threshold for the jet of 20 GeV. Central and plug electromagnetic clusters, and 1muon' candidate tracks are selected with minimal cuts. The probability to pass the standard electron and muon identification is then measured. The fake rates are determined separately for central isolated and non-isolated tracks or clusters. This separation is necessary because in the dilepton selection, all events are required to have at least one central(CE, MU or MI) isolated lepton. Fake rates are tabulated in Table 7.9.

When looking through the jet data for jets which fake leptons, we will also find some real leptons from  $b$  decay. The effect of this is to increase the fake probability we would get from light quark jets alone. It is desirable to use fake probabilities which have the contributions from  $b$  quarks subtracted. To accomplish this, we refer to a study [50] which estimates the  $b$  fraction of ELES banks which pass our tight central electron cuts to be  $46\% \pm 8\%$ . We use this number both to scale back the fake probabilities for central electrons, and also as an indicator of the number of CMUO banks we should expect from  $b$ 's in the jet data. We multiply the number of central electrons we expect from  $b$  decay by the ratio of acceptances for CMUO muons and central electrons, and use this as our estimate of the number of CMUO muons we expect from  $b$  in the jet data. We do not

---

<sup>5</sup>One of the partons fragmenting into an electromagnetic rich jet is identified as an electron (or stiff track, for muons)



Type	Iso?	$P_{fake}$ before b subtraction	$P_{fake}$ after b subtraction
CE(tight)	yes	$.075 \pm .028$	$.059 \pm .028$
CE(tight)	no	$.035 \pm .011$	$.012 + .013 - .012$
CE(loose)	yes	$.150 \pm .041$	$.132 \pm .040$
CE(loose)	no	$.063 \pm .015$	$.038 \pm .017$
MU	yes	$.121 \pm .067$	$.111 \pm .066$
MU	no	$.009 \pm .007$	$.004 + .007 - .004$
MX	yes	$.333 \pm .219$	$.310 + .315 - .310$
MX	no	$.071 \pm .055$	$.052 + .055 - .052$
MI	yes	$.048 \pm .029$	$.048 \pm .029$
MI	no	$<.013$	$<.013$
PE	yes	$<.013$	$<.013$

Table 7.9: Fake rates for each lepton category ,before and after b subtraction.

perform the b subtraction for plug electrons or CMIO muons because we expect the calorimeter isolation cuts on these categories to reduce the b contamination. We don't apply the 2 jet cut and opposite sign cuts when counting events which have one good lepton and one lepton bank passing the relaxed cuts. Assuming the relaxed lepton track is from a hadron, we expect its sign to be uncorrelated with the sign of the good lepton. We therefore count both opposite sign and same sign events, and divide by 2 to get the expectation for opposite sign alone. There are 15 opposite sign events and 10 same sign events. The statistics suffer badly when the 2 jet cut is applied. We have looked at W+jet events to find the rejection factor of the 2 jet cut after the other topology cuts are applied, and we use this rejection factor to obtain the number of events we expect in the signal region. Tables 7.10 and 7.11 show the expected numbers of background events for 15-15 and 20-20 lepton  $Pt$  cuts, before and after the 2-jet cut is applied.

Fake Background in 21.4 pb <sup>-1</sup> Before 2-jet Cut		
Category	15 GeV Lepton $P_T$ Cuts	20 GeV Lepton $P_T$ Cuts
CE-CE	.339±.168	.169±.111
CE-PE	<.034	<.033
MU-MU	.140+.257-.140	.073+.238-.073
MU-MI	.091±.064	.022+.038-.022
CE-MU	.385±.300	.111+.240-.111
CE-MI	.148±.102	.061±.051
PE-MU	<.023	<.023
PE-MI	<.028	<.028
TOTAL	1.10±.41	.436±.292
SS Data	1	0

Table 7.10: Expected background due to hadron misidentification for 15 GeV and 20 GeV lepton  $P_T$  cuts. All cuts except for the 2-jet cut are applied. Also shown are the number of same-sign events found in the data for these cuts.

Fake Background in 21.4 pb <sup>-1</sup> After 2-jet Cut		
Category	15 GeV Lepton $P_T$ Cuts	20 GeV Lepton $P_T$ Cuts
CE-CE	.056±.028	.028±.018
CE-PE	<.006	<.005
MU-MU	.023+.042-.023	.012+.039-.012
MU-MI	.015±.010	.004+.006-.004
CE-MU	.063±.049	.018+.039-.018
CE-MI	.024±.017	.010±.008
PE-MU	<.038	<.038
PE-MI	<.005	<.005
TOTAL	.181±.068	.072±.048
SS Data	0	0

Table 7.11: Expected background due to hadron misidentification for 15 GeV and 20 GeV lepton  $P_T$  cuts after the 2-jet cut is applied. Also shown are the number of same-sign events found in the data for these cuts.



## 7.8 Background Summary and Checks

The number of background events contributed to our selection criteria is summarized in table 7.12. The total background is  $0.56 \pm 0.14$  events after all cuts and the data yield is 2 events. When releasing the two-jet requirement, we expect  $2.5 \pm 0.5$  events and observe (the same) 2 events.

A better statistics check was done in the  $e\mu$  channel by lowering the  $P_T$  threshold to 15 GeV and comparing the background prediction with the number of events observed in the data after isolation cuts. The dilepton+0 jet sample should be dominated by background. Our ability to calculate the size of this background is an important check on the analysis. Our results are shown in table 7.13. There is agreement between the background prediction and the data. As an additional check of the reliability of our background predictions, we compared the number of same-sign events observed in the data with a  $P_T$  threshold of 15 GeV after isolation cuts, with predictions from fakes and  $b\bar{b}$ . We find that the sum of the  $b\bar{b}$  and fake predictions is  $19.8 \pm 4.0$ , compared to 10 same-sign events observed in the data. Again the agreement is good, although there is room to believe that our backgrounds could be somewhat overestimated and therefore conservative.

	Without $\cancel{E}_T$ and two-jet cuts	Without two-jet cut	All cuts
<i><math>e\mu</math></i>			
WW	1.1	0.74	$0.10 \pm 0.04$
$Z \rightarrow \tau\tau$	3.7	0.22	$0.07 \pm 0.02$
$b\bar{b}$	1.2	0.10	$0.04 \pm 0.03$
Fake	1.2	0.19	$0.03 \pm 0.03$
Total background	7.2	1.25	$0.24 \pm 0.03$
CDF data	5	2	2
<i><math>ee, \mu\mu</math></i>			
WW	0.6	0.43	$0.06 \pm 0.02$
$Z \rightarrow \tau\tau$	3.0	0.20	$0.06 \pm 0.02$
$b\bar{b}$	1.6	0.12	$0.05 \pm 0.03$
Fake	1.7	0.25	$0.04 \pm 0.03$
Drell-Yan	113	0.28	$0.10 \pm 0.10$
Total background	120	1.28	$0.31 \pm 0.11$
CDF data	120	0	0

Table 7.12: Number of background events expected  $21.4 \text{ pb}^{-1}$  and the number of events observed in the data.



$P_T > 15 \text{ GeV}/c$ , Isolation, and opp.-charge requirement	
$e\mu$	
WW	$1.2 \pm 0.4$
$Z \rightarrow \tau\tau$	$8.3 \pm 0.5$
$b\bar{b}$	$10 \pm 2$
Fake	$5.9 \pm 1.8$
Total background	$25 \pm 3$
CDF data	18

Table 7.13: Number of  $e\mu$  background events expected in  $21.4 \text{ pb}^{-1}$  and the number of opposite-charge dilepton events observed in the data after isolation cuts and a  $P_T$  threshold of  $15 \text{ GeV}/c$ .

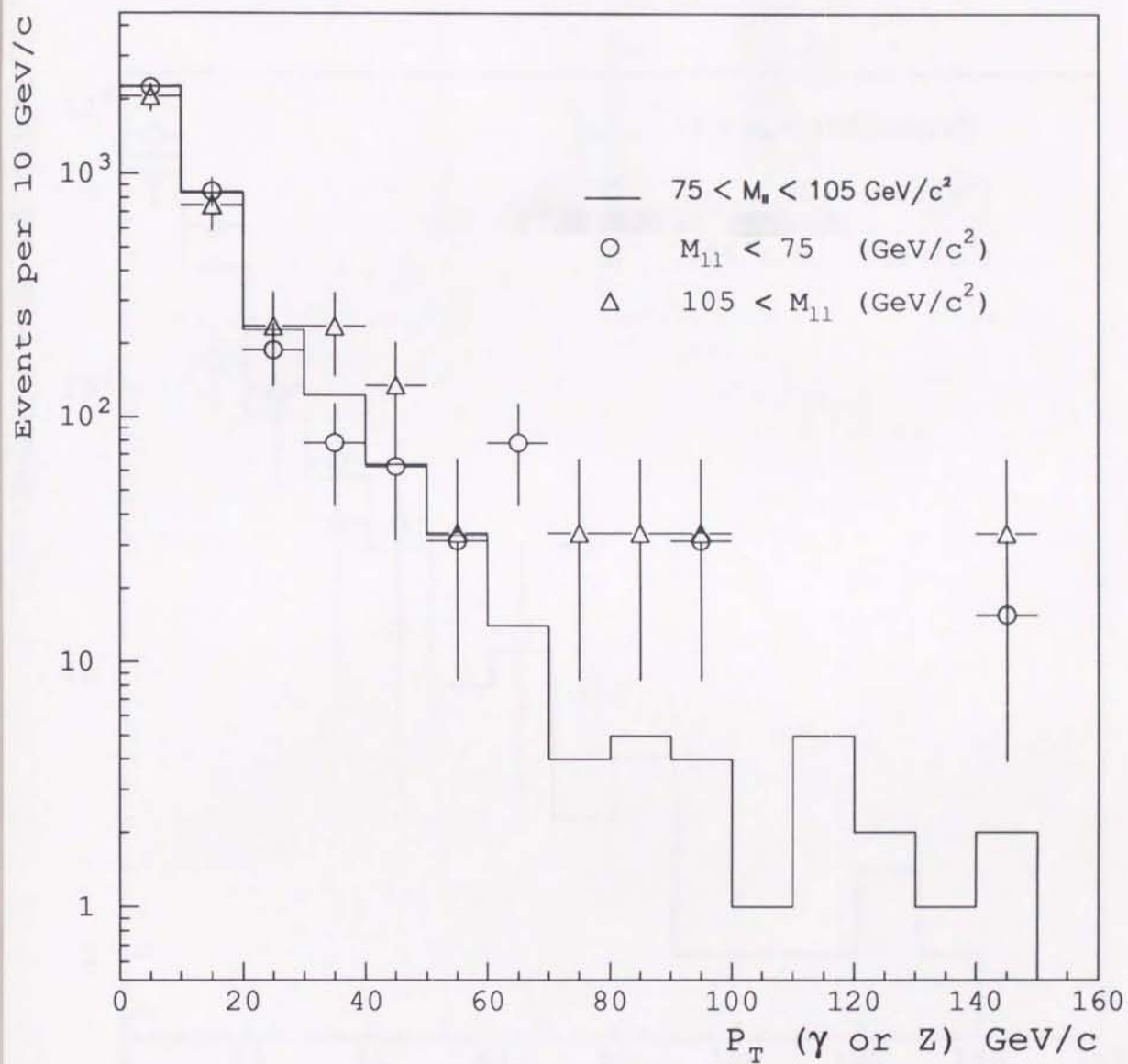


Figure 7.1: ISAJET Monte Carlo  $P_T(\gamma, Z)$  distribution in three mass region: 30-75 GeV/c, 75-105 GeV/c and above 105 GeV/c. The distributions are normalized to the number of events inside the Z mass region.



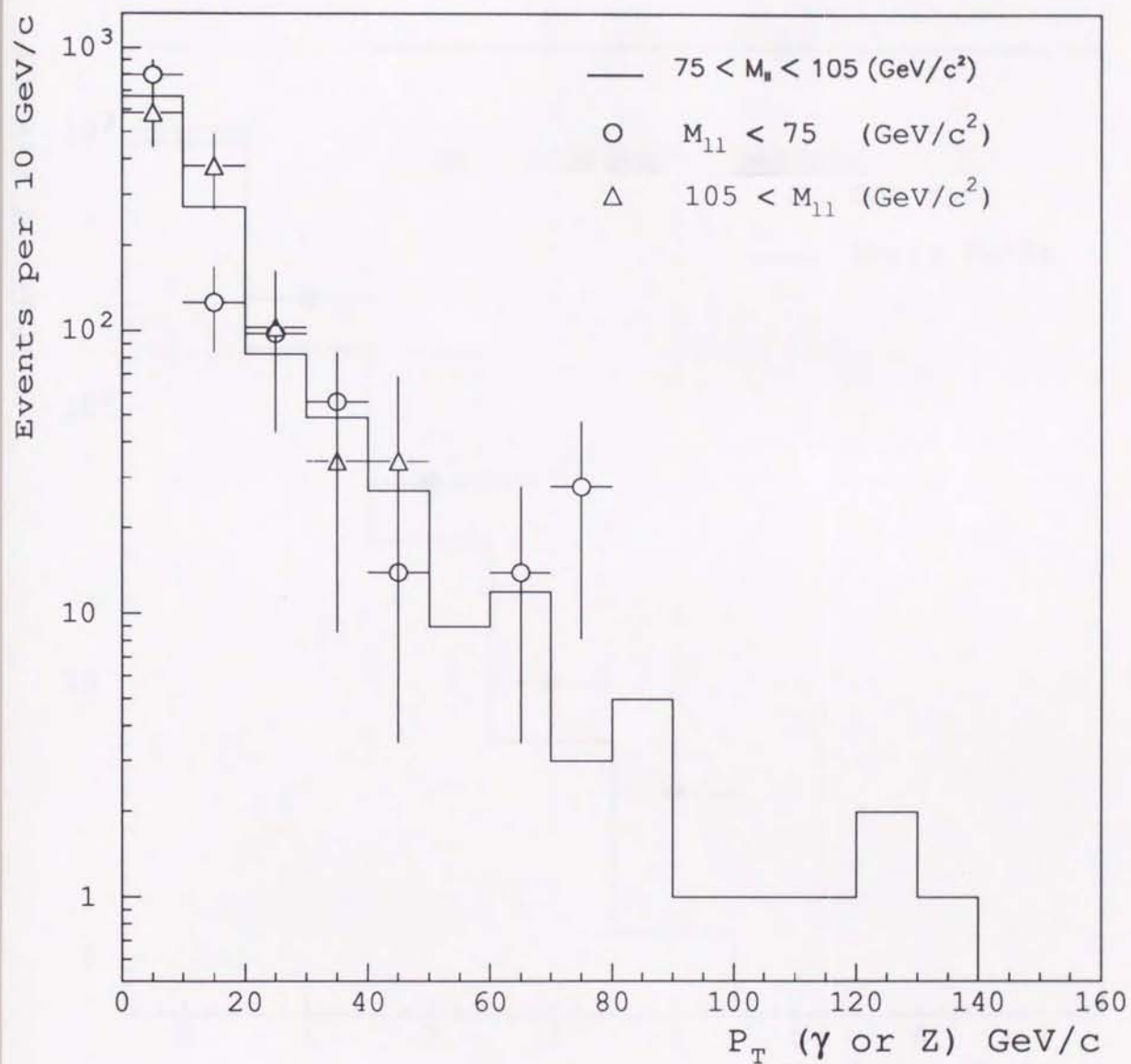


Figure 7.2:  $P_T(\gamma, Z)$  distribution from data in three mass region: 30-75 GeV/c, 75-105 GeV/c and above 105 GeV/c. The distributions are normalized to the number of events inside the Z mass region.

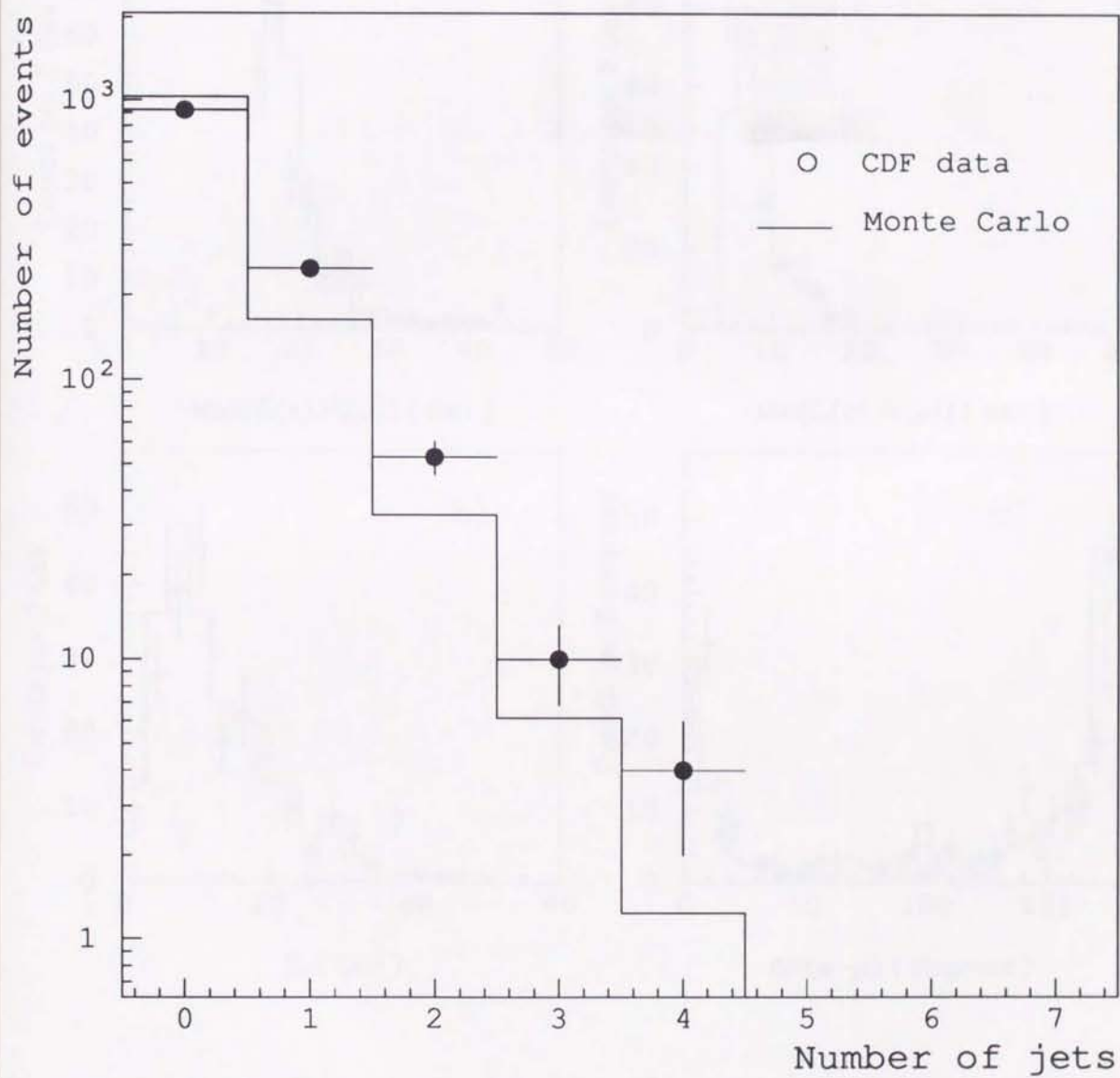


Figure 7.3: The number of jets for Z events from CDF data and Monte Carlo.



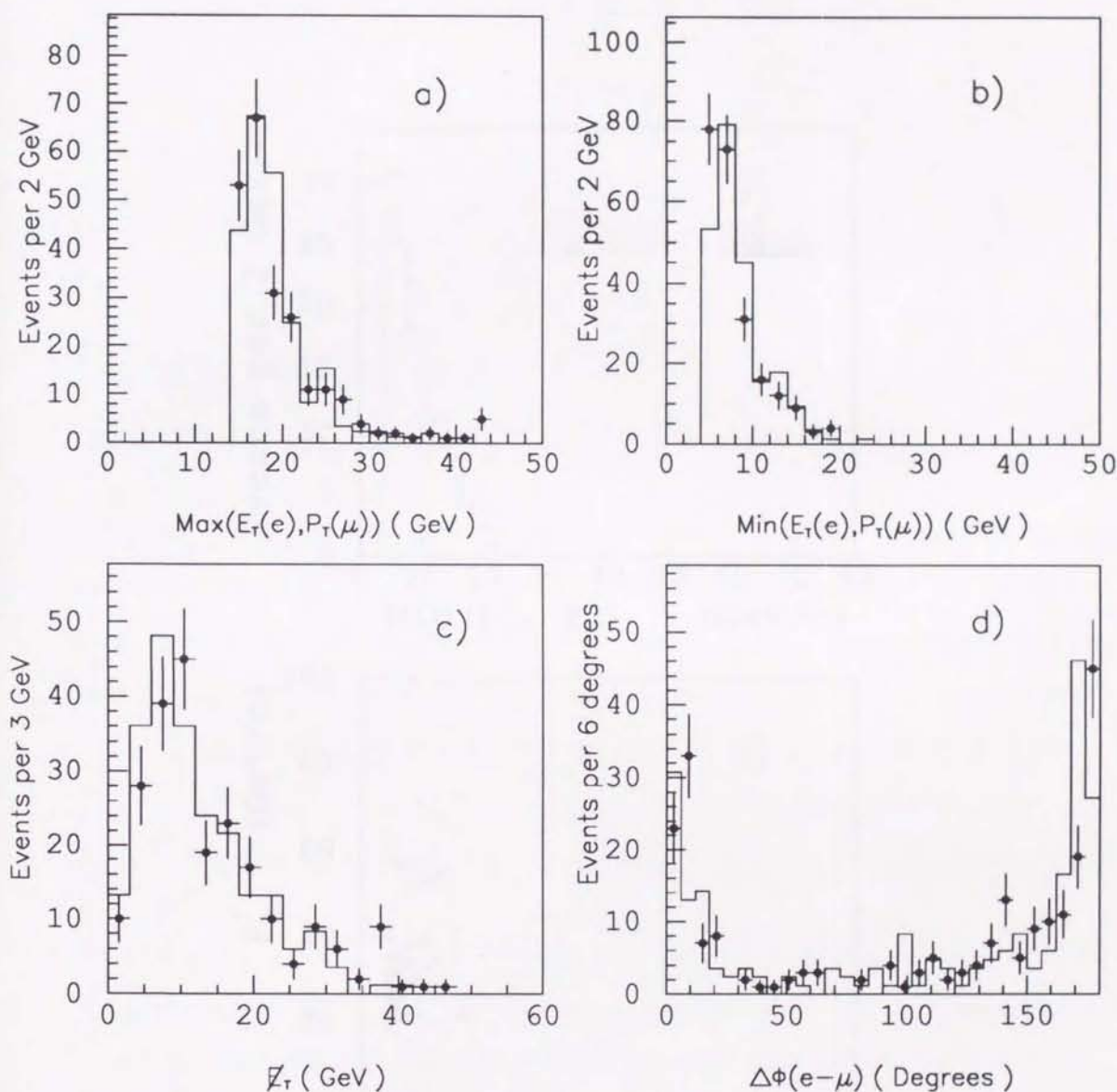


Figure 7.4: Distributions for  $e\mu$  data with  $P_T^{l_1} > 15$  GeV/ $c$  and  $P_T^{l_2} > 5$  GeV/ $c$  (points) compared to expectations from the ISAJET Monte Carlo (histograms). a)  $P_T$  spectrum of the leading lepton. b)  $P_T$  spectrum of the second lepton. c) Missing  $E_T$  distribution. d) Dilepton azimuthal angular separation.

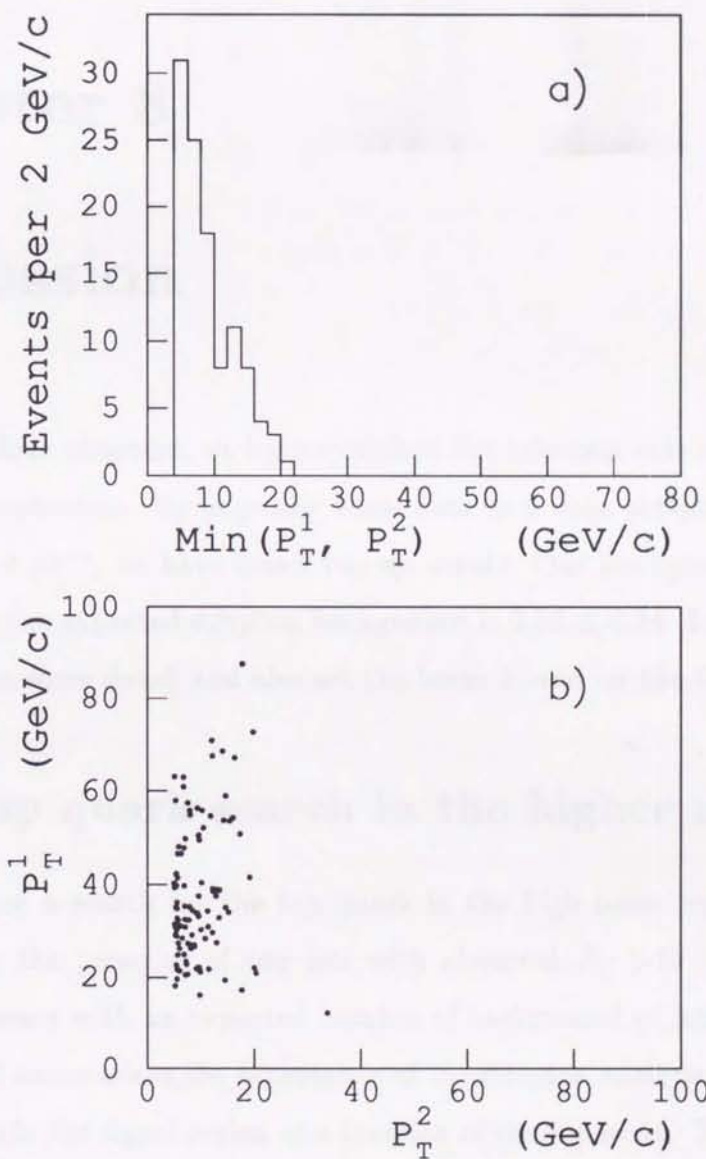


Figure 7.5:  $Wb\bar{b}$  Monte Carlo events: (a) Minimum of lepton  $P_T$ . (b)  $P_T^{l2}$  versus  $P_T^{l1}$ .



## Chapter 8

### Discussion

In the last three chapters, we have exploited the selection cuts to improve the signal to background separation. By imposing these cuts on a data sample of an integrated luminosity of  $21.4 \text{ pb}^{-1}$ , we have found two  $e\mu$  events. Our background study in Chapter 7 showed that the expected dilepton background is  $0.56 \pm 0.14$ . In this section we discuss our results in some detail and also set the lower bound on the top quark mass.

#### 8.1 Top quark search in the higher mass region

We performed a search for the top quark in the high mass region above  $120 \text{ GeV}/c^2$  by requiring the presence of two jets with observed  $E_T > 10 \text{ GeV}$ . We found two  $e\mu$  candidate events with an expected number of background of  $0.56 \pm 0.14$  events.

Table 8.2 summarizes the acceptance of the dilepton analysis and the expected number of events in the signal region as a function of the top mass. To compute the expected number of events, we used the theoretical central values with the next-to-next-leading order calculation. The uncertainties are the sum in quadrature of the statistical uncertainty on the number of observed events, the systematic uncertainty on the acceptance (a function of top mass), and the uncertainty on the luminosity (10%)

We see the excess of events over expected backgrounds. Estimation of the probability

that the expected background has fluctuated up to the number of candidate events seen or greater is 10.9 %. This is evaluated using Poisson statistics convoluted with a Gaussian smearing of the mean number of backgrounds expected.

$M_{\text{top}} \text{ (GeV/c}^2\text{)}$	100	120	140	160	180
$\sigma_{t\bar{t}}^{\text{Theory}}$	102	38.9	16.9	8.16	4.21
$\epsilon_{\text{total}} \cdot \text{Br (\%)}$	0.22	0.49	0.66	0.78	0.86
$N_{\text{expected}}$	4.9	4.1	2.4	1.4	0.8

Table 8.1: Theoretical prediction of  $t\bar{t}$  cross section from Ref [26]. Efficiency  $\times$  branching ratio and expected number of events in  $21.4 \text{ pb}^{-1}$ , as a function of top mass.

## 8.2 Low mass top search and limits on $t\bar{t}$ production

In a previous publication [7], based on a data sample of  $4.1 \text{ pb}^{-1}$  collected by CDF in 1988-89, we reported a lower bound of  $85 \text{ GeV/c}^2$  on  $M_{\text{top}}$  from the dilepton channel alone. When combined with the results from the lepton + jets, where the  $b$  was tagged through its semileptonic decay into muons, we obtained an improved limit of  $91 \text{ GeV/c}^2$  at the 95 % confidence level. In the dilepton search with the two-jet cut, we concentrate on top mass above  $120 \text{ GeV/c}^2$  where the event selection is reasonably efficient. This leaves a hole between our previously published mass limit of  $91 \text{ GeV/c}^2$  and  $120 \text{ GeV/c}^2$ . In this section we describe a search for the top quark in this relatively lower mass region and we extract a new lower bound on the top mass using the  $21.4 \text{ pb}^{-1}$  data sample from the 1992-93 run and the  $4.1 \text{ pb}^{-1}$  from the 1988-89 run. First of all, it should be noted that for top masses close to the previous lower limit of  $91 \text{ GeV/c}^2$ , the  $b$  quarks are produced near our jet  $E_T$  threshold, and hence most  $t\bar{t}$  dilepton events will not have two observable jets above  $10 \text{ GeV}$  in the calorimeter. For a search in this low mass region, we remove the two-jet requirement.



The search without the two-jet cut results in two candidate events passing our  $t\bar{t}$  selection criteria. These two events are the same as those passed the two-jet cut. With two events detected we can place upper limits on the  $t\bar{t}$  production cross section, using the theoretical calculation for this cross section. We can also derive a limit on the top quark mass.

The 95%-confidence level (C.L.) upper limits on the cross section is given by

$$\sigma_{t\bar{t}} < \frac{N_{top}}{\int \mathcal{L} dt a_{top}} \quad (8.1)$$

where  $N_{top}$  is the 95%-C.L. upper limit on the number of expected events, and  $\int \mathcal{L} dt$  is the integrated luminosity of the experiment, and  $a_{top}$  is the acceptance of our analysis to  $t\bar{t}$  events, normalized to assumed branching ratio. Since  $a_{top}$  varies slightly with the top mass, the limit on  $\sigma_{t\bar{t}}$  will also be a function of the top mass.

The systematic uncertainties in  $a_{top}$  and  $\int \mathcal{L} dt$ , which we discussed in Section 6.8, were listed in Table 6.14. The total uncertainty for the number of events predicted in data is estimated to be 13 % without the two-jet requirement. This systematic uncertainty is used as the standard deviation of a Gaussian distribution convoluted with the Poisson statistical probability. The resulting distribution is used to obtain the 95%-C.L. upper limit on the number of events expected as a function of the top mass. (The method we used to take uncertainties into account is explained in Appendix 9). Given that two events were observed and without the subtracting the backgrounds, we find an upper limit of  $N_{top}=6.54$ . (If ignoring the effects of systematic uncertainties, 6.30 would be hold.) The 95%-C.L. upper limit on is 33 pb for  $M_{top}=120$  GeV/c<sup>2</sup>.

Using the theoretical predictions for  $\sigma_{t\bar{t}}$  the limits on the cross section can be translated into a lower limit on the mass of the top quark. Figure 8.1 shows the upper limits on the  $t\bar{t}$  cross section as a function of the top mass together with the theoretical calculation of the cross section from Reference [26].

To set a lower limit on the top mass, we find the point at which the  $\sigma_{t\bar{t}}$ -limit curve crosses the lower (more conservatively) bound of the theoretical prediction. At



95% C.L. we obtain  $M_{top} > 116 \text{ GeV}/c^2$ , based on the analysis using a data sample from 1992-93 collider run alone.

We also combine the 1988-89 data sample with 1992-93 data sample. By adding in the 1988-89 data, the integrated luminosity becomes  $25.5 \text{ pb}^{-1}$ , the number of events observed remains 2, which is the same events found in this analysis using the 1992-93 data sample. One  $e\mu$  events in the previous analysis [7] fails the missing  $E_T$  requirement added to the  $e\mu$  channel in the 1992-93 analysis to reduce backgrounds expected in the larger luminosity data sample. The expected background becomes  $(2.5 \pm 0.5) + (0.5 \pm 0.3) = (3.0 \pm 0.6)$  events. To calculate upper limits with the combined 1988-89 and 1992-93 data sets, we used the following formula:

$$\sigma_{t\bar{t}}^{\text{upper limit}} = \frac{N^{\text{upper limit}}}{(\int \mathcal{L}_{89} dt \epsilon'_{89} + \int \mathcal{L}_{93} dt \epsilon_{93}) \cdot \text{Br}} \quad (8.2)$$

where  $\epsilon_{93}$  is the acceptance of the 'new' analysis with the 'new' detector, whereas  $\epsilon'_{89}$  is the acceptance of the 'new' analysis with the 'old' detector. We believe that  $\epsilon'_{89}$  is somewhat larger than  $\epsilon_{93}$ , because of the reduced 1993 muon trigger acceptance (the 1993 muon trigger requires a CMU-CMP coincidence in the  $\phi$  regions where CMP covers CMU). This only affects dimuon events (electron-muon events come in with the electron leg), so that the difference between the two acceptances should not be more than a few %. We made the conservative choice of setting  $\epsilon'_{89} = \epsilon_{93}$ ; this slightly increases the upper limits on the cross section. For each of these upper limits, we have calculated 95%-C.L. lower limits on the top mass as the intersection of the experimental upper limit with the theoretical lower limit to be  $M_{top} > 120 \text{ GeV}/c^2$ . Thus, we conclude that the top mass region between 91 and  $120 \text{ GeV}/c^2$  is excluded<sup>1</sup>. For comparison with previously published results, we use the same theoretical cross section with the next-to-leading

<sup>1</sup>The D0 Collaboration recently reported the lower bound on the top quark mass of  $131 \text{ GeV}/c^2$  at the 95%-C.L., assuming the Standard Model branching fractions. Our limit from this analysis is lower than the limit from D0 measurement, although they used the same method as this analysis, because the limit was calculated by combining four decay modes of  $t\bar{t} \rightarrow e\mu + \text{jets}, ee + \text{jets}, e + \text{jets}$  and  $\mu + \text{jets}$  in their measurement.



order calculation to obtain a lower bound on  $M_{top}$  of 115 GeV/c<sup>2</sup>.

$M_{top}$ (GeV/c <sup>2</sup> )	100	120	140	160
$\sigma_{t\bar{t}}^{Theory}$	102	38.9	16.9	8.16
$\epsilon_{total} \cdot Br$ (%)	$0.68 \pm 0.05$	$0.78 \pm 0.06$	$0.88 \pm 0.07$	$0.93 \pm 0.07$
$N_{expected}$	14.8	6.5	3.2	1.6
$\sigma_{t\bar{t}}$ (pb) at 95%-C.L.	38.3	33.3	29.5	28.2

Table 8.2: Theoretical prediction of  $t\bar{t}$  cross section from Ref [26]. Efficiency  $\times$  branching ratio and expected number of events in 21.4  $pb^{-1}$ , as a function of top mass.

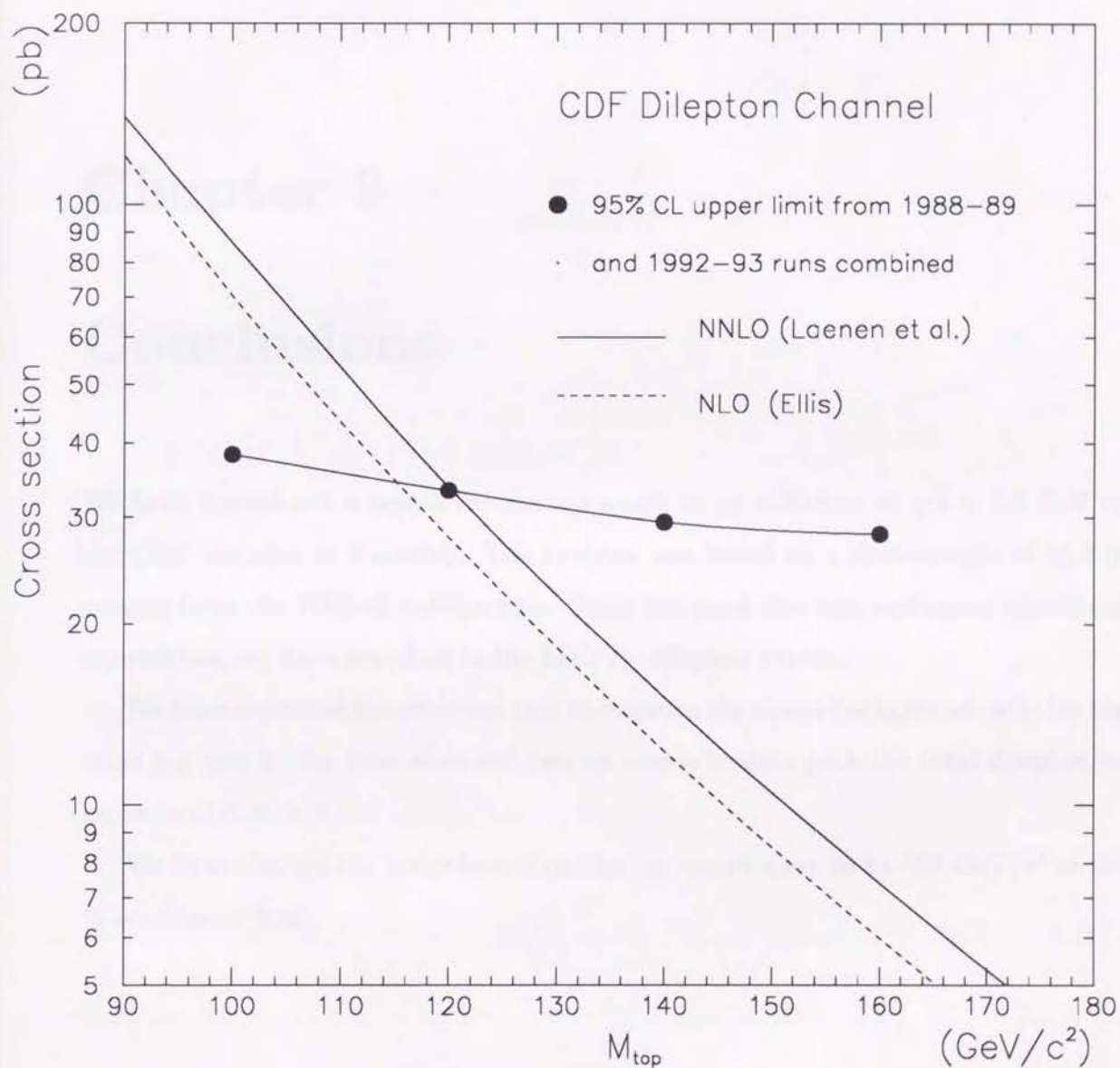


Figure 8.1: The 95-% C.L. on  $\sigma_{t\bar{t}}$  compared with the theoretical lower bound of a next-to-next-to leading order (NNLO) calculation from Ref. [26] and the theoretical lower bound of a next-to-leading order calculation from Ref. [25]



## Chapter 9

### Conclusions

We have carried out a search for the top quark in  $p\bar{p}$  collisions at  $\sqrt{s} = 1.8$  TeV using the CDF detector at Fermilab. The analysis was based on a data sample of  $21.4 \text{ pb}^{-1}$  coming from the 1992-93 collider run. Using the good electron and muon identification capabilities, we have searched in the high  $P_T$  dilepton events.

We have exploited the selection cuts to improve the signal-background ratio for higher mass top quark. We have observed two  $e\mu$  events in data with the total dilepton backgrounds of  $0.56 \pm 0.14$ .

We have also set the lower bound on the top quark mass to be  $120 \text{ GeV}/c^2$  at the 95 % confidence level.

## Appendix A

# Calculation of Upper Limits on Poisson Processes

In this appendix we briefly present and justify the equations we used to calculate upper limits on the  $t\bar{t}$  production cross section. In section A.1 we describe the calculation of upper limits in the simplest case, namely when there are no systematic uncertainties. Next we consider the case where there is background, and in the final section we incorporate the effect of systematic uncertainties.

### A.1 Upper limits without systematic uncertainties

If systematic errors are negligible in a counting experiment, the results of the counting is distributed according to the Poisson distribution:

$$P(\mu : n) = \frac{e^{-\mu} \mu^n}{n!},$$

where the mean  $\mu$  is the average number of observed events over a large number of experiments.

Confidence levels for Poisson distributions are usually defined in terms of quantities called 'upper limits': the C.L. associated with a given upper limit  $N$  and an observed



value  $n_0$ , is the probability that  $n > n_0$ . if the mean of th distribution is  $\mu=N$ . In other words, if the mean of the Poisson distribution is greeter or equal than the upper limit  $N$ , then the probability of observing  $n_0$  or fewer events is lower than or equal to 1-C.L..

## A.2 Upper Limits with systematic uncertainties

Systematic uncertainties are incorporated with the help of Gaussian smearing functions. Let  $\sigma_B$  be the uncertainty on the expected background  $\mu_B$ ,  $\sigma_S$  the *fractional* uncertainty on the expected signal  $\mu_S$ , and define:

$$G(x; \mu, \sigma) = A(\mu, \sigma) e^{-\frac{(x-\mu)^2}{2\sigma^2}} \quad (\text{A.1})$$

where  $A$  is a normalization factor:

$$A(\mu, \sigma) \int_0^\infty G(x; \mu, \sigma) dx = 1 \quad (\text{A.2})$$

It is important to realize that this normalization condition defines  $A$  as a *function* of  $\mu$  and  $\sigma$ . Upper limits are obtained by solving the following equation for  $N$ :

$$1 - \text{CL} = \int_0^\infty P_\mu(n) G(x; \mu, \sigma) dx \quad (\text{A.3})$$

# Bibliography

- [1] S.L. Glashow, Nucl. Phys. 22, 579(1961)  
S. Weinberg, Phys. Rev. Lett. 19, 1264 (1967)  
A. Salam, "in Elementary Particle Theory", edited by N.Svartholm (Almqvist and Wiksell, Sweden, 1968), p.367
- [2] S. Abachi et al.(D0 Collaboration), FERMILAB-Pub-94/004-E (1994).
- [3] C. Arbajar et al.(UA1 collab.), Z.Phys.C48(1990) 1.
- [4] T. Akkeson et al.(UA2 collab.), Z.Phys.C46(1990) 179.
- [5] F. Abe et al. (CDF collab.), Phys. Rev. Lett. 64(1990)142. and 147.
- [6] F. Abe et al. (CDF collab.), Phys. Rev. Lett. 64 147(1990)
- [7] F. Abe et al. (CDF collab.), Phys. Rev. Lett. 68, 447(1992)  
F. Abe et al. (CDF collab.), Phys. Rev. D45, 3921 (1992)
- [8] W. Bartle et al., Phys. Lett. 146B, 437 (1984)
- [9] U. Amardi et al., Phys. Rev. D36 (1987) 1385.  
G. Costa et al., Nucl. Phys. B297, 244(1988)  
J. Ellis and G.L. Fogli, Phys. Lett. B213, 526(1988) and B232, 139(1989)
- [10] J. Ellis and G.L. Folgi, Phys. Lett. B232 139 (1989)  
P.Langacker, Phys. Rev.Lett. 63 1920 (1989)  
J. Ellis and G.L. Folgi, Preprint CERN-TH. 5817/90 (1990)



- [11] W. Hollick, Proceedings of the XVI international Symposium on Lepton-Photon Interactions, 10-15, August 1993, to be published.
- [12] W. Bartel et al., CLLEO collab., Phys. Lett., 146B 437 (1984)
- [13] G.L. Kane and M. Peskin, Nucl. Phys. B195, 29 (1982)
- [14] A. Bean et al.(CLEO), Phys. Rev. D35 3533 (1987)
- [15] H. Arbrecht et al., ARGUS Collab., Phys. Lett., 192B 245 (1987)
- [16] C. Albajar et al., Phys. Lett. B186 247(1987)
- [17] I.I. Bigi and A.I.Sanda Phys. Rev. D29 1393(1984)
- [18] B. Adeva et.al., Phys. Lett. 241B, 416(1990)  
D.Decamp et. al., Phys. Lett. 244B, 551(1990)
- [19] F. Abe et al., CDF collab., Phys. Rev. Lett. 69, 28 (1992)
- [20] W.J. Marciano and A. Sirlin, Phys. Rev. D29, 945(1984)
- [21] C. Albajar et al.(UA1 Collaboration), Z.Phys. C37, 505(1988)
- [22] A.D. Martin, R.G. Roberts, W.J. Stirling, Z. Phys. C42, 277 (1989)
- [23] Alterelli, M.Diemoz, G. Martinelli and P.Nason, Nucl. Phys.
- [24] G. Alterelli, M.Diemoz, G. Martinelli and P.Nason, Nucl. Phys. B308, 724 (1988)
- [25] P. Nason, S. Dawson and R.K. Ellis, Nucl.Phys. B303, 607(1988).  
R.K. Ellis, FERMILAB-Pub-91/30-T, 1991.
- [26] E. Laenen, J. Smith, and W.L.van Neerven, Nucl. Phys. B369 543(1992); Fermilab-Pub-93/270-T
- [27] V. Barger and R. Phillips, Collider Physics, Collider Physics, Addison-Wesley Publishing Company (1987).

- [28] F. Abe et al., CDF collab., Nucl. Instr. Meth. A271, 387(1988)
- [29] K. Hara et al. "Cosmic-Ray Test of the CDF Central Muon Upgrade Chambers", CDF internal note 1513 (1992)
- [30] F. Paige and S.D. Protopopescu, BNL Report No.BNL 38034, 1986 (unpublished)
- [31] E.J. Eichten, I.Hinchliffe, K.D. Lane C. Quigg, Rev.Mod.Phys. 56 579 (1984)
- [32] G.C Fox and S. Wolfram, Nucl. Phys. B 168 (1980) 285;  
T. Sjostrand, Phys. Lett. B157 (1985) 321
- [33] C. Peterson, D.Schlatter, I.Schmitt, and P.Zerwas Phys. rev. D27 105(1983)
- [34] P. Avery, K. Read, and G. Trahern, Cornell Internal Note CSN-212 (1985) Unpublished.
- [35] R. G. Wagner (unpublished), based on calculations by F. Berend et al., Z. Phys. C27, 155 (1985)
- [36] J. Proudfoot, CDF internal note 935 (1989)
- [37] R.M. Harris, CDF internal note 1329.
- [38] M. Miller CDF internal note 1086
- [39] F. Abe et al. Phys. Rev. D44 29 (1991)
- [40] A. Gordon, D. Kestenbaum, M. Franklin and P. Hurst, CDF internal note 1811
- [41] L. Keeble and B. Flaughter, CDF internal note 1513
- [42] S. Kopp, CDF internal note 1942 J. Konigsberg and A.Gordon, Private communication.  
T. LeCompte, T. Liss and A. Martin, CDF internal note 2367
- [43] Private communication.



- [44] J.Wang and M. Contreras, CDF internal note 2108
- [45] F. Abe et al., Phys. Rev. D44, 29(1991)
- [46] L. Song et al., CDF internal note 2106
- [47] J. Ohnemus, Phys.Rev. D44, 1403(1991)  
J. Ohnemus, Phys. Rev. D44, 3477(1991)
- [48] M.L Mangano, Nucl. Phys. B405, 536(1993)
- [49] G.Marchesini and B.R Webber, Nucl.Phys. B310, 461(1988)  
G.Marchesini et al., Comput.Phys.Comm. 67, 465(1992)
- [50] S.Kopp, CDF internal note 2391
- [51] T.Han and S. Parke, Phys. Rev. Lett. 71 1494 (1993)



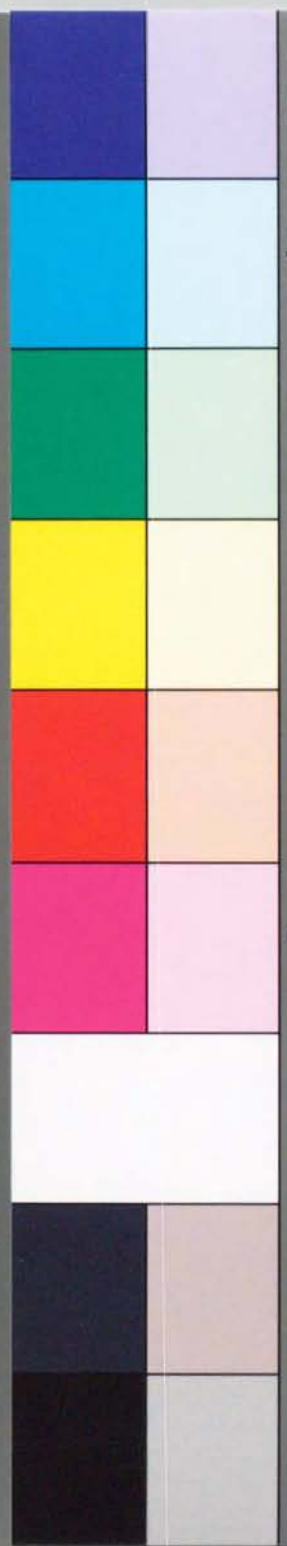


inches 1 2 3 4 5 6 7 8  
cm 1 2 3 4 5 6 7 8 9 10 11 12 13 14 15 16 17 18 19

# Kodak Color Control Patches

© Kodak, 2007 TM: Kodak

Blue Cyan Green Yellow Red Magenta White 3/Color Black



## Kodak Gray Scale



© Kodak, 2007 TM: Kodak

A 1 2 3 4 5 6 M 8 9 10 11 12 13 14 15 B 17 18 19

